Synthesis of Organic-Inorganic Hybrid Ferroelectric Materials and their Utility in Mechanical Energy Harvesting Applications

A Thesis

Submitted in Partial Fulfillment of the Requirements

for the Degree of

Doctor of Philosophy

by

Swati Deswal

ID: 20152030

Department of Chemistry

Indian Institute of Science Education and Research, Pune

2022

Dedicated to

My Parents

भारतीय विज्ञान शिक्षा एवं अनुसंधान संस्थान, पुणे
INDIAN INSTITUTE OF SCIENCE EDUCATION AND RESEARCH (IISER), PUNE
(An Autonomous Institution, Ministry of Human Resource Development, Govt. of India)
Dr. Homi Bhabha Road, Pune 411008.

Dr. R. Boomi Shankar
Professor
Department of Chemistry
IISER Pune

CERTIFICATE

Certified that the work incorporated in the thesis entitled "***Synthesis of Organic-Inorganic Hybrid Ferroelectric Materials and their Utility in Mechanical Energy Harvesting Applications"*** submitted by **Ms. Swati Deswal** was carried out by the candidate, under my supervision. The work presented here or any part of it has not been included in any other thesis submitted previously for the award of any degree or diploma from any other university or institution.

Date: 31st December 2021

Place: Pune

Prof. R. Boomi Shankar
(Research Supervisor)

boomi@iiserpune.ac.in •Ph: +91-20-25908208

भारतीय विज्ञान शिक्षा एवं अनुसंधान संस्थान, पुणे
INDIAN INSTITUTE OF SCIENCE EDUCATION AND RESEARCH (IISER), PUNE
(An Autonomous Institution, Ministry of Human Resource Development, Govt. of India)
Dr. Homi Bhabha Road, Pune 411008.

DECLARATION

I declare that this written submission represents my ideas in my own words and where other's ideas have been included; I have adequately cited and referenced the original sources. I also declare that I have adhered to all principles of academic honesty and integrity and have not misrepresented or fabricated or falsified any idea/data/fact/ source in my submission. I understand that violation of the above will be cause for disciplinary action by the Institute and can also evoke penal action from the sources which have thus not been properly cited or from whom proper permission has not been taken when needed.

Date: 31st December 2021 **Ms. Swati Deswal**

Place: Pune **ID: 20152030**

Acknowledgements

I am greatly indebted and grateful beyond words to my thesis advisor and supervisor Prof. R. Boomi Shankar, who has been instrumental in guiding my doctoral research, evolving my skills and providing all the necessary resources required for completing this thesis. I have had a great learning experience and excellent scientific training while working with him over the last four and half years at IISER-Pune.

I also thank my research advisory committee, which constitutes Dr. Pramod Pillai and Dr. Moumita Majumdar for their invaluable inputs in determining my research goals and also for keeping me encouraged, motivated, and focused on the objectives of my doctoral research.

I extend my sincere gratitude to all my collaborators Prof. Satishchandra Ogale (IISER Pune), Prof. Thomas Anthopoulos (KAUST, Saudi Arabia), Prof. Dinesh Kabra (IIT-Bombay), Dr. Jan K. Zaręba (Wroclaw, Poland), Dr. B. Praveenkumar (ARDE, DRDO) and Parveen Nasa and their respective students, Dr. Sachin, Dr. Dipti, Dr. Richa, Priyangi and Prashant for their cooperation and help in performing the experiments.

I also thank all faculties and non-teaching staff of the Department of Chemistry for their support and easy disposal of the formalities necessary to drive my academics. I am grateful to my family and friends for keeping faith in me and showing confidence in me. I express my deepest gratitude to my lab mates for all the help, friendship, and their collaborative and supportive environment.

Contents

Contents

Contents

Synopsis

*The thesis entitled "**Synthesis of Organic-Inorganic Hybrid Ferroelectric Materials and their Utility in Mechanical Energy Harvesting Applications**" focuses on the synthesis of non-centrosymmetric polar organic-inorganic hybrid salts supported by organo-ammonium, –phosphonium and alkylated-phosphazenium cations and mono and multi-atomic anions, examining their crystal structures, ferroelectric, piezoelectric and dielectric behaviour and employing them for mechanical energy harvesting and storage applications.*

Chapter 1: Introduction

This chapter presents a brief introduction to the fundamentals of dielectrics, piezoelectrics, pyroelectrics and ferroelectrics. Particularly, an overview of molecular ferroelectrics encompassing diverse organic and hybrid organic-inorganic ferroelectric materials has been comprehensively described. Furthermore, literature with notable examples on the use of piezoelectric and ferroelectric materials and their polymeric composites towards mechanical energy harvesting applications have been highlighted. Finally, an outline of the present thesis is discussed.

Chapter 2: Flexible Composite Energy Harvesters from Ferroelectric A_2MX_4 type Hybrid Halogenometallates

Two new molecular organic-inorganic hybrid halogenometallates $[BnNMe_2R]CdBr_4$ (Bn = benzyl; **1**: R = Me; **2**: R = n-Pr) have been synthesized and found to crystallize in the acentric crystal systems suitable for ferroelectric behaviour. Both these compounds exhibit well-resolved rectangular polarization vs. electric field (*P*-*E*) hysteresis loops at room temperature for their polycrystalline thin films. The compounds **1** and **2** exhibited fairly high remnant polarization (P_r) values of 18.59 and 14.24 μCcm^{-2}, respectively. Moreover, flexible composite thin-films of these halogenometallate salts with polydimethylsiloxane (PDMS) were prepared and employed as mechanical energy harvesting devices using an impact test setup operating at a frequency of 25 Hz and an applied force of 40 N. The maximum output voltages of 52.9 V and 63.8 V have been recorded for the PDMS-fabricated devices of 5 wt.% of **1** and 10 wt.% of **2**, respectively. Also, the obtained power densities of 13.8 and 37.1 μWcm^{-2} for the respective 5 wt.% **1**-PDMS and 10 wt.% **2**-PDMS

devices are much higher than all known devices made up of organic-inorganic hybrid materials embedded in PDMS. The energy harvested from these devices was further utilized to charge a capacitor through a full-wave bridge rectifier (Figure 1).

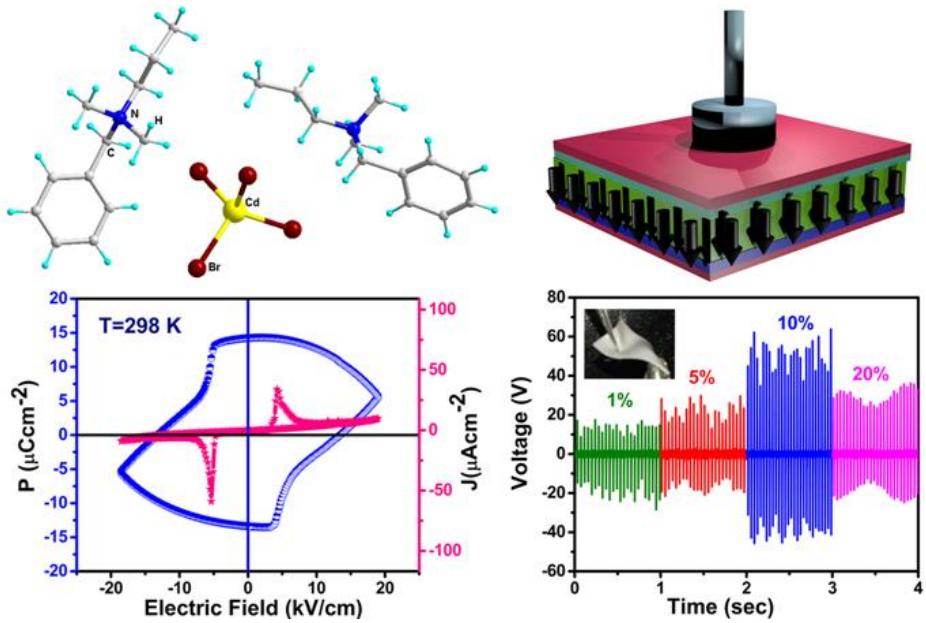

Figure 1: *Molecular structure of [BnNMe$_2$^{n}Pr]CdBr$_4$ and its ferroelectric hysteresis loop. The output voltages obtained from the fabricated devices with various loading percentages of [BnNMe$_2$^{n}Pr]CdBr$_4$.*

Chapter 3: Neutral 1D-Perovskite Type ABX$_3$ Ferroelectric with High Mechanical Energy Harvesting Performance

Organic-inorganic ABX$_3$ hybrids with perovskite structures have drawn enormous attention owing to their intriguing chemical variability, structural tunability and diversity of application-worthy properties. Herein, we report the synthesis of a new neutral ABX$_3$ hybrid ferroelectric compound [Me$_3$NCH$_2$CH$_2$OH]CdCl$_3$ (**1**), which exhibits a 1D-chain structure of edge-sharing CdCl$_5$O octahedra that are connected to the cationic [Me$_3$NCH$_2$CH$_2$OH]$^+$ units via its peripheral OH functionality. The single-crystal X-ray diffraction analysis of the compound at 363 K reveals the conversion of **1** to its coordination isomer **1'**, in which the anionic chain consists of face sharing CdCl$_6$ octahedra and the cations are uncoordinated. The piezoresponse force microscopy (PFM) analysis performed on a single crystal of **1** confirms the existence of polarizable domains in it. The ferroelectric *P-E* loop measurements on **1** show a high remnant

polarization value of 17.1 μCcm^{-2}. Composite devices based on **1** and polydimethylsiloxane (PDMS) prepared with varying wt % are examined for mechanical energy harvesting application. A highest open-circuit voltage of 55.2 V and a maximum power density of 70.9 μWcm^{-2} at an optimal load of 4 MΩ were obtained for the 15 wt % 1-PDMS device. The harvested energy is shown to be effective for capacitor charging and LED flash lighting applications (Figure 2).

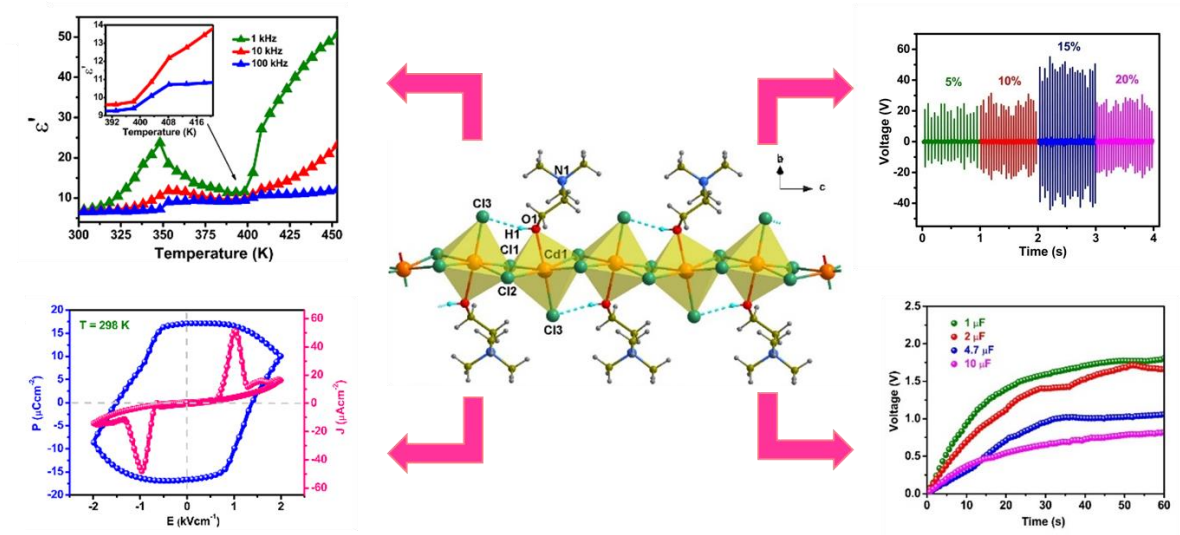

Figure 2: *View of the molecular structure of [$Me_3NCH_2CH_2OH$]$CdCl_3$ and its dielectric, ferroelectric and piezoelectric properties together with its energy-storing capabilities.*

Chapter 4: Piezoelectric Energy Harvesting from a Discrete Hybrid Bismuth Bromide Ferroelectric Templated by Phosphonium Cation

Bismuth containing hybrid molecular ferroelectrics are receiving tremendous attention in recent years owing to their stable and non-toxic composition. However, these perovskite-like structures are primarily limited to ammonium cations. Herein, we report a new phosphonium based 0D perovskite-like hybrid ferroelectric with a formula $[Me(Ph)_3P]_3[Bi_2Br_9]$ (MTPBB) and its mechanical energy harvesting capability. The Polarization-Electric field (*P-E*) measurements resulted in a well-defined ferroelectric hysteresis loop with a high remnant polarization value of 23.6 μC cm^{-2} at 0.1 Hz frequency. Piezoresponse force microscopy experiments enabled visualization of the ferroelectric domain structure and evaluation of the piezoelectric strain coefficient (d_{33}) for MTPBB single-crystal and thin-film sample. Furthermore, flexible devices

incorporating MTPBB in Polydimethylsiloxane (PDMS) matrix at various concentrations were fabricated and explored for their mechanical energy harvesting properties. The champion device with 20 wt. % of MTPBB in PDMS rendered a maximum peak-to-peak open-circuit voltage of 22.9 V and a maximum power density of 7 μW cm^{-2} at an optimal load of 4 MΩ. Moreover, the potential of MTPBB-based devices in low power electronics was demonstrated by storing the harvested energy in various electrolytic capacitors (Figure 3).

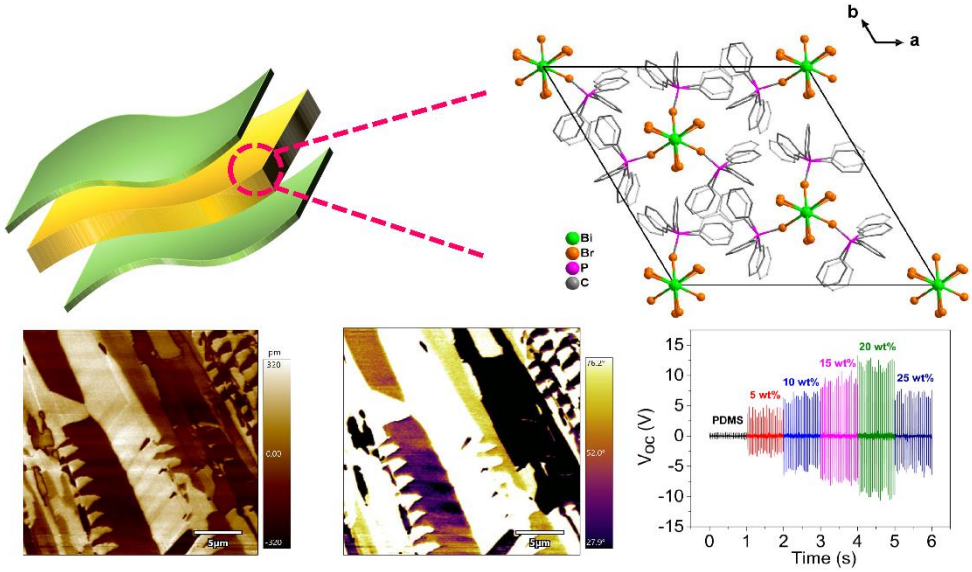

Figure 3: *Schematic of the as-fabricated device using [Me(Ph)$_3$P]$_3$[Bi$_2$Br$_9$] and the PDMS matrix for mechanical energy harvesting application. The figures on the bottom left side are the lateral PFM amplitude and phase response of [Me(Ph)$_3$P]$_3$[Bi$_2$Br$_9$].*

Chapter 5: Design and Mechanical energy harvesting properties of a new ferroelectric N-methylated aminophosphazenium salt

Molecular ferroelectrics are gaining tremendous interest owing to their easy synthesis, structural flexibility and the presence of lightweight and environment-friendly components. Endowed with rich structural diversity and functionality, organophosphazenes have led to significant academic interest for myriad of applications but has scarcely been investigated for ferroelectric applications. Herein, for the first time, we report an organophosphazene based two-component supramolecular ferroelectric [(PhCH$_2$NH)$_6$P$_3$N$_3$Me]I. Due to its polar order, facilitated

by the N-methyl phosphazenium cations and iodide anions, the compound crystallizes in polar acentric space group *Pc* suitable for ferroelectricity. *P-E* measurements reveal a good remnant polarization of 5 μC cm^{-2} on its thin-film sample. Moreover, flexible composites of [PME]I were fabricated for mechanical energy harvesting applications using thermoplastic polyurethane as the matrix. The highest open-circuit voltages of 20.1 V and the maximum power density of 3.2 μW cm^{-2} have been recorded for the 20 wt % [PME]I/TPU device. Importantly, the harvested energy can be successfully stored in various aluminium electrolytic capacitors as would be required for any practical applications. The present work demonstrates the unprecedented example of employing rich cyclophosphazene chemistry in obtaining two-component ferroelectric systems, which will inspire further research in the design of supramolecular ferroelectrics (Figure 4).

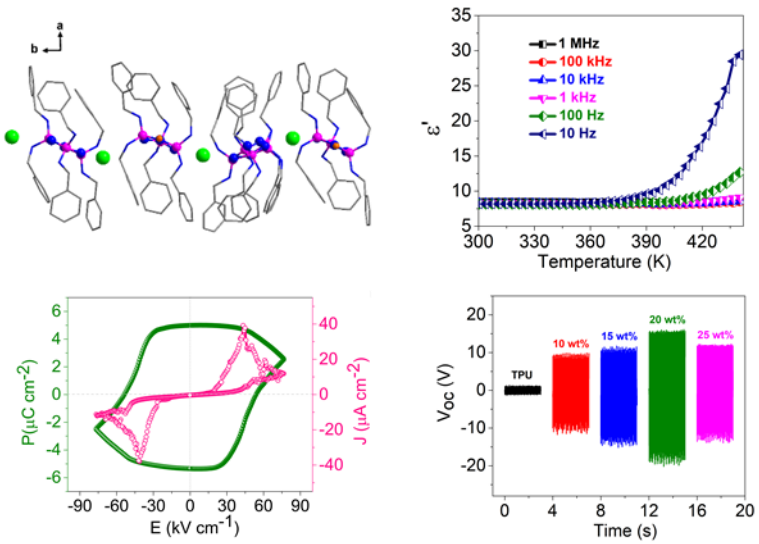

Figure 4: *View of the molecular structure of [(PhCH$_2$NH)$_6$P$_3$N$_3$Me]I, temperature-dependence of the real-part of its dielectric constants, Ferroelectric hysteresis loop and the output performance from its as-fabricated devices in TPU.*

****

Abbreviations

Anal.	Analysis
Calcd.	Calculated
CIF	Crystallographic Information File
DSC	Differential Scanning Calorimetry
DTA	Differential Thermal Analysis
d_{33}	Piezoelectric Coefficient
E_c	Coercive Field
g_{33}	Piezoelectric Voltage Coefficient
ESI	Electron Spray Ionization
FeRAM	Ferroelectric Random Access Memory
FT-IR	Fourier Transform Infrared Spectroscopy
Hz	Hertz
HRMS	High-Resolution Mass Spectrometry
MALDI-TOF	Matrix-Assisted Laser Desorption/Ionization – Time of Flight
MEMS	Micro-electromechanical System
mg	Milligram
min	Minutes
ml	Milliliter
mm	Millimeter
mmol	Millimoles
M.P.	Melting Point
NEMS	Nano-electromechanical System
NMR	Nuclear Magnetic Resonance
PFM	Piezoresponse Force Microscopy
P_r	Remnant Polarization
P_s	Saturation Polarization
PXRD	Powder X-ray Diffraction
RAM	Random Access Memory
RT	Room Temperature
SCXRD	Single Crystal X-ray Diffraction
SEM	Scanning Electron Microscopy
T_c	Curie Temperature
TGA	Thermogravimetric Analysis
V_{oc}	Open Circuit Voltage

Rights & Permissions

Chapter 2

Chapter 3

Publications

Contributions Included in the Thesis:

1. Flexible Composite Energy Harvesters from Ferroelectric A_2MX_4-Type Hybrid Halogenometallates

   Deswal, S.; Singh, S. K.; Rambabu, P.; Kulkarni, P.; Vaitheeswaran, G.; Praveenkumar*, B.; Ogale*, S.; Boomishankar*, R.

   Chem. Mater. **2019**, *31,* 4545-4552.

2. Neutral 1D Perovskite-Type ABX_3 Ferroelectrics with High Mechanical Energy Harvesting Performance

   Deswal, S.; Singh, S. K.; Pandey, R.; Nasa, P.; Kabra*, D.; Praveenkumar*, B.; Ogale*, S.; Boomishankar*, R.

   Chem. Mater. **2020**, *32,* 8333-8341.

3. Piezoelectric Energy Harvesting from a Discrete Hybrid Bismuth Bromide Ferroelectric Templated by Phosphonium Cation

   Deswal, S; Pandey R.; Naphade D. R.; Zareba*, J. K; Anthopoulos* T. D.; Ogale*, S.; Boomishankar*, R.

   (Manuscript under preparation)

4. Design and Mechanical energy harvesting properties of a new ferroelectric N-methylated aminophosphazenium salt

   Deswal, S; Naphade D. R.; Zareba*, J. K; Anthopoulos* T. D.; Ogale*, S.; Boomishankar*, R.

   (Manuscript under preparation)

Contributions not included in the Thesis:

5. Seed Power: Natural Seed and Electrospun Poly(vinyl difluoride) (PVDF) Nanofiber Based Triboelectric Nanogenerators with High Output Power Density

   Singh, S. K.; Kumar, P.; Magdum, R.; Khandelwal, U.; **Deswal, S.**; More, Y.; Muduli, S.; Boomishankar, R.; Pandit*, S.; Ogale*, S.

   ACS Appl. Bio Mater. **2019**, *2,* 3164-3170.

6. Selective Enhancement of Third Harmonic Up-Conversion in 1D Hybrid Pyridinium Lead Iodide with Broad Self-Trapped Excitonic Emission

   Maqbool, S.; Sheikh, T.; Thekkayil, Z.; **Deswal, S**.; Boomishankar*, R.; Nag* A.; Mandal*, P.

   J. Phys. Chem. C **2021**, *125,* 22674–22683.

7. A Flexible Energy Harvester from an All-organic Ferroelectric Ammonium Salt

   Gupta, R.; Sahoo, S.; **Deswal, S**.; Premkumar, K, Dixit, P; Zareba*, J. K; Kadhiravan*, S; Boomishankar*, R.

   Chem. Asian J. **2021**, *16,* 4122-4129.

Chapter 1

Introduction

1.1 Introduction to organic-inorganic hybrid materials for mechanical energy harvesting applications

Materials that find applications in energy, environment, health, and other strategic sectors have been receiving enormous attention lately owing to their significance for emerging global high technologies. Among several classes of materials, organic-inorganic hybrid materials are experiencing unparalleled rapid development in myriad of applications due to their remarkable properties such as solution-based processing, strong optical absorption, high carrier mobility, tailorable exciton diffusion length, and bandgap tunability.[1,2] With a breakthrough established with unprecedented power conversion efficiencies, these materials are currently being perceived as promising materials for next-generation cost-effective solar cells.[3,4] Regardless of the prompt and noteworthy performance exhibited by hybrid perovskites in the field of solar cells, they unfold advancements to a broad range of other applications such as in light-emitting diodes, thin-film transistors, photodetectors, lasers and memory devices.[5-9] It is only in recent times that they have drawn immense attention towards piezoelectric energy harvesting devices owing to the discovery of intriguing ferroelectric properties in these compounds.[10,11]

Although the history of ferroelectrics began in the 1920s with a molecular compound Rochelle salt ($NaKC_4H_4O_6{\cdot}4H_2O$),[12] it was later that inorganic ceramics like BTO ($BaTiO_3$), PZT ($PbZrTiO_3$) dominated the commercial market due to their high polarization and large Curie temperature values.[13-15] Thus, in the early research, numerous inorganic ferroelectric ceramics, semiconductors, PVDF (polyvinylidene difluoride) and its co-polymers were utilized to fabricate piezoelectric energy harvesting devices.[16-22] However, the ceramics suffer from considerable difficulties of toxicity, rigidity and high-temperature syntheses, hindering their applicability for flexible and wearable electronics.[11, 23-26] Though PVDF (polyvinylidene difluoride) and its co-polymers provide flexibility and compliance, their ferroelectric active β phase demands high-voltage poling and high-temperature annealing, thus triggering extensive research in finding suitable alternatives for the high performing inorganic materials.[27-29] In this context, novel materials with high piezo/ferroelectric properties

that can be synthesized within the framework of cost-effective solution processing methods at low temperatures are highly desirable.

This thesis describes the synthesis and characterization of new ferroelectric materials derived from organic-inorganic hybrid ammonium and phosphonium salts and their embedded polymeric composites for piezoelectric energy harvesting applications. This chapter provides a detailed insight into the background and concept of dielectrics and their classification, along with a brief discussion about the mechanism of polarization. It provides essential information on novel examples of ferroelectric materials based on organic-inorganic hybrid compounds and key literature comprising polymer composite mechanical harvesting devices encompassing piezoelectric and ferroelectric materials.

1.2 Dielectric

A dielectric is an insulator, which implies that no current flows through the material on the application of voltage. However, specific changes occur at the atomic scale under the influence of an electric field. As the atoms are constituted of the positively charged nucleus and negatively charged electrons, a slight shift of these positive and negative charges occurs from their equilibrium position, as a result of which electric dipoles are generated. These dipoles deliver dipole moment to the system, and the alignment of these dipoles in the direction of the applied electrical field generates dielectric polarization.[30]

The polarization in a dielectric material occurs due to four polarization mechanisms as discussed below.[31,32]

1. **Electronic Polarization**: This polarization mechanism is experienced by all materials under the influence of an electric field. When an electric field is applied, the nucleus of the atom and the centre of its electron cloud shift away from their equilibrium position, generating a tiny dipole with a minuscule polarization.

2. **Ionic Polarization**: This effect predominantly occurs in ionic compounds, in which the ions are symmetrically positioned in a crystal lattice. On the

application of an electric field, the positive and negative ions start moving in opposite directions, resulting in a relatively more significant displacement as compared to electronic polarization.

3. **Dipole (or Orientation) Polarization**: This happens in materials that possess permanent dipole moment. When such materials are placed under an electric field, they rotate themselves in the direction of the applied field, creating a net average dipole moment per molecule.

4. **Space Charge (or Interfacial) Polarization**: This phenomenon primarily emanates from peripheral charges that happen to arise from contaminants or irregular geometry in the interfaces of polycrystalline solids. These charges are highly mobile and tend to migrate when placed under an electric field, resulting in this extraneous type of polarization.

The extent of polarization that occurs in the dielectric materials directly impacts the amount of electrical energy that can be stored in the electric field. This is defined by a parameter called dielectric permittivity (ε), which is the ability of a substance to store electrical energy in the presence of an electric field.

It is to be noted that the dielectric permittivity of the system is frequency-dependent as each polarization mechanism exhibits different time response potential to applied electric field (Figure 1.1).[31,32]

- Electronic polarization is very swift, and therefore this polarization persists at very high frequencies of 10^{17}
- In comparison to electronic polarization, ionic displacement is a bit slower and occurs at frequencies of 10^{13}
- Orientation polarization is much more time taking than ionic polarization and hence appears at frequencies less than 10^{10}
- Space charge polarization is the slowest and takes place at less than 10^{4}

Thus, the dielectric constant of a material increases with a decrease in frequency as all four polarization mechanism contribute at lower frequencies.

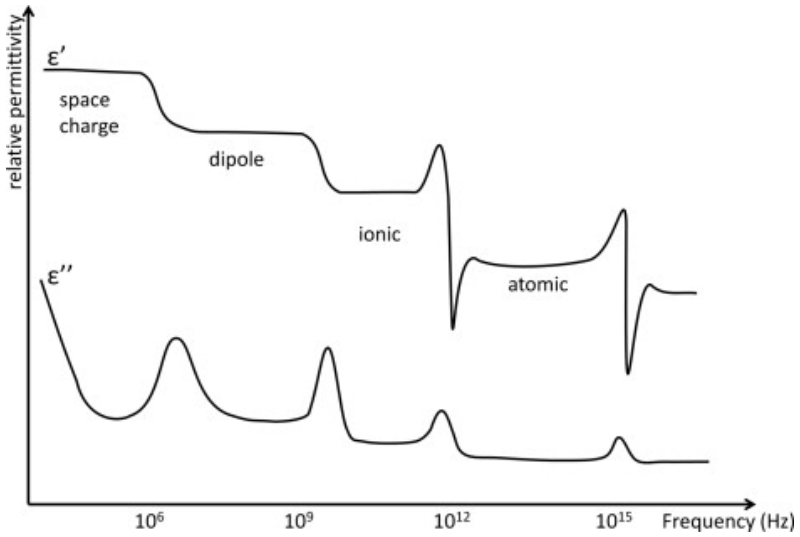

Figure 1.1: *Different polarization mechanism response as a function of frequency. Reprinted from ref 31 Copyright © 2012, with permission from Elsevier.*

A dielectric material gets polarization when placed in an external electric field. In many materials, the degree of polarization varies linearly with the net field and are therefore, referred to as linear dielectrics. Besides, there is some unique class of materials that do not respond to an external field linearly and possess non-zero polarization in the absence of an electric field. Such special class of dielectrics are known as non-linear dielectrics. They display relevant distinct physical phenomenon such as coupling of stress and electric field (piezoelectricity), polarization as a result of thermal gradient (pyroelectricity) and presence of polarization in the absence of electric field which can be reversed on the application of electric field (ferroelectricity) (Figure 1.2). These unique features enable them to be extremely useful in several applications such as capacitors, transformers, dielectric resonators, actuators, motors, transducers, power cables, imaging and data storage etc.[33]

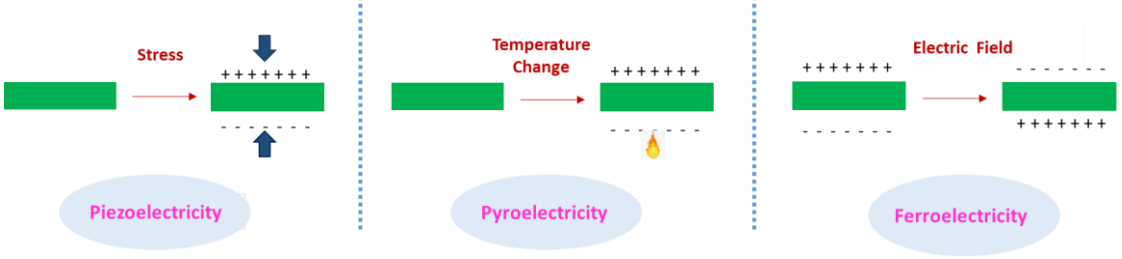

Figure 1.2: *Schematics displaying piezo-, pyro- and ferroelectricity.*

Materials can be either piezoelectric, pyroelectric or ferroelectric depending upon their inherent crystalline symmetricity (lack of centre of inversion). This insight was expressed by Neuman's principle, which states that "*the symmetry elements of any physical property of a crystal must include all the symmetry elements of the point group of the crystal*".[34] Among the existing 32 crystallographic point groups, 11 exhibit centre of symmetry, leaving 21 as non-centrosymmetric point groups (Figure 1.3a). Out of these 21 groups, apart from 432 point group, 20 of them display asymmetric point groups.[35] All the crystals belonging to this class feature piezoelectric properties. Out of the remaining 20 point groups, only 10 hold a unique polar axis, required to exhibit spontaneous polarization in the absence of an electric field, and exhibit pyroelectric and ferroelectric properties. The classification of these materials and their relationship is schematically illustrated in Figure 1.3b. As noted, pyroelectric materials are a subgroup of piezoelectric materials, which in turn are subgroups to ferroelectric materials. Thus, it is obvious that all ferroelectric materials are simultaneously piezoelectric and pyroelectric, while the reverse does not hold true.[35]

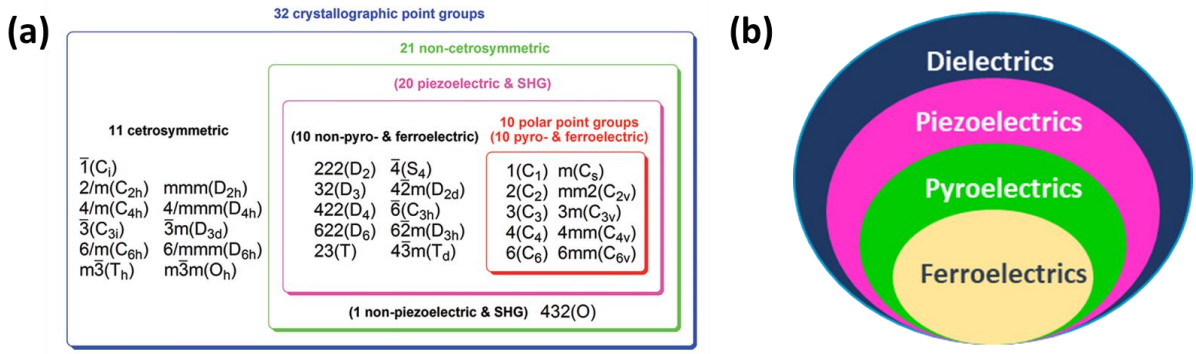

Figure 1.3: *(a) Crystal systems and their division into polar ferroelectric groups. (b) Relationship diagram of dielectrics, piezo-, pyro- and ferroelectrics. Adapted with permission from ref. 35. Copyright © 2012 American Chemical Society.*

1.2.1 Piezoelectric

Piezoelectricity is defined as the coupling phenomenon of mechanical stress and electric charge separation. The phenomenon was first discovered by the brothers Pierre Curie and Jacques Curie in 1880 by using crystals of quartz and Rochelle salt.[36] When an asymmetric crystal structure is subjected to mechanical stress, the crystal structure gets deformed, resulting in the separation of charges labelled as direct

piezoelectric effect (Figure 1.4a). Since the piezoelectric effect is a reversible process, materials that exhibit direct piezoelectric effect also demonstrate converse piezoelectric effect, i.e. induction of mechanical stress upon the application of electric field (Figure 1.4b). While the direct effect finds versatile applications in sensing, microphones, hydrophones and energy harvesting, the converse effect is essential for constructing actuators and motors.[37,38]

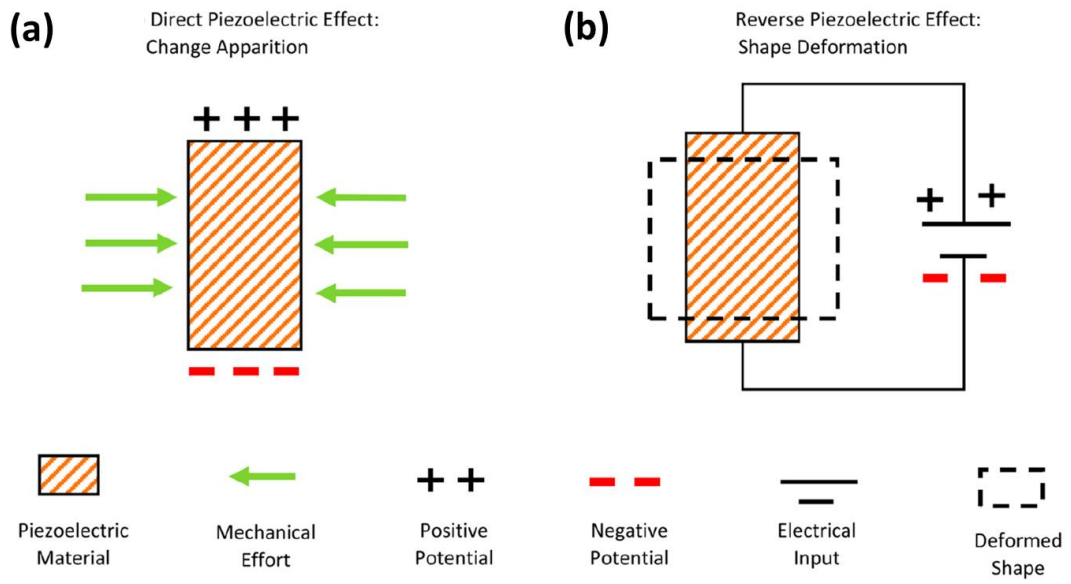

Figure 1.4: *(a) Direct and (b) Converse Piezoelectric Effect. Reproduced from ref 39.*

The direction of applied stress with respect to the polar axis greatly affects the piezoelectric energy harvesting performance. They are comprised by two common modes of operation. Generally, the polar axis is indicated as “3” direction, and the other one at right angles to it are represented as “1” direction. The 33 and 31 mode configurations can be respectively obtained by applying stress either along the polar axis (3) or at right angles (1).[39] The 33 mode signifies the applied stress and voltage generation along the same direction, while 31 mode denotes the application of stress in axial direction and the generation of voltage in the perpendicular direction (Figure 1.5). The piezoelectric material performance is quantified by piezoelectric coefficient (d_{3i}), which is known by two units, pC N^{-1} (direct piezoelectric effect) and pm V^{-1} (converse piezoelectric effect).

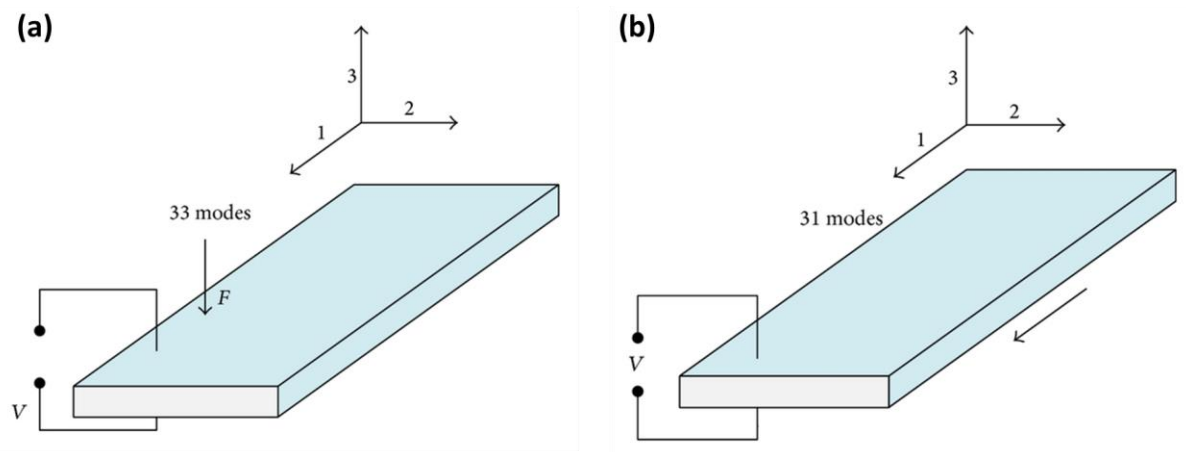

Figure 1.5: *Schematic illustration of (a) d_{33} and (b) d_{31} modes. Reproduced from ref 39.*

1.2.2 Pyroelectric

Pyroelectric materials form an important subclass of piezoelectric materials and are exhibited by crystalline molecules belonging to 10 polar point groups substances (1, 2, m, mm2, 3, 3m, 4, 4mm, 6, 6mm). This effect is defined as the ability of polar materials to produce electrical energy in response to thermal fluctuations. The pyroelectric effect is applied in several fields such as temperature sensing, pyroelectric imaging, infrared detectors, gas analysis and pyroelectric power generation.[40]

1.2.3 Ferroelectric

Ferroelectricity is the ability of a material to possess a spontaneous polarization which can be switched on the application of an external electric field.[41] These materials are a subclass of pyro- and piezoelectrics, and therefore simultaneously display piezoelectricity and pyroelectricity. Compelled by the symmetry considerations, ferroelectrics must adopt one of the ten polar point groups, that is, triclinic 1 (C_1), monoclinic *m* (C_s), 2 (C_2), orthorhombic *mm*2 (C_{2v}), trigonal 3 (C_3), 3*m* (C_{3v}), tetragonal 4 (C_4), 4*mm* (C_{4v}), hexagonal 6 (C_6), and 6*mm* (C_{6v}).[35]

The polarization of ferroelectrics is influenced not only by the applied electric field but also by its history, which affords a *P-E* hysteresis loop. At point O, all the domains are randomly oriented, and hence there is no net polarization in the system (Figure 1.6).

On the application of an external electric field, the polarization tends to orient along the direction of applied field and eventually reaches a state of saturation where all the domains are aligned in one direction. However, upon removing the electric field, the polarization does not annihilate to zero, rather a remnant polarization remains due to the kinetic arrest of polar domains. Further, an electric field in the opposite direction, known as coercive field, is required to bring the molecule back to a state of zero polarization. Similarly, a further increase in electric field in the opposite direction completes the hysteresis loop.[35]

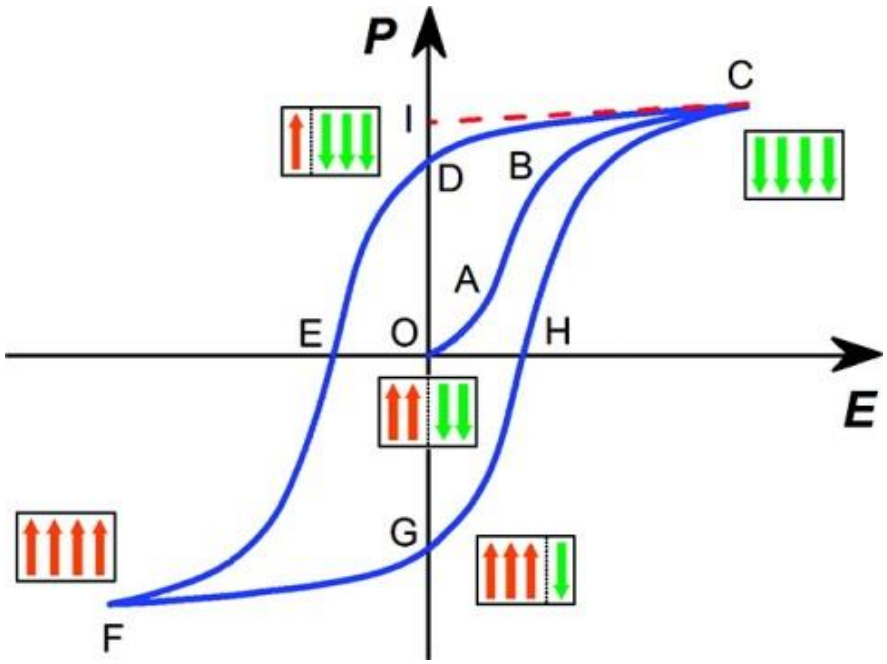

Figure 1.6: *Polarization (P) vs Electric field (E) hysteresis loop. Adapted with permission from ref. 35. Copyright © 2012 American Chemical Society.*

These materials undergo temperature prompted transitions from a low-temperature, low symmetry ferroelectric phase to a high-temperature, high symmetry paraelectric phase at Curie Temperature (T_c).[42] The classification of ferroelectric-paraelectric phase transitions based on the nature of phase change occurring at T_c are broadly classified into 1) displacive and 2) order-disorder type (Figure 1.7). Inorganic ceramics such as $BaTiO_3$ undergo displacive type transition, where spontaneous polarization is created due to the relative displacement of the ions. $NaNO_2$ belongs to the order-disorder type, in which the reorientation of dipolar NO_2 ions produce ferroelectricity.[35]

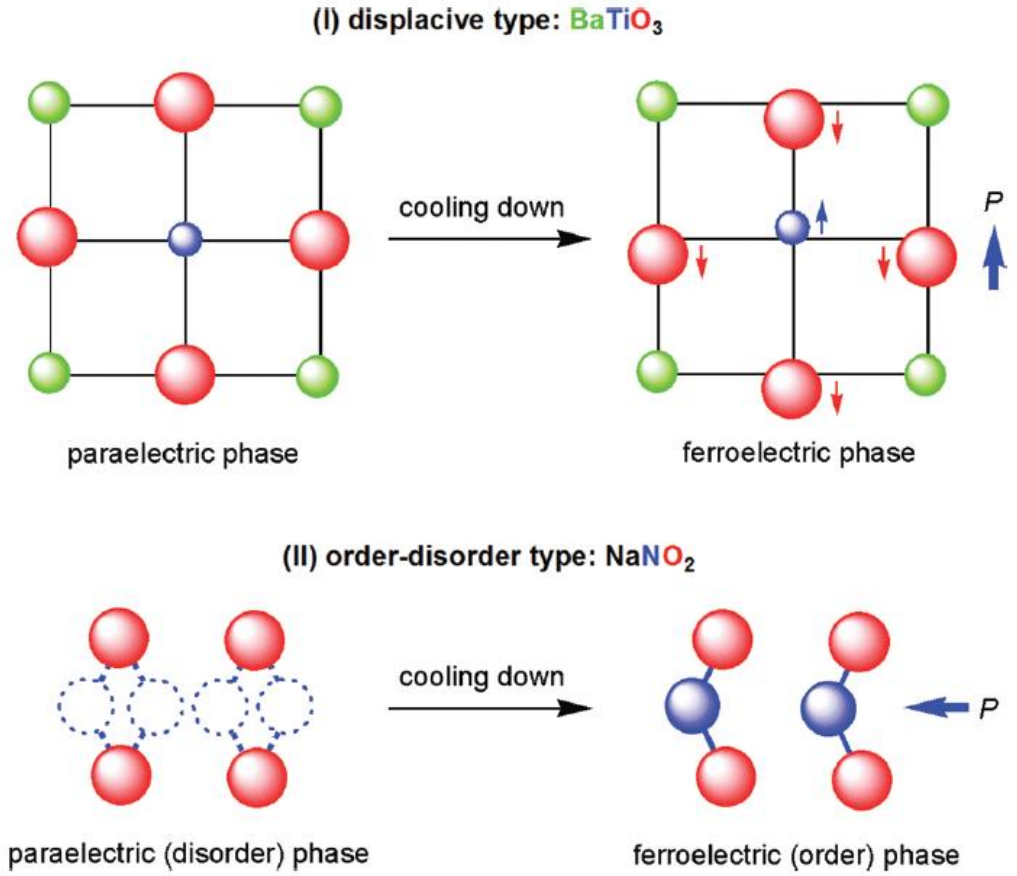

Figure 1.7: *Types of paraelectric-ferroelectric transition. Adapted with permission from ref. 35. Copyright © 2012 American Chemical Society.*

To examine ferroelectricity and associated properties, a wide variety of scientific techniques can be employed. This includes at the foremost studying the asymmetric crystal structure which can be characterized by XRD, SHG, TEM and advanced microscopic techniques.[43] An indispensable proof of ferroelectricity can be afforded by measuring the *P-E* hysteresis loop. The occurrence and the nature of phase transition can be studied by Differential scanning calorimetry and temperature-dependent dielectric permittivity measurements. Solid evidence of ferroelectricity can also be furnished by engaging independent methods such as piezoelectric and pyroelectric measurements.

1.3 History of Ferroelectric materials and their classification

The history of ferroelectrics can be traced back to 1920, when Valasek explored the hysteresis nature of Rochelle salt polarization (sodium potassium tartrate tetrahydrate,

$NaKC_4H_4O_6 \cdot 4H_2O$) and consequently coined the term “ferroelectric” to reflect its resemblance with ferromagnetism.[12] For a very long period, it was the only known ferroelectric material, until Busch and Scherrer discovered ferroelectricity in KDP (potassium dihydrogen phosphate, KH_2PO_4) in 1935.[44] However, the instability, low ferroelectric polarization and poor crystal stability under ambient conditions prevented any technological application of these materials. A major breakthrough was established in 1940 when the first non-hydrogen bonded perovskite ferroelectric ceramic $BaTiO_3$ (BTO) was discovered.[45] Soon after its discovery, a lot of ferroelectric ceramics with perovskite structure such as Pb (Zr, Ti) O_3 (PZT), $LiNbO_3$ (LNO), $KNbO_3$ (KNO) etc. were discovered, which occupied the mainstream with remarkable ferroelectric polarization and great utilization potential.[46,47]

Attributed to the superior performance and stability of the oxides, they find relevance to a significant number of industrial and commercial applications such as high dielectric constant capacitors, non-volatile memory elements, piezoelectric sonar and ultrasonic transducers, actuators, ferroelectric thin film memories and more recently in the arena of mechanical energy harvesting devices.[48,49] Nevertheless, the high processing temperatures, structural rigidity, time-consuming fabrication techniques, high cost, and the usage of toxic element such as Pb impedes their dynamic utilization for future flexible and wearable electronics.

To address these growing issues, researchers have intensified the quest for obtaining new flexible and heavy metal-free ferroelectric systems as viable alternatives to their inorganic counterparts. This was followed by the discovery of strong piezoelectricity and ferroelectricity in polyvinylidene fluoride (PVDF) and its co-polymers, favouring them for many applications as they are highly flexible and durable.[50,51,52] However, the coercive field for polarization reversal in these materials is extremely high as the process necessitates the rotation of side groups around the main chain.

Alternatively, low molecular weight organic and organic-inorganic hybrid molecular ferroelectric materials have been the focus of current research as they are comprised of lightweight elements, flexibility, structural tunability, environment-friendliness, ease of low-temperature processing, low coercive field, and noteworthy ferroelectric properties.[11]

Molecular ferroelectrics are generally classified into organic and organic-inorganic hybrid ferroelectrics. In this regard, the current section underlines some key examples of ferroelectrics derived from organic and hybrid materials.

1.4 Organic Ferroelectrics

This class of ferroelectrics is highly desirable for wearable and flexible electronics as they contain lightweight elements, exhibit structural tunability, flexibility and easy processability and are environment-friendly compared to their inorganic counterparts.[53,54] Several organic ferroelectrics based on thiourea, TEMPO, (2,2,6,6-tetramethyl-1-piperidinyloxy), Benzil, DNP (diacetylene-1,6-bis(2,4-dinitrophenoxy)-2,4-hexadiyne), CDA (cyclohexane-1,1-diacetic acid), TCAA (trichloro acetamide), etc. have been realized but most of these suffered from low polarization and Curie temperature values.[53, 55-58]

In an effort to develop efficient and robust molecular ferroelectric materials, significant breakthroughs were achieved for low molecular weight single-component organic compounds and two-component ionic systems. For instance, croconic acid belongs to the class of single component hydrogen-bonded ferroelectrics that possess a high polarization value of 21 μC cm^{-2} and a relatively lower coercive field of 14 kV cm^{-1}.[59] Polarization switching in this molecule occurs due to change in the chemical structure polarity which is induced by π-bond switching and intermolecular proton-transfer process (Figure 1.8a, b). Remarkably, croconic acid did not display any phase transitions upto 400 K, thereby marking the absence of any Curie temperature in the material.

Amongst several well-known two-component ionic ferroelectrics, a milestone in the field of molecular ferroelectrics was achieved by the bromide salt of diisopropyl ammonium cation (DIPAB) that displays a strikingly high T_c of 426 K and large spontaneous polarization value of 23 μC cm^{-2} (Figure 1.8c, d).[60] Its high stability and outstanding properties position it significantly unique to its chlorine counterpart, which exhibits a polarization of only 8.9 μC cm^{-2}.[61] For both the compounds, an order-disorder transition of N atoms of the diisopropyl unit was responsible for ferroelectric behaviour. Moreover, a very high dielectric constant of ~ 1600 was obtained at a

frequency of 400 Hz, making DIPAB highly attractive as a dielectric in capacitors for energy storage applications.

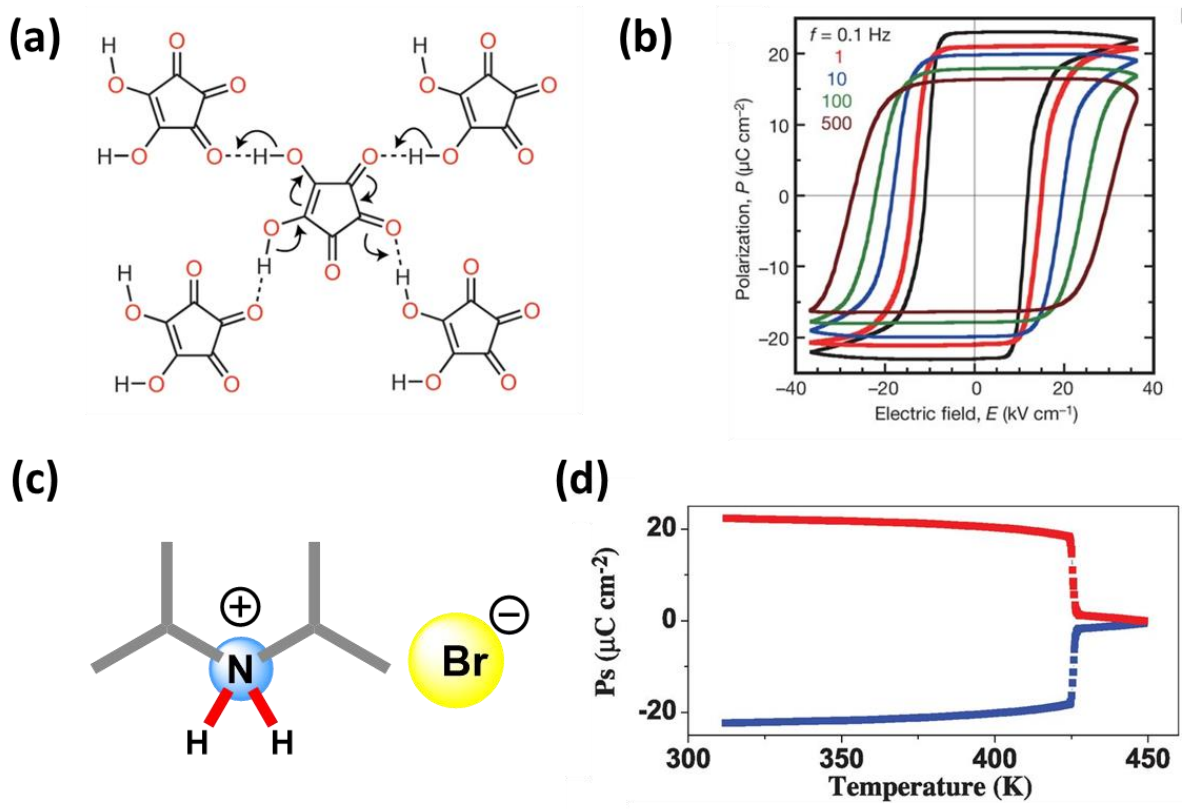

Figure 1.8: *(a) Polarization switching mechanism in croconic acid (b) Ferroelectric hysteresis loop measured on a single crystal of croconic acid. (c) Chemical structure of DIPAB and (d) measurement of its polarization as a function of temperature. Adapted with permission from ref. 54. Copyright © 2015, Nature Publishing Group and ref. 59. Copyright © 2010, Macmillan Publishers Limited. Adapted with permission from ref. 60. Copyright © 2013, American Association for the Advancement of Science.*

1.5 Organic-Inorganic Hybrid (OIH) Ferroelectrics

ABX_3 (X=O) perovskite compositions have featured in many frontiers of research, especially in solar cells, and light-emitting diodes. Additional functionalities and structural flexibilities for these materials have been achieved by introducing organic cations and other anions, such as halides (Cl^-, Br^-, and I^-), azide (N_3^-), cyanide (CN^-), borohydride (BH_4^-), formates ($HCOO^-$) and dicyanamides ($N(CN)_2^-$). According to the employed cations and anions, they have been used to construct a large number of

hybrid frameworks ranging from 3D to 2D and 1D assemblies.[62-66] This section outlines some notable examples of hybrid organic-inorganic materials with pronounced ferroelectric properties.

1.5.1 Three-dimensional halogen-bridged ferroelectrics

Concerning the stability of the 3D perovskite structure, only a few organic cations with appropriate dimensions are permitted inside the voids of octahedral moieties. Besides the typical usage of FA^+(formamidinium) and MA^+(methylammonium) cations, a new concept for forming 3D metal halide perovskite was conceived by Patron et al. in 2010, in which divalent cation H_2dabco^{2+} (1,4-diazabicyclo [2.2.2]octane) occupied the A sites and interacted with $RbCl_3^-$ framework via NH…Cl hydrogen bonds.[67] Motivated by this work, Xiong and co-workers synthesized a new 3D hybrid perovskite (3 AP) $RbBr_3$ (3AP= 3-ammoniopyrrolidinium).[68] The compound was found to crystallize in polar space group *Ia* at room temperature, which undertook a transition to a paraelectric phase at 440 K. This high Curie temperature of 440 K was attributed to the stability of alkali metal halide framework, wherein the well-ordered cations interacted with the host framework through weak hydrogen bonds. Ferroelectric measurements performed on the thin film sample of the compound manifested a relatively good remnant polarization value of 2.3 $\mu C\ cm^{-2}$. Very significantly, the 3D perovskite exhibited 12 equivalent ferroelectric axes signifying their propensity for application in polycrystalline forms.

Aided by molecular design strategy and organic cation template effect, Zhang et al. synthesized a new 3D perovskite ferroelectric [MeHdabco]RbI_3 (MeHdabco = N-methyl-N'-diazabicyclo[2.2.2]octonium) with considerably high T_c of 430 K (Figure 1.9).[69] Construction of a polar crystal structure and ferroelectricity was triggered by endowing $[H_2dabco]^{2+}$ unit with a methyl substituent. The compound displayed a well resolved rectangular *P-E* hysteresis loop on its polycrystalline thin sample. Moreover, iodine doped sample of [MeHdabco]RbI_3 exhibited intense saffron yellow luminescence under UV excitation, expanding its utilization potential in ferroelectric luminescence/multifunctional devices.

A molecular perovskite $(C_4H_{12}N_2)(NH_4Cl_3).H_2O$ was proposed by Bremner et al. in 2002, marking the beginning of metal-free perovskite.[70] To extend potential

ferroelectricity in such a system, Xiong and co-worker in 2018, synthesized a family of ABX_3 metal-free 3D perovskites ferroelectrics with a general formula $A(NH_4)X_3$ (where A is a divalent organic cation and X is Cl, Br, or I) (Figure 1.10).[71]

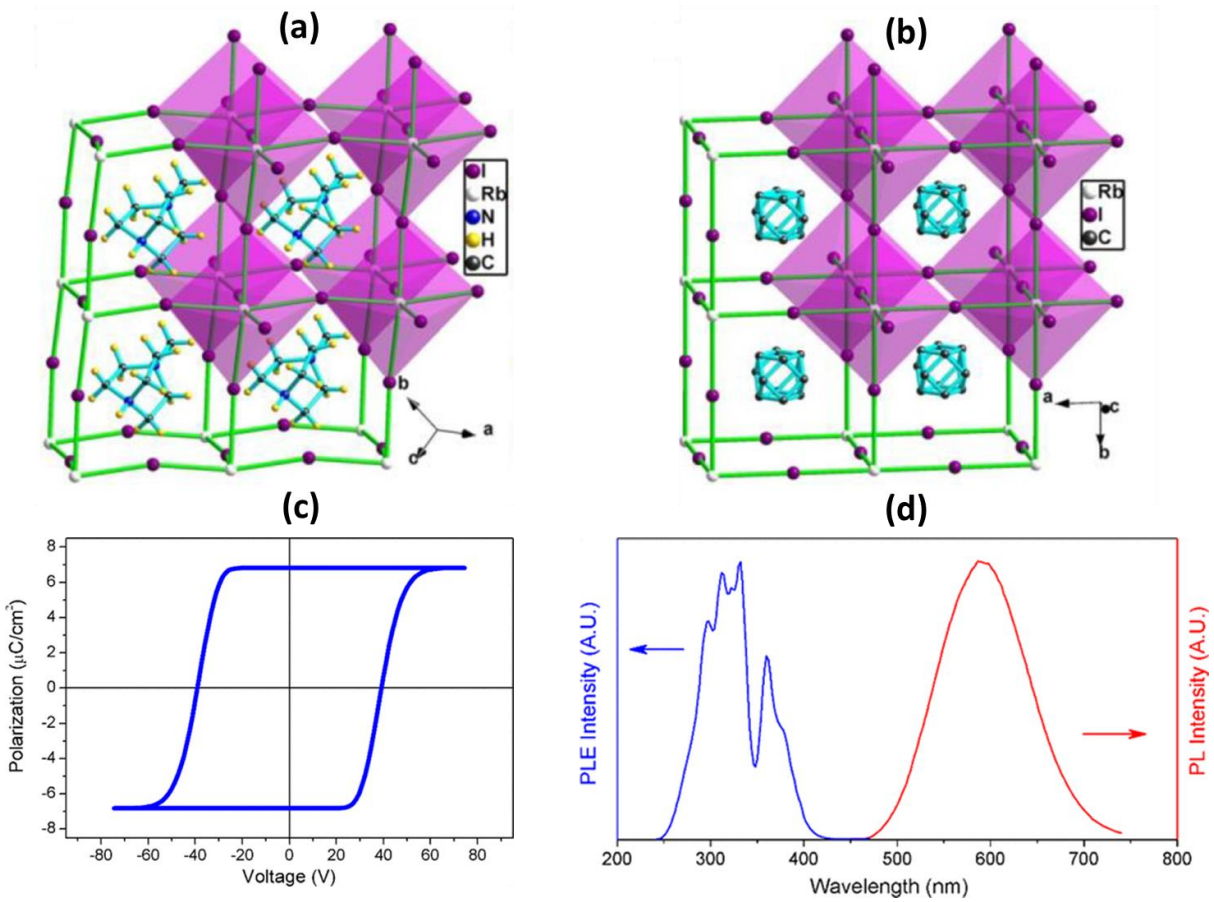

Figure 1.9: *(a) Crystal packing diagrams of [MeHdabco]RbI_3 in the (a) ferroelectric phase at 273 K and the (b) paraelectric phase at 413 K. (c) Ferroelectric hysteresis loops measured on thin film of [MeHdabco]RbI_3 at room temperature. (d) Photoluminescence excitation (blue) and Photoluminescence (red) spectra obtained under excitation using 360 nm. Adapted with permission from ref. 69 Copyright © 2017 American Chemical Society.*

Specifically, $(MeHdabco)NH_4I_3$ exhibits a remarkable spontaneous polarization of 22 $\mu C\ cm^{-2}$ (close to inorganic ceramic BTO, 26 $\mu C\ cm^{-2}$) and a very high Curie temperature of 448 K beyond that of BTO (390 K) along with eight possible polarization directions. Besides this molecule, the authors examined a wide variety of metal-free 3D perovskites by engaging different A-site cations and X anions such as ODABCO-NH_4Br_3 (ODABCO is N-hydroxy-N-diazabicyclo[2.2.2]octonium) and rac-3AP-NH_4Br_3

(rac-3-ammoniopyrrolidinium), (ODABCO)NH_4Cl_3, (rac-3AP)NH_4Cl_3 and (S-3AQ)NH_4Br_3 (S-3AQ = S-3-ammonioquinuclidinium). These materials hold great potential to be applied in the next generation of biomedical devices, soft robotics, flexible devices, and wearable electronics.

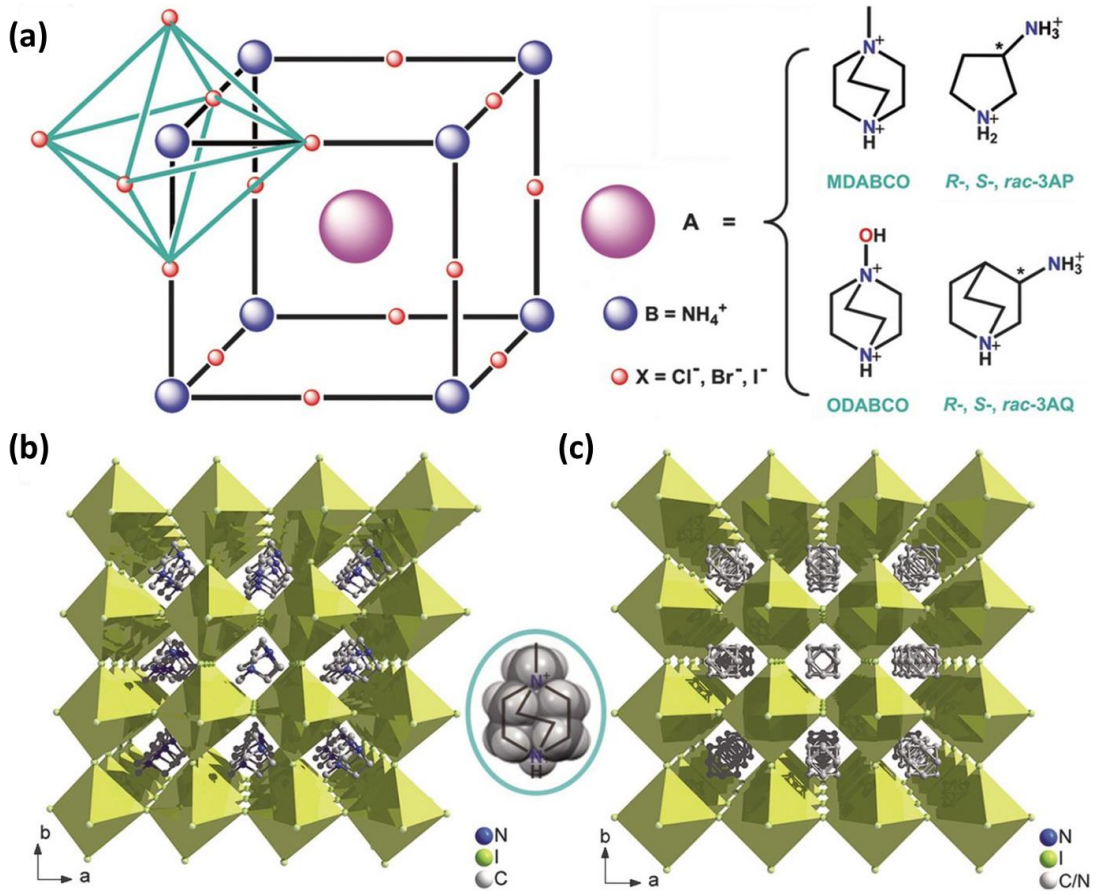

Figure 1.10: *(a) Structures of metal free family of $A(NH_4)X_3$ 3D perovskites. (b) Crystal packing diagram of $(MeHdabco)NH_4I_3$ in the (b) ferroelectric phase at 293 K and (c) the paraelectric phase at 463 K. Adapted with permission from ref. 71. Copyright © 2018 The American Association for the Advancement of Science*.

Till today, most of the employed A sites encompass ammonium-based cations while their corresponding phosphonium analogues have been scantly studied. Recently, Zhang et al. developed a 3D perovskite ferroelectric semiconductor $MPSnBr_3$ by employing methyl phosphonium $[CH_3PH_3]^+$ (MP) as the A-site cation.[72] The compound resulted in the above room temperature ferroelectricity and a direct bandgap of 2.62 eV. Prominently, $MPSnBr_3$ exhibits as many as 12 ferroelectric polar axes implying the

synthesis of a multiaxial 3D ferroelectric semiconductor, rarely seen among organic-inorganic hybrid (OIH) ferroelectrics. Ferroelectric-paraelectric phase transition at 357 K occurred due to the order-disorder transition of the cation and the reorganization of Sn-Br bonds in $[SnBr_3]^-$ framework. Besides the exciting phenomenon of ferroelectricity and semiconducting property, $MASnBr_3$ demonstrates intriguing thermochromism, highlighting its promising deployment towards smart photovoltaic windows.

1.5.2 Two-dimensional halogen-bridged ferroelectrics

Unlike 3D perovskites, 2D hybrid materials have a more comprehensive range for choosing A-site cations, enhanced stability, and a striking range of tunability on B and the X sites. As a result, innovative layered perovskite structures and intriguing physical properties can be realized by chemically tailored protocols.[73-75]

In an interesting study, Li et al. recently reported the first 2D multi-layered hybrid perovskite ferroelectric by alloying mixed organic ammonium cations $(C_4H_9NH_3)_2(CH_3NH_3)2Pb_3Br_{10}$, in which the synergetic ordering of organic moieties accounted for a ferroelectric polarization of 2.9 μC cm^{-2}.[76] It experienced a ferroelectric transition from *Cmc*2$_1$ space group to a paraelectric phase with *Cmca* centrosymmetric space group at Curie temperature of 315 K. Additionally, single-crystal photodetectors constructed on thin wafers displayed exceedingly low dark current, large on/off current ratio and quick response rate. These merits open up immense possibilities of such 2D perovskite ferroelectrics for constructing high performing optoelectronic devices.

Lately, a new phosphonium based 2D hybrid ferroelectric $(EATMP)PbBr_4$ (EATMP = (2-aminoethyl)trimethylphosphanium) was reported by Zhang et al., which possess a very high T_c of 534 K, highest among the known 2D OIH ferroelectrics (Figure 1.11).[77] In contrast to its ammonium analogue EATMA (2-aminoethyl)trimethylammonium), the incorporation of larger phosphonium cation EATMP resulted in the ordered alignment of dipoles at room temperature. Macroscopical polarization reversal examined on its single-crystal resulted in a saturation polarization value of 0.95 μC cm^{-2}, validating its ferroelectricity. Besides ferroelectricity, $(EATMP)PbBr_4$ exhibits semiconducting property with a bandgap of 2.84 eV and a very large electrostrictive coefficient of 3.96 m^{4}C^{-2}, surpassing those of inorganic oxides (~0.034–0.096 m^4 C^{-2}). These findings

encourage further exploration of electrostrictive effects in molecular ferroelectrics for designing smart actuators and transducers.

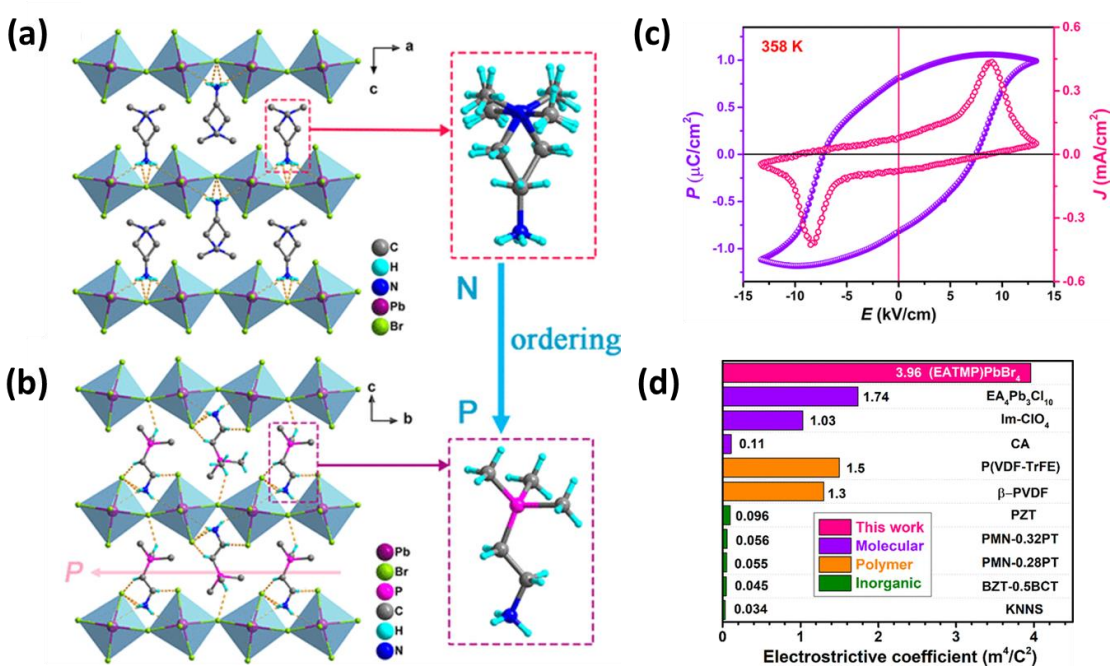

Figure 1.11: *Crystal packing diagrams of (a) (EATMA)PbBr₄ displaying disordered EATMA⁺ cations and (b) (EATMP)PbBr₄ with ordered EATMP⁺ cations at 293 K. (c) Ferroelectric hysteresis loop of (EATMP)PbBr₄ measured at 358 K using the double-wave method. (d) Comparison of electrostrictive coefficient of (EATMP)PbBr₄ with well know inorganic ceramics, polymers and molecular ferroelectrics. Adapted with permission from ref 77 Copyright © 2021 American Chemical Society.*

1.5.3 One-dimensional halogen-bridged ferroelectrics

In recent years, a unique series of hexagonal stacking of ABX_3 typed perovskites are gaining widespread attention due to the discovery of extraordinary ferroelectric and piezoelectric properties in them.

Of late, You et al. discovered a new 1D ABX_3 perovskite $(TMCM)MnCl_3$ (TMCM: trimethylchloromethylammonium), by replacing Me_4N^+ with a $Me_3NCH_2Cl^+$ (TMCM) cation using a quasi-spherical approach (Figure 1.12).[78] The piezoelectric coefficient (d_{33}) measured for this compound reached upto 185 pC N^{-1}, which is well comparable with piezoceramics like BTO(~ 190 pC N^{-1}). Facilitated by the order-disorder transition of the cations from ferroelectric to the paraelectric phase, $(TMCM)MnCl_3$ exhibits a

very high Curie temperature (T_c) of 406 K and a spontaneous polarization value of 4 μC cm^{-2}. Moreover, the same group also synthesized its cadmium (TMCM)$CdCl_3$, which also featured an extremely high piezoelectric coefficient (d_{33} =220 pC N^{-1}). On similar lines, their isomorphs like (TMBM)$MnBr_3$ (TMBM: trimethylbromomethylammonium) and (TMCM)$CdBr_3$ were systematically developed

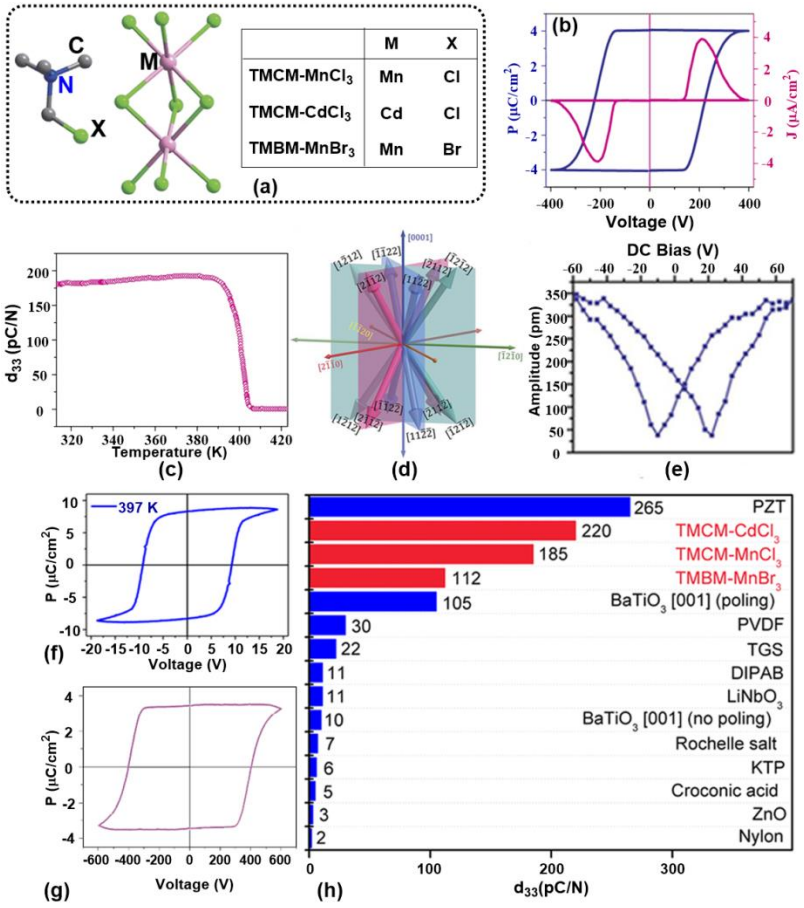

Figure 1.12: *(a) Family of 1D ABX_3 perovskites derived from $(TMCM)^+$ and $(TMBM)^+$ cations. (b) P-E loop along with its corresponding leakage current density plot for (TMCM)$MnCl_3$. (c) (c) Piezoelectric coefficient of (TMCM)$MnCl_3$ as a function of temperature. (d) Photo displaying twelve unique polarization directions in (TMCM)$MnCl_3$ and (e) its amplitude versus bias voltage butterfly loop obtained from PFM measurements. P-E hysteresis loops of (f) (TMCM)$CdCl_3$ and (g) (TMBM)$MnBr_3$. (h) A comparison diagram of measured d_{33} values of these new 1D ABX3 perovskites with a few well-known piezoelectric materials. Adapted with permission from ref. 78. Copyright © 2017 The American Association for the Advancement of Science and ref. 79. Copyright © 2017 American Chemical Society.*

and examined for their piezoelectric properties.[79,80] A relatively high T_c of 415 K and significant piezoelectric coefficient of 112 pC N^{-1} was shown by (TMBM)$MnBr_3$ while, on the other hand, (TMCM)$CdBr_3$ exhibited a lower T_c of 346 K but way larger d_{33} of 139 pC N^{-1}. These favourable merits ensure their candidacy for future micro-electro-mechanical systems (MEMS), flexible devices and biomedical applications.

Though the achieved piezoelectric properties in the examples mentioned above were encouraging, they still did not compete with the high-end PZT ceramics. Thus, in a quest for a higher piezoelectric coefficient, Liao et al. discovered a solid solution $(TMFM)_x(TMCM)_{1-x}CdCl_3$ ($0 \leq x \leq 1$) [TMFM: trimethylfluoromethylammonium] via a molecular design strategy demonstrating the existence of an unprecedented piezoelectric coefficient of 1540 pC N^{-1} at x= 0.26 composition.[81] The morphotropic phase boundary between monoclinic and hexagonal phase at this composition was the main reason for the exceedingly high d_{33} value, almost two times that of commercially employed PZT piezoceramics. This ground-breaking result extends the feasibly of molecular perovskites towards next-generation piezoelectric medical devices.

1.5.4 Cyano-bridged ferroelectrics

In an exciting study by Xiong and co-workers, a multi-axial room temperature ferroelectricity was demonstrated in $[(CH_3)_3NOH]_2[KFe(CN)_6]$(TMAO-Fe), which was seen to exhibit a spontaneous polarization value of 0.55 μC cm^{-2} and very high T_c of 402 K along with 24 equivalent ferroelectric directions (6 in BTO).[82] However, the most distinguishing property of this material is endured by its bond switching mechanism of phase transition (Figure 1.13). The paraelectric to ferroelectric phase transition was triggered by the replacement of K-N bonds with K-O bonds (O from $TMAO^+$ cations) in the low-temperature phase. Being categorized as high temperature molecular ferroelectric, the compound suffered from drawbacks related to its relatively narrow stability of high-temperature phase, restricting its widespread utilization.

Thus, in a subsequent study by Rok et al. in 2020, an isostructural variant of TMAO-Fe was discovered by replacing Fe^{3+} with other trivalent metal cation Co^{3+}.[83] Detailed analysis of the compound depicted an increase in Curie temperature by 10 K and

broadening of separation between T_c and decomposition temperature by 46 K (Figure 1.13d). Moreover, the ferroelectric attributes in the compound remained well preserved, as evidenced by the polarization values of 0.9 and 0.63 μC cm^{-2} along crystallographic axis a and c, respectively (Figure 1.13e). Additionally, a two-fold enhancement in second harmonic generation response was observed compared to TMAO-Fe, which enabled the demonstration of high-temperature SHG switching between on and off states for TMAO-Co (Figure 1.13f). These results shed light on designing highly stable ferroelectrics for a range of emerging optoelectronic applications.

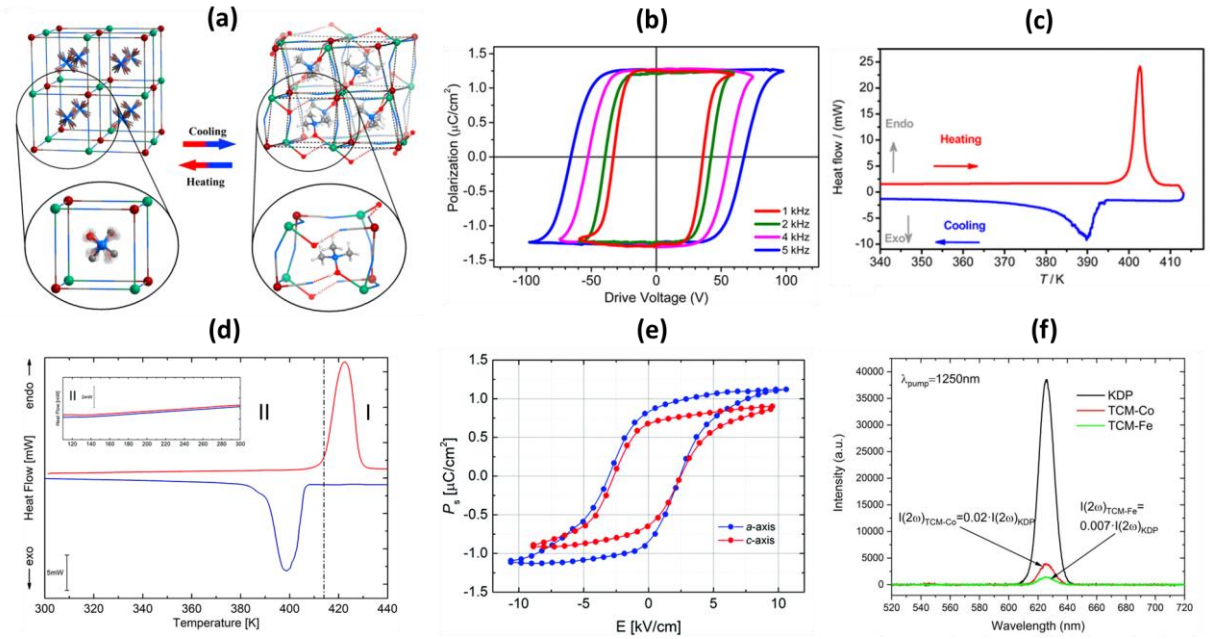

Figure 1.13: *(a) Bond switching mechanism in TMAO-Fe induced by temperature. (b) P-E loop of TMAO-Fe measured at room temperature. DSC curves of (c) TMAO-Fe and (d) TMAO-Co displaying a phase transition at 402 K and 417 K, respectively. (e) Ferroelectric hysteresis loops of TMAO-Co at room temperature. (f) Second Harmonic Generation signals of TMAO-Fe and TMAO-Co with respect to standard KDP. Adapted with permission from ref. 82. Copyright © 2017 American Chemical Society and ref. 83. Copyright © 2020 The Royal Society of Chemistry.*

1.5.5 Formate-bridged ferroelectrics

They have a general formula of (Cation) $[M^{II}(HCOO)_3]$ or $(Cation)_2[M^{I}M^{III}(HCOO)_6]$, which comprises six connected nodes of octahedral $[MO_6]$ units bridged by $HCOO^-$ anions in anti-anti coordination mode.[84,85]

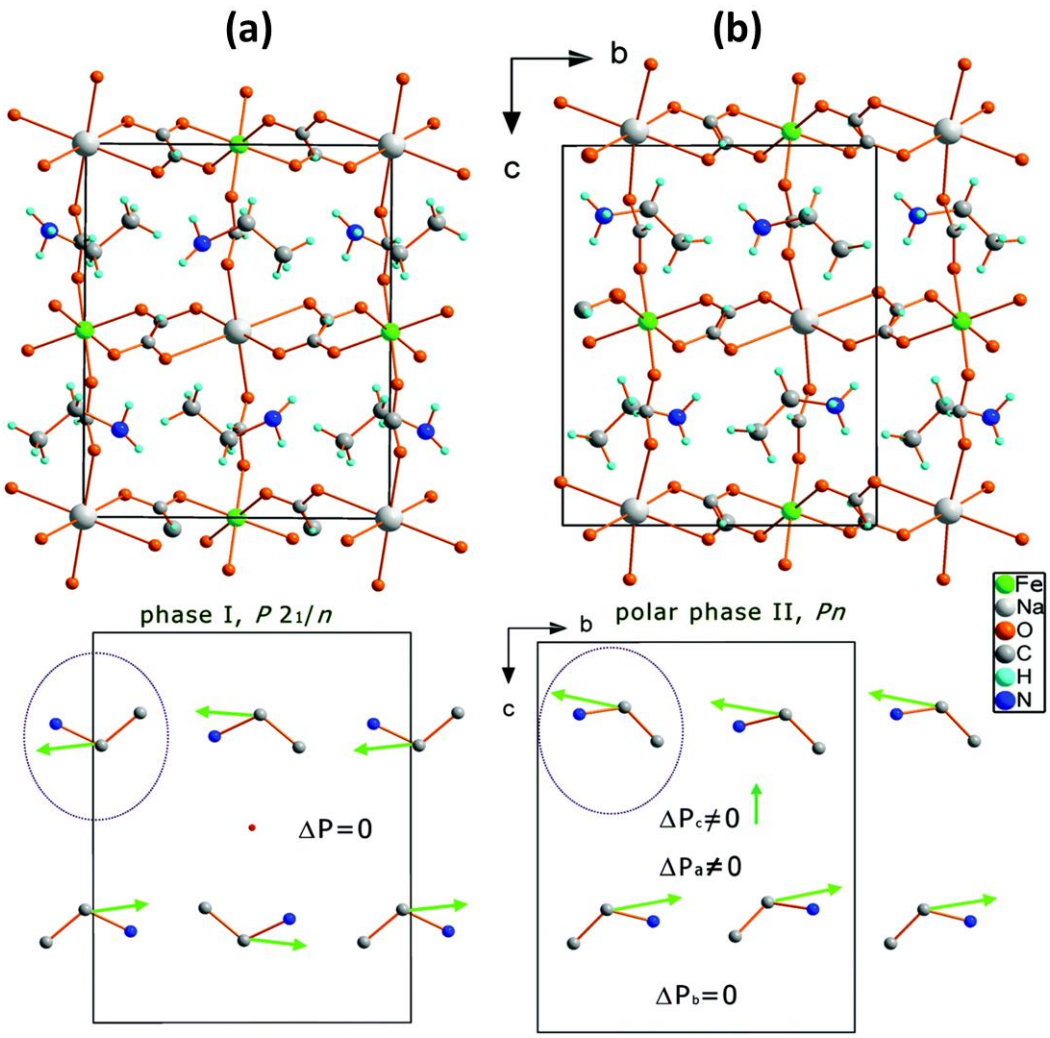

Figure 1.14: *Crystal packing diagram of* $(EA)_2[NaFe^{III}(HCOO)_6]$ *in (a) High temperature centrosymmetric phase I at 377 K and (b) low temperature non-centrosymmetric polar phase II at 297 K. The bottom diagrams depict the* EA^+ *cations (hydrogen omitted for clarity) with an internal dipole moment (denoted by green arrows). Resultant dipole moment arising from phase I cancels out to zero, while that in polar II gives rise to a spontaneous polarization perpendicular to b-axis. Adapted with permission from ref. 96. Copyright © 2016 The Royal Society of Chemistry.*

Jain et al. synthesized a multiferroic $[(CH_3)_2NH_2]Mn(HCOO)_3$ perovskite in 2009,[86] after which several reports on $AM^{II}(HCOO)_3$ analogues with various cations such as formamidinium,[87,88] guanidinium,[89,90] hydrazinium,[91-93] imidazolium[94,95] etc. and various divalent metal ions like Cd, Co, Cu, Fe, Zn etc. were reported.

Apart from this, heterometallic formate bridged double perovskite ferroelectric $(EA)_2[NaFe^{III}(HCOO)_6]$ (EA = $C_2H_5NH_3$) was synthesized by Ptak et al. by employing NaO_6 and $Fe^{III}O_6$ as the building blocks (Figure 1.14).[96] The compound crystallized in the ferroelectric polar space *Pn*, which transformed into a paraelectric centrosymmetric space group $P2_1/n$ at 360 K. Ferroelectricity in the compound originated from the ordering of EA^+ cation and considerable distortion of the metal formate framework. Polarization values of 0.2 and 0.8 $\mu C\ cm^{-2}$ were computed using theoretical calculations along the a and c axis, respectively.

1.6 Application of ferroelectric materials

Since their inception, ferroelectric materials have unveiled a multitude of vital applications (Figure 1.15). The most extensively used property is the polarization switchability under an external electric field that forms the basis for its deployment in ferroelectric random-access memories (FeRAM) and field-effect transistors (FeFET).[97-100]

Besides this, ferroelectric materials unfold various other applications due to versatile physical properties of piezoelectricity, pyroelectricity, dielectric permittivity and non-linear optical behaviour.[101-108] Owing to the inherent piezoelectric nature of the ferroelectric materials, they are widely utilized in transducers, actuators, microsensors, microphones, micro speakers, micro-electro-mechanical systems (MEMS) etc. Additionally, they outline the basis for several scientific instruments such as atom force microscopy, time reference sources in quartz watches etc. They form attractive candidates for thermal imaging and infrared detectors due to their intrinsic pyroelectric properties. The high dielectric permittivity exhibited by ferroelectric materials paves the way for the construction of capacitors and dielectric resonators.[41]

Apart from them, hybrid ferroelectric materials with strong optical absorption, high carrier mobility, long diffusion length, tunable band gap, and high solution

processability are utilized in photovoltaics as solar cells.[4] Moreover, in recent times, the electromechanical coupling of ferroelectric materials has sparked an enormous interest in waste mechanical energy harvesting and conversion. Thus, ferroelectric materials are poised to be novel materials for the fabrication of future flexible self-powered electronics.[109]

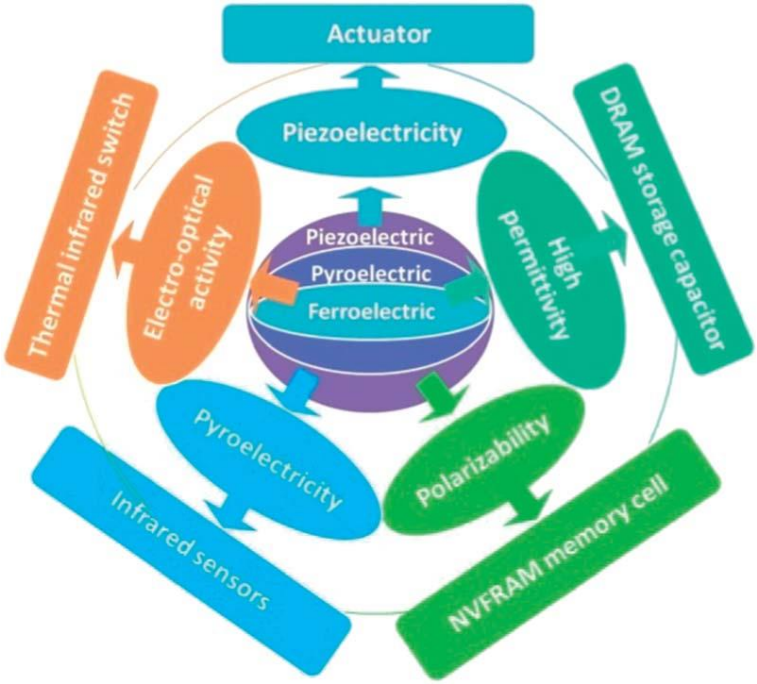

Figure 1.15: *Various applications of non-linear dielectric materials (piezo, pyro and ferroelectric materials). Adapted with permission from ref. 108. Copyright © 2014 The Royal Society Chemistry*.

In view of this, the current section focuses on the use of piezo and ferroelectric materials in mechanical energy harvesting applications.

1.7 Piezo and ferroelectric materials for mechanical energy harvesting applications

In recent years, the rapidly increasing industrialization and the population have escalated global energy consumption. As a result of this, power generation derived from fossil fuel energy has encountered severe critical issues, which includes a deficit of resources, environmental pollution, and global warming. To curb this problem, renewable energy sources have attracted a great deal of attention in the scientific

community. Commonly accessible natural energy sources such as solar, wind, hydro, geothermal are highly influenced by place and are thus not readily available for use.[110,111,112]

In this regard, mechanical energy harvesters that can scavenge mechanical energy and convert it into usable electrical signal have emerged as promising tool for energy generation. These energy sources are utterly prevalent and abundant in the environment encompassing gentle airflow, ambient noise, vibration and various activities of the human body such as walking, finger bending, arms swinging, heart beating, breathing etc.[113,114] The electromechanical responses furnished by the diverse mechanical energy sources can be effectively harnessed by a device called nanogenerator and can be utilized as intended for variety of applications such as sustainable power sources for wearable electronics and sensors for biomedical applications, as shown in Figure 1.16.[115]

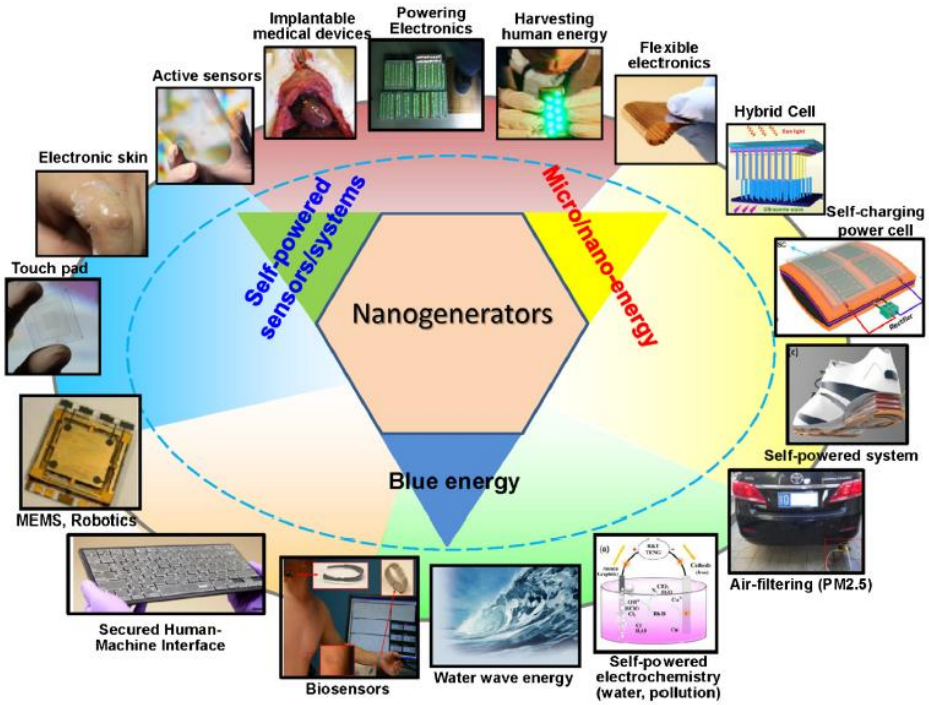

Figure 1.16: *Various application fields of nanogenerators. Reproduced from ref.115.*

Accompanying the discovery of piezoelectricity in ZnO nanowires, the technology of piezoelectric nanogenerators (PENGs) was first coined by Prof. Wang in 2006 (Figure 1.17).[116] The nanoscale mechanical energy conversion into electrical energy was

demonstrated by an array of Zinc oxide Nanowires which were seen to deflect with a conductive atomic force microscope tip working in contact mode. As a result of its bending, strain field and charge separation developed across the nanowires due to the piezoelectric nature of zinc oxide. An output of 8 mV and output power of 0.5 pW was obtained on an active area of 10 μm x 10 μm with an applied frequency of 1 MHz.

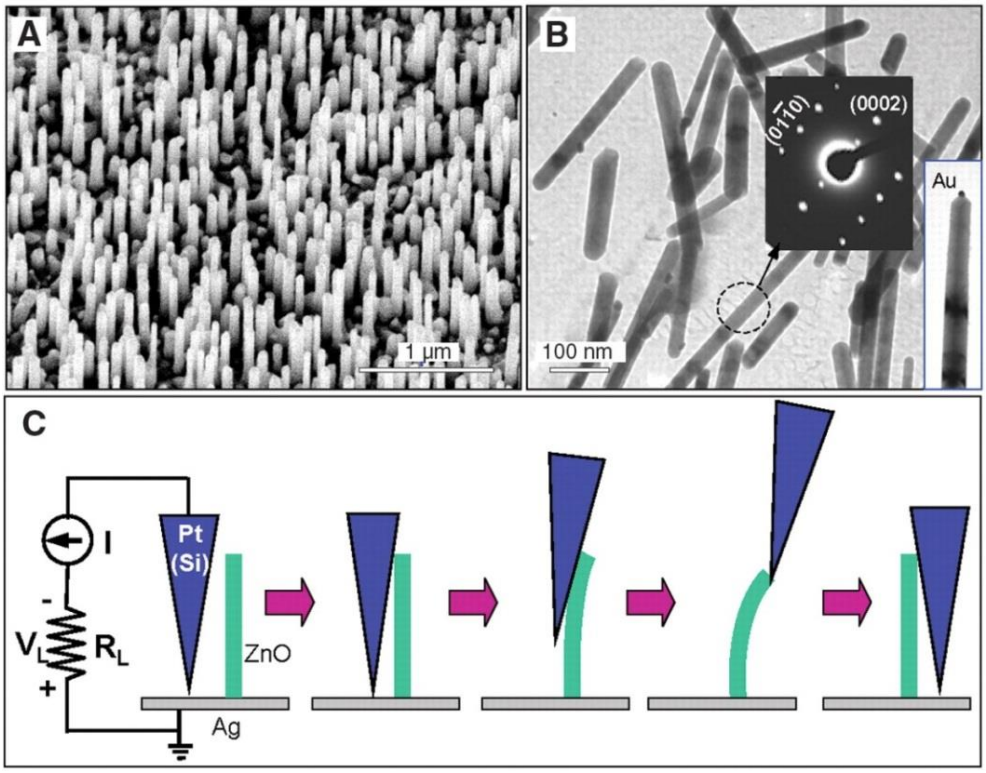

Figure 1.17: *(a) Scanning electron and (b) and Transmission electron microscopy images of ZnO nanowires. (c) Experimental setup and methods for producing electricity by deforming a nanowire with conductive AFM tip. Adapted with permission from ref. 116. Copyright © 2006, The American Association for the Advancement of Science.*

The obtained output voltages from these energy harvesters are considerably very low to be employed for any commercial application. This might stem from its low d_{33} (12 pCN^{-1}) value, which is one of the key factors influencing the nanogenerator performance. Since the piezoelectric coefficient is directly proportional to the remnant polarization of the material (d_{33} α εP_r), piezoelectric and ferroelectric compounds with underlying permanent dipole moment and high spontaneous polarization are desired to boost the overall output performance of the device.

Since its invention in 2006, the upcoming several years have witnessed tremendous progress in piezoelectric nanogenerators based on inorganic compounds and ceramic perovskites materials such as $ZnSO_3$,[117,118] $NaNbO_3$,[119] $KNbO_3$,[120] PZT,[121] PMN-PT[122], $BaTiO_3$,[123] CdS,[124] GaN[125] owing to their remarkable piezoelectric and ferroelectric properties (Figure 1.18). However, cumbersome synthesis, energy-intensive fabrication procedures, and the brittle and rigid nature of these ceramics impede their utilization for flexible wearable electronics.

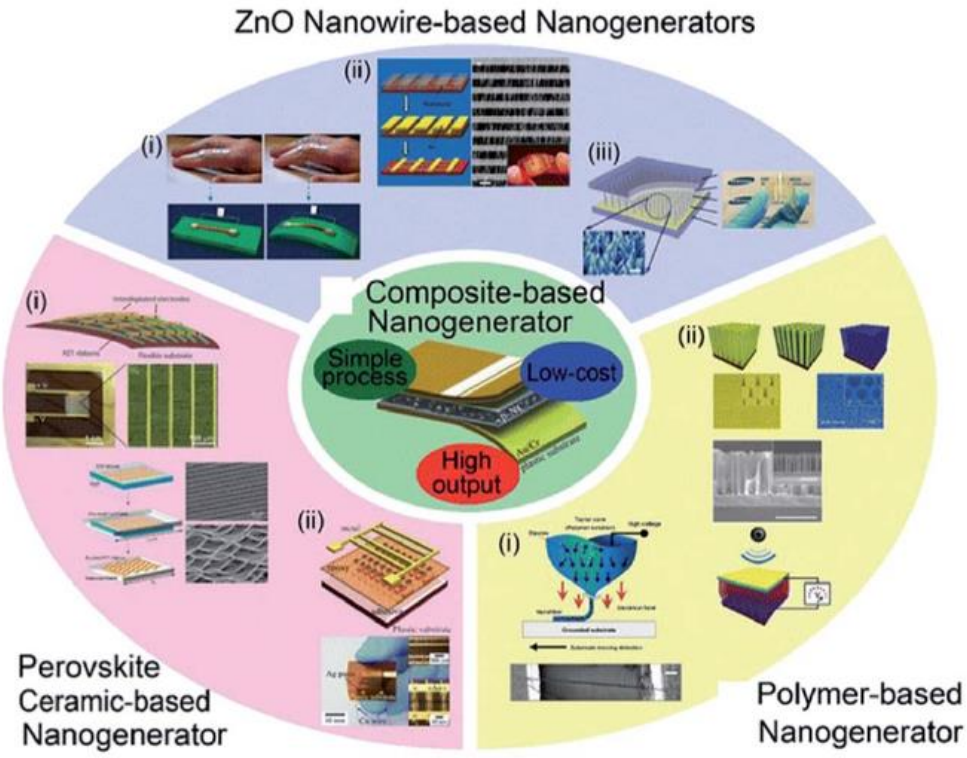

Figure 1.18: *Diverse types of piezoelectric energy harvesters since the first discovery of ZnO nanowire in 2006. Reproduced from ref.130.*

To overcome this, organic piezoelectric and ferroelectric polymer (poly(vinylidene fluoride) (PVDF), polyvinylidenefluoride-trifluoroethylene (P(VDF-TrFE)), poly(vinylidene fluorideco-hexafluoropropylene) (P(VDF-HFP)); PA-11, Nylon11, polypropylene (PP), polyacrylonitrile (PAN)) are gaining particular interest due to their high compliance, flexibility and lightweightness.[126] However, they suffer from meagre energy conversion rates. Among the piezoelectric polymers, PVDF and its co-

polymers are the most widely employed piezoelectric polymers for energy harvesting applications as they are instilled with excellent mechanical and thermal properties.[127,128] Among the distinct five crystallographic forms (α-, β-, γ-, and δ- and ε phase), the most commonly occurring phase is the α phase, known to possess the least piezoelectric properties. Thus, achieving the most suitable β-form remains very challenging.[129]

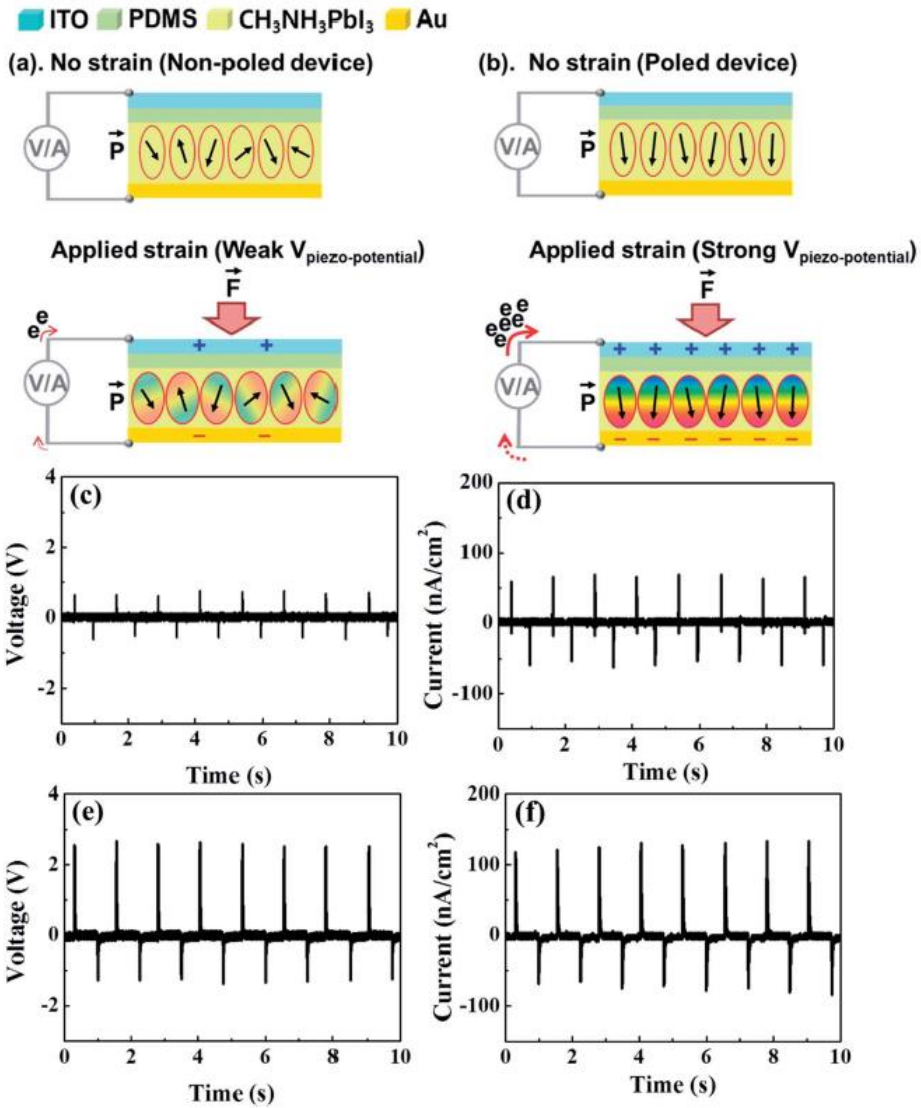

Figure 1.19: *Power generation mechanism of $MAPbI_3$ thin film under (a) unpoled and (b) poled conditions (c) and (d) Output voltage and current density of $MAPbI_3$-PDMS nanogenerator for unpoled device. (e) and (f) Output voltage and current density of $MAPbI_3$-PDMS nanogenerator poled at 80 $kVcm^{-1}$. Adapted with permission from ref. 131. Copyright © 2016 The Royal Society of Chemistry*.

On this account, polymeric composites consisting of organic-inorganic hybrid materials with high piezoelectricity and ferroelectricity render an attractive approach because of their simple solution processing along with enhanced mechanical flexibility (Figure 1.18)[130] Kim et al. firstly exploited an organic-inorganic hybrid piezoelectric nanogenerator based on methylammonium lead iodide-PDMS composite films.[131] The piezoelectric output performance was evaluated by subjecting the devices to mechanical pressure of 0.5 MPa normal to its surface on an active area of 1 x 1 cm^2. The enhancement in the output voltage from 1 V to 2.7 V and in the current density from 50 nA cm^{-2} to 140 nA cm^{-2} was obtained by poling at an electric field of 80 kV cm^{-1} (Figure 1.19). However, the attained overall piezoelectric performance of the device was inferior, rendering them impractical for applications.

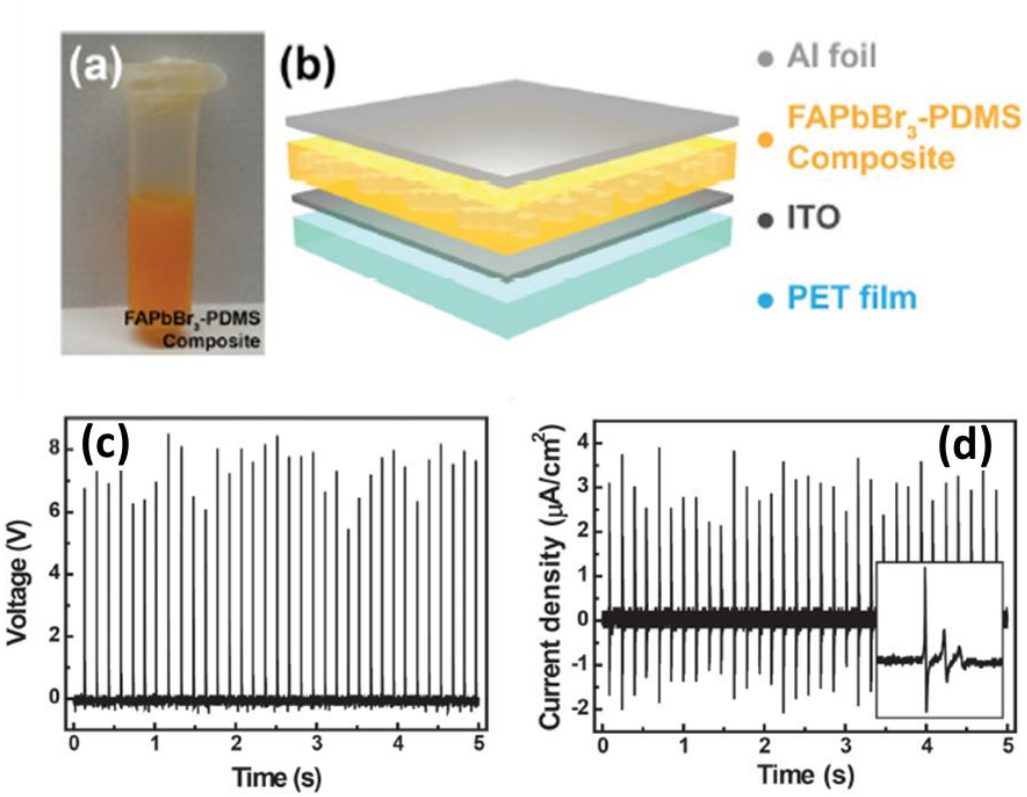

Figure 1.20: *(a) Image of $FAPbBr_3$-PDMS composite solution. (b) Schematic diagram of the as fabricated device (c) and (d) Mechanical harvesting performance of $FAPbBr_3$-PDMS composite device. Adapted with permission from ref. 132. Copyright © 2016 WILEY-VCH Verlag GmbH & Co. KGaA, Weinheim.*

Consequently, in 2016, Ding et al. realized a high performing composite piezoelectric nanogenerator based on $FAPbBr_3$ nanoparticles and PDMS polymer.[132] The device was

fabricated by spin-coating $FAPbBr_3$-PDMS solution onto PET substrate, which acted as the bottom electrode. Finally, the device architecture was completed by integrating Aluminium foil as the top electrode (Figure 1.20). A maximum recordable output voltage of 8.5 V and current density of 3.8 $uAcm^{-2}$ was obtained from an optimized 35 wt% device under periodic vertical compression and release cycle of 0.5 MPa mechanical pressure. The generated output voltage was successfully stored in a capacitor and demonstrated for lightning a commercial red LED.

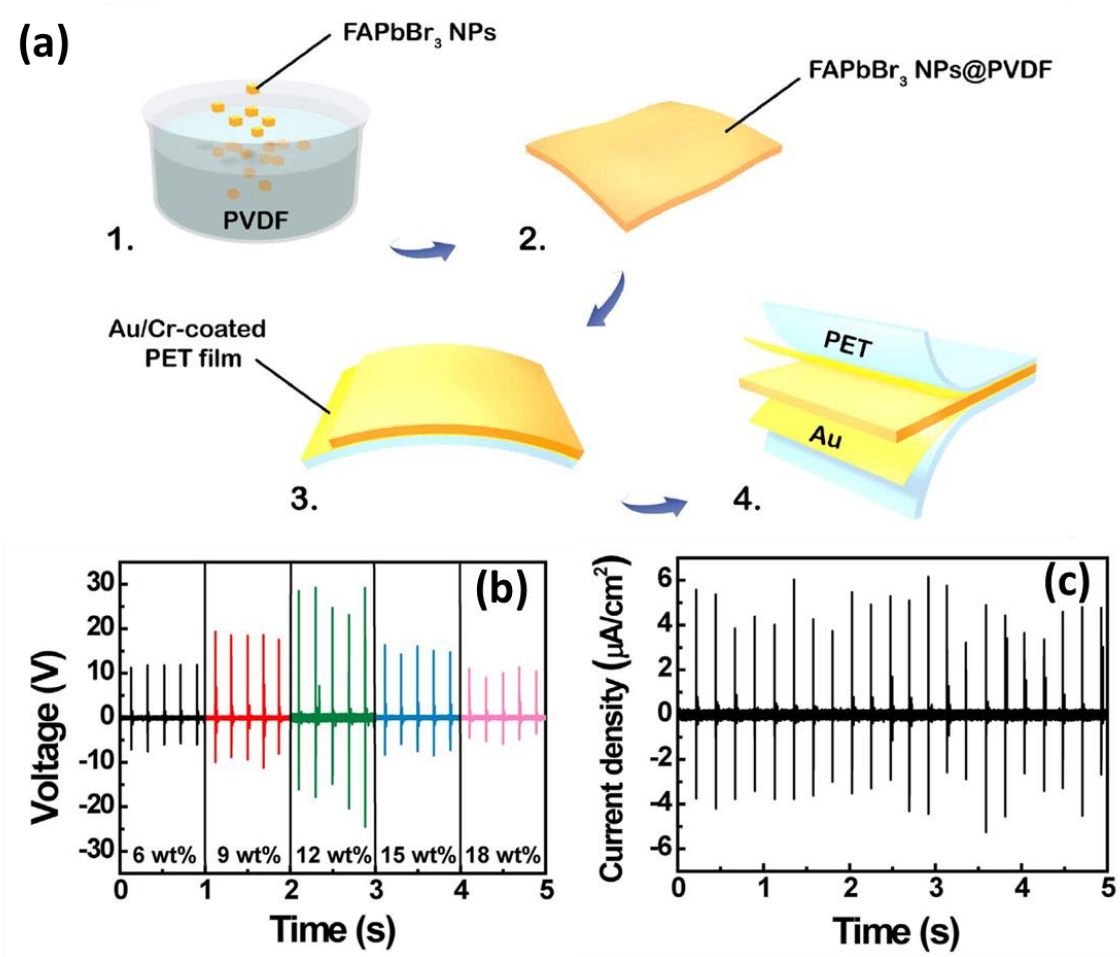

Figure 1.21: *(a) Composite device fabrication procedure of $FAPbBr_3$ NPs @PVDF. (b) and (c) Piezoelectric energy harvesting performance of $FAPbBr_3$ NPs @PVDF nanogenerator. Adapted with permission from ref. 133. Copyright © 2017 Elsevier Ltd.*

Yet, in a subsequent study by the same group in 2017, the overall performance of the device was dramatically increased by 3.5 folds by using a piezoelectric polymer PVDF as the polymeric matrix.[133] In this study, $FAPbBr_3$ NPs were homogeneously dispersed into the PVDF matrix. The obtained composite film was then sandwiched between two

Au/Cr-coated polyethylene terephthalate (PET) films as flexible top and bottom electrodes (Figure 1.21). Before examining the output performance, the composite devices were subjected to high electric field poling of 50 $kVcm^{-1}$. Maximum output voltage and current density of 30 V and 6.2 $uAcm^{-2}$ were achieved from the best performing 12 wt% composite device under an applied stress of 0.5 MPa and a frequency of 5 Hz. Practical applications of the device were demonstrated by charging a 3.3 µF capacitor and lightning a led.

Though the enhancement in the output performance is promising, it raises serious concerns about the viability of lead-based hybrid perovskites piezoelectric nanogenerators for practical use. Thus, lead-free alternatives are drawing significant attention towards their use in energy harvesting applications.[134,135]

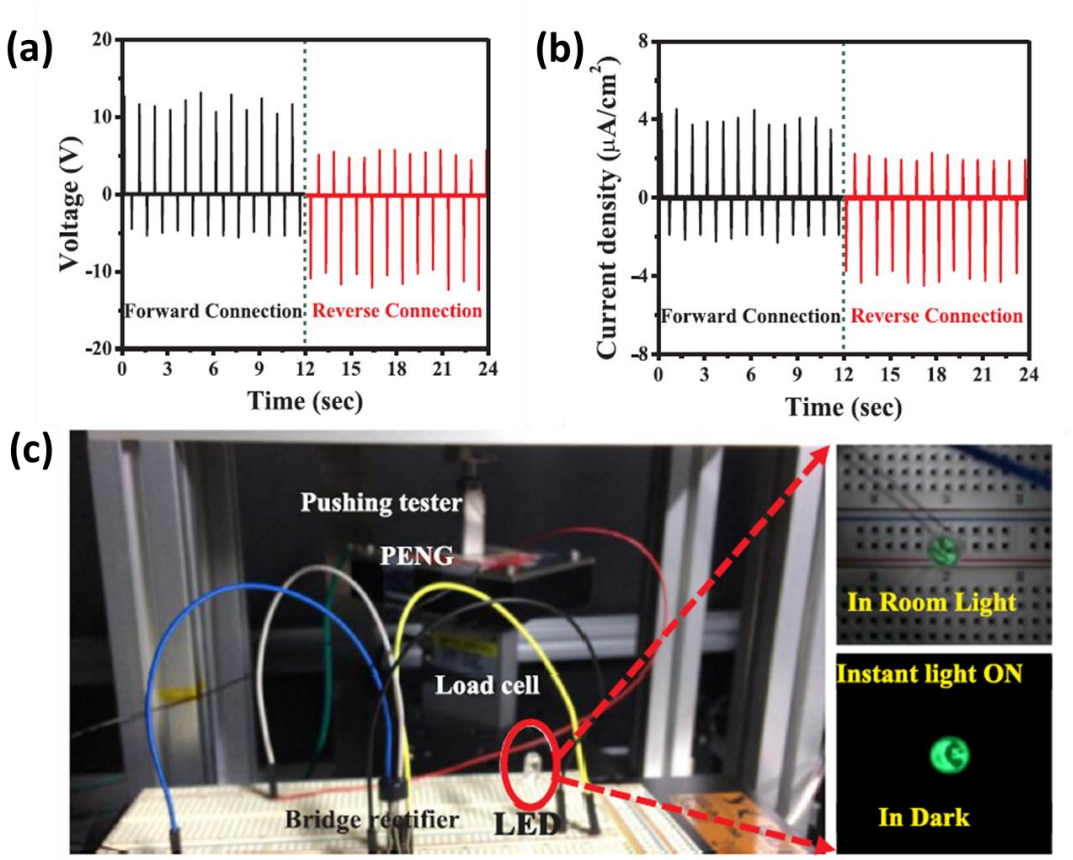

Figure 1.22: *(a) and (b) Output performance from $MASnI_3$-PVDF composite device poled at 60 kV cm^{-1} and (c) Photograph of instant lightning of a green led on applying mechanical force to the device. Adapted with permission from ref. 136. Copyright © 2019 Elsevier Ltd.*

Very recently, Swathi et al. synthesized an environment-friendly lead-free $MASnI_3$ perovskite by utilizing an antisolvent-assisted collision technique (ACT) under ambient atmosphere (Figure 1.22).[136] The piezoelectric nanogenerator fabricated by employing $MASnI_3$ films revealed an output voltage of ~ 3.8 V and a current density of 0.35 μA cm^{-2} under an applied pressure of 0.5 MPa. The piezoelectric performance was further enhanced by a composite formed by $MASnI_3$ with PVDF polymer. A maximum output voltage of 12.0 V and current density of 4.0 μA cm^{-2} was obtained by PVDF-$MASnI_3$ composite-based piezoelectric nanogenerator. An instant glowing of a green LED was achieved by the output power generation from PVDF-$MASnI_3$ composite under an applied force of 0.5 MPa.

Lately, Pandey et al. demonstrated a high performing flexible piezoelectric nanogenerator by incorporating $FASnI_3$ in the PVDF polymer matrix (Figure 1.23).[137] The as-fabricated device resulted in an output voltage of 23 V and a power density of 35.05 mW cm^{-2} at an applied pressure of 0.1 MPa. The soft elastic nature and soft polar optic phonons were proposed to be responsible for the high piezoelectric response of $FASnI_3$. Moreover, the alternating output obtained from the device were successfully stored into a capacitor by means of a full-wave bridge rectifier circuit and utilized for lightning up a commercial LED.

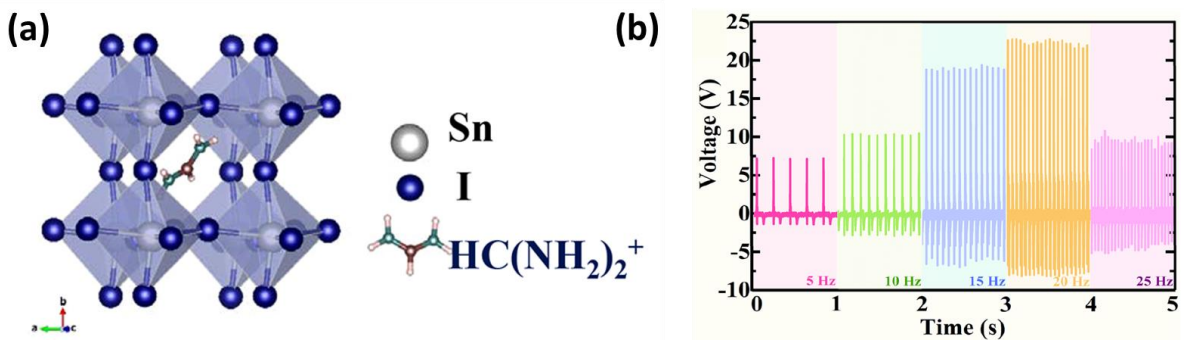

Figure 1.23: *(a) Schematic crystal structure of $FASnI_3$ (b) Signal generation from 0.5 $FASnI_3$:0.5 PVDF nanocomposite piezoelectric nanogenerator device at various frequencies. Adapted with permission from ref. 137. Copyright © 2019, American Chemical Society.*

Furthermore, by substituting A, B and X sites and employing different polymeric matrices, several examples of piezoelectric nanogenerators such as $MAPbBr_3$-

PVDF,[138] $MAPbI_3$-PVDF,[139] $MAPb_{1-x}Fe_xI_3$[140] $MASnBr_3$-PDMS,[141] etc., were fabricated and shown to display modest output performance.

Despite significant advances, several of these composites suffer from either Pb toxicity or severe instability arising from Sn under ambient conditions thus, presenting huge barriers to their commercialization.[142,143]

1.8 Outline and objectives of the present thesis

The aforementioned issues call for a great need to systematically develop new stable families of organic-inorganic hybrid ferroelectric materials at ambient conditions to yield durable devices with superior output performance.

This thesis demonstrates the synthesis of ammonium and phosphonium based hybrid organic-inorganic ferroelectric materials for mechanical energy harvesting applications. Chapter 2 will discuss the synthesis of two new A_2MX_4 type hybrid halogenometallates derived from heteroleptic ammonium cations that display excellent ferroelectric and dielectric properties. For the first time, the use of A_2MX_4 based systems was demonstrated for mechanical energy harvesting applications. Chapter 3 will describe the synthesis of an unusual neutral perovskite-type hybrid ferroelectric ABX_3 which exhibits reversible coordination isomerism at higher temperatures. The compound unveils remarkable ferroelectric polarization and displays outstanding output performance among the non-piezoelectric polymer composites containing hybrid ferroelectrics employed as nanogenerators. Chapter 4 illustrates a new $A_3B_2X_9$ phosphonium based discrete perovskite-like hybrid ferroelectric and its mechanical energy harvesting capabilities. The ferroelectric polarization of the hybrid compound was investigated both at micro and macroscopic levels. And finally, Chapter 5 elucidates the foundation for exploring rich organophosphazene chemistry in the design of ferroelectric nanogenerators.

Thus, the objectives of the present thesis are:

- ✓ To synthesize lower symmetric organo-ammonium and phosphonium cations in their corresponding charge-separated state in the presence of diverse anions

- ✓ To evaluate the dielectric, piezoelectric and ferroelectric behaviour of the synthesized non-centrosymmetric hybrid assemblies
- ✓ To evaluate the potential of these assemblies for mechanical energy harvesting applications in the presence of non-piezoelectric polymers and demonstrate their energy-storing capabilities.

1.9 REFERENCES

1. Fu, Y.; Zhu, H.; Chen, J.; Hautzinger, M. P.; Zhu, X.-Y.; Jin, S., Metal halide perovskite nanostructures for optoelectronic applications and the study of physical properties. *Nat. Rev. Mater.* **2019,** *4*, 169-188.
2. Pham, H. D.; Xianqiang, L.; Li, W.; Manzhos, S.; Kyaw, A. K. K.; Sonar, P., Organic interfacial materials for perovskite-based optoelectronic devices. *Energy Environ. Sci.* **2019,** *12*, 1177-1209.
3. Huang, Y.; Lei, X.; He, T.; Jiang, Y.; Yuan, M., Recent Progress on Formamidinium-Dominated Perovskite Photovoltaics. *Adv. Energy Mater.* **2021**, 2100690.
4. Dey, A.; Ye, J.; De, A.; Debroye, E.; Ha, S. K.; Bladt, E.; Kshirsagar, A. S.; Wang, Z.; Yin, J.; Wang, Y., State of the Art and Prospects for Halide Perovskite Nanocrystals. *ACS nano* **2021**.
5. Tan, Z.-K.; Moghaddam, R. S.; Lai, M. L.; Docampo, P.; Higler, R.; Deschler, F.; Price, M.; Sadhanala, A.; Pazos, L. M.; Credgington, D., Bright light-emitting diodes based on organometal halide perovskite. *Nat. Nanotechnol.* **2014,** *9*, 687-692.
6. Chin, X. Y.; Cortecchia, D.; Yin, J.; Bruno, A.; Soci, C. Lead iodide perovskite light-emitting field-effect transistor. *Nat. Commun.* **2015**, *6*, 7383.
7. Tian, W.; Zhou, H.; Li, L., Hybrid Organic–Inorganic Perovskite Photodetectors. *Small* **2017**, *13*, 1702107.
8. Dong, H.; Zhang, C.; Liu, X.; Yao, J.; Zhao, Y. S., Materials chemistry and engineering in metal halide perovskite lasers. *Chem. Soc. Rev.* **2020**, *49*, 951-982.
9. Yoo, E. J.; Lyu, M.; Yun, J.-H.; Kang, C. J.; Choi, Y. J.; Wang, L., Resistive Switching Behavior in Organic–Inorganic Hybrid $CH_3NH_3PbI_{3-x}Cl_x$ Perovskite for Resistive Random Access Memory Devices. *Adv. Mater.* **2015**, *27*, 6170-6175.
10. Park, H.; Ha, C.; Lee, J.-H., Advances in piezoelectric halide perovskites for energy harvesting applications. *J. Mater. Chem. A* **2020**, *8*, 24353-24367.
11. Jella, V.; Ippili, S.; Eom, J.-H.; Pammi, S. V. N.; Jung, J.-S.; Tran, V.-D.; Nguyen, V. H.; Kirakosyan, A.; Yun, S.; Kim, D.; Sihn, M. R.; Choi, J.; Kim, Y.-J.; Kim, H.-J.; Yoon,

S.-G., A comprehensive review of flexible piezoelectric generators based on organic-inorganic metal halide perovskites. *Nano Energy* **2019**, *57*, 74-93.

12. Valasek, J., Piezo-electric and allied phenomena in Rochelle salt. *Phys. Rev.* **1921,** *17*, 475-481.
13. Bretos, I.; Jiménez, R.; Wu, A.; Kingon, A. I.; Vilarinho, P. M.; Calzada, M. L., Activated solutions enabling low-temperature processing of functional ferroelectric oxides for flexible electronics. *Adv. Mater.* **2014,** *26*, 1405-1409.
14. Cohen, R. E., Origin of ferroelectricity in perovskite oxides. *Nature* **1992,** *358*, 136-138.
15. Haertling, G. H., Ferroelectric ceramics: history and technology. *J. Am. Ceram. Soc.* **1999,** *82*, 797-818.
16. Liu, Y.; Chang, Y.; Sun, E.; Li, F.; Zhang, S.; Yang, B.; Sun, Y.; Wu, J.; Cao, W., Significantly enhanced energy-harvesting performance and superior fatigue-resistant behavior in [001] c-textured $BaTiO_3$-based lead-free piezoceramics. *ACS Appl. Mater. Interfaces* **2018,** *10*, 31488-31497.
17. Lee, H.; Kim, H.; Kim, D. Y.; Seo, Y., Pure piezoelectricity generation by a flexible nanogenerator based on lead zirconate titanate nanofibers. *ACS Omega* **2019,** *4*, 2610-2617.
18. Johar, M. A.; Waseem, A.; Hassan, M. A.; Bagal, I. V.; Abdullah, A.; Ha, J. S.; Ryu, S. W., Highly Durable Piezoelectric Nanogenerator by Heteroepitaxy of GaN Nanowires on Cu Foil for Enhanced Output Using Ambient Actuation Sources. *Adv. Energy Mater.* **2020,** *10*, 2002608.
19. Le, A. T.; Ahmadipour, M.; Pung, S.-Y., A review on ZnO-based piezoelectric nanogenerators: Synthesis, characterization techniques, performance enhancement and applications. *J. Alloys Compd.* **2020,** *844*, 156172.
20. Choi, M.-J.; Eom, J.-H.; Shin, S.-H.; Nah, J.; Choi, J.-S.; Song, H.-A.; An, H.; Kim, H. Y.; Pammi, S.; Choi, G., Most facile synthesis of Zn-Al: LDHs nanosheets at room temperature via environmentally friendly process and their high-power generation by flexoelectricity. *Mater. Today Energy* **2018,** *10*, 254-263.
21. Lu, L.; Ding, W.; Liu, J.; Yang, B., Flexible PVDF based piezoelectric nanogenerators. *Nano Energy* **2020**, 105251.
22. Nguyen, T. M. T.; Ippili, S.; Eom, J.-H.; Jella, V.; Van Tran, D.; Yoon, S.-G., Enhanced Output Performance of Nanogenerator Based on Composite of Poly Vinyl Fluoride (PVDF) and Zn: Al Layered-Double Hydroxides (LDHs) Nanosheets. *Transact. Electr. and Electron. Mater.* **2018,** *19*, 403-411.

23. Bai, Y.; Jantunen, H.; Juuti, J., Energy harvesting research: the road from single source to multisource. *Adv. Mater.* **2018,** *30*, 1707271.
24. Safaei, M.; Sodano, H. A.; Anton, S. R., A review of energy harvesting using piezoelectric materials: state-of-the-art a decade later (2008–2018). *Smart Mater. Struct.* **2019,** *28*, 113001.
25. Liu, H.; Zhong, J.; Lee, C.; Lee, S.-W.; Lin, L., A comprehensive review on piezoelectric energy harvesting technology: Materials, mechanisms, and applications. *Appl. Phys. Rev.* **2018,** *5*, 041306.
26. Ippili, S.; Jella, V.; Thomas, A. M.; Yoon, S.-G., The recent progress on halide perovskite-based self-powered sensors enabled by piezoelectric and triboelectric effects. *Nanoenergy Adv.* **2021,** *1*, 3-31.
27. Park, S.-H.; Lee, H. B.; Yeon, S. M.; Park, J.; Lee, N. K., Flexible and stretchable piezoelectric sensor with thickness-tunable configuration of electrospun nanofiber mat and elastomeric substrates. *ACS Appl. Mater. Interfaces* **2016,** *8*, 24773-24781.
28. Alluri, N. R.; Chandrasekhar, A.; Jeong, J. H.; Kim, S.-J., Enhanced electroactive β-phase of the sonication-process-derived PVDF-activated carbon composite film for efficient energy conversion and a battery-free acceleration sensor. *J. Mater. Chem. C C* **2017,** *5*, 4833-4844.
29. Park, J. H.; Kurra, N.; AlMadhoun, M.; Odeh, I. N.; Alshareef, H. N., A two-step annealing process for enhancing the ferroelectric properties of poly (vinylidene fluoride)(PVDF) devices. *J. Mater. Chem. C* **2015,** *3*, 2366-2370.
30. Richerson, D. W.; Lee, W. E., *Modern ceramic engineering: properties, processing, and use in design*. CRC press: 2018.
31. Dorey, R. Microstructure−Property Relationships: How the Microstructure of the Film Affects Its Properties. In *Ceramic Thick Films for MEMS and Microdevices*; Dorey, R., Ed.; William Andrew Publishing: Oxford, 2012; Chapter 4, pp 85−112.
32. Rosenberg, H. M. The Solid State: An Introduction to the Physics of Crystals for Students of Physics. *Materials Science, and Engineering, 3rd ed.(Oxford University Press, Oxford, New York, 1988)* **1988**, 326.
33. Sebastian, M. T., *Dielectric materials for wireless communication*. Elsevier: 2010.
34. Hang, T.; Zhang, W.; Ye, H.-Y.; Xiong, R.-G., Metal–organic complex ferroelectrics. *Chem. Soc. Rev.* **2011,** *40*, 3577-3598.
35. Zhang, W.; Xiong, R.-G., Symmetry breaking in molecular ferroelectrics. *Chem. Rev.* **2012,** *112*, 1163-1195.
36. Curie, J.; Curie, P., Development par compression de l'électricité polaire dans les cristaux hémièdres à faces inclinées. *Bull Minéral* **1880,** *3*, 90-93.

37. Kim, H. S.; Kim, J.-H.; Kim, J., A review of piezoelectric energy harvesting based on vibration. *Int. J. Precis. Eng. Manuf.* **2011,** *12* (6), 1129-1141.
38. Rajabi, A. H.; Jaffe, M.; Arinzeh, T. L., Piezoelectric materials for tissue regeneration: A review. *Acta Biomater.* **2015,** *24*, 12-23.
39. Sezer, N.; Koç, M., A comprehensive review on the state-of-the-art of piezoelectric energy harvesting. *Nano Energy* **2021,** *80*, 105567.
40. Zhang, D.; Wu, H.; Bowen, C. R.; Yang, Y., Recent Advances in Pyroelectric Materials and Applications. *Small* **2021**, 2103960.
41. Lines, M. E.; Glass, A. M., *Principles and applications of ferroelectrics and related materials*. Oxford university press: 2001.
42. Shi, P.-P.; Tang, Y.-Y.; Li, P.-F.; Liao, W.-Q.; Wang, Z.-X.; Ye, Q.; Xiong, R.-G., Symmetry breaking in molecular ferroelectrics. *Chem. Soc. Rev.* **2016,** *45*, 3811-3827.
43. Paz De Araujo, C. A.; McMillan, L. D.; Melnick, B. M.; Cuchiaro, J. D.; Scott, J. F., Ferroelectric memories. *Ferroelectrics* **1990,** *104*, 241-256.
44. Busch, G.; Scherrer, P., Eine neue seignette-elektrische Substanz. *Naturwissenschaften* **1935,** *23,* 737-737.
45. Von Hippel, A.; Breckenridge, R.; Chesley, F.; Tisza, L., High dielectric constant ceramics. *Ind. Eng. Chem.* **1946,** *38*, 1097-1109.
46. Shirane, G.; Takeda, A., Phase transitions in solid solutions of $PbZrO_3$ and $PbTiO_3$ (I) small concentrations of $PbTiO_3$. *J. Phys. Soc. Jpn.,* **1952,** *7*, 5-11.
47. Sawaguchi, E., Ferroelectricity versus antiferroelectricity in the solid solutions of $PbZrO_3$ and $PbTiO_3$. *J. Phys. Soc. Jpn.,* **1953,** *8*, 615-629.
48. Scott, J., Applications of modern ferroelectrics. *Science* **2007,** *315*, 954-959.
49. Scott, J. F.; De Araujo, C. A. P., Ferroelectric memories. *Science* **1989,** *246*, 1400-1405.
50. Kawai, H., The piezoelectricity of poly (vinylidene fluoride). *Jpn. J. Appl. Phys.,* **1969,** *8*, 975.
51. Bergman Jr, J.; McFee, J.; Crane, G., Pyroelectricity and optical second harmonic generation in polyvinylidene fluoride films. *Appl. Phys. Lett.* **1971,** *18*, 203-205.
52. Kepler, R.; Anderson, R., Ferroelectricity in polyvinylidene fluoride. *J. Appl. Phys.* **1978,** *49*, 1232-1235.
53. Horiuchi, S.; Tokura, Y., Organic ferroelectrics. *Nat. Mater.* **2008,** *7*, 357-366.
54. Tayi, A. S.; Kaeser, A.; Matsumoto, M.; Aida, T.; Stupp, S. I., Supramolecular ferroelectrics. *Nature Chem.* **2015,** *7*, 281-294.

55. Horiuchi, S.; Ishii, F.; Kumai, R.; Okimoto, Y.; Tachibana, H.; Nagaosa, N.; Tokura, Y., Ferroelectricity near room temperature in co-crystals of nonpolar organic molecules. *Nat. Mater.* **2005,** *4*, 163-166.
56. Horiuchi, S.; Kumai, R.; Tokura, Y., A supramolecular ferroelectric realized by collective proton transfer. *Angew. Chem. Int. Ed.* **2007,** *119*, 3567-3571.
57. Horiuchi, S.; Kagawa, F.; Hatahara, K.; Kobayashi, K.; Kumai, R.; Murakami, Y.; Tokura, Y., Above-room-temperature ferroelectricity and antiferroelectricity in benzimidazoles. *Nat. Commun.* **2012,** *3*, 1-6.
58. Horiuchi, S.; Kobayashi, K.; Kumai, R.; Ishibashi, S., Proton tautomerism for strong polarization switching. *Nat. Commun.* **2017,** *8*, 1-9.
59. Horiuchi, S.; Tokunaga, Y.; Giovannetti, G.; Picozzi, S.; Itoh, H.; Shimano, R.; Kumai, R.; Tokura, Y., Above-room-temperature ferroelectricity in a single-component molecular crystal. *Nature* **2010,** *463*, 789-792.
60. Fu, D.-W.; Cai, H.-L.; Liu, Y.; Ye, Q.; Zhang, W.; Zhang, Y.; Chen, X.-Y.; Giovannetti, G.; Capone, M.; Li, J., Diisopropylammonium bromide is a high-temperature molecular ferroelectric crystal. *Science* **2013,** *339*, 425-428.
61. Fu, D. W.; Zhang, W.; Cai, H. L.; Ge, J. Z.; Zhang, Y.; Xiong, R. G., Diisopropylammonium chloride: a ferroelectric organic salt with a high phase transition temperature and practical utilization level of spontaneous polarization.*Adv. Mater.* **2011**, *23*, 5658-5662.
62. Li, W.; Wang, Z.; Deschler, F.; Gao, S.; Friend, R. H.; Cheetham, A. K., Chemically diverse and multifunctional hybrid organic–inorganic perovskites. *Nat. Rev. Mater.* **2017,** *2*, 1-18.
63. Bermudez-Garcia, J. M.; Sanchez-Andujar, M.; Senaris-Rodriguez, M. A., A new playground for organic–inorganic hybrids: barocaloric materials for pressure-induced solid-state cooling. *J. Phys. Chem. Lett*. **2017**, *8*, 4419-4426.
64. Wu, Y.; Shaker, S.; Brivio, F.; Murugavel, R.; Bristowe, P. D.; Cheetham, A. K., [Am] $Mn(H_2POO)_3$: a new family of hybrid perovskites based on the hypophosphite ligand. *J. Am. Chem. Soc.* **2017,** *139*, 16999-17002.
65. Kieslich, G.; Goodwin, A. L., The same and not the same: molecular perovskites and their solid-state analogues. *Mater. Horiz.* **2017,** *4*, 362-366.
66. Mao, L.; Stoumpos, C. C.; Kanatzidis, M. G., Two-dimensional hybrid halide perovskites: principles and promises. *J. Am. Chem. Soc.* **2018,** *141*, 1171-1190.
67. Paton, L. A.; Harrison, W. T., Structural Diversity in Non-Layered Hybrid Perovskites of the $RMCl_3$ Family. *Angew. Chem. Int. Ed.* **2010,** *49*, 7684-7687.

68. Pan, Q.; Liu, Z.-B.; Tang, Y.-Y.; Li, P.-F.; Ma, R.-W.; Wei, R.-Y.; Zhang, Y.; You, Y.-M.; Ye, H.-Y.; Xiong, R.-G., A three-dimensional molecular perovskite ferroelectric:(3-ammoniopyrrolidinium) $RbBr_3$. *J. Am. Chem. Soc.* **2017,** *139*, 3954-3957.
69. Zhang, W.-Y.; Tang, Y.-Y.; Li, P.-F.; Shi, P.-P.; Liao, W.-Q.; Fu, D.-W.; Ye, H.-Y.; Zhang, Y.; Xiong, R.-G., Precise Molecular Design of High-T_c 3D Organic–Inorganic Perovskite Ferroelectric: [MeHdabco] RbI_3 (MeHdabco= N-Methyl-1, 4-diazoniabicyclo [2.2.2] octane). *J. Am. Chem. Soc.* **2017,** *139* (31), 10897-10902.
70. Bremner, C. A.; Simpson, M.; Harrison, W. T., New Molecular Perovskites: Cubic $C_4N_2H_{12}{\cdot}NH_4Cl_3{\cdot}H_2O$ and 2-H Hexagonal $C_6N_2H_{14}{\cdot}NH_4Cl_3$. *J. Am. Chem. Soc.* **2002,** *124*, 10960-10961.
71. Ye, H.-Y.; Tang, Y.-Y.; Li, P.-F.; Liao, W.-Q.; Gao, J.-X.; Hua, X.-N.; Cai, H.; Shi, P.-P.; You, Y.-M.; Xiong, R.-G., Metal-free three-dimensional perovskite ferroelectrics. *Science* **2018,** *361*, 151-155.
72. Zhang, H. Y.; Chen, X. G.; Zhang, Z. X.; Song, X. J.; Zhang, T.; Pan, Q.; Zhang, Y.; Xiong, R. G., Methylphosphonium Tin Bromide: A 3D Perovskite Molecular Ferroelectric Semiconductor. *Adv. Mater.* **2020,** *32*, 2005213.
73. Lin, H.; Zhou, C.; Tian, Y.; Siegrist, T.; Ma, B., Low-dimensional organometal halide perovskites. *ACS Energy Lett.* **2017,** *3*, 54-62.
74. Ma, S.; Cai, M.; Cheng, T.; Ding, X.; Shi, X.; Alsaedi, A.; Hayat, T.; Ding, Y.; Tan, Z. a.; Dai, S., Two-dimensional organic-inorganic hybrid perovskite: from material properties to device applications. *Sci. China Mater.* **2018,** *61*, 1257-1277.
75. Shi, E.; Gao, Y.; Finkenauer, B. P.; Coffey, A. H.; Dou, L., Two-dimensional halide perovskite nanomaterials and heterostructures. *Chem. Soc. Rev.* **2018,** *47*, 6046-6072.
76. Li, L.; Sun, Z.; Wang, P.; Hu, W.; Wang, S.; Ji, C.; Hong, M.; Luo, J., Tailored engineering of an unusual $(C_4H_9NH_3)_2(CH_3NH_3)2Pb_3Br_{10}$ two-dimensional multilayered perovskite ferroelectric for a high-performance photodetector. *Angew. Chem. Int. Ed.* **2017,** *129*, 12318-12322.
77. Zhang, H.-Y.; Zhang, Z.-X.; Chen, X.-G.; Song, X.-J.; Zhang, Y.; Xiong, R.-G., Large Electrostrictive Coefficient in a Two-Dimensional Hybrid Perovskite Ferroelectric. *J. Am. Chem. Soc.* **2021,** *143*, 1664-1672.
78. You, Y.-M.; Liao, W.-Q.; Zhao, D.; Ye, H.-Y.; Zhang, Y.; Zhou, Q.; Niu, X.; Wang, J.; Li, P.-F.; Fu, D.-W., An organic-inorganic perovskite ferroelectric with large piezoelectric response. *Science* **2017**, *357*, 306-309.

79. Liao, W.-Q.; Tang, Y.-Y.; Li, P.-F.; You, Y.-M.; Xiong, R.-G., Large piezoelectric effect in a lead-free molecular ferroelectric thin film. *J. Am. Chem. Soc.* **2017,** *139*, 18071-18077.
80. Liao, W.-Q.; Tang, Y.-Y.; Li, P.-F.; You, Y.-M.; Xiong, R.-G., Competitive halogen bond in the molecular ferroelectric with large piezoelectric response. *J. Am. Chem. Soc.* **2018,** *140*, 3975-3980.
81. Liao, W.-Q.; Zhao, D.; Tang, Y.-Y.; Zhang, Y.; Li, P.-F.; Shi, P.-P.; Chen, X.-G.; You, Y.-M.; Xiong, R.-G., A molecular perovskite solid solution with piezoelectricity stronger than lead zirconate titanate. *Science* **2019,** *363*, 1206-1210.
82. Xu, W.-J.; Li, P.-F.; Tang, Y.-Y.; Zhang, W.-X.; Xiong, R.-G.; Chen, X.-M., A molecular perovskite with switchable coordination bonds for high-temperature multiaxial ferroelectrics. *J. Am. Chem. Soc.* **2017,** *139*, 6369-6375.
83. Rok, M.; Ciżman, A.; Zarychta, B.; Zaręba, J. K.; Trzebiatowska, M.; Mączka, M.; Stroppa, A.; Yuan, S.; Phillips, A. E.; Bator, G., Cyano-bridged perovskite $[(CH_3)_3NOH]_2[KM(CN)_6]$,[M: Fe(iii), and Co(iii)] for high-temperature multi-axial ferroelectric applications with enhanced thermal and nonlinear optical performance. *J. Mater. Chem. C* **2020,** *8*, 17491-17501.
84. Wang, X.-Y.; Wang, Z.-M.; Gao, S., Constructing magnetic molecular solids by employing three-atom ligands as bridges. *Chem. Commun.* **2008,** *3,* 281-294.
85. Wang, Z.; Hu, K.; Gao, S.; Kobayashi, H., Formate-Based Magnetic Metal–Organic Frameworks Templated by Protonated Amines. *Adv. Mater.* **2010,** *22*, 1526-1533.
86. Jain, P.; Ramachandran, V.; Clark, R. J.; Zhou, H. D.; Toby, B. H.; Dalal, N. S.; Kroto, H. W.; Cheetham, A. K., Multiferroic behavior associated with an order−disorder hydrogen bonding transition in metal−organic frameworks (MOFs) with the perovskite ABX_3 architecture. *J. Am. Chem. Soc.* **2009,** *131*, 13625-13627.
87. Rossin, A.; Chierotti, M. R.; Giambastiani, G.; Gobetto, R.; Peruzzini, M., Amine-templated polymeric Mg formates: crystalline scaffolds exhibiting extensive hydrogen bonding. *Cryst Eng Comm* **2012,** *14*, 4454-4460.
88. Mączka, M.; Ciupa, A.; Gagor, A.; Sieradzki, A.; Pikul, A.; Macalik, B.; Drozd, M., Perovskite metal formate framework of $[NH_2\text{-}CH^+\text{-}NH_2]Mn(HCOO)_3$]: phase transition, magnetic, dielectric, and phonon properties. *Inorg. Chem.* **2014,** *53*, 5260-5268.
89. Stroppa, A.; Jain, P.; Barone, P.; Marsman, M.; Perez-Mato, J. M.; Cheetham, A. K.; Kroto, H. W.; Picozzi, S., Electric control of magnetization and interplay between orbital ordering and ferroelectricity in a multiferroic metal–organic framework. *Angew. Chemie Int. Ed.* **2011,** *50*, 5847-5850.

90. Li, W.; Thirumurugan, A.; Barton, P. T.; Lin, Z.; Henke, S.; Yeung, H. H.-M.; Wharmby, M. T.; Bithell, E. G.; Howard, C. J.; Cheetham, A. K., Mechanical tunability via hydrogen bonding in metal–organic frameworks with the perovskite architecture. *J. Am. Chem. Soc.* **2014,** *136*, 7801-7804.
91. Chen, S.; Shang, R.; Hu, K.-L.; Wang, Z.-M.; Gao, S., $[NH_2NH_3][M(HCOO)_3]$(M= Mn^{2+}, Zn^{2+}, Co^{2+} and Mg^{2+}): structural phase transitions, prominent dielectric anomalies and negative thermal expansion, and magnetic ordering. *Inorg. Chem. Front.* **2014,** *1*, 83-98.
92. Mączka, M.; Pasińska, K.; Ptak, M.; Paraguassu, W.; da Silva, T. A.; Sieradzki, A.; Pikul, A., Effect of solvent, temperature and pressure on the stability of chiral and perovskite metal formate frameworks of $[NH_2NH_3][M(HCOO)_3]$ (M = Mn, Fe, Zn). *Phys. Chem. Chem. Phys.* **2016,** *18*, 31653-31663.
93. Kieslich, G.; Kumagai, S.; Butler, K. T.; Okamura, T.; Hendon, C. H.; Sun, S.; Yamashita, M.; Walsh, A.; Cheetham, A. K., Role of entropic effects in controlling the polymorphism in formate ABX_3 metal–organic frameworks. *Chem. Commun.* **2015,** *51*, 15538-15541.
94. Mączka, M.; Costa, N. L. M.; Gągor, A.; Paraguassu, W.; Sieradzki, A.; Hanuza, J., Structural, thermal, dielectric and phonon properties of perovskite-like imidazolium magnesium formate. *Phys. Chem. Chem. Phys.* **2016,** *18*, 13993-14000.
95. Pato-Doldán, B.; Gómez-Aguirre, L. C.; Bermúdez-García, J. M.; Sánchez-Andújar, M.; Fondado, A.; Mira, J.; Castro-García, S.; Señarís-Rodríguez, M. A., Coexistence of magnetic and electrical order in the new perovskite-like $(C_3N_2H_5)[Mn(HCOO)_3]$ formate. *RSC Adv.* **2013,** *3*, 22404-22411.
96. Ptak, M.; Mączka, M.; Gągor, A.; Sieradzki, A.; Stroppa, A.; Di Sante, D.; Perez-Mato, J. M.; Macalik, Experimental and theoretical studies of structural phase transition in a novel polar perovskite-like $[C_2H_5NH_3][Na_{0.5}Fe_{0.5}(HCOO)_3]$ formate. L., *Dalton Trans.* **2016,** *45*, 2574-2583.
97. Das, S.; Appenzeller, J., FETRAM. An organic ferroelectric material based novel random access memory cell. *Nano Lett.* **2011,** *11*, 4003-4007.
98. De Araujo, C. A. P.; Cuchiaro, J. D.; McMillan, L. D.; Scott, M. C.; Scott, J. F., Fatigue-free ferroelectric capacitors with platinum electrodes. *Nature* **1995,** *374*, 627-629.
99. Han, S. T.; Zhou, Y.; Roy, V., Towards the development of flexible non-volatile memories. *Adv. Mater.* **2013**, *25*, 5425-5449.
100. Scott, J. F.; De Araujo, C. A. P., Ferroelectric memories. *Science* **1989,** *246*, 1400-1405.

101. Zhang, Y.; Xie, M.; Roscow, J.; Bao, Y.; Zhou, K.; Zhang, D.; Bowen, C. R., Enhanced pyroelectric and piezoelectric properties of PZT with aligned porosity for energy harvesting applications. *J. Mater. Chem. A* **2017,** *5*, 6569-6580.

102. Wan, C.; Bowen, C. R., Multiscale-structuring of polyvinylidene fluoride for energy harvesting: the impact of molecular-, micro- and macro-structure. *J. Mater. Chem. A* **2017,** *5*, 3091-3128.

103. Bowen, C.; Kim, H.; Weaver, P.; Dunn, S., Piezoelectric and ferroelectric materials and structures for energy harvesting applications. *Energy Environ. Sci.* **2014,** *7*, 25-44.

104. Bowen, C. R.; Taylor, J.; LeBoulbar, E.; Zabek, D.; Chauhan, A.; Vaish, R., Pyroelectric materials and devices for energy harvesting applications. *Energy Environ. Sci.* **2014,** *7*, 3836-3856.

105. Fan, Z.; Sun, K.; Wang, J., Perovskites for photovoltaics: a combined review of organic–inorganic halide perovskites and ferroelectric oxide perovskites. *J. Mater. Chem. A* **2015,** *3*, 18809-18828.

106. Chen, B.; Shi, J.; Zheng, X.; Zhou, Y.; Zhu, K.; Priya, S., Ferroelectric solar cells based on inorganic–organic hybrid perovskites. *J. Mater. Chem. A* **2015,** *3*, 7699-7705.

107. Bai, Y.; Siponkoski, T.; Peräntie, J.; Jantunen, H.; Juuti, J., Ferroelectric, pyroelectric, and piezoelectric properties of a photovoltaic perovskite oxide. *J. Appl. Phys. Lett.* **2017,** *110*, 063903.

108. Jie, W.; Hao, J. Graphene-based hybrid structures combined with functional materials of ferroelectrics and semiconductors. *Nanoscale* **2014,** *6*, 6346-6362.

109. Fan, F. R.; Tang, W.; Wang, Z. L., Flexible nanogenerators for energy harvesting and self-powered electronics. *Adv. Mater.* **2016,** *28*, 4283-4305.

110. Priya, S.; Inman, D. J., *Energy harvesting technologies*. Springer: 2009; Vol. 21.

111. Ryu, H.; Yoon, H. J.; Kim, S. W., Hybrid energy harvesters: toward sustainable energy harvesting. *Adv. Mater.* **2019,** *31*, 1802898.

112. Ryu, H.; Kim, S. W., Emerging pyroelectric nanogenerators to convert thermal energy into electrical energy. *Small* **2021,** *17*, 1903469.

113. Park, K. I.; Son, J. H.; Hwang, G. T.; Jeong, C. K.; Ryu, J.; Koo, M.; Choi, I.; Lee, S. H.; Byun, M.; Wang, Z. L., Highly-efficient, flexible piezoelectric PZT thin film nanogenerator on plastic substrates. *Adv. Mater.* **2014,** *26*, 2514-2520.

114. Yang, R.; Qin, Y.; Li, C.; Zhu, G.; Wang, Z. L., Converting biomechanical energy into electricity by a muscle-movement-driven nanogenerator. *Nano Lett.* **2009,** *9*, 1201-1205.

115. Wang, Z. L., On Maxwell's displacement current for energy and sensors: the origin of nanogenerators. *Mater. Today* **2017,** *20*, 74-82.

116. Wang, Z. L.; Song, J., Piezoelectric nanogenerators based on zinc oxide nanowire arrays. *Science* **2006,** *312*, 242-246.
117. Wu, J. M.; Xu, C.; Zhang, Y.; Yang, Y.; Zhou, Y.; Wang, Z. L., Flexible and transparent nanogenerators based on a composite of lead-free $ZnSnO_3$ triangular-belts. *Adv. Mater.* **2012,** *24*, 6094-6099.
118. Lee, K. Y.; Kim, D.; Lee, J. H.; Kim, T. Y.; Gupta, M. K.; Kim, S. W., Hybrid Nanocomposites: Unidirectional High-Power Generation via Stress-Induced Dipole Alignment from $ZnSnO_3$ Nanocubes/Polymer Hybrid Piezoelectric Nanogenerator. *Adv. Funct. Mater.* **2014,** *24*, 1-1.
119. Jung, J. H.; Lee, M.; Hong, J.-I.; Ding, Y.; Chen, C.-Y.; Chou, L.-J.; Wang, Z. L., Lead-free $NaNbO_3$ nanowires for a high output piezoelectric nanogenerator. *ACS Nano* **2011,** *5*, 10041-10046.
120. Jung, J. H.; Chen, C.-Y.; Yun, B. K.; Lee, N.; Zhou, Y.; Jo, W.; Chou, L.-J.; Wang, Z. L., Lead-free $KNbO_3$ ferroelectric nanorod based flexible nanogenerators and capacitors. *Nanotechnology* **2012,** *23*, 375401.
121. Park, K. I.; Son, J. H.; Hwang, G. T.; Jeong, C. K.; Ryu, J.; Koo, M.; Choi, I.; Lee, S. H.; Byun, M.; Wang, Z. L., Highly-efficient, flexible piezoelectric PZT thin film nanogenerator on plastic substrates. *Adv. Mater.* **2014,** *26*, 2514-2520.
122. Xu, S.; Yeh, Y.-w.; Poirier, G.; McAlpine, M. C.; Register, R. A.; Yao, N., Flexible piezoelectric PMN–PT nanowire-based nanocomposite and device. *Nano Lett.* **2013,** *13*, 2393-2398.
123. Koka, A.; Sodano, H. A., A low-frequency energy harvester from ultralong, vertically aligned $BaTiO_3$ nanowire arrays. *Adv. Energy Mater.* **2014,** *4*, 1301660.
124. Lin, Y.-F.; Song, J.; Ding, Y.; Lu, S.-Y.; Wang, Z. L., Piezoelectric nanogenerator using CdS nanowires. *Appl. Phys. Lett.* **2008,** *92*, 022105.
125. Lin, L.; Lai, C.-H.; Hu, Y.; Zhang, Y.; Wang, X.; Xu, C.; Snyder, R. L.; Chen, L.-J.; Wang, Z. L., High output nanogenerator based on assembly of GaN nanowires. *Nanotechnology* **2011,** *22*, 475401.
126. Mishra, S.; Unnikrishnan, L.; Nayak, S. K.; Mohanty, S., Advances in piezoelectric polymer composites for energy harvesting applications: a systematic review. *Macromol. Mater. Eng.* **2019,** *304*, 1800463.
127. Chen, X.; Tian, H.; Li, X.; Shao, J.; Ding, Y.; An, N.; Zhou, Y., A high performance (PVDF-TrFE) nanogenerator with self-connected and vertically integrated fibers by patterned EHD pulling. *Nanoscale* **2015,** *7*, 11536-11544.

128. Saxena, P.; Shukla, P., A comprehensive review on fundamental properties and applications of poly (vinylidene fluoride) (PVDF). *Adv. Compos. Hybrid Mater.* **2021**, 1-19.
129. Mahanty, B.; Ghosh, S. K.; Garain, S.; Mandal, D., An effective flexible wireless energy harvester/sensor based on porous electret piezoelectric polymer. *Mater. Chem. Phys.* **2017,** *186*, 327-332.
130. Park, K.-I.; Jeong, C. K.; Kim, N. K.; Lee, K. J., Stretchable piezoelectric nanocomposite generator. *Nano Converg.* **2016,** *3*, 1-12.
131. Kim, Y.-J.; Dang, T.-V.; Choi, H.-J.; Park, B.-J.; Eom, J.-H.; Song, H.-A.; Seol, D.; Kim, Y.; Shin, S.-H.; Nah, J., Piezoelectric properties of $CH_3NH_3PbI_3$ perovskite thin films and their applications in piezoelectric generators. *J. Mater. Chem. A* **2016,** *4*, 756-763.
132. Ding, R.; Liu, H.; Zhang, X.; Xiao, J.; Kishor, R.; Sun, H.; Zhu, B.; Chen, G.; Gao, F.; Feng, X., Flexible piezoelectric nanocomposite generators based on formamidinium lead halide perovskite nanoparticles. *Adv. Funct. Mater.* **2016,** *26*, 7708-7716.
133. Ding, R.; Zhang, X.; Chen, G.; Wang, H.; Kishor, R.; Xiao, J.; Gao, F.; Zeng, K.; Chen, X.; Sun, X. W., High-performance piezoelectric nanogenerators composed of formamidinium lead halide perovskite nanoparticles and poly (vinylidene fluoride). *Nano Energy* **2017,** *37*, 126-135.
134. Hao, F.; Stoumpos, C. C.; Cao, D. H.; Chang, R. P.; Kanatzidis, M. G., Lead-free solid-state organic–inorganic halide perovskite solar cells. *Nat. Photonics* **2014,** *8*, 489-494.
135. Song, T.-B.; Yokoyama, T.; Stoumpos, C. C.; Logsdon, J.; Cao, D. H.; Wasielewski, M. R.; Aramaki, S.; Kanatzidis, M. G., Importance of reducing vapor atmosphere in the fabrication of tin-based perovskite solar cells. *J. Am. Chem. Soc.* **2017,** *139*, 836-842.
136. Ippili, S.; Jella, V.; Eom, J.-H.; Kim, J.; Hong, S.; Choi, J.-S.; Tran, V.-D.; Van Hieu, N.; Kim, Y.-J.; Kim, H.-J., An eco-friendly flexible piezoelectric energy harvester that delivers high output performance is based on lead-free $MASnI_3$ films and $MASnI_3$-PVDF composite films. *Nano Energy* **2019,** *57*, 911-923.
137. Pandey, R.; SB, G.; Grover, S.; Singh, S. K.; Kadam, A.; Ogale, S.; Waghmare, U. V.; Rao, V. R.; Kabra, D., Microscopic origin of piezoelectricity in lead-free halide perovskite: application in nanogenerator design. *ACS Energy Lett.* **2019,** *4*, 1004-1011.
138. Sultana, A.; Alam, M. M.; Sadhukhan, P.; Ghorai, U. K.; Das, S.; Middya, T. R.; Mandal, D., Organo-lead halide perovskite regulated green light emitting poly (vinylidene fluoride) electrospun nanofiber mat and its potential utility for ambient mechanical energy harvesting application. *Nano Energy* **2018,** *49*, 380-392.

139. Sultana, A.; Sadhukhan, P.; Alam, M. M.; Das, S.; Middya, T. R.; Mandal, D., Organo-lead halide perovskite induced electroactive β-phase in porous PVDF films: an excellent material for photoactive piezoelectric energy harvester and photodetector. *ACS Appl. Mater. Interfaces* **2018,** *10*, 4121-4130.
140. Ippili, S.; Jella, V.; Kim, J.; Hong, S.; Yoon, S.-G., Enhanced piezoelectric output performance via control of dielectrics in Fe^{2+}-incorporated $MAPbI_3$ perovskite thin films: Flexible piezoelectric generators. *Nano Energy* **2018,** *49*, 247-256.
141. Ippili, S.; Jella, V.; Kim, J.; Hong, S.; Yoon, S.-G., Unveiling predominant air-stable organotin bromide perovskite toward mechanical energy harvesting. *ACS Appl. Mater. Interfaces* **2020,** *12*, 16469-16480.
142. Stoumpos, C. C.; Malliakas, C. D.; Kanatzidis, M. G., Semiconducting tin and lead iodide perovskites with organic cations: phase transitions, high mobilities, and near-infrared photoluminescent properties. *Inorg. Chem.* **2013,** *52*, 9019-9038.
143. Grätzel, M., The light and shade of perovskite solar cells. *Nature Mater.* **2014,** *13*, 838-842.

End of Chapter 1

Chapter 2

Flexible Composite Energy Harvesters from Ferroelectric A_2MX_4-Type Hybrid Halogenometallates

2.1 Introduction

Materials based on organic-inorganic hybrid ferroelectrics have attracted enormous attention in recent years as possible substitutes for conventional inorganic ferroelectrics owing to their lightweight character, structural tunability, mechanical flexibility and amenability towards low-temperature device fabrication.[1-9] Several hybrid ferroelectrics have been constructed and investigated for applications in the domain of detectors, microactuators, FeRAMs and lately in photovoltaics and nano (mechanical) generators.[10-13] Amongst the existing environment-friendly energy sources, mechanical energy is quite prevalent and can be scavenged into usable electrical energy by a generator device.[14-16] Many inorganic piezoelectric and ferroelectric materials such as zinc oxide, barium titanate, lead zirconate titanate and zinc stannate have so far been utilized for fabricating nano- and mechanical generators.[17-20] Nevertheless, the poor flexibility of many of these ceramics impedes their applicability and life for certain practical applications. In this context, the use of hybrid organic-inorganic materials and their polymer composites is advantageous due to their enhanced mechanical durability in addition to the simple solution-based process for obtaining their thin films.[21] Yoon and co-workers fabricated the first hybrid piezoelectric energy-harvesting device employing methylammonium lead iodide ($MAPbI_3$) perovskite thin films that manifest an output voltage of 2.7 V and a current density of 140 $nAcm^{-2}$.[22] Subsequently, many such ferroelectric perovskites and other organic-inorganic hybrids embedded in the polymer matrices have been prepared and investigated for their mechanical energy harvesting properties.[23-25] However, most of these perovskite thin films suffer from low polarization values which limit their device output performances. Since the piezoelectric coefficient is directly related to the polarization of the material,[26] a ferroelectric substance with high remnant polarization is desirable for a device with high output performance.[27]

In this chapter, we report two new ferroelectric hybrid molecular halogenometallates **1** and **2** of formula A_2CdBr_4, where the A-sites are occupied by the heteroleptic ammonium cation of the type $[BnNMe_2R]^+$ (Bn = benzyl; **1**: R = Me; **2**: R = n-Pr). The compounds **1** and **2** exhibit high remnant polarization (P_r) values of 18.59 and 14.24 μCcm^{-2}, respectively. Further, flexible composites incorporating various weight

percentages (wt.%) of these ferroelectric materials were prepared with polydimethylsiloxane (PDMS) polymer which yielded fairly high output performances with the maximum open-circuit voltages (V_{oc}) of 52.9 and 63.8 V and current densities of 0.23 and 0.59 μAcm^{-2} for the 5 wt.% and 10 wt.% composites of **1** and **2**, respectively. To the best of our knowledge, this is the first report on the use of A_2MX_4 based systems for mechanical energy harvesting applications and the highest reported output voltages for any known hybrid halogenometallate-polymer composite device.[28-30] In addition, these new composite films exhibit high mechanical durability and retain their high output performance even after prolonged mechanical impacts.[31] These results demonstrate the applicability of discrete hybrid molecular halogenometallates, which can be fine-tuned by choice of the substituents on the organic backbone, as efficient mechanical energy harvesters within the framework of cost-effective solution processing methods.

2.2 Experimental section

2.2.1 General Remarks

Cadmium bromide tetrahydrate, benzyl trimethylammonium bromide, bromoethane and bromopropane were purchased from Sigma Aldrich and used without any further purification. Polydimethylsiloxane was purchased from Dow Corning and used as received. NMR spectra were recorded on a Bruker 400 MHz spectrometer (^{1}H NMR: 400.13 MHz; ^{13}C{^{1}H}NMR: 100.62 MHz) at room temperature using $SiMe_4$ (^{1}H, ^{13}C). The ESI spectra were obtained using a Waters Synapt G2 spectrometer. The variable temperature powder X-ray diffraction data were measured on a Bruker D8 Advance diffractometer on the polycrystalline samples obtained by grinding the single crystals or on the drop-casted thin films. The PXRD scans were collected in the 2θ range of 5 to 50 at 0.3 seconds per degree. Thermal analysis data was acquired from a Perkin-Elmer STA6000 thermogravimetric analyzer. FT-IR spectra were measured on a Perkin-Elmer spectrophotometer using KBr pellets. Melting points were analyzed using an Electrothermal melting point apparatus and were uncorrected. Kurtz and Perry's method was utilized to measure the SHG effect on the powder unsieved samples. Q-switch Nd: YAG laser generated the fundamental wavelength of 1064 nm. Powdered KDP was used as a reference for all the measurements.

2.2.2 Synthesis

2.2.2.1 Synthesis of 1: Single crystals of **1** were directly obtained by the slow evaporation of an aqueous solution containing stoichiometric amounts (2:1) of benzyltrimethylammonium bromide and cadmium bromide tetrahydrate. Colourless single crystals suitable for single-crystal X-ray diffraction were obtained after a week with a yield of 86%. M.P. 160-162°C. ^{1}H NMR (400 MHz, D_2O, ppm) δ 7.62 – 7.48 (m, 5H), 4.47 (s, 2H), 3.08 (s, 9H). ^{13}C NMR (101 MHz, D_2O, ppm) δ 132.79, 130.81, 129.15, 127.37, 69.56, 52.33 (s). FT-IR (cm^{-1}): 702, 728, 781, 894, 916, 972, 986, 1216, 1243, 1345, 1388, 1454, 1470, 1480, 1488, 1581, 1601, 2957, 2985, 3021, 3038. ESI-MS: calculated *m/z* for $[M]^+$ = 150.13, found m/z = 150.13.

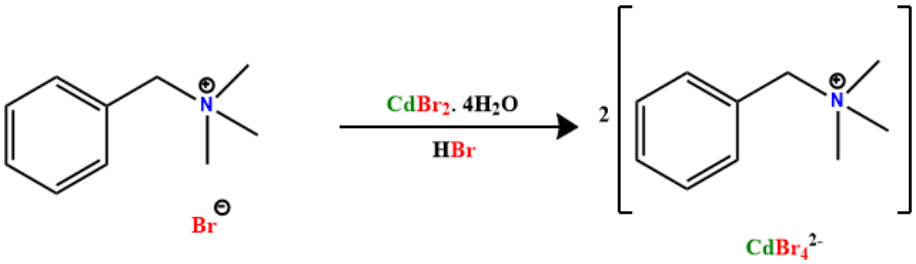

Scheme 2.1. Synthesis of N,N,N-trimethyl-1-phenylmethanaminium cadmium bromide, **1**.

2.2.2.2 Synthesis of 2·Br: The compound N-benzyl-N,N-dimethylpropan-1-aminium bromide was synthesized by dissolving equimolar ratios of bromopropane and N, N-dimethylbenzylamine in acetone at 273K. The resulting solution was slowly allowed to reach room temperature to give colorless single crystals of **2**·Br. Yield: 89%. M. P. 139-141°C.^{1}H NMR (400 MHz, D_2O, ppm) δ 7.70 – 7.45 (m, 5H), 4.44 (s, 2H), 3.31 – 3.12 (m, 2H), 2.99 (s, 6H), 1.96 – 1.77 (m, 2H), 0.96 (t, *J* = 7.3 Hz, 3H). ^{13}C NMR (101 MHz, D_2O, ppm) δ 132.79, 130.77, 128.89, 127.24, 67.83, 65.59, 49.63, 15.86, 9.94. ESI-MS: calculated *m/z* for $[M]^+$ = 178.16, found *m/z* = 178.16.

2.2.2.3 Synthesis of 2: The compound N-benzyl-N,N-dimethylpropan-1-aminium cadmium bromide was synthesized by the evaporation of the aqueous solution containing 2:1 stoichiometric ratio of the corresponding ammonium bromide salt **2**·Br and $CdBr_2.4H_2O$. Colourless single crystal was afforded after one week. Yield 87 %. M.P. 120-122°C. ^{1}H NMR (400 MHz, D_2O, ppm) δ 7.66 – 7.42 (m, 5H), 4.46 (s, 2H),

3.33 – 3.14 (m, 2H), 2.99 (s, 6H), 1.99 – 1.72 (m, 2H), 0.95 (t, *J* = 7.3 Hz, 3H). ^{13}C NMR (101 MHz, D_2O, ppm) δ 132.84, 130.71, 129.13, 127.22, 67.81, 65.53, 49.54, 15.76, 9.78. FT-IR (cm^{-1}): 705, 736, 780, 863, 929, 987, 1003, 1214, 1358, 1472, 1486, 1585, 1603, 2880, 2935, 2980, 3008, 3022. ESI-MS: calculated *m/z* for $[M]^+$ = 178.16, found *m/z* = 178.16.

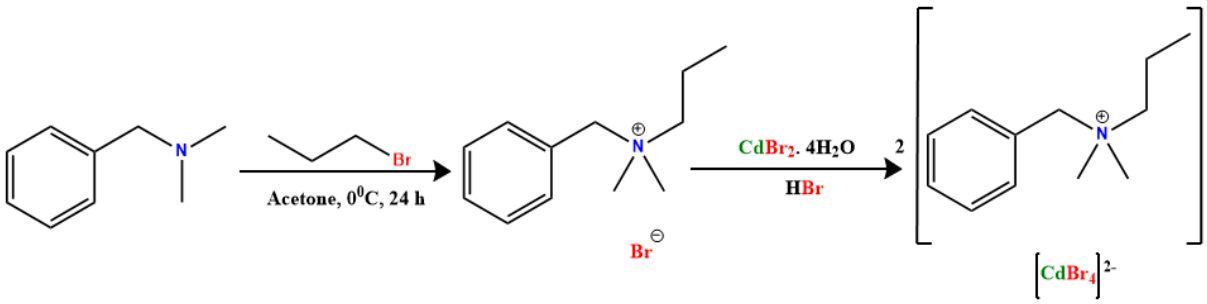

Scheme 2.2. Synthesis of N-benzyl-N,N-dimethylpropan-1-aminium cadmium bromide, **2**.

2.2.2.4 Synthesis of 3·Br: The compound N-Benzyl-N,N-dimethylethanaminium bromide was synthesized according to the literature procedure.[32] Equimolar amounts of bromoethane and N,N-dimethylbenzylamine were dissolved in acetone at 273 K. The solution was then slowly allowed to reach room temperature which resulted in the formation of single crystals of **3**·Br. Yield: 85 %. M.P. 163-165°C.^{1}H NMR (400 MHz, D_2O, ppm) δ 7.68 – 7.45 (m, 5H), 4.44 (s, 2H), 3.37 (q, *J* = 7.3 Hz, 2H), 2.97 (s, 6H), 1.42 (t, *J* = 7.3 Hz, 3H).^{13}C NMR (101 MHz, D_2O, ppm) δ 132.95, 130.76, 129.21, 127.21, 67.29, 59.88, 49.03, 7.77. ESI-MS: calculated *m/z* for $[M]^+$ = 164.14, found *m/z* = 164.14.

2.2.2.5 Synthesis of 3: The compound **3** was prepared by dissolving 2:1 stoichiometric ratios of **3**·Br and $CdBr_2.4H_2O$ in water. Slow evaporation of the solution afforded colourless crystals suitable for single crystal X-ray diffraction. Yield: 92 %. M.P. 145-147°C. ^{1}H NMR (400 MHz, D_2O, ppm) δ 7.63 – 7.40 (m, 5H), 4.45 (s, 2H), 3.37 (q, *J* = 7.3 Hz, 2H), 2.97 (s, 6H), 1.41 (ddd, *J* = 7.3, 4.5, 1.7 Hz, 3H). ^{13}C NMR (101 MHz, D_2O, ppm) δ 132.86, 130.70, 129.12, 127.20, 67.33, 59.84, 48.92, 7.61. FT-IR (cm^{-1}): 702, 714, 722, 766, 869, 870, 1018, 1081, 1216, 1305, 1344, 1412, 1460, 1471, 1585, 1602, 2960, 2989, 2999, 3014, 3043. ESI-MS: calculated *m/z* for $[M]^+$ = 164.14, found *m/z* = 164.14.

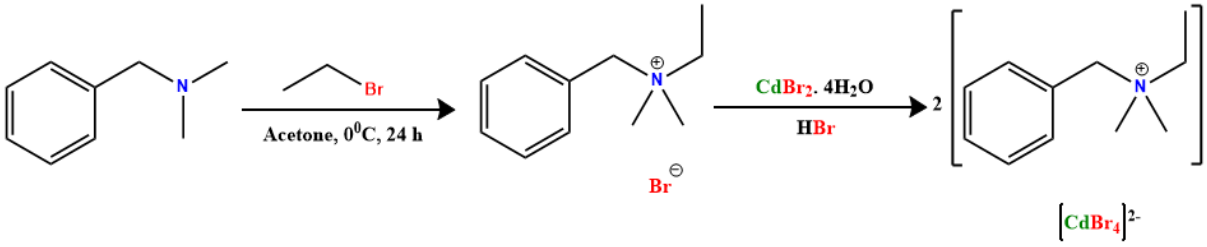

Scheme 2.3. Synthesis of N-Benzyl-N,N-dimethylethanaminium cadmium Bromide, **3**.

2.2.3 Crystallography: Reflections for **1**, **2** and **3** were acquired on a Bruker Smart Apex Duo diffractometer at various temperatures using MoKα radiation (λ = 0.71073 Å). Crystal structures were solved using the direct method and then refined by full-matrix least squares against F^2 using SHELXL-2014/7 built in the Apex 3 program.[33] All the non-hydrogen atoms were refined anisotropically while the hydrogen atoms were constrained in geometric positions to their parent atoms.[34] Crystallographic refinement data for DPDP·PF_6 at various temperatures is listed in (Table 2.1).

Table 2.1: Details of crystallographic data collection of 1, 2 and 3.

Compound	1	3	2
Chemical formula	C_{20} H_{32} Br_4 Cd N_2	C_{22} H_{36} Br_4 Cd N_2	C_{24} H_{40} Br_4 Cd N_2
Formula weight	732.51	760.57	788.62
Temperature	100(2) K	100(2) K	100(2) K
Crystal system	Monoclinic	Triclinic	Orthorhombic
Space group	*$P2_1$*	*P-1*	*$Pna2_1$*
a(Å): α(°)	9.554(4); 90	9.675(2); 94.071(6)	9.8897(10); 90
b(Å); β(°)	9.071(4); 94.369(13)	9.911(2); 104.294(6)	31.038(3); 90
c (Å); γ (°)	15.206(6); 90	16.382(4); 115.155(5)	9.6570(9); 90
V(Å^3); Z	1314.0(9); 2	1349.8(5); 2	2964.3(5); 4
P(calc.) mg m^{-3}	1.851	1.871	1.767
μ(Mo K_α)mm^{-1}	6.921	6.741	6.143
$2\theta_{max}$ (°)	56	56	56
R (int)	0.1098	0.1051	0.1082
Completeness to θ	100.0	100	100
Data/param.	6455/ 251	6746/ 268	7245/ 275
GOF	1.008	1.047	1.051
R1[F>4σ(F)]	0.0604	0.0452	0.0573
wR2 (all data)	0.1342	0.1147	0.1363
max. peak/hole (e.Å^{-3})	1.240/ -1.182	1.038/-1.566	2.253/-2.307

2.2.4 Dielectric, Ferroelectric and Piezoelectric Measurements: The dielectric data for both **1** and **2** were measured using the Novocontrol Dielectric Spectrometer. The powder samples of **1** and **2** were compacted in the form of discs to measure the dielectric properties. Aluminum adhesive foils were integrated as top and bottom electrodes to these compacted discs for the measurements. The ferroelectric hysteresis loop was recorded on the thin films of **1** and **2** by using the Sawyer-Tower circuit. These thin films were prepared by utilizing a chemical solution procedure. A DMF solution containing **1** and **2** were drop casted on Aluminum sheet serving as the bottom electrode. These films were then heated in the oven at 70 °C for 5 hours. A homogeneous film (~ 20 µm) with continual microcrystals was obtained for both the cases. After drying up the films, aluminum adhesive foils were assimilated as the top electrode. The polarization measurements were performed using an aixACCT TF-2000E model hysteresis loop analyzer. Leakage currents were measured dynamically for varied voltage steps in the course of hysteresis loop measurements. The d_{33} measurements were performed on Berlincourt Piezo d_{33} meter on **1**-PDMS and **2**-PDMS composite films.

For evaluating the mechanical energy harvesting performance of the thin film devices of **1** and **2**, a home built vertical impact force set-up operating in a periodic compression and release function coupled with an oscilloscope was used. The fabricated devices were subjected to an impact force of 40 N with a tapping frequency of 25 Hz on an active area of 3 x 3 cm^2. All the output voltage and current measurements were recorded on Keithley DMM7510 7.5 multimeter. The output current density was calculated across the various load resistance ranging from 100 kΩ to 50 MΩ. The obtained current density was then multiplied with the maximum voltage to yield the power density.

2.2.5 Theoretical Calculations: All the calculations for ferroelectric polarization were performed with QuantumATK[35] package. The experimental lattice parameters were used as such for the calculations. The self-consistent field (scf) calculations were performed with LCAO (Linear Combination of Atomic Orbitals) method as implemented in QuantumATK with the generalized gradient approximation (GGA) in the Perdew−Burke−Ernzerhof (PBE) form[36] and a fine k-point mesh of 19x12x11 was employed in Monkhorst-Pack[37] scheme. A density mesh cut-off of 100 Hartree was

applied in the calculation with an electronic convergence of $1x10^{-5}$ Hartee. For ferroelectric polarization, the Berry phase method[38] as implemented in QuantumATK was used. For Berry phase calculations, a Monkhorst-Pack grid of 30x7x7, 7x30x7 and 7x7x30 k points were used for sampling the Brillouin zone along reciprocal a, b, and c directions. The total polarization was obtained as a summation of electronic and ionic fractional polarizations as stated in Modern theory of Polarization.

2.3 Results and discussion

2.3.1 Syntheses and Crystal Structures: The compound **1**, $[BnNMe_3]_2CdBr_4$, was directly isolated as single crystals from the aqueous phase reaction of benzyl trimethyl ammonium bromide with $CdBr_2{\cdot}4H_2O$. The compound **2**, $[BnNMe_2{}^nPr]_2CdBr_4$, was obtained in a two-step procedure involving the reaction of N,N-dimethyl benzylamine, n-propyl bromide and $CdBr_2{\cdot}4H_2O$ in water. A similar reaction in the presence of ethyl bromide instead of n-propyl bromide gave the compound **3** of formula $[BnNMe_2Et]_2CdBr_4$ (Chart 1, Scheme 2.1-2.3). However, compound **3** was found to crystallize in the centrosymmetric triclinic space group *P-1* (Table S1, Supporting Information). The analytical and spectroscopic characterization of these compounds is given in the supplementary material (Figures 2A.1-2A.10, Appendix 2).

Chart 1: Schematic diagrams of the synthesized discrete ammonium halogenometallate salts of Cd(II) ions.

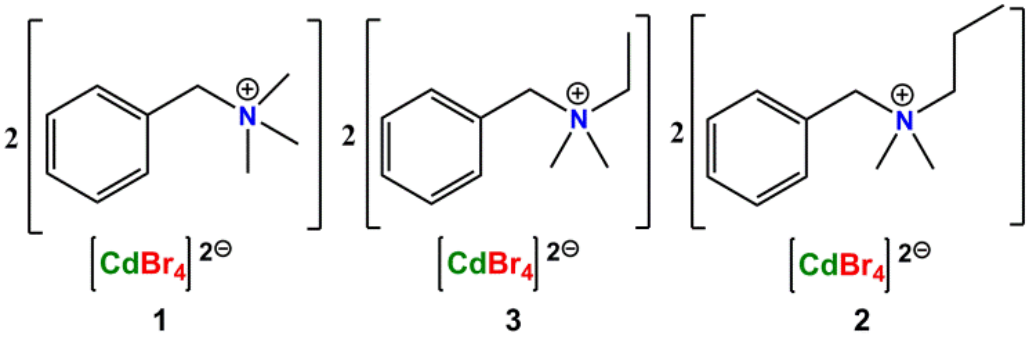

The molecular structures of these halogenometallates were established by single-crystal X-ray diffraction analysis at 100 K. The compounds **1** and **2** crystallize in polar space groups $P2_1$ (point group: C_2) and $Pna2_1$ (point group: C_{2V}), respectively. Their asymmetric unit consists of two heteroleptic ammonium cations and a distorted

tetrahedral $(CdBr_4)^{2-}$ anion (Figure 1 and Tables 2.1 and 2A.1, Appendix 2). The unit cell packing of **1** comprises two such motifs while that of **2** is constituted by four of them (Figure 2A.11 and 2A.13, Appendix 2). The packing structure of **1** consists of the stacks of $(CdBr_4)^{2-}$ ions surrounded by the bi-stacks of ammonium cations (of N1 and N2) down the b-axis. (Figure 2A.13, Appendix 2). Similarly, **2** consists of the stacks $(CdBr_4)^{2-}$ ions and ammonium cations in its packing along the c-axis. (Figure 2A.14, Appendix 2). A closer look at the extended structures reveals interesting non-classical C-H...Br interactions in both **1** and **2**. (Figure 2A.11-2A.12 and Tables 2A.2 and 2A.3, Appendix 2). Thus in **1**, the $(CdBr_4)^{2-}$ unit is H-bonded with twelve H-atoms of the methyl and benzylic α-carbon atoms. These interactions result in the formation of columnar arrays of H-bonding interactions, which are built around a central helical channel that runs along the b-axis. (Figure 2A.13, Appendix 2). Due to the bulkier nature of the cations in **2**, the $(CdBr_4)^{2-}$ ions in it are associated with only eight ammonium cations via C-H...Br interactions. The non-classical H-bonding in **2** is supported by the CH_3 moieties, benzylic α-CH_2 groups and aromatic C-H groups. The H-bonded assembly in **2** is built up of a central tubular channel along the c-axis that holds the smaller channels around it. (Figure 2A.14, Appendix 2). The H…Br distances in these assemblies are ranging from 2.7913(15) to 3.1470(16) Å and C-H…Br angles are between 145.029 (75) and 163.184(11) °.

The non-centrosymmetric packing of these discrete halogenometallates is further confirmed by their second harmonic generation (SHG) efficiencies. Thus, **1** and **2** showed the SHG efficiencies of 0.21 and 0.25, respectively, with respect to the standard KDP. Both the compounds exhibit thermal stabilities up to 523 K as revealed by the thermogravimetric analysis. The DTA profile displays one heat anomaly at 435 K for **1** and one at 392 K for **2** corresponding to their respective melting points. The differential scanning calorimetric data of **1** and **2** showed no phase transitions displaying prominent peaks only due to their melting points (Figures 2A.15 and 2A.16, Appendix 2).

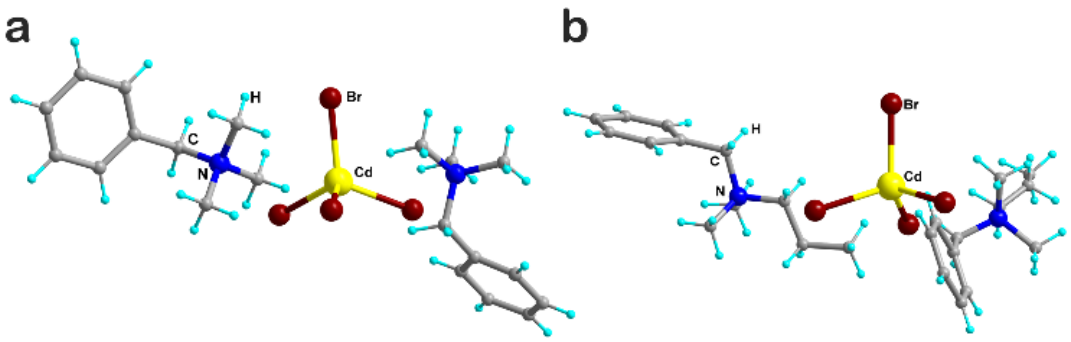

Figure 2.1: *Molecular structures of (a)* ***1*** *and (b)* ***2****.*

Variable temperature single crystal X-ray diffraction (VT-SCXRD) analyses were performed to investigate the presence of any centrosymmetric phase in these structures. These analyses revealed that their corresponding space groups remained the same at all the measured temperatures albeit with marginal increase in their cell volumes (Figure 2A.17, Appendix 2). It may be due to the thermal motion of atoms at higher temperatures leading to a volume expansion of the unit cells. Similarly, no change of phase was detected for both **1** and **2** from the variable temperature powder X-ray diffraction data (VT-PXRD) as well, at all the measured temperatures ranging from 298 to 393 K (for **1**) and 298 to 363 K (for **2**) (Figure 2A.18, Appendix 2).

2.3.2 Ferroelectric and Dielectric Studies

The potential ferroelectric nature of these compounds was further probed by polarization (*P*) vs. electric-field (*E*) loop measurements. The polarization reversals were examined on the thin-film samples of **1** and **2** in a Sawyer-Tower circuit. The thin films of **1** and **2** were obtained by drop casting their corresponding DMF solutions on top of aluminum sheets which themselves serve as the bottom electrodes. The SEM analyses revealed the formation of homogeneous films in each of these cases (Figure 2A.19, Appendix 2). The PXRD and SEM analysis of the as-prepared thin films of **1** and **2** displayed the existence of crystallites along multiple directions signifying the preparation of polycrystalline films for both the compounds. (Figure 2A.20-2A.21, Appendix 2). Finally, a layer of adhesive aluminum tape was placed to provide the top electrode for the electrical measurements.

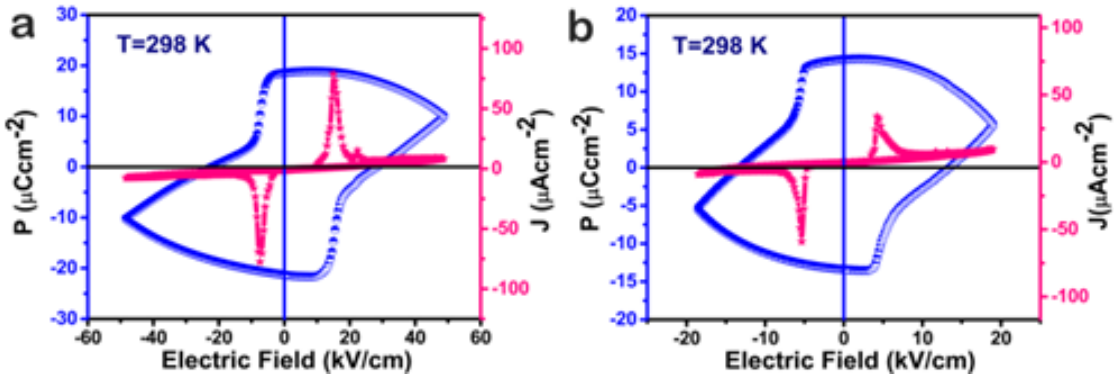

Figure 2.2: *Ferroelectric hysteresis loops of (a)* ***1*** *and (b)* ***2*** *along with their corresponding leakage current density plots measured on their thin films of ~20 μm thickness.*

The *P-E* loop measurements on these films gave a rectangular hysteresis loop at an operating frequency of 0.1 Hz. The obtained coercive voltages are 57 V (E_c: 28.5 kVcm^{-1}) for **1** and 28 V (E_c: 14 kVcm^{-1}) for **2** (Figure 2.2). The measurements gave the P_r values of 18.59 and 14.24 μCcm^{-2} and P_s values of 10.11 and 5.75 μCcm^{-2} for **1** and **2**, respectively, which compare very well with the recently reported hybrid molecular ferroelectric thin films.[8,39-42] The leakage current density plots of both of these *P-E* loops gave peaks associated with their coercive fields with low-leakage currents (of the order of 10^{-6} A) which confirms the ferroelectric nature of the obtained loops. Preliminary theoretical calculations performed on the structures of **1** and **2** resulted in the polarization values of 11.8 and 16.7 μCcm^{-2}, respectively, which very well supports the experimental observation of ferroelectric polarization for these compounds.

The temperature dependence of the dielectric permittivity was measured on the polycrystalline compacted discs of **1** and **2**. For both **1** and **2**, the values of the real part of dielectric constant (ε') displayed the absence of any notable dielectric anomaly peak upon increasing the temperatures from 298 to 413 K and 298 to 373 K for **1** and **2**, respectively (Figure 2.3). These outcomes are in agreement with the obtained variable temperature single crystal and powder X-ray diffraction data. The maximum ε' values were found to be 228 and 159.9 for **1** (415 K) and **2** (373 K), respectively, at 1 KHz, as observed from the frequency dependent dielectric constant measurements. A similar trend was noticed in the dielectric loss data of these compounds that gave reasonably low tan δ values at room temperatures. Also, the observed increase in the

ε' values with a decrease in frequencies indicates the contribution of all the four polarization mechanisms for the overall dipole moments of these hybrid materials (Figure 2A.22, Appendix 2).

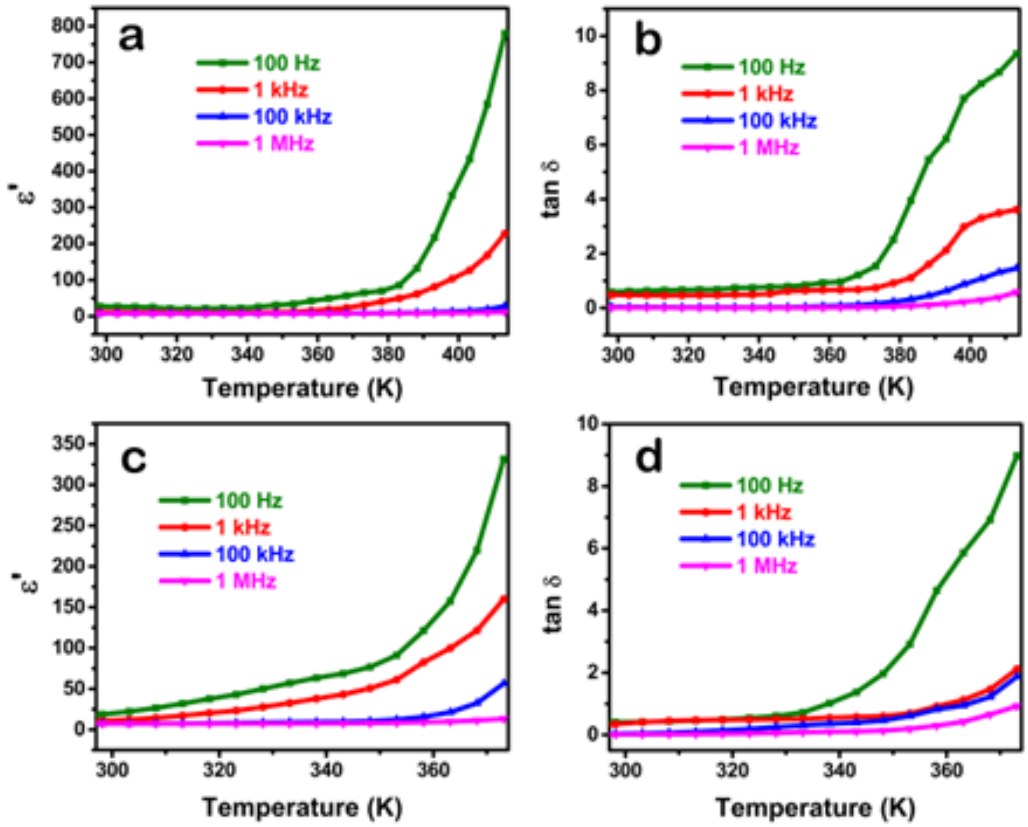

Figure 2.3: *The temperature-dependent real part of the complex dielectric constant (a) of* ***1*** *and (c)* ***2*** *and dielectric loss (tan δ) (b) of* ***1*** *and (d)* ***2*** *measured at different frequencies.*

2.3.3 Mechanical energy harvester

Spurred by the high and robust polarization characteristics of **1** and **2**, we set out to test the potential of these molecular halogenometallates for the fabrication of flexible mechanical energy harvesting devices. Suitable quantities of **1** and **2** were dispersed homogeneously into the PDMS precursor solutions to prepare polymer composites of varying weight percentages (1, 5, 10 and 20 wt. %). The devices were fabricated by drop casting the composite solutions onto the PET wrapped Al tape and curing at 70 °C. The device connections were finally made by soldering the copper wires onto the copper tape adhered to the electrodes. A schematic diagram of the fabricated device

constructed from **2**-PDMS composite is shown in Figure 2.4a. All of the devised composites presented high mechanical flexibility signifying their propensity as mechanical energy harvesters (Figure 2.4b and Figure 2A.23, Appendix 2).

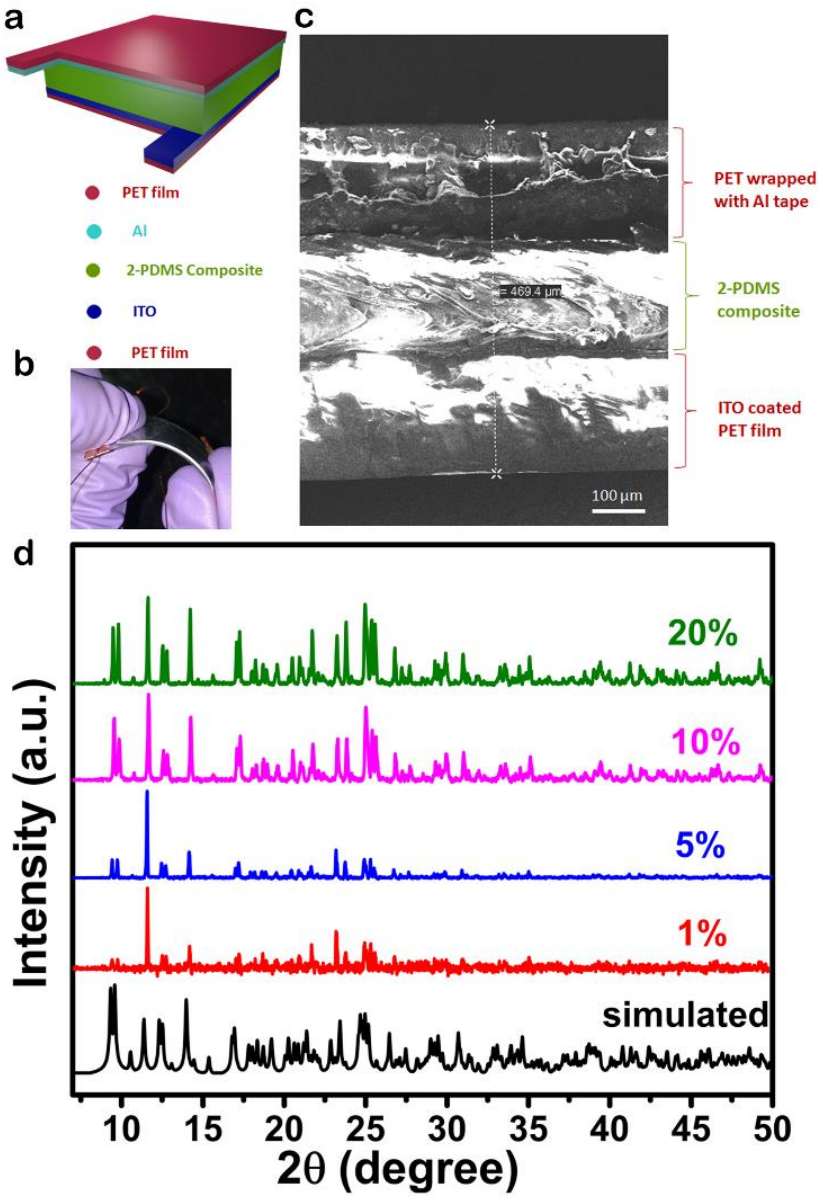

Figure 2.4: *(a) Schematic diagram depicting the construction of the composite device based on **2**-PDMS (b) Photograph of a flexible device incorporating the ferroelectric material encapsulated into PDMS. (c) Cross-sectional SEM image of the **2**-PDMS composite device. (d) XRD patterns of as-prepared composites with varying concentrations of **2**.*

The cross-sectional scanning electron microscopy (SEM) image reveals the thickness of the composites to be ~140 µm and the obtained morphologies signify random

distribution of **1** and **2** in the polymer matrix (Figure 2.4c and Figure 2A.24-2A.27, Appendix 2). The structural integrity of both **1** and **2** was found to be maintained in all the wt.% composites as evident from their PXRD analysis (Figure 2.4d and Figure 2A.24b, Appendix 2).

The piezoelectric output performance was evaluated by subjecting the fabricated devices to an impact force of 40 N with a tapping frequency of 25 Hz on an active area of 3 x 3 cm^2. A home built vertical impact force set-up operating in a periodic compression and release function coupled with an oscilloscope was used for the device measurements. The output voltage was seen to elevate with an increase in the concentrations of **1** and **2**, saturating at 5 wt.% for **1** and 10 wt.% for **2** and then declining with the further increase in the loading. The maximum output voltage values as high as 52.9 V for 5 wt.% of **1** and 63.8 V for 10 wt.% of **2** have been recorded (Figures 2.5a and 2.5b and Figures 2A.28-2A.29, Appendix 2). The effect of external applied force (10, 15, 20, 30 N) on the output performances of the optimal 5 wt.% **1**-PDMS and 10 wt.% **2**-PDMS devices were further investigated. These experiments show that the output voltage increases with increase in the applied external force (Figures 2.5c and 2.5d and Figures 2A.30-31, Appendix 2). Furthermore, a device based on PDMS alone resulted in the output voltage of only 3.5 V, thus confirming that the large output voltage generation is from its composites devices of **1** and **2** (Figure 2A.32, Appendix 2).

The observed variations in the optimal loading conditions for **1**-PDMS and **2**-PDMS can originate from the differences in the molecular bonding and related strain distributions in the composite system, the attendant polarizations, the interactions of the polarization fields against deformations and constitution of the active layers.[43-46] As a result, the optimum concentration at which the output voltage maximizes could be different for different embedded molecules, which is 5 wt.% for **1** and 10 wt.% for **2** in the present instance. However, a further increase in the concentration above the threshold limit (beyond 5 wt.% (**1**) and 10 wt.% (**2**)) renders a weaker insulation of the composites leading to the electrical breakdown and hence a drop in the output voltages.[43,44]

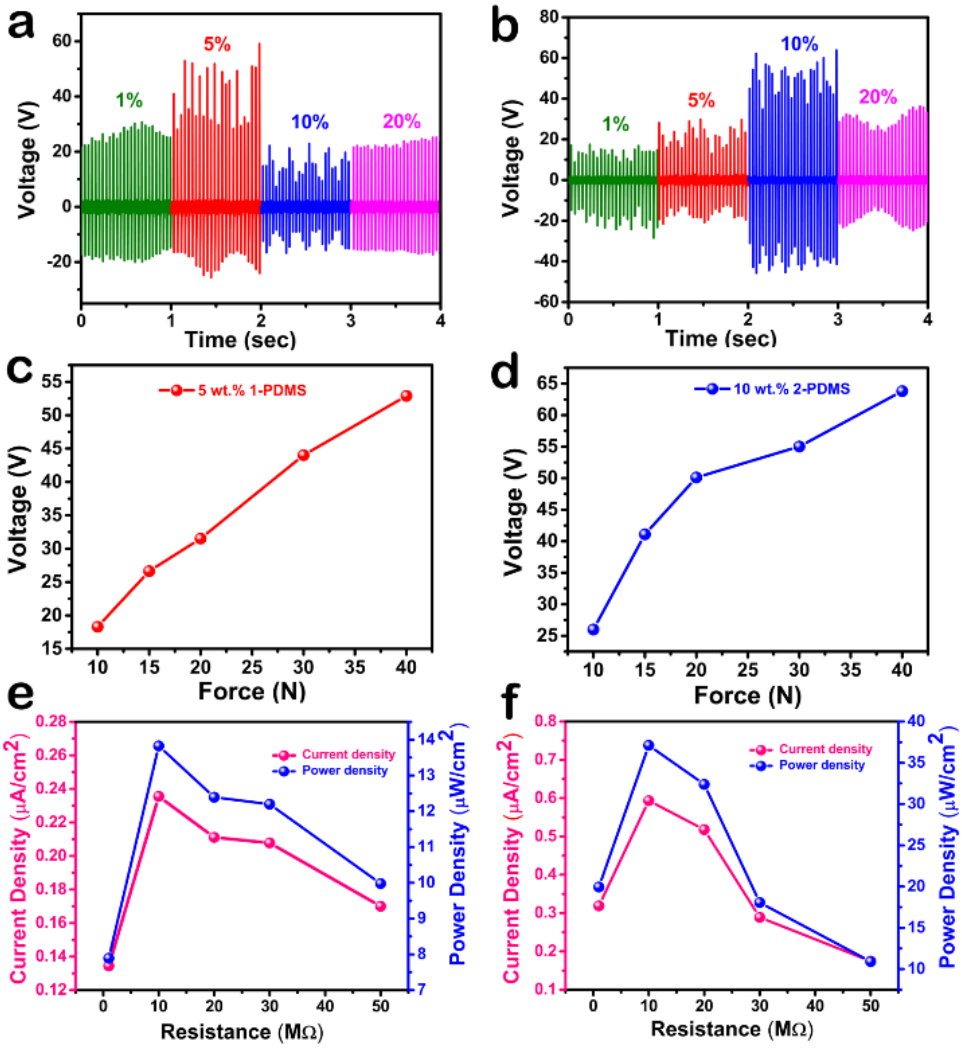

Figure 2.5: *(a) The output performance of (a) **1**-PDMS composite device and (b) **2**-PDMS composite device with varying concentrations of **1** and **2**, respectively. Effect of applied force on the output voltage generation from (c) 5 wt.% **1**-PDMS and (d) 10 wt.% **2**-PDMS. The current density and the power density as a function of load resistance corresponding to (e) 5 wt.% **1**-PDMS device and (f) 10 wt.% **2**-PDMS device.*

Figure 6 depicts the working mechanism of the mechanical energy harvester devices based on the composites **1**-PDMS and **2**-PDMS. When a vertical compressive force is exercised, the dipoles pertaining to the composites tend to align in one direction and generate a piezoelectric potential across the electrodes.[47,48] Subsequently, both the positive and negative charges are accumulated on the electrodes in order to counter the piezoelectric potential and thereby generating a positive signal from the device. When the vertical compressive force is liberated, the generated piezoelectric potential

across the electrodes will decline because of which the accumulated charges traverse back in the opposite direction producing the negative signal. The output signals can therefore be acquired continuously by subjecting the device to a constant vertical compression and release cycles.

In addition to these piezoelectric effects, the presence of triboelectric effects has also been detected in the **1**-PDMS and **2**-PDMS devices by performing the single electrode measurements. A relatively much lower output voltages of 6.09 and 10.28 V have been obtained from the respective 5wt.% **1**-PDMS and 10 wt.% **2**-PDMS devices in these measurements (Figure 2A.33, Appendix 2). The origin of the tribo-effect can be tracked to the residual friction between the electrode and composite layers. However, the major contribution to the overall output voltages can be attributed to piezoelectric nature of the materials.

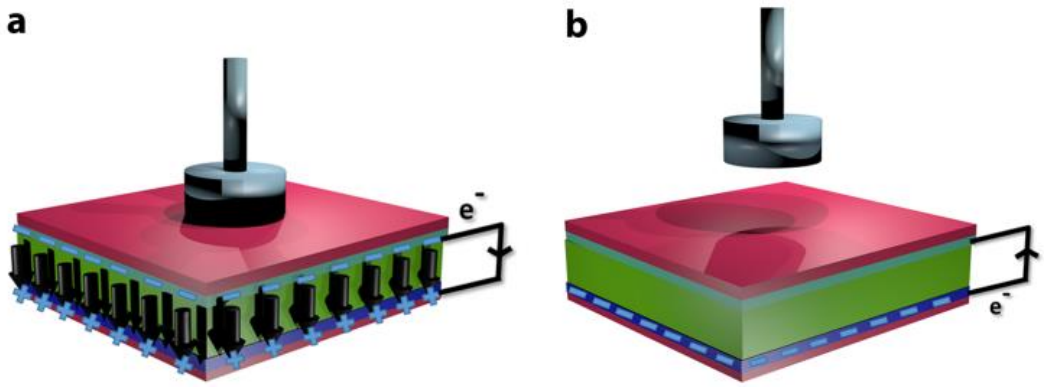

Figure 2.6: *(a) Dipole alignment assisting the electron movement from the top to bottom electrode due to the generation of piezoelectric potential during the vertical compressive force. (b) Reverse flow of the accumulated electrons upon release of the compressive force.*

Subsequent investigations on the dependence of current and power densities on diverse external load impedance ranging from 100 kΩ to 50 MΩ gave the maximum current densities of 0.23 and 0.59 μAcm^{-2} for the optimal 5 wt.% **1**-PDMS and 10 wt.% **2**-PDMS composites, respectively. Similarly, the maximum power densities of 13.8 and 37.1 μWcm^{-2} have been recorded for the respective 5 wt.% **1**-PDMS and 10 wt.% **2**-PDMS devices at the operating resistance of 10MΩ (Figures 5e and 5f). The mechanical durability of the optimal 5 wt.% **1**-PDMS and 10 wt.% **2**-PDMS devices were confirmed by subjecting them to extended compression and release cycles with

an impact force of 40 N, which demonstrated the retention of the output voltages even after 1500 cycles. (Figure 2A.34, Appendix 2). The piezoelectric measurements performed on the optimal 5 wt.% **1**-PDMS and 10 wt.% **2**-PDMS gave the piezoelectric coefficient (d_{33}) values of 6 and 7 pCN^{-1} at an operating frequency of 20 Hz and an applied force of 4 N. These d_{33} values are consistent with those obtained for the corresponding compacted pellets of **1** and **2** (6 and 7 pCN^{-1}).

To demonstrate the role of these composite generators as possible energy sources for low consumption electronic devices, the output power generated from 5 wt.% **1**-PDMS and 10 wt.% **2**-PDMS were directly employed to charge a 10 µF capacitor through a full wave-bridge rectifier circuit, as shown in Figure 2.7a. The output voltage across the capacitor was seen to increase gradually reaching a value of 1.39 V for 5 wt.% **1**-PDMS and 1.8 V for 10 wt.% **2**-PDMS (Figure 2.7b) and the respective stored electrical energies were calculated to be 9.6 and 16.2 µJ.

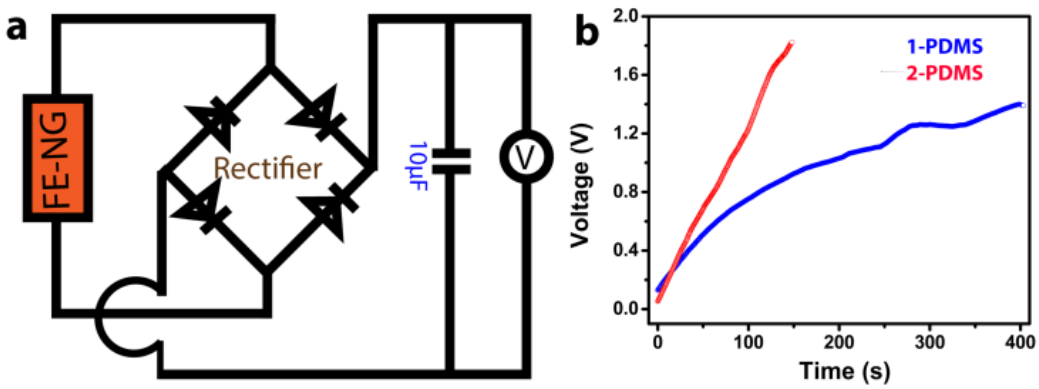

Figure 2.7: *(a) Schematic diagram of a full wave-bridge rectifier circuit used for the capacitor charging experiment. (b) The charging of a 10 µF capacitor using the 5 wt.% **1**-PDMS and 10 wt.% **2**-PDMS devices.*

2.4 Conclusion

In conclusion, we have shown the utilization of strategically designed discrete hybrid halogenometallates for mechanical energy harvesting applications. The ammonium halogeneometallates **1** and **2** were found to crystallize in the polar point groups and their polycrystalline thin films were found to exhibit high ferroelectric remnant polarization values of 18.59 and 14.24 μCcm^{-2}, respectively. Flexible composite devices based on **1** and **2** were prepared with the help of polydimethylsiloxane and

tested for mechanical energy harvesting with the help of a vertical impact setup. Substantially high output voltages of 52.9 and 63.8 V have been recorded for the 5 wt.% **1**-PDMS and 10 wt.% **2**-PDMS devices, respectively, for an applied frequency of 25 Hz and impact force of 40 N. The energy harvested from these devices was subsequently employed to charge a 10μF capacitor by applying a full wave-bridge rectifier. These results demonstrate the possibilities of simple discrete hybrid halogenometallates as efficient mechanical energy harvesters. Also, the performances of these devices present a significant step towards realizing next-generation flexible self-powered electronics.

2.5 References

(1) Leblanc, N.; Mercier, N.; Zorina, L.; Simonov, S.; Auban-Senzier, P.; Pasquier, C., Large Spontaneous Polarization and Clear Hysteresis Loop of a Room-Temperature Hybrid Ferroelectric Based on Mixed-Halide [BiI_3Cl_2] Polar Chains and Methylviologen Dication. *J. Am. Chem. Soc.* **2011,** *133*, 14924-14927.

(2) Zhang, W.; Xiong, R.-G., Ferroelectric Metal-Organic Frameworks. *Chem. Rev.* **2012,** *112*, 1163-1195.

(3) Zhang, Y.; Liu, Y.; Ye, H. Y.; Fu, D. W.; Gao, W.; Ma, H.; Liu, Z.; Liu, Y.; Zhang, W.; Li, J.; Yuan, G. L.; Xiong, R. G., A Molecular Ferroelectric Thin Film of Imidazolium Perchlorate That Shows Superior Electromechanical Coupling. *Angew. Chem. Int. Ed.* **2014,** *53*, 5064-5068.

(4) Piecha-Bisiorek, A.; Białońska, A.; Jakubas, R.; Zieliński, P.; Wojciechowska, M.; Gałązka, M., Strong Improper Ferroelasticity and Weak Canted Ferroelectricity in a Martensitic-Like Phase Transition of Diisobutylammonium Bromide. *Adv. Mater.* **2015,** *27*, 5023-5027.

(5) Martin, L. W.; Rappe, A. M., Thin-film ferroelectric materials and their applications. *Nat. Rev. Mater.* **2016,** *2*, 16087.

(6) Li, W.; Wang, Z.; Deschler, F.; Gao, S.; Friend, R. H.; Cheetham, A. K., Chemically diverse and multifunctional hybrid organic–inorganic perovskites. *Nat. Rev. Mater.* **2017,** *2*, 16099.

(7) Tang, Y.-Y.; Li, P.-F.; Shi, P.-P.; Zhang, W.-Y.; Wang, Z.-X.; You, Y.-M.; Ye, H.-Y.; Nakamura, T.; Xiong, R.-G., Visualization of Room-Temperature Ferroelectricity and Polarization Rotation in the Thin Film of Quinuclidinium Perrhenate. *Phys. Rev. Lett.* **2017,** *119*, 207602.

(8) Tang, Y.-Y.; Li, P.-F.; Zhang, W.-Y.; Ye, H.-Y.; You, Y.-M.; Xiong, R.-G., A Multiaxial Molecular Ferroelectric with Highest Curie Temperature and Fastest Polarization Switching. *J. Am. Chem. Soc.* **2017,** *139*, 13903-13908.

(9) Tang, Y.-Y.; Li, P.-F.; Liao, W.-Q.; Shi, P.-P.; You, Y.-M.; Xiong, R.-G., Multiaxial Molecular Ferroelectric Thin Films Bring Light to Practical Applications. *J. Am. Chem. Soc.* **2018,** *140*, 8051-8059.

(10) Lines, M. E.; Glass, A. M., *Principles and applications of ferroelectrics and related materials*. Clarendon Press: Oxford, UK, 1977.

(11) Scott, J. F., Applications of Modern Ferroelectrics. *Science* **2007,** *315*, 954-959.

(12) Ye, Z.-G., *Handbook of Advanced Dielectric, Piezoelectric and Ferroelectric Materials: Synthesis, Properties and Applications*. Elsevier: 2008.

(13) Ishiwara, H., Ferroelectric Random Access Memories. *J. Nanosci. Nanotechnol.* **2012,** *12*, 7619-7627.

(14) Wang, Z. L.; Song, J., Piezoelectric Nanogenerators Based on Zinc Oxide Nanowire Arrays. *Science* **2006,** *312*, 242-246.

(15) Yu, A.; Jiang, P.; Lin Wang, Z., Nanogenerator as self-powered vibration sensor. *Nano Energy* **2012,** *1*, 418-423.

(16) Xu, S.; Yeh, Y.-w.; Poirier, G.; McAlpine, M. C.; Register, R. A.; Yao, N., Flexible Piezoelectric PMN-PT Nanowire-Based Nanocomposite and Device. *Nano Lett.* **2013,** *13*, 2393-2398.

(17) Park, K. I.; Son, J. H.; Hwang, G. T.; Jeong, C. K.; Ryu, J.; Koo, M.; Choi, I.; Lee, S. H.; Byun, M.; Wang, Z. L.; Lee, K. J., Highly-Efficient, Flexible Piezoelectric PZT Thin Film Nanogenerator on Plastic Substrates. *Adv. Mater.* **2014,** *26*, 2514-2520.

(18) Shin, S.-H.; Kim, Y.-H.; Lee, M. H.; Jung, J.-Y.; Nah, J., Hemispherically Aggregated $BaTiO_3$ Nanoparticle Composite Thin Film for High-Performance Flexible Piezoelectric Nanogenerator. *ACS Nano* **2014,** *8*, 2766-2773.

(19) Kang, H. V. N. a. D. J., Flexible, transparent and exceptionally high power output nanogenerators based on ultrathin ZnO nanoflakes. *Nanoscale* **2016**, *8*, 5059-5066.

(20) Guo, R.; Guo, Y.; Duan, H.; Li, H.; Liu, H., Synthesis of Orthorhombic Perovskite-Type $ZnSnO_3$ Single-Crystal Nanoplates and Their Application in Energy Harvesting. *ACS Appl. Mater. Interfaces* **2017,** *9*, 8271-8279.

(21) Alluri, N. R.; Saravanakumar, B.; Kim, S.-J., Flexible, Hybrid Piezoelectric Film ($BaTi_{(1-x)}Zr_xO_3$)/PVDF Nanogenerator as a Self-Powered Fluid Velocity Sensor. *ACS Appl. Mater. Interfaces* **2015,** *7*, 9831-9840.

(22) Kim, Y.-J.; Dang, T.-V.; Choi, H.-J.; Park, B.-J.; Eom, J.-H.; Song, H.-A.; Seol, D.; Kim, Y.; Shin, S.-H.; Nah, J.; Yoon, S.-G., Piezoelectric properties of $CH_3NH_3PbI_3$ perovskite thin films and their applications in piezoelectric generators. *J. Mater. Chem. A* **2016,** *4*, 756-763.

(23) Ding, R.; Liu, H.; Zhang, X.; Xiao, J.; Kishor, R.; Sun, H.; Zhu, B.; Chen, G.; Gao, F.; Feng, X.; Chen, J.; Chen, X.; Sun, X.; Zheng, Y., Flexible Piezoelectric Nanocomposite Generators Based on Formamidinium Lead Halide Perovskite Nanoparticles. *Adv. Funct. Mater.* **2016,** *26*, 7708-7716.

(24) Ding, R.; Zhang, X.; Chen, G.; Wang, H.; Kishor, R.; Xiao, J.; Gao, F.; Zeng, K.; Chen, X.; Sun, X. W.; Zheng, Y., High-performance piezoelectric nanogenerators composed of formamidinium lead halide perovskite nanoparticles and poly(vinylidene fluoride). *Nano Energy* **2017,** *37*, 126-135.

(25) Jella, V.; Ippili, S.; Eom, J.-H.; Choi, J.; Yoon, S.-G., Enhanced output performance of a flexible piezoelectric energy harvester based on stable $MAPbI_3$-PVDF composite films. *Nano Energy* **2018,** *53*, 46-56.

(26) Liao, W.-Q.; Zhao, D.; Tang, Y.-Y.; Zhang, Y.; Li, P.-F.; Shi, P.-P.; Chen, X.-G.; You, Y.-M.; Xiong, R.-G., A molecular perovskite solid solution with piezoelectricity stronger than lead zirconate titanate. *Science* **2019,** *363*, 1206.

(27) Luo, C.; Hu, S.; Xia, M.; Li, P.; Hu, J.; Li, G.; Jiang, H.; Zhang, W., A Flexible Lead-Free $BaTiO_3$/PDMS/C Composite Nanogenerator as a Piezoelectric Energy Harvester. *Energy Technol.* **2018,** *6*, 922-927.

(28) Liao, W.-Q.; Zhang, Y.; Hu, C.-L.; Mao, J.-G.; Ye, H.-Y.; Li, P.-F.; Huang, S. D.; Xiong, R.-G., A lead-halide perovskite molecular ferroelectric semiconductor. *Nat. Commun.* **2015,** *6*, 7338.

(29) Ye, H. Y.; Liao, W. Q.; Hu, C. L.; Zhang, Y.; You, Y. M.; Mao, J. G.; Li, P. F.; Xiong, R. G., Bandgap Engineering of Lead-Halide Perovskite-Type Ferroelectrics. *Adv. Mater.* **2016,** *28*, 2579-2586.

(30) Yang, C. K.; Chen, W. N.; Ding, Y. T.; Wang, J.; Rao, Y.; Liao, W. Q.; Tang, Y. Y.; Li, P. F.; Wang, Z. X.; Xiong, R. G., The First 2D Homochiral Lead Iodide Perovskite Ferroelectrics: $[R\text{- and }S\text{-}1\text{-}(4\text{-Chlorophenyl})\text{ethylammonium}]_2PbI_4$. *Adv. Mater.* **2019,** *31*, 1808088.

(31) Pandey, R.; Sb, G.; Grover, S.; Singh, S. K.; Kadam, A.; Ogale, S.; Waghmare, U. V.; Rao, V. R.; Kabra, D., Microscopic Origin of Piezoelectricity in Lead-Free Halide Perovskite: Application in Nanogenerator Design. *ACS Energy Lett.* **2019**, *4*, 1004-1011.

(32) Hodorowicz, M.; Stadnicka, K., Benzylethyldimethylammonium bromide. *Acta Crystallogr. E* **2008,** *64*, o601.

(33) Sheldrick, G. M. A short history of SHELX. *Acta Crystallogr. A* **2008**, *64*, 112-122.

(34) Spek, A., Structure validation in chemical crystallography. *Acta Cryst.* **2009,** *65*, 148-155.

(35) https://www.synopsys.com

(36) Perdew, J. P.; Burke, K.; Ernzerhof, M., Generalized Gradient Approximation Made Simple. *Phys. Rev. Lett.* **1996,** *77*, 3865-3868.

(37) Monkhorst, H. J.; Pack, J. D., Special points for Brillouin-zone integrations. *Phys. Rev. B* **1976,** *13*, 5188-5192.

(38) King-Smith, R. D.; Vanderbilt, D., Theory of polarization of crystalline solids. *Phys. Rev. B* **1993,** *47*, 1651-1654.

(39) Ye, H.-Y.; Ge, J.-Z.; Tang, Y.-Y.; Li, P.-F.; Zhang, Y.; You, Y.-M.; Xiong, R.-G., Molecular Ferroelectric with Most Equivalent Polarization Directions Induced by the Plastic Phase Transition. *J. Am. Chem. Soc.* **2016,** *138*, 13175-13178.

(40) Pan, Q.; Liu, Z. B.; Zhang, H. Y.; Zhang, W. Y.; Tang, Y. Y.; You, Y. M.; Li, P. F.; Liao, W. Q.; Shi, P. P.; Ma, R. W.; Wei, R. Y.; Xiong, R. G., A Molecular Polycrystalline Ferroelectric with Record-High Phase Transition Temperature. *Adv. Mater.* **2017,** *29*, 1700831.

(41) You, Y.-M.; Tang, Y.-Y.; Li, P.-F.; Zhang, H.-Y.; Zhang, W.-Y.; Zhang, Y.; Ye, H.-Y.; Nakamura, T.; Xiong, R.-G., Quinuclidinium salt ferroelectric thin-film with duodecuple-rotational polarization-directions. *Nat. Commun.* **2017,** *8*, 14934.

(42) Zhang, W.-Y.; Tang, Y.-Y.; Li, P.-F.; Shi, P.-P.; Liao, W.-Q.; Fu, D.-W.; Ye, H.-Y.; Zhang, Y.; Xiong, R.-G., Precise Molecular Design of High-T_c 3D Organic–Inorganic Perovskite Ferroelectric: [MeHdabco]RbI_3 (MeHdabco = N-Methyl-1,4-diazoniabicyclo [2.2.2]octane). *J. Am. Chem. Soc.* **2017,** *139*, 10897-10902.

(43) Arous, M.; Hammami, H.; Lagache, M.; Kallel, A., Interfacial polarization in piezoelectric fibre–polymer composites. *J. Non-Cryst. Solids* **2007**, *353*, 4428-4431.

(44) Hammami, H.; Arous, M.; Lagache, M.; Kallel, A., Study of the interfacial MWS relaxation by dielectric spectroscopy in unidirectional PZT fibres/epoxy resin composites. *J. Alloys Compd.* **2007,** *430*, 1-8.

(45) Yang, D.; Zhang, L.; Liu, H.; Dong, Y.; Yu, Y.; Tian, M., Lead magnesium niobate-filled silicone dielectric elastomer with large actuated strain. *J. Appl. Polym. Sci.* **2012,** *125*, 2196-2201.

(46) Lee, K. Y.; Kim, D.; Lee, J. H.; Kim, T. Y.; Gupta, M. K.; Kim, S. W., Unidirectional High-Power Generation via Stress-Induced Dipole Alignment from $ZnSnO_3$ Nanocubes/Polymer Hybrid Piezoelectric Nanogenerator. *Adv. Funct. Mater.* **2014,** *24*, 37-43.

(47) Gupta, M. K.; Kim, S.-W.; Kumar, B., Flexible High-Performance Lead-Free $Na_{0.47}K_{0.47}Li_{0.06}NbO_3$ Microcube-Structure-Based Piezoelectric Energy Harvester. *ACS Appl. Mater. Interfaces* **2016,** *8*, 1766-1773.

(48) Lee, K. Y.; Kim, D.; Lee, J. H.; Kim, T. Y.; Gupta, M. K.; Kim, S. W., Unidirectional High-Power Generation via Stress-Induced Dipole Alignment from $ZnSnO_3$ Nanocubes/Polymer Hybrid Piezoelectric Nanogenerator. *Adv. Funct. Mater.* **2014,** *24*, 37-43.

End of Chapter 2

Chapter 3

Neutral 1D-Perovskite Type ABX_3 Ferroelectric with High Mechanical Energy Harvesting Performance

2.1 Introduction

Materials that find applications in energy, environment, health and other strategic sectors have been receiving enormous attention lately in view of their significance for the emergent global high technologies. Among several classes of materials, the perovskites of ABX_3 (X = O) compositions have featured in many frontiers of research, especially, in solar cells, LEDs and self-powered electronics.[1,2] Additional functionalities and structural flexibilities in these perovskite materials have been achieved by introducing the organic cations at the A-sites and other anions such as halides (Cl^-, Br^-, I^-), azide (N_3^-), cyanide (CN^-) and borohydride (BH_4^-), formates ($HCOO^-$) and dicyanamides ($N(CN)_2^-$) for the X-sites.[3-8] The combined effects of the individual compositions at the A, B and X-sites have a profound influence on the modulation of their physical properties, thereby imparting to them functional behavior such as ferroelectricity, magnetism, multiferroicity, optoelectronic effects along with unique mechanical and thermal properties.[9-16] For instance, the synthetic advancements in hybrid perovskites with strong optical absorption, high carrier mobility, long diffusion length, tunable bandgap and solution processability have led to breakthroughs in photovoltaics with remarkable power conversion efficiencies.[17-19] Lately, they are also being investigated as potential materials for thermoelectric and piezoelectric energy harvesting applications.[20,21] In the past, many nanogenerators, where mechanical energy is converted into electrical energy, have been fabricated by utilizing the traditional materials like ZnO, $BaTiO_3$, $PbZr_xTi_{1-x}$, $ZnSnO_3$, GaN, CdS, CdTe and piezoelectric polymers such as polyvinylidene fluoride (PVDF) and its copolymers.[22-24] More recently, hybrid perovskites embedded in the polymer matrix have been fabricated as mechanical energy harvesters to realize lightweight, mechanical flexibility and low device processing temperature.[21,25]

Yoon and co-workers reported a nanogenerator employing $MASnI_3$ (MA = methylammonium) embedded in the PVDF matrix, which manifested an output voltage of 12 V and a power density of 21.6 μWcm^{-2}.[26] However, the output performances for such devices, except for a few systems, were found to be modest owing to their low polarization values.[27-29] As the piezoelectric coefficient is directly related to polarization, ferroelectric materials with high polarization are expected to exhibit

improved mechanical energy harvesting behavior.[30] In hybrid perovskites, the ordering of the cations is essentially responsible for their ferro- and piezoelectric properties.[31-32] Most hybrid 1D-perovskites contain face-sharing infinite metal-halide octahedra and discrete cations, though other less-common classes of structures are known for the halogenometallate ABX_3 system.[33] While the anionic structure in them offers a robust backbone, it is still challenging to realize the perfect ordering of these discrete cations that can impart high ferroelectric polarization. One of the ways to address this issue is to align the cations along the infinite anionic chains via certain non-covalent interactions.

In this chapter, we show the ferroelectric properties of a neutral framework of formula $[Me_3NCH_2CH_2OH]CdCl_3$ (**1**) that exhibits an unusual ABX_3 type 1D-perovskite like structure. The $[Me_3NCH_2CH_2OH]^+$ ion in it is closely positioned with the anionic framework through the coordination of its hydroxyl group with one of the axial sites at the Cd(II) atom, which renders the framework zwitterionic in nature. This arrangement along with additional H-bonding interactions facilitates a long-range ordering of the cations and anions along the polar axis. Above 360 K, this framework transforms to a normal 1D-perovskite structure consisting of discrete cations and face-sharing $CdCl_6$ octahedral repeat units. The piezo-responsive force microscopy (PFM) measurements performed on a single crystal of **1** gave a clear visualization of its ferroelectric domains. Also, it shows a sizable remnant polarization of 17.1 μCcm^{-2} in a classical P-E loop study that is in good agreement with our calculation. Polymer composites of **1** with various weight percentage (wt %) compositions were prepared with polydimethylsiloxane (PDMS) and explored for mechanical energy harvesting application. A maximum open-circuit voltage (V_{oc}) of 55.2 V has been obtained for the 15 wt % composite device. The highest power density of 70.9 μWcm^{-2} is recorded for this device at an optimal load of 4 MΩ. To the best of our knowledge, the obtained power density is the highest among the non-piezoelectric polymer composites of ferroelectric organic-inorganic hybrid salts. Moreover, the energy harvested from the 15 wt % device was utilized for capacitor charging and LED flash lighting applications. These outcomes demonstrate the development of hybrid ABX_3 type perovskites for high-performance nanogenerator devices.

3.2 Experimental section

3.2.1 General Remarks

The (2-hydroxyethyl)trimethyl ammonium chloride and cadmium chloride were purchased from Sigma Aldrich and used without further purification. Poly(dimethylsiloxane) (Sylgard 184, Silicone Elastomer Kit) was obtained from Dow Corning and used as received. Powder X-ray diffraction data were measured on a Bruker D8 Advance diffractometer on the polycrystalline samples obtained by grinding the single crystals and on the composite films. The PXRD scans were collected in the 2θ range of 5 to 55° at 50 seconds per degree (1.2 °C per minute). Thermal analysis data was acquired from a Perkin-Elmer STA6000 thermogravimetric analyzer at the heating rate of 10 °C/min in the nitrogen atmosphere. Differential scanning calorimetry (DSC) measurements were performed on a TA Q20 differential scanning calorimeter (DSC) at heating and cooling rates of 10 °C/min under nitrogen atmosphere. NMR spectra were recorded on a Bruker 400 MHz spectrometer (^{1}H NMR, 400.13 MHz; ^{13}C{^{1}H} NMR, 100.62 MHz in D_2O solvent. FT-IR spectra were recorded on a Perkin-Elmer spectrophotometer in the ATR mode. Melting points were analyzed using an Electrothermal melting point apparatus and were uncorrected. The surface morphology and the thickness of the composites were examined with the help of field emission scanning electron microscopy (Zeiss ultra plus FESEM instrument). Kurtz and Perry's method was utilized to measure the SHG effect on the unsieved powder samples. Q-switch Nd: YAG laser generated the fundamental wavelength of 1064 nm. Powdered KDP was used as a reference for the measurement.

3.2.2 Synthesis

3.2.2.1 Synthesis of 1: To a stirred solution of (2-hydroxyethyl)trimethylammonium chloride (1.3962 g, 0.01 mol) in 0.1 N HCl solution (~100 mL), cadmium chloride monohydrate (2.0133 g, 0.01 mol) was slowly added. The reaction mixture was allowed to stir at room temperature for a further period of 30 minutes. The obtained solution was left for crystallization at room temperature. Colorless single-crystals suitable for single-crystal X-ray diffraction were obtained after a week. Yield of 87% (2.81 g). M.P. 294-296 ˚C. ^{1}H NMR (D_2O): δ 3.18 (S, 9H, N-CH_3), δ 3.48-3.52 (m, 2H, N-CH_2CH$_2$OH), δ 4.01-4.07 (m, 2H, N-CH$_2$CH_2OH) ^{13}C {^{1}H} NMR (D_2O): δ 53.84-53.92

(m), 55.62 (s), 67.42 (s). FT-IR (cm^{-1}): 569, 637, 874, 946, 1009, 1057, 1080, 1364, 1485, 1976, 2355, 3026, 3183. Anal. Calcd. for 1: C 18.60; H 4.37; N 4.34. Found: C 18.65; H 4.30; N 4.39.

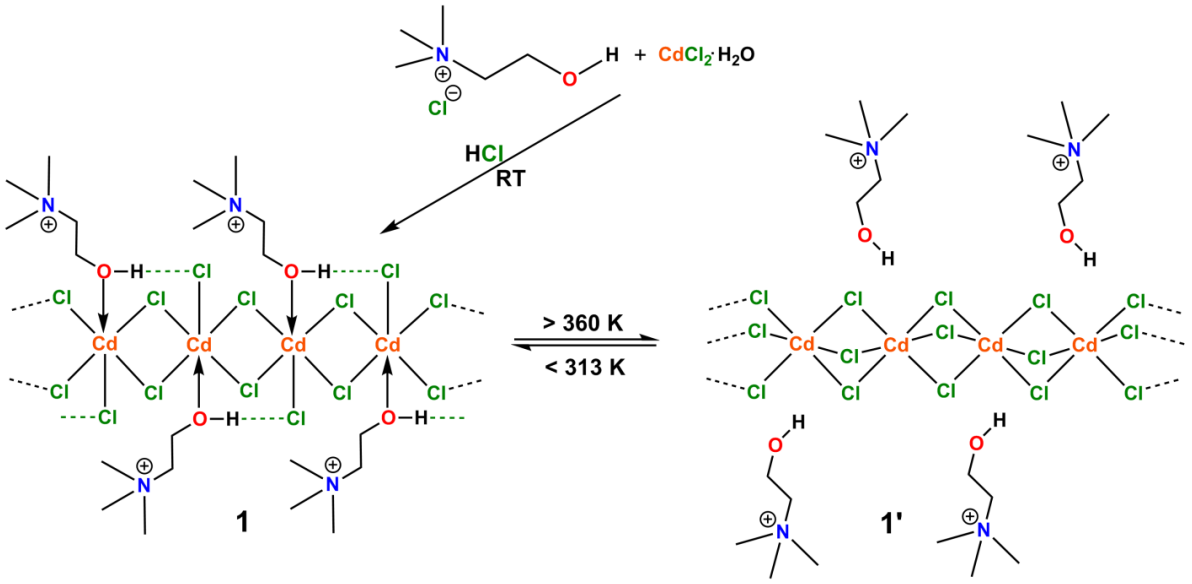

Scheme 3.1. Schematic for the preparation of **1** and its intermediate temperature phase **1'**.

3.2.3 Crystallography: Reflections for **1** and **1'** were collected on a Bruker Smart Apex-Duo Diffractometer using Mo Kα radiation (λ = 0.71073 Å). Crystal structures were solved via direct method and refined by full-matrix least squares against F^2 using all data (SHELX).[34] All non-hydrogen atoms were refined anisotropically if not stated otherwise. Hydrogen atoms were constrained in geometric positions to their parent atoms.[35] The crystals of **1'** diffracted very weakly at higher angles and hence a 2θ cutoff of 50 ° was applied. The HETMA cation in the structure of **1'** is highly disordered and diffused. The atom positions of the disordered segments were minimally restrained over only two positions using similar distances and similar U-restraints (SAME/SADI) of the SHELX. Attempts to find any further atom positions and connectivity patterns for the HETMA cation in **1'** were unsuccessful owing to its high-temperature data collection. The crystallographic data for the compounds are listed in Table 3.1 and the selected bond-lengths and angles are listed in Table 3.2 and 3.3.

Table 3.1: Details of crystallographic data.

Compound	1 (100 K)	1 (RT)	1' (363 K)
Chemical formula	$C_5 H_{14} Cl_3 Cd N O$	$C_5 H_{14} Cl_3 Cd N O$	$C_5 H_{14} Cl_3 Cd N O$
Formula weight	322.92	322.92	322.92
Temperature	100(2) K	298(2) K	363(2) K
Crystal system	Orthorhombic	Orthorhombic	Orthorhombic
Space group	*Pna*2_1	*Pna*2_1	*Pna*2_1
a(Å): α(°)	16.790(2); 90	16.942(4); 90	6.741(16); 90
b(Å); β(°)	8.0795(11); 90	8.202(2); 90	16.67(4); 90
c (Å); γ (°)	7.7649(11); 90	7.811(2); 90	9.65(2); 90
V(Å^3); Z	1053.3(3); 4	1085.4(5); 4	1084.39(5); 4
P(calc.) mg m^{-3}	2.036	1.976	1.978
μ(Mo K_α)mm^{-1}	2.784	2.702	2.705
$2\theta_{max}$ (°)	56	56	50
R (int)	0.0480	0.0405	0.4856
Completeness to θ	100.0	100	99.3
Data/param.	2633/ 107	2697/ 107	1895/ 94
GOF	1.086	1.153	1.005
R1[F>4σ(F)]	0.0124	0.0169	0.0976
wR2 (all data)	0.0298	0.0382	0.3430
Flack parameter	-0.015(12)	-0.008(13)	0.7(9)
max. peak/hole (e.Å^{-3})	0.222/ -0.539	0.249/-0.910	1.391/-1.016

Table 3.2: Selected bond lengths [Å] and angles [°] for compound 1 at 100 K and 298 K.

	Parameters	1 (100 K)	1 (298 K)
Bond Length	Cd(1)-O(1)	2.3645(17)	2.391(2)
	Cd(1)-Cl(3)	2.5594(6)	2.5607(9)
	Cd(1)-Cl(1)	2.6358(7)	2.6570(10)
	Cd(1)-Cl(2)	2.6400(7)	2.6446(10)
	O(1)-C(5)	1.435(3)	1.440(4)
	O(1)-H(1)	0.84(3)	0.85(3)
	N(1)-C(1)	1.494(3)	1.495(4)
	N(1)-C(2)	1.499(3)	1.501(4)
	N(1)-C(3)	1.502(3)	1.503(4)
	N(1)-C(4)	1.522(3)	1.522(4)
	C(5)-C(4)	1.508(3)	1.509(4)
Bond Angle	O(1)-Cd(1)-Cl(3)	174.49(4)	174.79(6)
	O(1)-Cd(1)-Cl(1)	87.03(5)	87.13(6)
	Cl(3)-Cd(1)-Cl(1)	91.43(2)	91.65(3)
	O(1)-Cd(1)-Cl(2)	89.05(4)	88.92(6)
	Cl(3)-Cd(1)-Cl(2)	96.03(2)	95.96(3)
	Cl(1)-Cd(1)-Cl(2)	83.14(2)	83.04(3)
	C(5)-O(1)-Cd(1)	128.65(14)	128.97(18)

	C(5)-O(1)-H(1) Cd(1)-O(1)-H(1) C(1)-N(1)-C(2) C(1)-N(1)-C(3) C(2)-N(1)-C(3) C(1)-N(1)-C(4)	109(2) 103(2) 108.69(19) 109.7(2) 107.30(18) 111.31(19)	105(2) 105(2) 108.8(3) 110.6(3) 106.6(3) 111.3(3)

Table 3.3: Selected bond lengths [Å] and angles [°] for compound 1' at 363 K

Bond Length	Bond Angle
Cd(1)-Cl(3): 2.62(3) Cd(1)-Cl(1): 2.64(3) Cd(1)-Cl(2): 2.608(12) O(1)-C(5): 1.50(2) O(1)-H(1): 0.82 N(1)-C(1): 1.50(2) N(1)-C(2): 1.50(3) N(1)-C(3): 1.50(3) N(1)-C(4): 1.50(3) C(5)-C(4): 1.38(14)	Cl(3)-Cd(1)-Cl(1): 177.7(12) Cl(3)-Cd(1)-Cl(2): 96.7(9) Cl(1)-Cd(1)-Cl(2): 84.5(7) C(5)-O(1)-H(1): 109.5 C(4)-N(1)-C(3):145(9) C(4)-N(1)-C(2):83(8) C(3)-N(1)-C(2): 87(9) C(4)-N(1)-C(1): 35(6) C(3)-N(1)-C(1): 113(8) C(2)-N(1)-C(1): 60(7) C(4)-C(5)-O(1): 87(8) C(5)-O(1)-H(1): 109.5

3.2.4 Piezo-responsive Force Microscopy Characterization: The polarization switching and local piezoelectric response of the single crystals of **1** were studied at room temperature with an Asylum Research MFP-3D atomic force microscope working in contact mode. The measurements were performed by using the ASYELEC-01 tip (cantilever made of a tetrahedral silicon tip coated with titanium / Iridium (5/20)) which has a spring constant of 2 N/m, tip radius of 28 +/- 10 nm and free air resonance of ~70 kHz. The PFM data were taken in the vertical (contact) mode, with an ac voltage (V_{bias}) applied to the conductive AFM tip and the bottom electrode grounded. The PFM imaging was recorded close to the resonant frequency of the cantilever in contact (300 ± 20 kHz) at a V_{bias} value of 2.5 V. All the measurements were performed by applying two oscillating voltages with frequencies below and above resonance (320 kHz) and the operation of the cantilever in the dual ac-resonance-tracking mode. The instrumental setup was optimized for the earlier published results from our groups on molecular and hybrid materials.[25,36]

3.2.5 Fabrication of Hybrid Composite Mechanical Energy Harvester: The PDMS solution was initially prepared by the addition of curing agent to the base in the ratio of 1:10 followed by the dispersion of **1** with varying concentrations of 5, 10, 15 and 20 wt % (Table S6, Supporting Information). The prepared solution was drop-casted onto the Al wrapped PET and then placed in the vacuum desiccator and finally cured at 70 ˚C for 5 hours. Thereafter, ITO coated PET was placed as the bottom electrode to the cured 1-PDMS composites. The electrical contacts were established at the end of the electrodes with the help of copper wires. Finally, the fabricated device was laminated with the Kapton tape to attain electrical isolation. Thickness and the effective size of the as-fabricated device were found to be ~1.3 mm and 2 x 2 cm^2 respectively.

3.2.6 Dielectric, Ferroelectric, Piezoelectric and Mechanical Energy Harvesting measurements: Powdered sample of compound **1** compacted in the form of disk was employed for the dielectric measurements. Aluminum adhesive foils were integrated as the top and the bottom electrodes to the compacted disk. The temperature and the frequency-dependent dielectric permittivity were recorded on a Novocontrol Alpha-AN Dielectric / Impedance Analyzer coupled with a QUATRO Cryosystem. In order to determine the ferroelectric polarization, single crystals with aluminium adhesive foil integrated on the opposite ends were employed. Ferroelectric hysteresis loops were recorded on an aixACCT TF-2000E model analyzer using a Sawyer-Tower Circuit. Leakage currents were measured dynamically for various voltage steps during the hysteresis loop measurements. The d_{33} measurement on the single-crystals of **1** was performed on a Piezotest meter model PM300.[37] The output signals of **1**-PDMS devices were generated by periodic compression and release of 40 N force produced by a home built vertical impact force set up.[38] All the output signals were collected on a Keithley DMM7510 7.5 multimeter.

3.3 Results and discussion

3.3.1 Synthesis, Characterization and Crystal Structure: Compound **1** was crystallized from the slow evaporation of an acidified solution containing equimolar amounts of (2-hydroxyethyl)trimethylammonium chloride and cadmium chloride (Scheme 3.1). At room temperature, **1** crystallizes in the orthorhombic polar space group *Pna*2_1 (C_{2v} point group) with unit cell parameters a = 16.942(4), b = 8.202(2), c

= 7.811(2) and α = β = γ = 90˚ as determined from the single-crystal X-ray diffraction (SCXRD) analysis (Table 3.1). Preliminary second harmonic generation measurements on the powered unsieved samples of **1** gave a SHG efficiency of 0.14 with respect to standard KDP, which confirms its non-centrosymmetric structure.

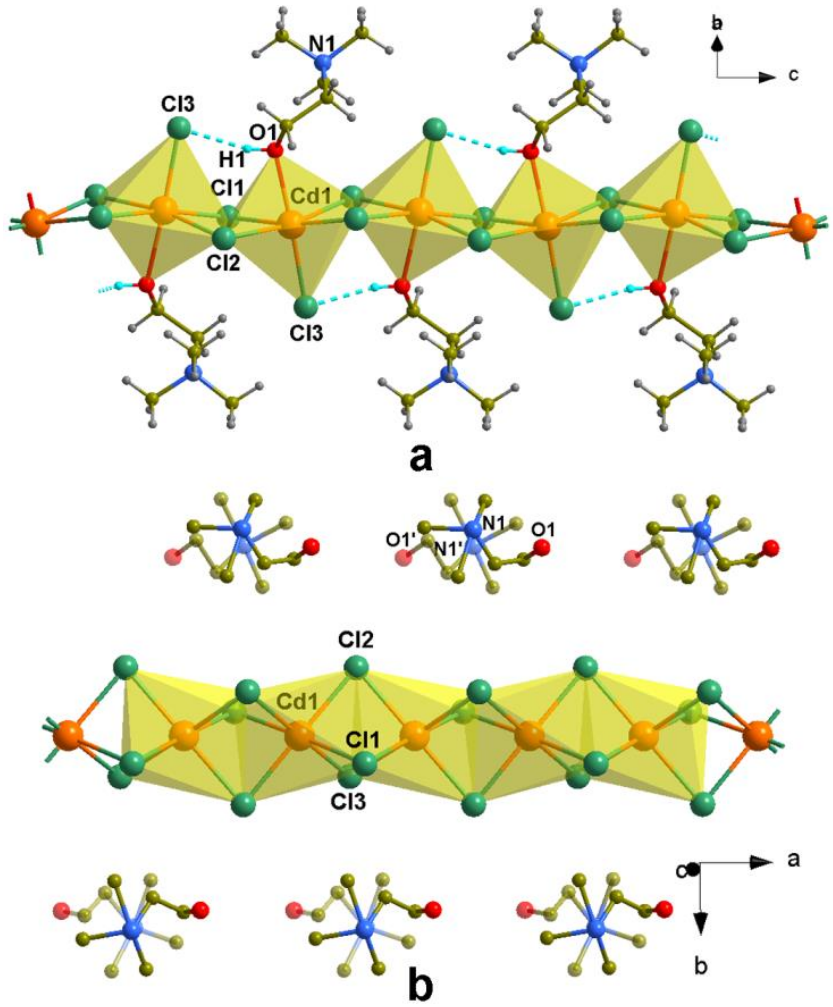

Figure 3.1: *(a) Molecular structure of **1** depicted as the edge-sharing $CdCl_5O$ octahedra (shaded in yellow). The HETMA cations are coordinated alternatively above and below the 1D-chain. The O-H···Cl interactions are shown as the dotted line. (b) Molecular structure of **1'** depicted as the face-sharing $CdCl_6$ octahedra (shaded in yellow). The HETMA cations are uncoordinated and disordered. One of the disordered fragments is shown as the transparent unit. H-atoms are omitted for clarity.*

The molecular structure of **1** can be visualized as an infinite array of edge-sharing $CdCl_5O$ octahedra in which the 2-hydroxyethyl)trimethylammonium (HETMA) cations

are coordinated alternately above and below the 1D-framework (Figure 3.1a). Two μ_2-bridging chloride ions act as the link between the adjacent Cd(II) centers. The asymmetric unit features a $[CdCl_3]^-$ ion and a HETMA cation that is coordinated with the Cd(II) center via its hydroxyl group leading to a zwitterionic structure for **1** (Figure 3A.1a, Appendix 3). The coordination environment at the Cd(II) center is distorted octahedral that consists of four equatorial bridging chloride ions, one terminal chloride at the axial position and a coordinated oxygen atom from the HETMA cation at the opposite axial site. The dative bond of moderate strength between lone pair on the -OH group and the soft Lewis-acidic Cd(II) ion (B-site) facilitates an optimal placing of the dipoles responsible for the long-range order along the 1D-chain. These hydroxyl groups are further involved in hydrogen bonding with terminal chloride ions mediated by O-H···Cl interactions (Figure 3.1a and Figure 3A.1b, Appendix 3). The H···Cl distance and O-H···Cl angle measured for this H-bonding interactions are found to be 2.138 (39) Å and 163.287 (35)˚, respectively. The packing structure of **1** displays the linear arrays of HETMA-$CdCl_3$ 1D-chains propagating along the polar c-axis. The adjacent chains are further connected by non-classical C-H···Cl interactions (Figures 3A.1c and 3A.1d, Appendix 3).

The bulk phase purity of **1** was confirmed by Powder X-ray diffraction analysis (PXRD), in which the observed profile at room-temperature matches well with the simulated patterns from the 298 K SCXRD data (Figure 3A.2, Appendix 3). The thermogravimetric analysis showed no significant weight loss up to 570 K (Figure 3A.3, Appendix 3). The existence of any structural phase transition in **1** was probed by Differential Scanning Calorimetry (DSC). In the DSC runs of **1**, two pairs of reversible heat anomalies at 360/313 K and 400/393 K (heating/cooling) were observed indicating that **1** exhibit two phase transitions at T_1= 360 K and T_2= 400 K (Figure 3.2a). For simplicity, the phase above T_2 is referred as the high-temperature phase (HTP), the phase between T_1 and T_2 as the intermediate-temperature phase (ITP), and the phase below T_1 as the low-temperature phase (LTP).

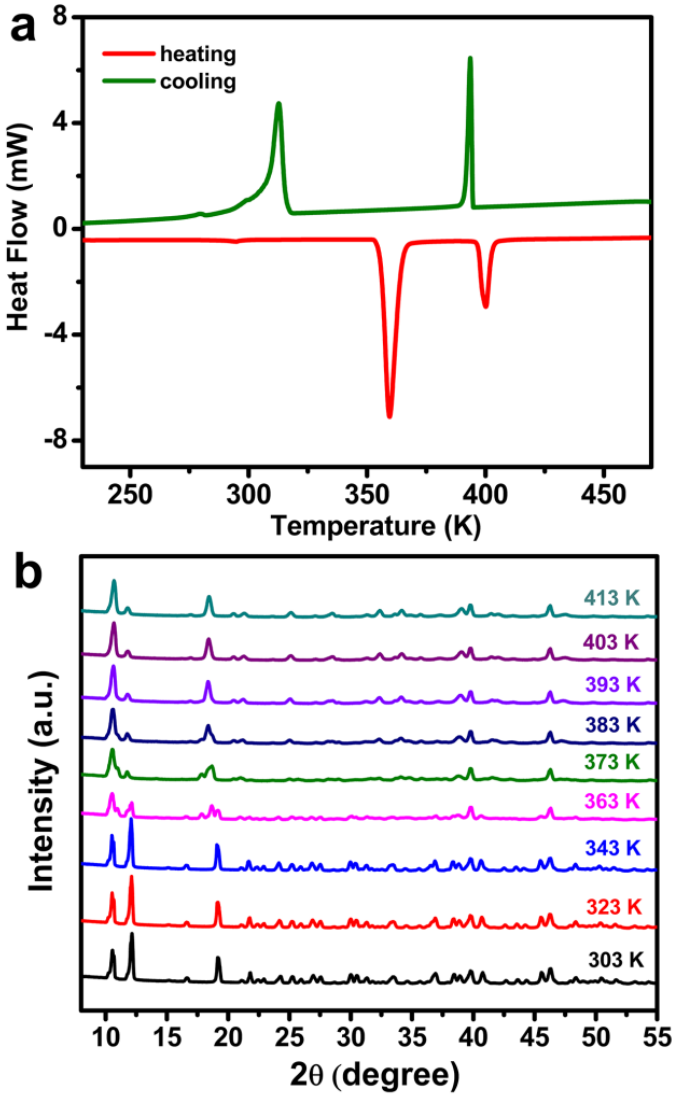

Figure 3.2: *(a) The DSC curves and (b) the VT-PXRD profile of* ***1*** *showing its phase transitions.*

The SCXRD analysis of **1** at 363 K in the ITP showed the formation of its coordination isomer (**1'**) in the same polar space group *Pna*2_1 with a slightly modified unit cell parameters a = 6.741(16), b = 16.67(4), c = 9.65(2) and α = β = γ = 90˚ (Table 3.1). The structural analysis of **1'** reveals the transformation of the edge-sharing octahedral $CdCl_5O$ units into the face-sharing $CdCl_6$ moieties. The HETMA cations in **1'** were disconnected from Cd(II) atoms and found to exhibit a highly disordered structure (Figure 1b). Owing to the poor quality of the diffraction and the flexibility of the hydroxy ethyl chain, we applied a simplified two-site disorder model for the HETMA cation in **1'**. However, the connectivity pattern for $[CdCl_3]^-$ chain was firmly established that shows

the typical 1D-perovskite type structure. The distances between the Cd-atoms in adjacent chains (9.650 Å) of the ITP is longer than those found in the LTP (8.202 Å), which leads to the complex disorder of HETMA cations caused by its orientational motion. The crystal packing diagram of **1'** consists of infinite linear $[CdCl_3]^-$ chains of face-sharing $CdCl_6$ octahedra running along the a-axis and HETMA cations occupying the cavities between them (Figure 3A.4, Appendix 3). The crystals of **1** (or **1'**) crack at higher temperatures and turn opaque above 380 K, precluding any structural determination for the species in the HTP (Figure 3A.5, Appendix 3).

To gain further insights into phase transitions in **1**, variable temperature (VT) PXRD analysis was performed. It shows the onset of a new phase at 363 K, which settles down to a single-phase above 393 K (Figure 3.2b). Furthermore, the 403 K PXRD pattern was indexed to extract the unit cell parameters for the HTP (Figure 3A.6 and Table 3A.1, Appendix 3). The obtained hexagonal lattice parameter values of a = 9.634 (4), b = 9.634 (4), c = 6.753 (3) and α = β = 90, γ = 120˚ in the centrosymmetric space group of *P*6$_3$/*mmc*, suggests the existence of a ferroelectric to paraelectric transformation for **1'** in the HTP.

Owing to the propensity of the halide salts of HETMA to undergo decomposition upon heating, we investigated the stability of **1** by heating at 150 °C for 48 hrs.[39] The ^{1}H- and ^{13}C-NMR of the as-made crystals of **1** and the sample treated at high-temperature (**1**$_{HT}$) in D_2O showed identical spectral patterns, giving peaks pertaining to all the expected hydrogen and carbon atoms of the HETMA cation (Figures 3A.7-3A.10, Appendix 3). Also, the FT-IR spectrum of **1**$_{HT}$ matched very well to that of pristine crystals of **1** confirming the stability of the HETMA cation in **1**$_{HT}$ (Figures 3A.11, Appendix 3).

3.3.2 Piezoelectric, Ferroelectric and Dielectric Studies

Piezo-response force microscopy (PFM) is an extremely powerful non-destructive tool for the visualization of ferroelectric domains at the nanometer scale.[40-42] Hence, to probe the existence of local ferroelectric polarization in **1**, vertical-PFM measurements were performed on its single crystal. Figure 3.3 shows the obtained images of (a) topography, (b) amplitude *(A)* and (c) phase *(φ)* with an active area of 5μm × 5μm. The presence of electrically active polarizable domains is evident from the PFM

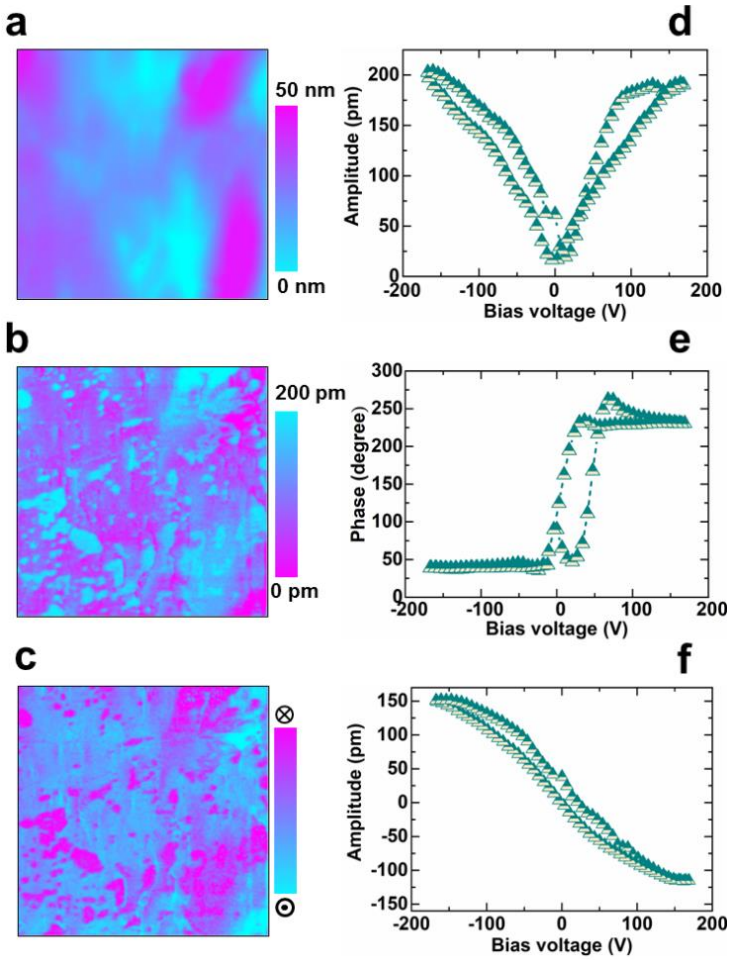

Figure 3.3: *Local piezoelectric behavior of a single crystal of **1**: (a) Topography image of the crystal, (b) PFM amplitude and (c) PFM phase image of a polarization pattern produced by applying a scanning voltage of 2.5 V using the tip. The blue regions correspond to upward polarization, while purple regions indicate downward polarization, (d) Amplitude "butterfly" loop (A(E)). (e) Phase hysteresis loop (φ(E)) obtained with a DC voltage of 2.5 V. (f) The piezoresponse hysteresis loop, PR(E).*

amplitude (Figure 3.3b) and phase (Figure 3.3c) images. The plots in respective figures 3.3d and 3.3e depict the *butterfly-shaped* amplitude loop, A(E) and phase angle derived hysteresis loop, [φ(E)]. The piezoresponse hysteresis loop (Figure 3.3f) can be calculated and plotted using the equation PR(E) = A(E) cos [φ(E)].[43] Furthermore, from the obtained phase image (Figure 3.3c) and hysteresis loop (Figure 3.3e), the dominant 180-degree switching of the polarization can be visualized under the external electric field. Based on these amplitude and phase

images and loops, the existence of piezoelectric effects and the orientation of the domain polarization in **1** can be firmly established.

The macroscopic polarization reversal in **1** was further examined by using a Sawyer-Tower circuit. A well-resolved *P-E* hysteresis loop was obtained on a single crystal of **1** at room-temperature along the polar c-axis. The measurements resulted in the remnant polarization value of 17.1 μCcm^{-2} with a relatively small coercive field of 1.01 $kVcm^{-1}$ (Figure 3.4a). The observed polarization is consistent with the calculated polarization value of 18.1 μCcm^{-2} based on the point-charge model analysis (Table 3A.2, Appendix 3). Also, it can be noted that a similar calculation based on the structure of **1'** gave a much lower polarization value of 4.4 μCcm^{-2} (Table 3A.3, Appendix 3). This indicates that the unique zwitterionic structure of **1** coupled with its intra-molecular O-H···Cl H-bonding plays a vital role in restoring an efficient long-range order that is responsible for its high polarization. The obtained polarization is comparable with several recently reported small-molecule based ferroelectrics and cadmium-containing halide perovskites.[12,40,44-48] The J-E curve measured along the P-E loop trace indicates a low leakage current density along with the peaks at the coercive fields typical for ferroelectric materials (Figure 3.4a). Preliminary piezoelectric coefficient measurements performed on the crystals of **1** gave the d_{33} value of 3 pCN^{-1} at an operating frequency of 110 Hz and an applied force of 0.25 N, which indicates the piezoelectric nature of this neutral framework.

The temperature dependence of the dielectric permittivity was measured on the compressed power pellets of **1** in the frequency range of 1 kHz to 100 kHz. As depicted in Figure 3.4b, the real part of the complex dielectric permittivity (ε') exhibited two anomalous dielectric behavior around 360 and 400 K, which is consistent with the structural changes observed from the single-crystal diffraction and the DSC data. The maximum ε' value of 23.7 was observed at 350 K at a frequency of 1 kHz related to the first phase transition from LTP to ITP. An ε' value of 11.52 was again observed in the temperature range of 400 K at 1 kHz pertaining to the transition from the ITP to HTP. Furthermore, frequency-dependent dielectric permittivities were recorded at varying temperatures (Figure 3A.12, Appendix 3). Moreover, the compound displays considerably low dielectric loss factors (tan delta) as observed from the electrical energy dissipation (Figures 3A.13 and 3A.14, Appendix 3). The apparent increase in

the ε' values in the vicinity of T_c with decreasing frequencies are attributed to the dominance of all polarization mechanism at lower frequencies.

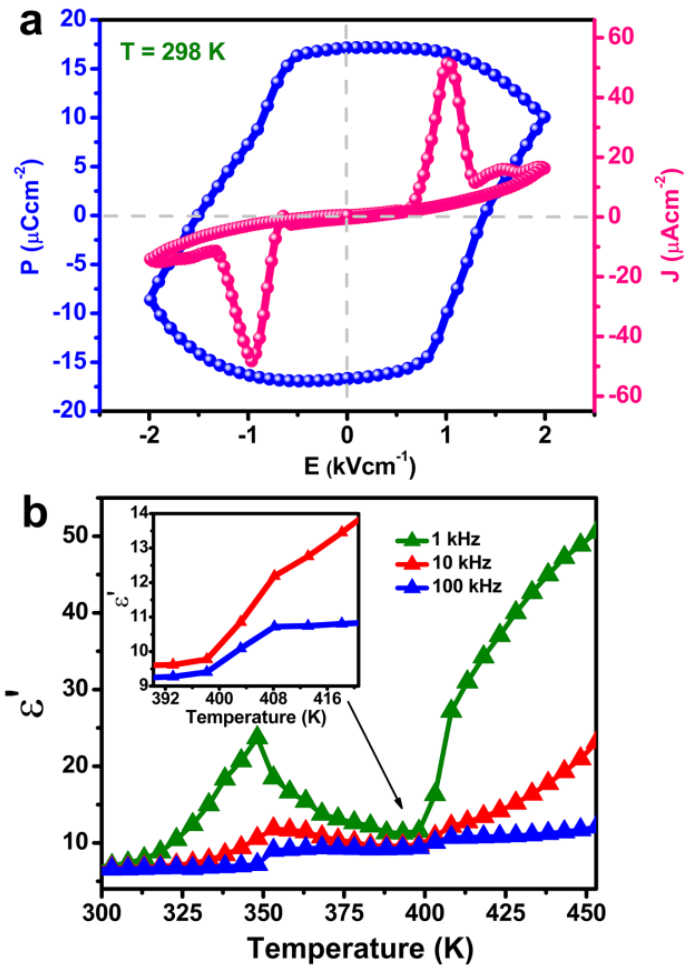

Figure 3.4: *(a) P-E hysteresis loop of* ***1*** *and (b) Temperature-dependent real part of the complex dielectric constant.*

3.3.3 Fabrication and Testing of Mechanical Energy Harvesting Device

Encouraged by the recent findings on ammonium halogenometallates as efficient nanogenerators, we set out to probe the utility of the hybrid-assembly of **1** as a mechanical-energy harvesting device.[30] To obtain flexible devices, homogeneous polymer composites of 5, 10, 15 and 20 weight percentages (wt %) of **1** were prepared by dispersing appropriate quantities of **1** into PDMS under an intensive mechanical stirring (Table 3A.4, Appendix 3). A simple multi-layer device was fabricated for each of these **1**-PDMS composites by placing the ITO coated PET as the bottom electrode

and Al foil integrated on PET as the top electrode (Figure 3A.15, Appendix 3). The schematic of the fabricated device is illustrated in Figure 3.5a. The final devices exhibit high degrees of mechanical flexibility (Figure 3A.16, Appendix 3). The phase purity of the prepared composite films was verified by PXRD analysis, which shows an increase in the crystallinity of the composite films with the increased loading (wt %) of **1** (Figure 3.5b). The surface morphologies of the films were further probed by Scanning Electron Microscopy (SEM). The SEM images of the composite films indicate the random distribution of the particles in the polymer matrix. Also, a rise in the particle distribution is evidenced upon increasing the loading of **1** in the composite films (Figure 3A.17, Appendix 3). The cross-sectional SEM image of the multi-layer **1**-PDMS device shows a sandwiched structure of the composite films with an approximate thickness of 1.3 mm (Figure 3A.18, Appendix 3).

The piezoelectric output performances of all the fabricated devices were examined by applying a constant force of 40 N normal to the surface of the as-fabricated device. A custom-built force set up attached with an oscilloscope was employed for the device measurements.[49] A maximum recordable piezoelectric output voltage (V_{oc}) of 55.2 V and a peak to peak voltage (V_{pp}) of 99 V was attained for the 15 wt % **1**-PDMS device with an effective area of 2 X 2 cm^2 (Figures 3.5c and 3A.19, Appendix 3). It is distinct that the output voltage escalates at the beginning with the increasing concentration of **1** in the PDMS matrix saturating at 55.2 V for the 15 wt % **1**-PDMS device. The V_{oc} drops to 30.4 V as the concentration of **1** is further increased to 20 wt % (Table 3A.5, Appendix 3). Also, the V_{oc} measured over three independent devices gave an average value of 53.5 V for the 15 wt % **1**-PDMS device (Figure 3A.20 and Table 3A.6, Appendix 3). To verify the contribution of **1** in **1**-PDMS, a device based on pure PDMS was tested under the same condition (Figure 3A.21, Appendix 3). A V_{oc} of only 6.9 V was observed from this device signifying the contribution of **1** for the high output generation in the composites.[50]

The increase in the output performance with an increase in the concentration of **1** is attributed to the increasing dielectric constants of **1**-PDMS composite which occur as a result of interface polarization between the hybrid salt and the PDMS matrix. The presence of interfaces in heterogeneous materials leads to Maxwell-Wagner-Sillars type polarization that causes an abrupt change in the total dielectric constant. Hence,

when the optimal loading (15 wt %) of **1** is reached, the separation between the individual dipoles contract with a rapid increase in the polarization yielding the maximum output voltage. In contrast, a further increase in the concentration above the threshold limit (beyond 15 wt %) renders weak insulation of the composites leading to the electrical breakdown and hence a drop in the output voltages.[27,37,51]

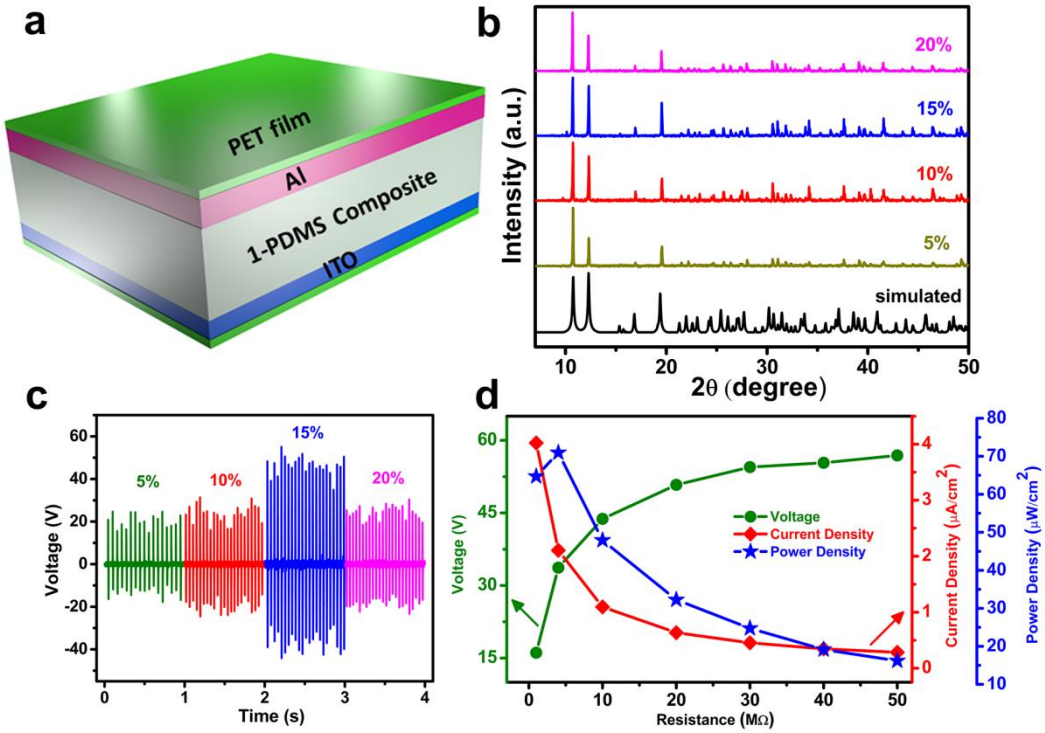

Figure 3.5: *(a) Schematic diagram of the as-fabricated device. (b) PXRD data of the as-prepared composites with varying concentration of **1**. (c) Output performance of all wt % **1**-PDMS composite devices with shifted time-axis. (d) Voltage (●) current density (◆) and power density (★) as a function of load resistance corresponding to 15 wt % **1**-PDMS device.*

The output characteristics of the device were further examined as a function of load resistance (Figure 3.5d). A rise in the V_{oc} and a drop in the current density amplitude was observed on increasing the load resistance from 1 to 50 MΩ. Consequently, the maximum power density of 70.9 μWcm^{-2} was obtained at an optimal load of 4 MΩ for the 15 wt % **1**-PDMS. The mechanical durability of this device was tested for over 1500 cycles at 40 N impact force, which indicated no apparent reduction in the output voltages (Figure 3A.22, Appendix 3). It must be noted that the output performance of a device is dependent on the thickness of the composite layer, its structural

morphology and composition, device architecture and the applied force and frequency.[52]

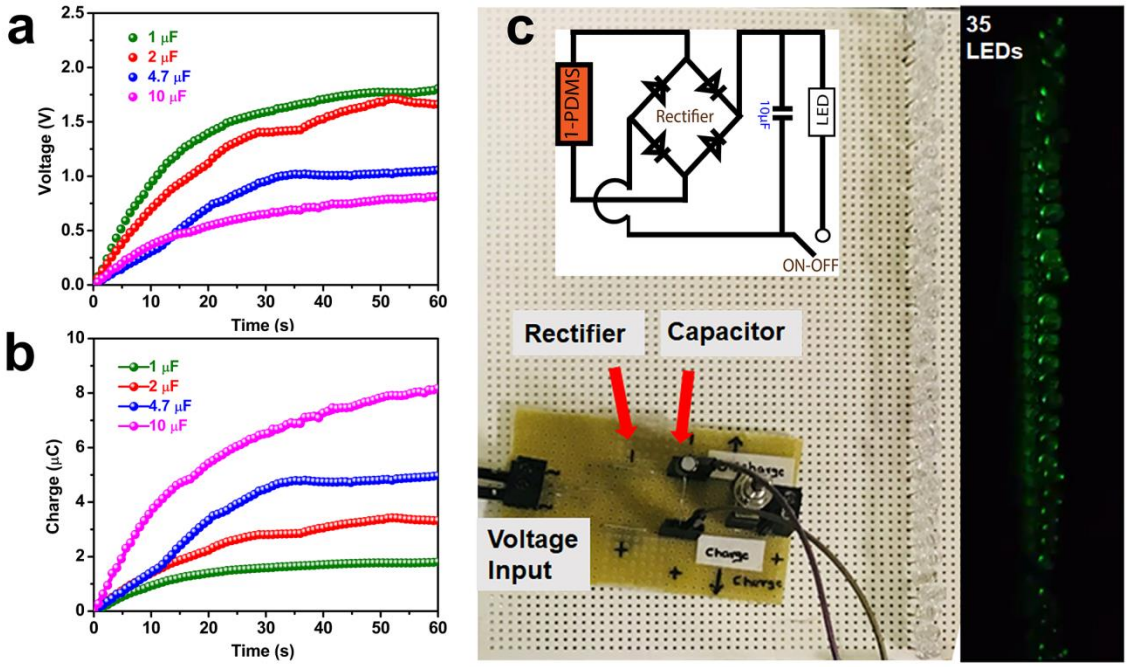

Figure 3.6: *Plots of capacitor charging (a) and corresponding accumulated charges (b) for the various capacitors. (c) Schematic of a full wave-bridge rectifier circuit diagram and the photograph of the circuit utilized for the instant flash-lighting of 35 LEDs.*

The potential utility of the best performing 15 wt % **1**-PDMS device was demonstrated by storing the harvested energy in different capacitors. As observed from the charging curves, the output voltage rises gradually and reaches a value of 1.81, 1.66, 1.05 and 0.81 V in 60 seconds across the respective 1, 2, 4.7 and 10 µF capacitors (Figure 3.6a). The measured charges corresponding to 1, 2, 4.7 and 10 µF capacitors were calculated to be 1.81, 3.32, 4.99 and 8.24 µC, respectively (Figure 3.6b). Also, a set of 35 LEDs flash lit up through the charging of the 10 µF capacitor under an applied constant force of 40 N and a frequency of 25 Hz (Figure 3.6c). This result implies that the mechanical energy harvester can be envisaged as a promising power source for low consumption micropower electronics.

3.4 Conclusion

In conclusion, we have rationally designed and synthesized an unusual neutral perovskite-type hybrid ferroelectric ABX_3 compound, which exhibits a high remnant polarization of 17.1 μCcm^{-2}. This compound exhibits reversible coordination isomerism at higher temperatures as determined by DSC, SCXRD and VT-PXRD analysis. Flexible composite devices of **1** were prepared and explored for mechanical energy harvesting applications. A high V_{oc} of 55.2 V was recorded for the optimal device made-up of 15 wt % of **1**-PDMS. The obtained power density of 70.9 μWcm^{-2} is the highest among the non-piezoelectric polymer composites containing hybrid ferroelectrics that are employed as nanogenerators. The piezoelectric energy generated from the 15 wt % **1**-PDMS device was further utilized for charging the capacitors and flash-lighting the LEDs. These findings encourage the design and development of new types of ferroelectric hybrids and their utility in self-powered electronics.

3.5 References

(1) Bai, Y.; Jantunen, H.; Juuti, J., Energy Harvesting Research: The Road from Single Source to Multisource. *Adv. Mater.* **2018,** *30*, 1707271.

(2) Pandey, R.; Vats, G.; Yun, J.; Bowen, C. R.; Ho-Baillie, A. W. Y.; Seidel, J.; Butler, K. T.; Seok, S. I., Mutual Insight on Ferroelectrics and Hybrid Halide Perovskites: A Platform for Future Multifunctional Energy Conversion. *Adv. Mater.* **2019,** *31*, 1807376.

(3) Weber, D., $CH_3NH_3PbX_3$, ein Pb(II)-System mit kubischer Perowskitstruktur / $CH_3NH_3PbX_3$, a Pb(II)-System with Cubic Perovskite Structure. *Z. Naturforsch.,* **1978,** *33b*, 1443.

(4) Zhang, W.; Cai, Y.; Xiong, R.-G.; Yoshikawa, H.; Awaga, K., Exceptional Dielectric Phase Transitions in a Perovskite-Type Cage Compound. *Angew. Chem. Int. Ed.* **2010,** *49*, 6608-6610.

(5) Mautner, F. A.; Krischner, H., Preparation and structure determination of tetraethylammonium calcium azide, $[N(C_2H_5)_4]Ca(N_3)_3$. *Cryst. Mater.*, **1986**, *175*, 105.

(6) Schouwink, P.; Ley, M. B.; Tissot, A.; Hagemann, H.; Jensen, T. R.; Smrčok, Ľ.; Černý, R., Structure and properties of complex hydride perovskite materials. *Nat. Commun.* **2014,** *5*, 5706.

(7) Wang, Z.; Zhang, B.; Otsuka, T.; Inoue, K.; Kobayashi, H.; Kurmoo, M., Anionic NaCl-type frameworks of $[Mn^{II}(HCOO)^{3-}]$, templated by alkylammonium, exhibit weak ferromagnetism. *Dalton Trans.* **2004,** *15*, 2209-2216.

(8) Tong, M.-L.; Ru, J.; Wu, Y.-M.; Chen, X.-M.; Chang, H.-C.; Mochizuki, K.; Kitagawa, S., Cation-templated construction of three-dimensional α-Po cubic-type $[M(dca)_3]^-$ networks. Syntheses, structures and magnetic properties of $A[M(dca)_3]$ (dca = dicyanamide; for A = benzyltributylammonium, M = Mn^{2+}, Co^{2+}; for A = benzyltriethylammonium, M = Mn^{2+}, Fe^{2+}). *New J. Chem.* **2003,** *27*, 779-782

(9) Cheetham, A. K.; Rao, C. N. R., There's Room in the Middle. *Science* **2007,** *318*, 58-59.

(10) Saparov, B.; Mitzi, D. B., Organic–Inorganic Perovskites: Structural Versatility for Functional Materials Design. *Chem. Rev.* **2016,** *116*, 4558-4596.

(11) Li, W.; Wang, Z.; Deschler, F.; Gao, S.; Friend, R. H.; Cheetham, A. K., Chemically diverse and multifunctional hybrid organic–inorganic perovskites. *Nat. Rev. Mater.* **2017,** *2*, 16099.

(12) Zhang, H.-Y.; Song, X.-J.; Cheng, H.; Zeng, Y.-L.; Zhang, Y.; Li, P.-F.; Liao, W.-Q.; Xiong, R.-G., A Three-Dimensional Lead Halide Perovskite-Related Ferroelectric. *J. Am. Chem. Soc.* **2020,** *142*, 4604-4608.

(13) Wang, X.-Y.; Wang, Z.-M.; Gao, S., Constructing magnetic molecular solids by employing three-atom ligands as bridges. *Chem. Commun.* **2008,** *3*, 281-294.

(14) Stranks, S. D.; Snaith, H. J., Metal-halide perovskites for photovoltaic and light-emitting devices. *Nat. Nanotechnol.* **2015,** *10*, 391-402.

(15) Li, W.; Thirumurugan, A.; Barton, P. T.; Lin, Z.; Henke, S.; Yeung, H. H. M.; Wharmby, M. T.; Bithell, E. G.; Howard, C. J.; Cheetham, A. K., Mechanical Tunability via Hydrogen Bonding in Metal–Organic Frameworks with the Perovskite Architecture. *J. Am. Chem. Soc.* **2014,** *136*, 7801-7804.

(16) Kumawat, N. K.; Gupta, D.; Kabra, D., Recent Advances in Metal Halide-Based Perovskite Light-Emitting Diodes. *Energy Technol.* **2017,** *5*, 1734-1749.

(17) Yang, W. S.; Park, B.-W.; Jung, E. H.; Jeon, N. J.; Kim, Y. C.; Lee, D. U.; Shin, S. S.; Seo, J.; Kim, E. K.; Noh, J. H.; Seok, S. I., Iodide management in formamidinium-lead-halide–based perovskite layers for efficient solar cells. *Science* **2017,** *356*, 1376-1379.

(18) Zhang, H.; Nazeeruddin, M. K.; Choy, W. C. H., Perovskite Photovoltaics: The Significant Role of Ligands in Film Formation, Passivation, and Stability. *Adv. Mater.* **2019,** *31*, 1805702.

(19) Fu, Y.; Zhu, H.; Chen, J.; Hautzinger, M. P.; Zhu, X. Y.; Jin, S., Metal halide perovskite nanostructures for optoelectronic applications and the study of physical properties. *Nat. Rev. Mater.* **2019,** *4*, 169-188.

(20) Jin, H.; Li, J.; Iocozzia, J.; Zeng, X.; Wei, P.-C.; Yang, C.; Li, N.; Liu, Z.; He, J. H.; Zhu, T.; Wang, J.; Lin, Z.; Wang, S., Hybrid Organic–Inorganic Thermoelectric Materials and Devices. *Angew. Chem. Int. Ed.* **2019,** *58*, 15206-15226.

(21) Jella, V.; Ippili, S.; Eom, J.-H.; Pammi, S. V. N.; Jung, J.-S.; Tran, V.-D.; Nguyen, V. H.; Kirakosyan, A.; Yun, S.; Kim, D.; Sihn, M. R.; Choi, J.; Kim, Y.-J.; Kim, H.-J.; Yoon, S.-G., A comprehensive review of flexible piezoelectric generators based on organic-inorganic metal halide perovskites. *Nano Energy* **2019,** *57*, 74-93.

(22) Fan, F. R.; Tang, W.; Wang, Z. L., Flexible Nanogenerators for Energy Harvesting and Self-Powered Electronics. *Adv. Mater.* **2016,** *28*, 4283-4305.

(23) Bowen, C. R.; Kim, H. A.; Weaver, P. M.; Dunn, S., Piezoelectric and ferroelectric materials and structures for energy harvesting applications. *Energy Environ. Sci.* **2014,** *7*, 25-44.

(24) Whiter, R. A.; Narayan, V.; Kar-Narayan, S., A Scalable Nanogenerator Based on Self-Poled Piezoelectric Polymer Nanowires with High Energy Conversion Efficiency. *Adv. Energy Mater.* **2014,** *4*, 1400519.

(25) Pandey, R.; Sb, G.; Grover, S.; Singh, S. K.; Kadam, A.; Ogale, S.; Waghmare, U. V.; Rao, V. R.; Kabra, D., Microscopic Origin of Piezoelectricity in Lead-Free Halide Perovskite: Application in Nanogenerator Design. *ACS Energy Lett.* **2019,** *4*, 1004-1011.

(26) Ippili, S.; Jella, V.; Eom, J.-H.; Kim, J.; Hong, S.; Choi, J.-S.; Tran, V.-D.; Van Hieu, N.; Kim, Y.-J.; Kim, H.-J.; Yoon, S.-G., An eco-friendly flexible piezoelectric energy harvester that delivers high output performance is based on lead-free $MASnI_3$ films and $MASnI_3$-PVDF composite films. *Nano Energy* **2019,** *57*, 911-923.

(27) Ding, R.; Liu, H.; Zhang, X.; Xiao, J.; Kishor, R.; Sun, H.; Zhu, B.; Chen, G.; Gao, F.; Feng, X.; Chen, J.; Chen, X.; Sun, X.; Zheng, Y., Flexible Piezoelectric Nanocomposite Generators Based on Formamidinium Lead Halide Perovskite Nanoparticles. *Adv. Funct. Mater.* **2016,** *26*, 7708-7716.

(28) Jella, V.; Ippili, S.; Eom, J.-H.; Choi, J.; Yoon, S.-G., Enhanced output performance of a flexible piezoelectric energy harvester based on stable $MAPbI_3$-PVDF composite films. *Nano Energy* **2018,** *53*, 46-56.

(29) Ippili, S.; Jella, V.; Kim, J.; Hong, S.; Yoon, S.-G., Enhanced piezoelectric output performance via control of dielectrics in Fe^{2+}-incorporated $MAPbI_3$ perovskite thin films: Flexible piezoelectric generators. *Nano Energy* **2018,** *49*, 247-256.

(30) Deswal, S.; Singh, S. K.; Rambabu, P.; Kulkarni, P.; Vaitheeswaran, G.; Praveenkumar, B.; Ogale, S.; Boomishankar, R., Flexible Composite Energy Harvesters from Ferroelectric A_2MX_4-Type Hybrid Halogenometallates. *Chem. Mater.* **2019,** *31*, 4545-4552.

(31) Ye, H.-Y.; Zhou, Q.; Niu, X.; Liao, W.-Q.; Fu, D.-W.; Zhang, Y.; You, Y.-M.; Wang, J.; Chen, Z.-N.; Xiong, R.-G., High-Temperature Ferroelectricity and Photoluminescence in a Hybrid Organic–Inorganic Compound: (3-Pyrrolinium)$MnCl_3$. *J. Am. Chem. Soc.* **2015,** *137*, 13148-13154.

(32) Zhang, Y.; Liao, W.-Q.; Fu, D.-W.; Ye, H.-Y.; Liu, C.-M.; Chen, Z.-N.; Xiong, R.-G., The First Organic–Inorganic Hybrid Luminescent Multiferroic: (Pyrrolidinium)$MnBr_3$. *Adv. Mater.* **2015,** *27*, 3942-3946

(33) Chen, L.; Liao, W.-Q.; Ai, Y.; Li, J.; Deng, S.; Hou, Y.; Tang, Y.-Y., Precise Molecular Design Toward Organic–Inorganic Zinc Chloride ABX_3 Ferroelectrics. *J. Am. Chem. Soc.* **2020,** *142*, 6236-6243.

(34) Sheldrick, G. M. A short history of SHELX. *Acta Crystallogr.,Sect. A: Found. Crystallogr*. **2008**, *64*, 112−122.

(35) Spek, A. Structure validation in chemical crystallography. *Acta Crystallogr., Sect. D: Biol. Crystallogr*. **2009**, *65*, 148−155.

(36) Vijayakanth, T.; Pandey, R.; Kulkarni, P.; Praveenkumar, B.; Kabra, D.; Boomishankar, R., Hydrogen-bonded organo-amino phosphonium halides: dielectric, piezoelectric and possible ferroelectric properties. *Dalton Trans.* **2019,** *48*, 7331-7336.

(37) Stewart, M.; Cain, M. G. in *Characterization of Ferroelectric Bulk Materials and Thin Films*, ed. M. G. Cain, Springer, Dordrecht, **2014**, 37.

(38) Singh, S. K.; Muduli, S.; Dhakras, D.; Pandey, R.; Babar, R.; Singh, A.; Kabra, D.; Kabir, M.; Boomishankar, R.; Ogale, S., High power mechanical energy harvester based on exfoliated black phosphorous–polymer composite and its multiple applications. *Sustain. Energy Fuels* **2019,** *3*, 1943-1950.

(39) Collin, R. L., Polymorphism and radiation decomposition of choline chloride. *J. Am. Chem. Soc.* **1957,** *79*, 6086.

(40) You, Y.-M.; Liao, W.-Q.; Zhao, D.; Ye, H.-Y.; Zhang, Y.; Zhou, Q.; Niu, X.; Wang, J.; Li, P.-F.; Fu, D.-W.; Wang, Z.; Gao, S.; Yang, K.; Liu, J.-M.; Li, J.; Yan, Y.; Xiong, R.-G., An

organic-inorganic perovskite ferroelectric with large piezoelectric response. *Science* **2017,** *357*, 306-309.

(41) Liao, W.-Q.; Zhao, D.; Tang, Y.-Y.; Zhang, Y.; Li, P.-F.; Shi, P.-P.; Chen, X.-G.; You, Y.-M.; Xiong, R.-G., A molecular perovskite solid solution with piezoelectricity stronger than lead zirconate titanate. *Science* **2019,** *363*, 1206-1210.

(42) Vats, G.; Bai, Y.; Zhang, D.; Juuti, J.; Seidel, J., Optical Control of Ferroelectric Domains: Nanoscale Insight into Macroscopic Observations. *Adv. Opt. Mater.* **2019,** *7*, 1800858.

(43) Kalinin, S. V.; Gruverman, A., *Scanning Probe Microscopy: Electrical and Electromechanical Phenomena at the Nanoscale*. Springer: New York, 2007; Vol. 1.

(44) Vijayakanth, T; Ram, F.; Praveenkumar B.; Shanmuganathan K.; Boomishankar R., Organic-Composites of H-bonded Ferro- and piezoelectric Phosphonium Salts for Mechanical Energy Harvesting Application. *Chem. Mater.* **2019,** *31,* 5964-5972.

(45) Vijayakanth, T.; Srivastava, A. K.; Ram, F.; Kulkarni, P.; Shanmuganathan K.; Praveenkumar B.; Boomishankar R., A Flexible Composite Mechanical Energy Harvester from a Ferroelectric Organoamino Phosphonium Salt. *Angew. Chem. Int. Ed.* **2018***, 57,* 9054-9058.

(46) Yang, C.-K.; Chen, W.-N.; Ding, Y.-T.; Wang, J.; Rao, Y.; Liao, W.-Q.; Xie, Y.; Zou, W.; Xiong, R.-G., Directional Intermolecular Interactions for Precise Molecular Design of a High-T_c Multiaxial Molecular Ferroelectric. *J. Am. Chem. Soc.* **2019,** *141*, 1781-1787.

(47) Chen, X.-G.; Song, X.-J.; Zhang, Z.-X.; Li, P.-F.; Ge, J.-Z.; Tang, Y.-Y.; Gao, J.-X.; Zhang, W.-Y.; Fu, D.-W.; You, Y.-M.; Xiong, R.-G., Two-Dimensional Layered Perovskite Ferroelectric with Giant Piezoelectric Voltage Coefficient. *J. Am. Chem. Soc.* **2020,** *142*, 1077-1082.

(48) Ye, H.-Y.; Zhang, Y.; Fu, D.-W.; Xiong, R.-G., An Above-Room-Temperature Ferroelectric Organo–Metal Halide Perovskite: (3-Pyrrolinium)($CdCl_3$). *Angew. Chem. Int. Ed.* **2014,** *53*, 11242-11247.

(49) Chaturvedi, S.; Singh, S. K.; Shyam, P.; Shirolkar, M. M.; Krishna, S.; Boomishankar, R.; Ogale, S., Nanoscale $LuFeO_3$: shape dependent ortho/hexa-phase constitution and nanogenerator application. *Nanoscale* **2018,** *10*, 21406-21413.

(50) Jeong, C. K.; Park, K.-I.; Ryu, J.; Hwang, G.-T.; Lee, K. J., Large-Area and Flexible Lead-Free Nanocomposite Generator Using Alkaline Niobate Particles and Metal Nanorod Filler. *Adv. Funct. Mater.* **2014,** *24*, 2620-2629.

(51) Arous, M.; Hammami, H.; Lagache, M.; Kallel, A., Interfacial polarization in piezoelectric fibre–polymer composites. *J. Non-Cryst. Solids* **2007,** *353*, 4428-4431.

(52) Alluri, N. R.; Chandrasekhar, A.; Vivekananthan, V.; Purusothaman, Y.; Selvarajan, S.; Jeong, J. H.; Kim, S.-J., Scavenging Biomechanical Energy Using High-Performance, Flexible $BaTiO_3$ Nanocube/PDMS Composite Films. *ACS Sustain. Chem. Eng.* **2017,** *5*, 4730-4738.

End of Chapter 3

Chapter 4

Piezoelectric Energy Harvesting from a Discrete Hybrid Bismuth Bromide Ferroelectric Templated by Phosphonium Cation

4.1 Introduction

Recent advances in the field of hybrid organic-inorganic materials have provided state-of-the-art paradigms to address the growing demands of the energy sector from new materials with extraordinary properties of interest to energy harvesting. Although these materials have their own specific stability issues, several of their key device-worthy properties such as solution-based processing, strong optical absorption, high carrier mobility, tailorable exciton diffusion length, bandgap tunability, and the like[1,2] have led them to attain the centre stage in the field of solar photovoltaics.[3,4] These materials are also being actively pursued as highly tunable device materials in other diverse fields such as light-emitting diodes, thin-film transistors, photodetectors, lasers and solid-state memories.[5-9] This impressive application bandwidth is only recently expanded further to include them as platforms for piezoelectric energy harvesting (nanogenerators) on account of the benefits afforded by the organic and inorganic components they amalgamate at the molecular level.[10]

In early research, numerous piezoelectric nanogenerators were fabricated from traditional inorganic materials like ZnO, $BaTiO_3$, $ZnSnO_3$, $PbZr_xTi_{1-x}$, GaN and CdS and organic polymers such as polyvinylidene fluoride (PVDF) and its copolymers.[11-13] Recently, lead and tin-based perovskites embedded in the polymer matrix have been utilized as mechanical energy harvesters.[14] For instance, Swathi *et al.* have fabricated a nanogenerator using $MASnI_3$ integrated into the PVDF matrix, which demonstrated an output voltage of 12 V.[15] However, the toxicity of lead and the susceptibility of Sn-based materials to undergo rapid oxidation (from Sn^{+2} to Sn^{+4}) have stimulated search for other hybrid materials for this application.[16-18] In that context, air-stable and comparatively non-toxic Bi(III) cations have emerged as an attractive alternative to the low-valent Pb(II) or Sn(II) ions in compositionally flexible hybrid perovskites.[19] Amongst the several known subclasses of anionic Bi-based networks, the AMX_4, $A_3M_2X_9$, R_2MX_5 and $R_5M_3X_{11}$ analogues were shown to exhibit ferroelectricity.[20-26] Although a handful of these compounds features good ferroelectric behavior, many undergo phase transitions to centrosymmetric settings near room temperature, precluding their widespread applications. One way to tackle this issue is to introduce homologous pnictogen-centred cations, such as tetramethyl phosphonium

cations.[27,28]. However, these molecules suffer from low polarization properties owing to the spherical nature of the employed cations, despite the enhancements in their Curie temperatures. Thus, we envisioned that the introduction of lower-symmetric heteroleptic phosphonium cations with bulkier substituents would result in highly stable Bi-based hybrids with large polarizability, suitable for the fabrication of nanogenerators with good output performance characteristics. As shown in this study, this is indeed the case.

Herein, we report a new ferroelectric phosphonium cation supported lead-free hybrid perovskite $[Me(Ph)_3P]_3[Bi_2Br_9]$, abbreviated as **MTPBB**, characterized by a discrete bioctahedra with an anionic Bi-network. The perovskitoid crystallizes in the polar trigonal *R*3 space group and exhibits a high remnant polarization value of 23.6 μC cm^{-2} at 0.1 Hz frequency. Moreover, polymer composites of **MTPBB** with varying weight percentages were prepared with polydimethylsiloxane (PDMS) and examined for mechanical energy harvesting applications. A maximum open-circuit voltage of 22.9 V was recorded for the device based on 20 wt% **MTPBB/PDMS** hybrid material. The harvested energies from the best performing device were further demonstrated by capacitor charging experiments. These findings could potentially stimulate further explorations of phosphonium based ferroelectric perovskites as efficient energy harvesting devices.

4.2 Experimental section

4.2.1 General remarks

The starting materials methyltriphenylphosphonium bromide, bismuth oxide and hydrobromic acid were purchased from Sigma Aldrich and used without further purification. Poly(dimethylsiloxane) (Sylgard 184, Silicone Elastomer Kit) was obtained from Dow Corning and used as received. Thermal analysis data was obtained using a PerkinElmer STA6000 thermogravimetric analyzer at a heating rate of 10 °C/min in a nitrogen atmosphere. Melting points were examined using an electrothermal melting point apparatus and were uncorrected. FT-IR spectra were recorded on a PerkinElmer spectrophotometer in the ATR mode. Powder X-ray diffraction (PXRD) data were measured on a Bruker D8 Advance diffractometer for the polycrystalline samples, obtained by grinding the single crystals and the composite films. The PXRD scans

were collected in the 2θ range of 5−50˚ at 0.3 second per degree. The surface morphologies and the thicknesses of the composites were characterized with the help of field-emission scanning electron microscopy (Zeiss ultra plus FESEM instrument). The UV Visible spectrum was recorded at room temperature by using Shimadzu UV-3600 spectrophotometer.

4.2.2 Synthesis

The compound, $[Me(Ph)_3P]_3[Bi_2Br_9]$, was synthesized by mixing methyltriphenylphosphonium bromide (53.58 mg, 0.15 mmol) and bismuth oxide (46.59 mg, 0.1 mmol) in 5 mL aqueous solution of HBr (48% in water). Slow evaporation of the obtained solution afforded yellow crystals of **MTPBB** after a week. Yield 50%. M.P. 206-208 ˚C. ^{31}P NMR (162 MHz, $CDCl_3$) δ 22.29. FT-IR (cm^{-1}): 559, 685,782,897, 994, 1109, 1188, 1330, 1434, 1482, 1584, 2894, 2969, 3021, 3260, 3405, 3508. Anal. Calcd.: C 34.77; H 2.76. Found: C 33.91; H 2.42.

4.2.3 Crystallography: Reflections for **MTPBB** were acquired from Bruker Smart Apex Duo diffractometer at various temperatures using Mo Kα radiation (λ= 0.71073 Å). The crystal structures were solved using the direct method and then refined by the full-matrix least-squares against F^2 using SHELXL-2014/7 built in the Apex 3 program.[29] All the non-hydrogen atoms were refined anisotropically while the hydrogen atoms were constricted in geometric positions to their parent atoms.[30] Two of the three phenyl rings were disordered and atom positions of the disordered groups were refined by the same distance and same U-restraint (SAME/SADI) of the SHELX. The crystallographic data for the compounds are listed in Table 4.1.

Table 4.1: Details of crystallographic data of MTPBB.

Compound	MTPBB (120 K)	MTPBB (298 K)
Chemical formula	$C_{57}H_{54}Bi_2Br_9P_3$	$C_{57}H_{54}Bi_2Br_9P_3$
Formula weight	1969.06	1969.06
Temperature	120(2) K	298(2) K
Crystal system	Trigonal	Trigonal
Space group	*R3*	*R3*
a(Å): α(°)	20.670(3); 90	20.753(4); 90
b(Å); β(°)	20.670(3); 90	20.753(4); 90
c (Å); γ (°)	13.128(4); 120	13.269(7); 120
V(Å^3); Z	4857(2); 3	4949(3); 3
P(calc.) mg m^{-3}	2.019	1.982
μ(Mo K$_\alpha$)mm^{-1}	11.088	10.882
2θ$_{max}$ (°)	57.32	56.70
R (int)	0.1652	0.1444
Completeness to θ	100	100.0
Data/param.	5450/ 324	5474/ 204
GOF	1.043	1.025
R1[F>4σ(F)]	0.0573	0.0495
wR2 (all data)	0.1228	0.1200
max. peak/hole (e.Å^{-3})	1.578/ -1.821	0.989/ -1.679

4.2.4 Piezo-responsive Force Microscopy Characterization: PFM visualization of the ferroelectric domain structure on the $[Me(Ph)_3P]_3[Bi_2Br_9]$ microcrystal surface and the thin film was carried out using a commercial AFM system [MFP-3D, Asylum Research in the contact mode (Vector mode)]. Conductive Pt-coated silicon probe was used for domain imaging in lateral and vertical orientation [SCM-PIT-V2 by Bruker, (Pt/Ir coated tip) with spring constant of 2.8 N/m and tip radius of 25 nm]. Resonant enhanced PFM mode was used to enhance the signal with a frequency of 285 KHz and AC amplitude of 2 V. The d_{33} values were calculated by recording amplitude signal at first contact resonance of the cantilever by changing the tip bias voltage. For non-centrosymmetric materials due to converse piezoelectric effect, the Amp (cantilever) = d_{33} x V_{AC} x Qfactor $_{(tip)}$. We obtained the amplitude signal by varying the AC bias; and later calculated the d_{33} values using the above equation. The switching ability of the domains on thin films was checked by the application of external DC bias of ±40 V using the PFM tip in contact mode. The thin films of the compound were prepared by drop-casting 2 wt% solution **MTPBB** in DMSO followed by annealing at 100˚ C for 2 hours.

4.2.5 Nonlinear optical studies: Nonlinear optical studies were performed using a laser system consisting of a Coherent Astrella Ti:Sapphire regenerative amplifier providing 800 nm pulses (75 fs pulse duration, 1 kHz repetition rate) driving a wavelength-tunable TOPAS Prime optical parametric amplifier OPA. The output of OPA was set to 1350 nm.

Kurtz-Perry test was performed at 298K. Potassium dihydrogen phosphate (KDP) was used as a SHG reference. The single crystals of **MTPBB** and KDP were crushed with spatula and sieved through a mini-sieve set (Aldrich), collecting a microcrystal size fraction of 250 - 177 μm. Next, size-graded samples were fixed between microscope glass slides (forming tightly packed layers), sealed, and mounted to the sample holder. Average power of 1350 nm beam used for Kurtz-Perry study was equal to 275 mW, spot area of 0.5 cm^2. The laser beam was directed onto samples at 45 degrees and was unfocused in all cases. Signal-collecting optics, mounted to the glass optical fiber, was placed perpendicularly to the plane of sample (backscattering geometry) which was placed on a horizontally aligned holder. Scattered pumping radiation was suppressed with the use of 750 nm shortpass dielectric filter (FESH0750, Thorlabs). Temperature-resolved 2PEL study was performed in a separate measurement (800 nm beam – an attenuated output from regenerative amplifier, 350 mW, spot area of 0.7 cm^2), in which the temperature control of the sample was performed using Linkam LTS420 Heating/Freezing Stage. Excitation geometry, signal collection optics, and the sample preparation protocol were the same as for Kurtz-Perry test. The emission spectra collected in both experiments were recorded by an Ocean Optics Flame T spectrograph.

4.2.6 Fabrication of Hybrid Composite Mechanical Energy Harvester: Firstly, the PDMS solution was prepared by adding the base and curing agent in a 10:1 ratio. Pre-calculated amounts of **MTPBB** were then dispersed into the uncured PDMS to prepare composites of varying (5, 10, 15, 20 and 25) wt%. After uniform mixing, the formulated composites were drop-casted into a mould and kept for curing at 80 ˚C in an oven for 7 h. The obtained dried films were subsequently peeled off and aluminum adhesive tapes were physically attached as the top and bottom electrodes to either side of the films. The final device architecture was achieved by establishing electrical contacts to

the end of the electrodes followed by the enclosure of the entire device with the Kapton tape.

4.2.7 Dielectric, Ferroelectric and Piezoelectric measurements: The dielectric data on **MTPBB** was acquired on its compressed pellets using Aluminium adhesive tapes as the top and bottom electrodes. The measurements were performed by using the Solartron Analytical Impedance Analyzer 1260 coupled with a Dielectric Interface 1296A operating with Janis 129610A cryostat sample holder and a Lakeshore 336 model temperature controller. To perform the ferroelectric measurements, single crystals with Al adhesive contacts at the opposite ends were employed. Ferroelectric hysteresis loops were recorded by using aixACCT TF-2000E model analyzer equipped with a Trek model 609E-6 high-voltage amplifier. Leakage currents were assessed simultaneously for various voltage steps during the course of hysteresis loop measurements. The piezoelectric energy harvesting properties of **MTPBB** were examined by using a custom-designed mechanical system built with a vertical impact force.[3] The output performances of the devices were recorded with the help of a Keithley DMM7510 7.5 multimeter operating at an input impedance of 10 MΩ. The thickness and the active area of the devices under test were ~1.57 mm and 1.5 X 1.5 cm^2, respectively. The d_{33} measurement on 20 wt% **MTPBB/PDMS** composite film was performed using Piezotest, PM300 d_{33} meter. The best forming 20 wt% **MTPBB/PDMS** device was poled using the corona poling technique. A high voltage of (25 kV) was applied to the sample for a duration of 2 h through a multiple point electrode at room temperature.

4.3 Results and discussion

4.3.1 Synthesis, Structure and Characterization: Yellow prismatic crystals of $[Me(Ph)_3P]_3[Bi_2Br_9]$, (**MTPBB**) were obtained by slow evaporation of an aqueous HBr solution containing methyl(triphenyl)phosphonium bromide and bismuth oxide in a stoichiometric ratio of 3:2. Structural analysis performed by Single-crystal X-ray diffraction revealed that the compound crystallizes in the chiral trigonal space group *R*3 at room temperature (Table 4.1).

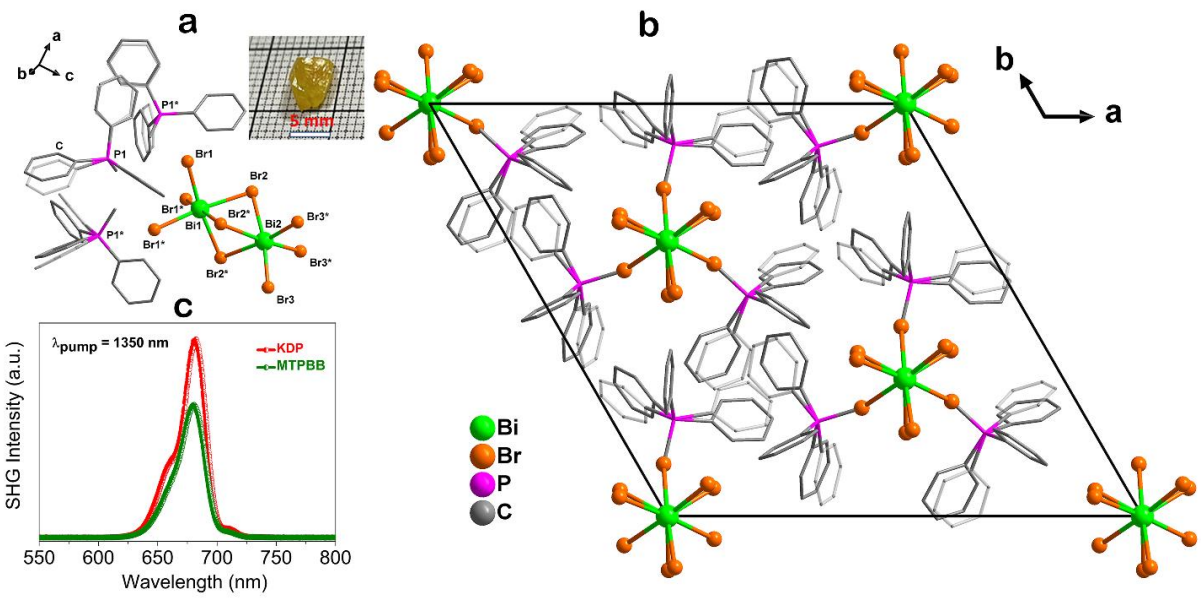

Figure 4.1: *(a) Molecular structure of* ***MTPBB*** *(photograph of its single crystal is displayed in the inset) and (b) its packing diagram viewed along the polar c-axis at 298 K. The disordered phenyl fragments are shown as semitransparent motifs (c) Overlay of SHG emission of* ***MTPBB*** *and that of KDP centred at 675 nm.*

The compound displays a discrete perovskite-type configuration, characterized by an isolated network of $[Bi_2Br_9]^{3-}$ ions (Figure 4.1a). The presence of a larger phosphonium cation inhibited the formation of a polymeric configuration for the anionic bismuth-halide framework, as found in the earlier reported structures of $[Bi_2Br_9]^{3-}$ with other cations.[21,22,27-28,31-32] The bimetallic $[Bi_2Br_9]^{3-}$ motif consists of two $BiBr_3$ segments that are connected via three additional μ2-bridged bromide ions. Each bismuth ion in the dimer is hexa-coordinated and is located in a face-shared bi-octahedral geometry. A closer inspection of the crystal structure of **MTPBB** reveals that the inorganic moieties adopt distorted geometries as evidenced by the subtle difference in the angles of the bi-octahedral units (Table 4A.1, Appendix 4). The bridging Bi-Br bond lengths of 2.978(2) Å (Bi1-Br2) and 3.060(2) Å (Bi2-Br2) are significantly larger than the terminal bonds distance of 2.783(2) Å (Bi1-Br1) and 2.714(2) Å (Bi2-Br3) at 298 K. The observed variations in the bond lengths of **MTPBB** are comparable with the previously reported structurally-similar Bi(III) compounds.[27,28] The C-P-C bond angles deviate from 102.3 (17) to 115.3(17), indicating a distorted tetrahedral environment around the cationic phosphorus atoms at room temperature. The packing structure of **MTPBB**

features nine phosphonium cationic units embedded in the cavities enclosed by the anionic framework (Figure 4.1b). Three $[Bi_2Br_9]^{3-}$ units are confined at the corners of 3-fold axis and three disordered phosphonium cations are located along the triangular edges. The non-centrosymmetric packing of the compound was verified by performing Kurtz-Perry powder test on sieved sample, using 1350 nm femtosecond laser pulses. A clear second harmonic signal at 675 nm generated with a relative efficiency of 69% vs. KDP unequivocally confirmed the non-centrosymmetric identity of **MTPBB** (Figure 4.1c).

The phase purity of the bulk phase of **MTPBB** was verified by the Powder X-ray diffraction analysis, which showed a good match between the experimental peaks and the simulated patterns (Figure 4A.2, Appendix 4). Furthermore, the unit cell parameters of **MTPBB** were derived from single-crystal X-ray diffraction data in the temperature range between 120 to 450 K (Figures 4A.3-4A.4, Appendix 4). These studies confirmed the absence of any phase transitions as the non-centrosymmetric space group of the compound was retained at all the measured temperatures with no marked changes in the lattice parameter values (Table 4A.2, Appendix 4). Moreover, no major deviations were observed in the bond length and angles for $[Me(Ph)_3P]^+$ and $[Bi_2Br_9]^{3-}$ moieties at both the 120 to 298 K structures of **MTPBB** precluding any drastic phase change in the crystal structure (Table 4A.1 and Figure 4A.5, Appendix 4). Simultaneous TGA and DTA measurements display peaks corresponding to its melting and decomposition temperatures (Figure 4A.6, Appendix 4). The high structural stability of **MTPBB** is primarily caused by the introduction of larger phosphonium cations, which are firmly retained in the non-centrosymmetric trigonal packing (*R*3), despite the tumbling motion of their phenyl rings visible across a wide range of temperatures.

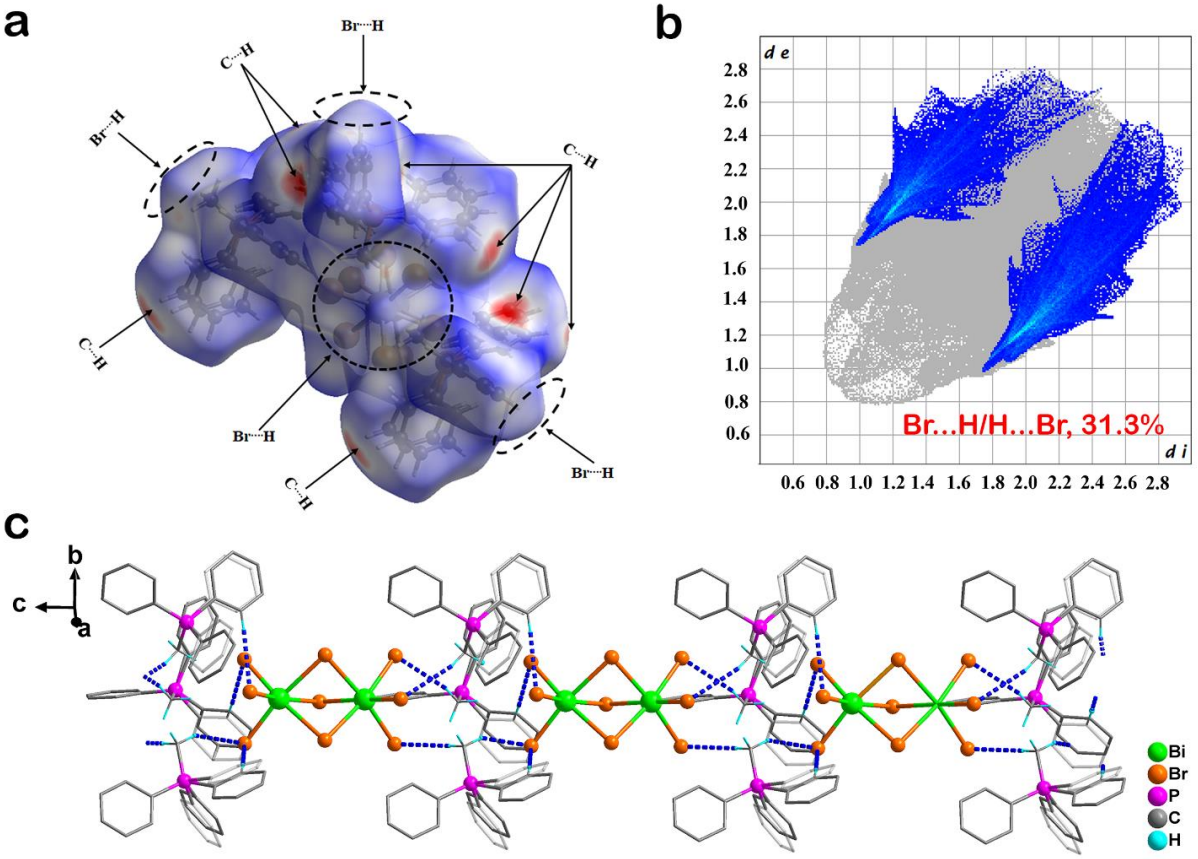

Figure 4.2: *(a) Hirshfeld surface of a single $[Me(Ph)_3P]_3[Bi_2Br_9]$ unit and (b) the two-dimensional fingerprint plot of C-H···Br interactions at 298 K (c) The hydrogen-bonded structure of* ***MTPBB*** *presenting the polar axis along which organic and inorganic moieties are linked by C-H···Br interactions.*

Furthermore, the quantification of intermolecular contacts present in the 298 K structure of **MTPBB** were evaluated by performing the Hirshfeld surface analysis and associated 2D-fingerprint plots (Figures 4.2a-b, 4A.7-4A.8 and Table 4A.3, Appendix 4). Several types of molecular contacts such as C···H, C···C, H···Br, H···H are shown on the Hirshfeld surface with an overall surface percent contributions of 23.8, 0.8, 31.3, and 40.9, respectively. The sites of the donor and acceptor atoms pertaining to the intermolecular C···H contacts are highlighted as bright red spots on the Hirshfeld surface. The C-H···Br hydrogen bonding contributes 31.3 % of the interactions, while dispersion and van der Waals contacts contribute 65.5 % of the interactions (Figure 4.2b). Although the latter set of forces has a higher percentage contribution for the overall contacts, it accounts for the short-range order in the molecule with lower stabilization energy of 0.4-4 kJ/mol.

However, the hydrogen bonding (C-H···X; X = Cl, Br) and ionic interaction account for strong long-range order with the structure stabilization energy of 3-9 kJ/mol. A closer look at the diagrams reveals that the methyl protons along with para C-H groups of the phosphonium phenyl ring interact with the terminal Br atoms on either sides of the $[Bi_2Br_9]^{3-}$ unit leading to 1D-hydrogen bonding network along the polar c-axis (Figure 4.2c, Table 4A.4-4A.5, Appendix 4).

4.3.2 Ferroelectric, Dielectric, Piezoelectric and Optical Properties

The structure of **MTPBB** exhibits the point group symmetry of *C3*, which is one of the ten polar point groups that can host ferroelectric property. The ferroelectric behavior of **MTPBB** was probed by recording its polarization vs. electric field (*P-E*) hysteresis loops using a Sawyer-Tower circuit system. The measurements were performed on a single crystal of **MTPBB** along the polar c-axis at room temperature. As depicted in Figure 4.3a, **MTPBB** yields a well-defined rectangular hysteresis loop at 0.9 Hz, resulting in a remnant polarization value of 2.1 μC cm^{-2} at a reasonably low coercive field of 0.59 kV cm^{-1}. To gain deeper insights into the ferroelectric nature of **MTPBB**, a point charge model-based polarization calculation was also carried out on its molecular structure at 298 K (Table 4A.6, Appendix 4). The computed polarization value of 19.7 μC cm^{-2} is higher in comparison with the experimental observed P_r at 0.9 Hz. This prompted us to further examine the ferroelectric characteristics at lower frequencies on its single crystal (Figure 4A.9-4A.10, Appendix 4). The measurement at 0.1 Hz manifests a higher P_r value of 23.6 μC cm^{-2}, albeit with a slightly distorted cubic-like shape (Figure 4A.10, Appendix 4). The observed value is slightly overestimated compared to the calculated one, indicating the contribution of leakage current. The attained polarization value compares well with those for recently emerging phosphonium based molecular ferroelectrics.[33-36] The *J-E* plots measured along the *P-E* loop trace shows peaks at the coercive fields with low leakage currents signifying the formation of two stable domain states with opposite polarization, corroborating the ferroelectric nature of the obtained loops (Figure 3a, Figures 4A.9-4A.10, Appendix 4). The excellent ferroelectricity of **MTPBB** stems from its stable charge-separated structure consisting of the cationic phosphonium motifs and the bi-octahedral $[Bi_2Br_9]^{3-}$ framework and their non-covalent interactions along the polar

axis. The higher polarization of **MTPBB** over the analogous compound $[Me_4P]_3[Bi_2Br_9]$ can be attributed to the presence of bulky phenyl substituents on the heteroleptic phosphonium backbone. Those substituents experience disorder of the phenyl groups on two well-resolved sites, unlike the multiple disorder of the methyl groups of the $[Me_4P]$ cation over several sites at room-temperature.[28]

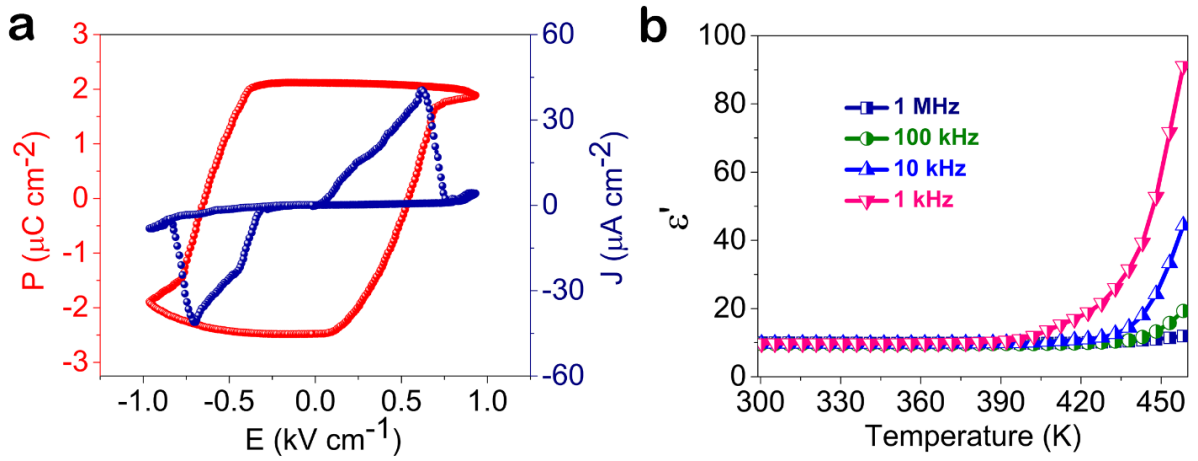

Figure 4.3: *(a) P-E hysteresis loop and leakage current density plot of **MTPBB** single crystal measured at 0.9 Hz at room temperature. (b) Temperature-dependent real part of dielectric permittivity (ε') of **MTPBB** at various frequencies.*

Furthermore, the dielectric permittivity as a function of temperature (T) was examined on its polycrystalline compacted pellets at various frequencies. The real part of the complex dielectric permittivity (ε′) displays no noticeable anomalies in the temperature range of 300 K to 458 K, consistent with the variable temperature SCXRD and DTA profiles (Figure 4.3b). The lack of ferroelectric-paraelectric transition in **MTPBB** is attributed to its greater structural stability assisted by the strong non-classical interactions between the $[Bi_2Br_9]^{3-}$ framework and the three phosphonium motifs. It is evident that the dielectric constant increases progressively with the increase in temperature from 300 to 410 K, beyond which it displays an abrupt rise (Figure 4.3b). Such anomalies in ε′ values arise from the formation of more polarizable dipoles and increased ionic conductivity near the melting point. The ε′ value of 9.8 was obtained at room temperature for **MTPBB** at a frequency of 1 kHz. The compound exhibits relatively low dielectric loss, as evidenced from its tan δ vs T plot (Figure 4A.11, Appendix 4). Moreover, the frequency-dependent ε′ and tan δ profiles reveal similar trends as observed for the temperature-dependent measurements (Figures 4A.12-4A.13, Appendix 4).

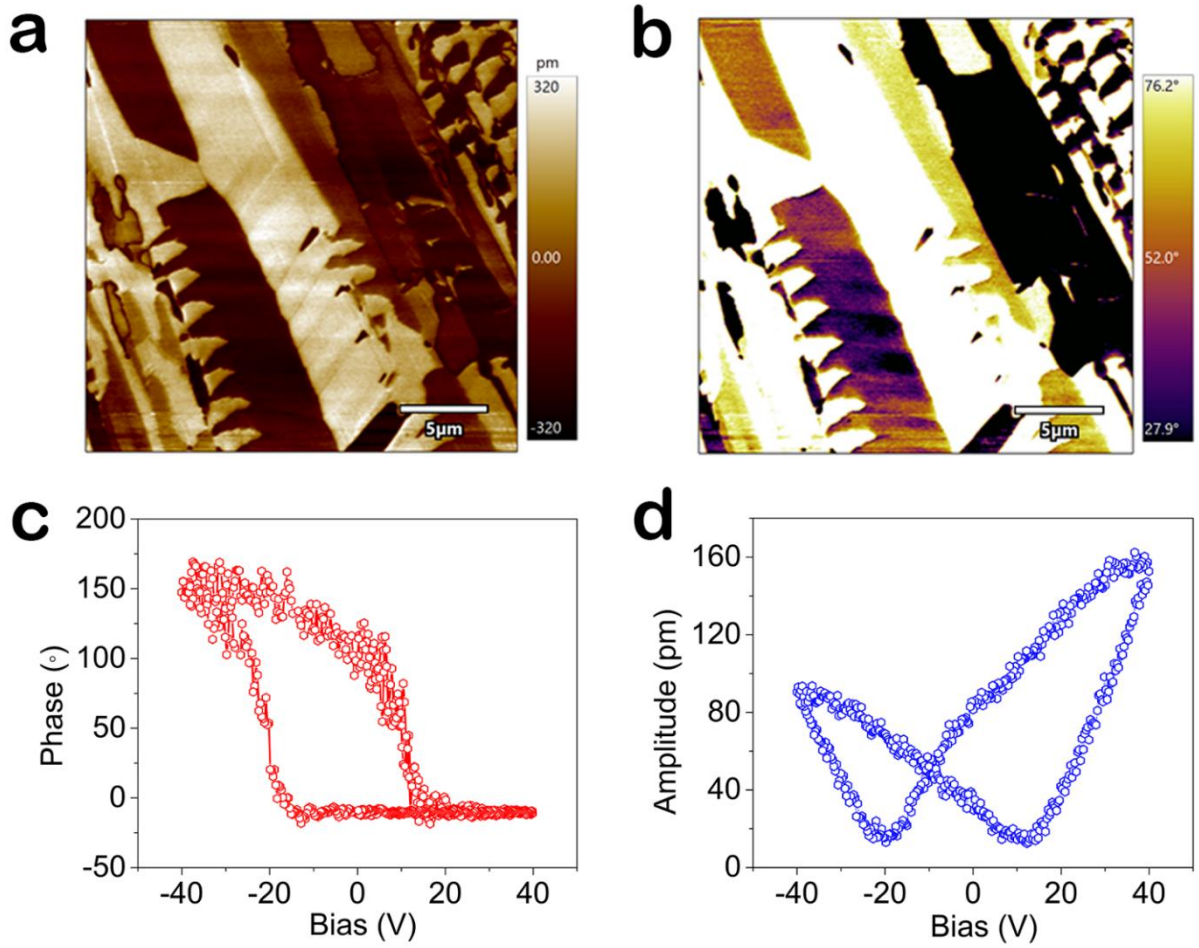

Figure 4.4: *(a) Domain strcutures observed in the as grown thin film of* ***MTPBB****. Lateral PFM (a) amplitude and (b) phase images; (c) Phase-voltage hysteresis loop and (d) amplitude-voltage butterfly loop for a selected point on the thin film surface.*

To further study the ferroelectric domain structure at the nanoscale, we performed Piezoresponse Force Microscopy (PFM) measurements on **MTPBB** single crystal (Figure 4A.14, Appendix 4) and its thin-film (Figure 4.4 and 4A.15, Appendix 4). Local lattice deformation was recorded in both vertical and lateral modes of PFM as amplitude and phase data, which results in the direct observation of the domain structure and orientation along lateral and vertical direction, respectively. Figure 4.4a-b depicts the lateral PFM amplitude and phase signals recorded on thin-film samples. Evidently, the ferroelectric domain structures appear to be arranged in strip-like texture. The domain walls, where the signal is minimum in the amplitude image, separates the adjacent domains. The phase patterns are consistent with the corresponding amplitude images, where the domains are seen to be orientated in the

upward and downward directions. Besides, the observation of ferroelectric domains in **MTPBB** thin film, the PFM spectroscopy was performed on a single point in the contact mode. These studies resulted in the signature rectangular phase hysteresis (Figure 4.4c) and butterfly-shaped amplitude loop (Figure 4.4d) for **MTPBB** confirming the reversible ferroelectric domain structure of the **MTPBB** thin film.

Furthermore, the displacements, induced by the driving ac voltage, were subsequently measured to determine the converse piezoelectric strain coefficient (d_{33}) value (Figure 4A.14f, Appendix 4). First, the single crystal surface was driven across the resonance frequency using a 2 V biased PFM tip. The curve displays a clear resonance peak which can be fitted well with the damped harmonic oscillator model.[37,38] The effective amplitude can thus be extracted by correcting the resonance amplification with the quality factor. Next, to verify the response arising from the intrinsic piezoelectricity, these measurements were performed under a set of drive voltages from 2 to 10 V using 2 V steps. As expected, the amplitude increased linearly with the driving ac voltage. Consequently, the magnitude of piezoelectric coefficient (d_{33}) was evaluated from the slope of the plot, which rendered a value of 8 pm V^{-1} for **MTPBB**. However, the direct piezoelectric coefficient measurements on the single crystals of **MTPBB** could not be performed due to the fragile nature of these crystals (Figure 4A.16, Appendix 4).

As piezoelectric voltage coefficient (g_{33}) is one of the factors determining the performance of piezoelectric elements, we evaluated the g_{33} of **MTPBB** using the relation $g_{33} = d_{33}/\varepsilon$ (where $\varepsilon = \varepsilon_r\varepsilon_0$). According to the obtained experimental results, the g_{33} of 92.2 x 10^{-3} V m N^{-1} is obtained for **MTPBB**. The high piezoelectric voltage coefficient combined with its lead-free composition make **MTPBB** an excellent candidate for application in different piezoelectric devices for possible wearable electronics, among other emerging applications.

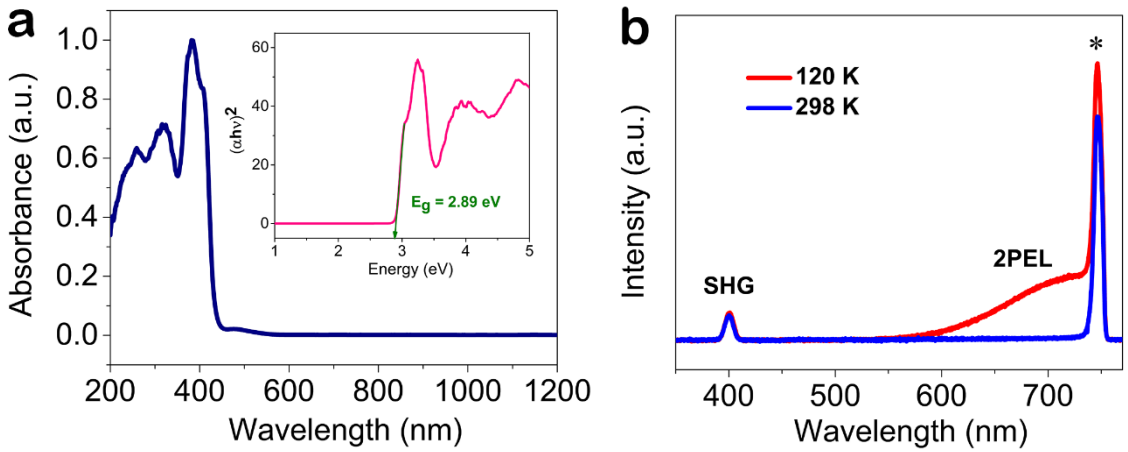

Figure 4.5: *(a) UV-Vis diffuse reflectance spectrum of **MTPBB** and its corresponding Tauc plot displayed in the inset. (b) Overlay of emission spectra collected at 120K and 298K under 800 nm femtosecond laser excitation of **MTPBB**. Note that the signal denoted with an asterisk is not sample-related, as it is a tail of the fundamental 800 nm beam that passed through a 750 nm short-pass filter.*

Since the bismuth halide analogues are known to exhibit semiconducting behavior, the optical properties of the title compound were examined. The solid-state UV-visible diffuse reflectance spectroscopy of **MTPBB** exhibits a strong absorption with the band edge onset at 430 nm (Figure 4.5a). The bandgap extracted from the Tauc plot is estimated to be 2.89 eV, which is comparable to many organic-inorganic lead-based ferroelectric semiconductors[39-42] and considerably lower than numerous inorganic ceramic materials.[43] Moreover, when we performed SHG tests on **MTPBB** in a wide temperature range with 800 nm pumping, we have found that apart from second harmonic signal at 400 nm, the two-photon excitation luminescence (2PEL) appears at low temperatures (Figure 4A.17, Appendix 4). Specifically, the observed 2PEL is a broad emission that peaks at around 710 nm and starts to be visible when temperature is below 200 K (Figure 4.5b) and rises further with decreasing temperature. These additional semiconducting and 2PEL emission behaviors signify the potential of **MTPBB** in the emerging area of lead-free hybrid photoferroelectric materials.[44]

4.3.3 Mechanical Energy Harvesting Applications

Encouraged by the dielectric, piezoelectric and ferroelectric properties of **MTPBB**, we set out to examine its efficacy towards mechanical energy harvesting application in the form of its polymer composite. For this purpose, we chose to employ PDMS, a non-piezoelectric polymer, for the device fabrication. Homogeneous flexible polymer composites with varying weight percentages (5, 10, 15, 20, and 25 wt. %) were obtained by dispersing appropriate quantities of **MTPBB** in the PDMS precursor solution under extensive mechanical stirring (Table 4A.7, Appendix 4). The device layout was subsequently completed by placing Al adhesive tapes on either side of the composite films as electrodes. All formulated composite devices reveal high degrees of flexibility (Figures 4.6a-d). The PXRD profiles of the composite films display all characteristic peaks present in the bulk **MTPBB**, implying the crystalline nature of

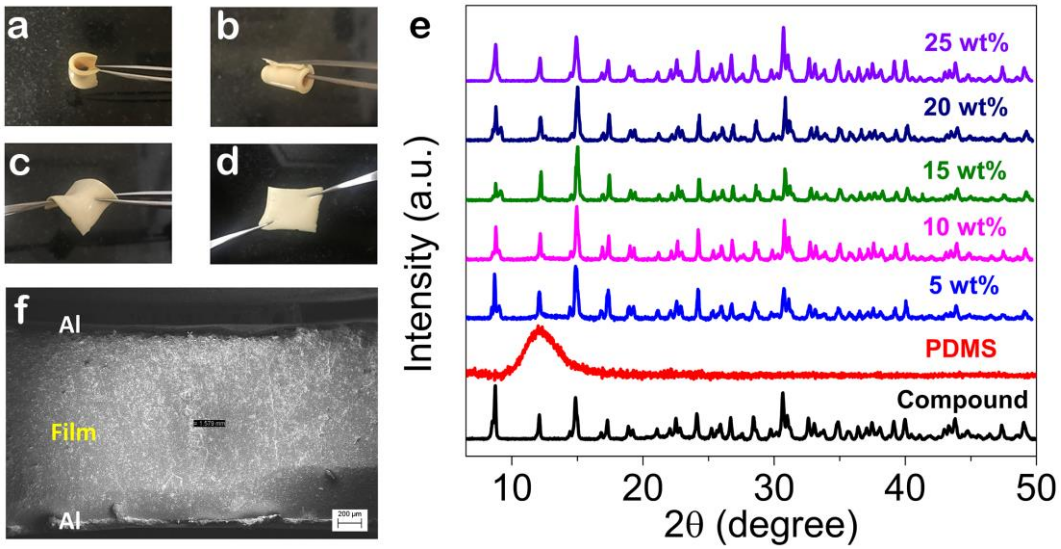

Figure 4.6: *Photographs of a flexible 20 wt% **MTPBB/PDMS** composite film subjected to (a) bending, (b) rolling, (c) twisting, and (d) stretching operations. (e) PXRD data of the as-prepared composites with varying concentrations of **MTPBB**. (f) Cross-sectional SEM image of **MTPBB/PDMS** based device showing a thickness of ~1.57 mm for the embedded film of **MTPBB**.*

the obtained composites (Figure 4.6e). Moreover, a significant rise in the intensity of the diffraction peaks is evident upon increasing the % loading of the ferroelectric particles, indicating the increased content of crystalline component in the obtained

films at higher weight percentages. The cross-sectional SEM image of the **MTPBB-PDMS** device reveals that the thickness of the composite film, sandwiched between the two Al electrodes, is ~1.57 mm (Figure 4.6f).

The piezoelectric output performance of all fabricated piezoelectric nanogenerators was tested by applying a periodic compressive force of 40 N at a tapping frequency of 24 Hz on unpoled devices. A custom-built force setup connected with a digital multimeter was employed for recording the output signals.[45,46] When an external force is applied to the device, a piezoelectric potential is developed between the electrodes, which leads to the flow of electrons in the external circuit. This results in a positive output signal. Upon releasing the force, the signal in the negative direction is generated as the accumulated free electrons return to their original state with the disappearance of the piezoelectric potential. Hence, the periodic cycle of compression and release produces alternating output signals from the composite devices.[47] The generated open-circuit voltages from the various weight percentage composite devices are given in Figure 4.7a. The piezoelectric output voltages are seen to gradually rise as the loading of **MTPBB** increases in the composites and a maximum peak-to-peak voltage (V_{pp}) of 22.9 V was obtained for the optimal 20 wt% **MTPBB/PDMS** film. A further increase in the loading to 25 wt % results in a sudden drop in the V_{pp} to 14.3 V (Figure 4A.18, Appendix 4). Notably, a device based on pure PDMS shows the V_{oc} of only 0.5 V under identical conditions, confirming the contribution of the embedded **MTPBB** crystallites for the high output performance of the devices. To further investigate the self-polarization of the fabricated composite films, we tested the best performing 20 wt% device under similar conditions after electric poling (25 kV, 2 h). However, no significant improvement in the output voltages were observed for the poled device exemplifying the macroscopic piezoelectricity of the embedded **MTPBB** particles originate from its ferroelectric behavior (Figure 4A.19, Appendix 4). This suggests that the applied external force aligns the **MTPBB** dipoles along one direction through stress-induced polarization which is a source of piezoelectricity in the material. Such instances of unpoled devices exhibiting self-polarization without any external electrical potential are well documented in literature.[47-50]

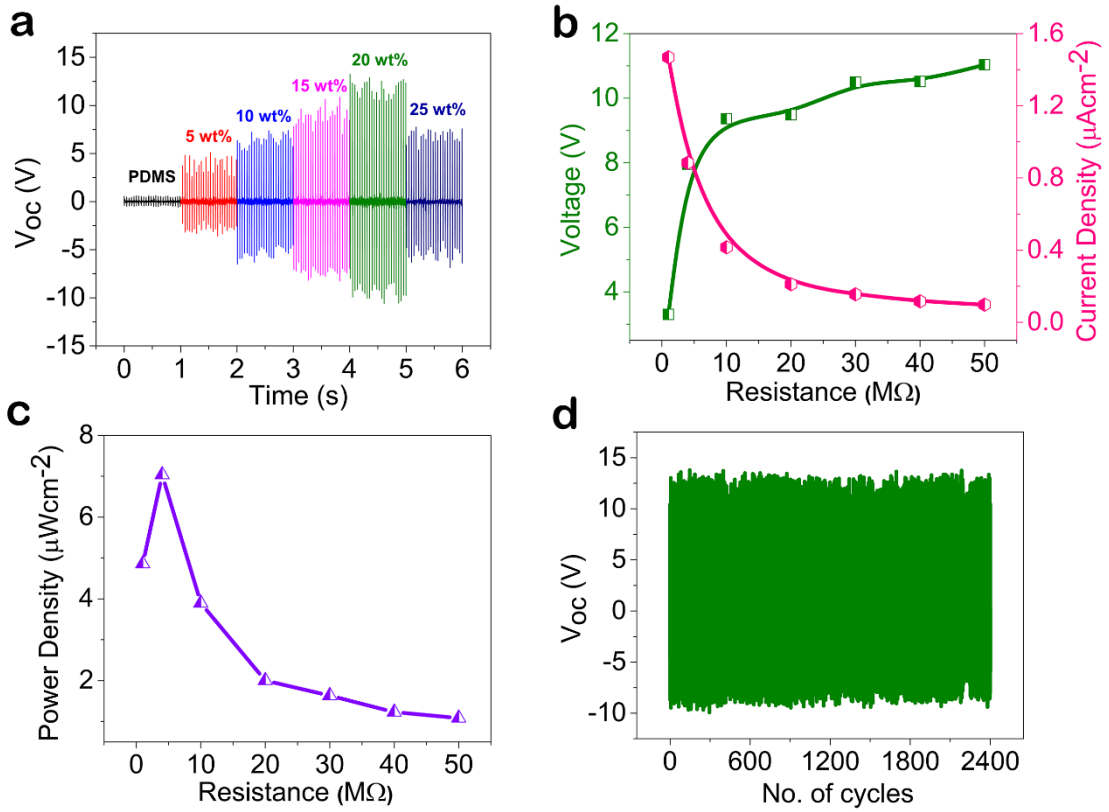

Figure 4.7: *(a) Comparative output voltage performance of all wt% **MTPBB/PDMS** composite devices with a shifted time axis. (b) Voltage, current density, (c) and power density plots as a function of load resistance corresponding to the 20 wt% **MTPBB/PDMS** device. Lines are drawn to guide the eyes. (d) Mechanical durability test performed on the 20 wt % **MTPBB/PDMS** device with an applied force of 40 N and frequency of 24 Hz.*

The observed enhancement in the output performance with increased loading of **MTPBB** is attributed to the existence of interfacial polarization between **MTPBB** and the polymer matrix. As evidenced from earlier reports, the interfaces in heterogeneous materials yields Maxwell-Wagner-Sillars polarization, which gives rise to noteworthy changes in the total dielectric constants of the composite films.[51-54] Thus, higher quantity of ferroelectric fillers in the films leads to higher interfacial charges, boosting the overall polarization of the composites. However, the enhancement in polarization saturates upon a critical level of particle loading due to the amalgamation of interfaces. In our case, the optimal loading level is realized at 20 wt.%, above which the insulation of the composites weakens and leads to the electrical breakdown with a significant drop in the output voltage.[55]

While the performance of the nanogenerators derived from **MTPBB/PDMS** is good, it is critical to explore how these would fit in for real-life applications. To this end, the influence of the external load resistance on the best performing 20 wt% **MTPBB/PDMS** device was investigated. These measurements showed a gradual increase in the output voltage and a decrease in the current density values as the load resistance was increased from 1 to 50 MΩ (Figure 4.7b). Subsequently, the power density of the device is computed by the formula, $P = V^2/RA$, where V, R and A stand for the output voltage, load resistance and the effective area, respectively. A maximum power density of 7 μW cm^{-2} is attained for the 20 wt% of **MTPBB/PDMS** at a threshold load resistance of 4 MΩ (Figure 4.7c). The mechanical endurance of the device was also tested under continuous compression and release cycles of 40 N force for 100 s, which resulted in no significant degradation in the output voltages and confirmed the reliability of the obtained signals (Figure 4.7d). The piezoelectric measurements performed on the best performing 20 wt% unpoled composite film resulted in the piezoelectric coefficient (d_{33}) value of 4.24 pC N^{-1} at an operating frequency of 110 Hz and an applied force of 0.25 N confirming the piezoelectric origin of the obtained voltages (Figure 4A.20, Appendix 4).

The practical utility of the energy harvested from the piezoelectric nanogenerator was further demonstrated by capacitor charging experiments. Since a dc output is required for powering miniature electrical products, the resulting ac signals from the device were rectified by means of a full-wave bridge rectifier circuit (Figure 4.8a). The charging curves of various electrolytic capacitors (2.2, 4.7 and 10 µF) are presented in Figure 4.8b. The voltage across the 2.2 µF capacitor is seen to increase exponentially and reach a steady-state value of 1.26 V in 60 s. The stored voltages were found to marginally decrease to 1.11 and 0.61 V for the higher rating capacitors of 4.7 and 10 µF, respectively, as demonstrated for other similar systems. The accumulated charges and the stored electrical energies for the respective 2.2, 4.7 and 10 µF capacitors are calculated to be 2.52, 5.22, 6.10 µC and 1.58, 2.89, 1.86 µJ, respectively (Figure 4A.21, Appendix 4). The stored voltages in the capacitor are found to be lower than the recorded open-circuit voltages, which presumably arise from the voltage drop across the rectifying diodes and leakage of the capacitor.[56] These results

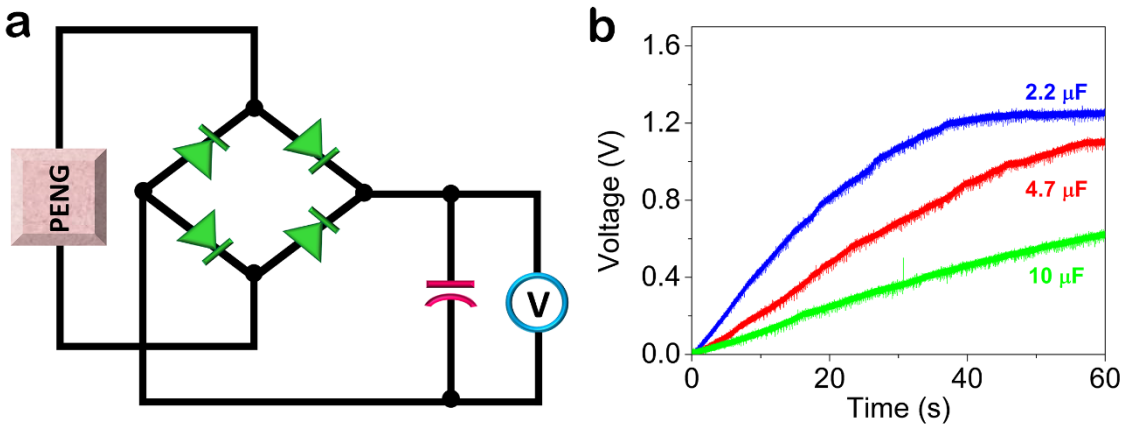

Figure 4.8: *(a) Schematic diagram of the full wave bridge rectifier circuit employed for capacitor charging experiments. (b) Capacitor charging curves for 2.2, 4.7, and 10 μF capacitors employing the 20 wt%* ***MTPBB/PDMS*** *composite.*

elucidate the remarkable potential of molecular ferroelectric materials for the next generation flexible self-powered electronics and sensors.

4.4 Conclusion

In summary, we have successfully designed a new hybrid phosphonium perovskite of the formula $[Me(Ph)_3P]_3[Bi_2Br_9]$, which is shown to exhibit a high remnant polarization of 23.6 $\mu C\ cm^{-2}$ at 0.1 Hz frequency. The incorporation of large phosphonium cations in the metal halide framework not only provides high thermal stability to the compound but also retains its ferroelectric ordered state at high temperatures. The ferroelectric and piezoelectric nature of this compound was further probed by PFM experiments. Moreover, its subsequent implementation for mechanical energy harvesting applications in the form of PDMS polymer composites results in a maximum peak-to-peak voltage of 22.9 V and power density value of 7 $\mu W\ cm^{-2}$ for the optimal 20 wt% **MTPBB/PDMS** device. The energy storage capabilities of the devices were also demonstrated by storing the harvested energy in a wide range of electrolytic capacitors. These findings lay out a promising platform for designing new phosphonium based perovskites for future self-powered electronics.

4.5 References

(1) Fu, Y.; Zhu, H.; Chen, J.; Hautzinger, M. P.; Zhu, X. Y.; Jin, S., Metal halide perovskite nanostructures for optoelectronic applications and the study of physical properties. *Nat. Rev. Mater.* **2019**, *4*, 169-188.

(2) Pham, H. D.; Xianqiang, L.; Li, W.; Manzhos, S.; Kyaw, A. K. K.; Sonar, P., Organic interfacial materials for perovskite-based optoelectronic devices. *Energy Environ. Sci.* **2019**, *12*, 1177-1209.

(3) Huang, Y.; Lei, X.; He, T.; Jiang, Y.; Yuan, M., Recent Progress on Formamidinium-Dominated Perovskite Photovoltaics. *Adv. Energy Mater.* **2021**, *na*, 2100690.

(4) Dey, A.; Ye, J.; De, A.; Debroye, E.; Ha, S. K.; Bladt, E.; Kshirsagar, A. S.; Wang, Z.; Yin, J.; Wang, Y.; Quan, L. N.; Yan, F.; Gao, M.; Li, X.; Shamsi, J.; Debnath, T.; Cao, M.; Scheel, M. A.; Kumar, S.; Steele, J. A.; Gerhard, M.; Chouhan, L.; Xu, K.; Wu, X.-g.; Li, Y.; Zhang, Y.; Dutta, A.; Han, C.; Vincon, I.; Rogach, A. L.; Nag, A.; Samanta, A.; Korgel, B. A.; Shih, C.-J.; Gamelin, D. R.; Son, D. H.; Zeng, H.; Zhong, H.; Sun, H.; Demir, H. V.; Scheblykin, I. G.; Mora-Seró, I.; Stolarczyk, J. K.; Zhang, J. Z.; Feldmann, J.; Hofkens, J.; Luther, J. M.; Pérez-Prieto, J.; Li, L.; Manna, L.; Bodnarchuk, M. I.; Kovalenko, M. V.; Roeffaers, M. B. J.; Pradhan, N.; Mohammed, O. F.; Bakr, O. M.; Yang, P.; Müller-Buschbaum, P.; Kamat, P. V.; Bao, Q.; Zhang, Q.; Krahne, R.; Galian, R. E.; Stranks, S. D.; Bals, S.; Biju, V.; Tisdale, W. A.; Yan, Y.; Hoye, R. L. Z.; Polavarapu, L., State of the Art and Prospects for Halide Perovskite Nanocrystals. *ACS Nano* **2021**, *15*, 10775–10981.

(5) Tan, Z.-K.; Moghaddam, R. S.; Lai, M. L.; Docampo, P.; Higler, R.; Deschler, F.; Price, M.; Sadhanala, A.; Pazos, L. M.; Credgington, D.; Hanusch, F.; Bein, T.; Snaith, H. J.; Friend, R. H., Bright light-emitting diodes based on organometal halide perovskite. *Nat. Nanotechnol.* **2014**, *9*, 687-692.

(6) Chin, X. Y.; Cortecchia, D.; Yin, J.; Bruno, A.; Soci, C., Lead iodide perovskite light-emitting field-effect transistor. *Nat. Commun.* **2015**, *6*, 7383.

(7) Tian, W.; Zhou, H.; Li, L., Hybrid Organic–Inorganic Perovskite Photodetectors. *Small* **2017**, *13*, 1702107.

(8) Dong, H.; Zhang, C.; Liu, X.; Yao, J.; Zhao, Y. S., Materials chemistry and engineering in metal halide perovskite lasers. *Chem. Soc. Rev.* **2020**, *49*, 951-982.

(9) Yoo, E. J.; Lyu, M.; Yun, J.-H.; Kang, C. J.; Choi, Y. J.; Wang, L., Resistive Switching Behavior in Organic–Inorganic Hybrid $CH_3NH_3PbI_{3-x}Cl_x$ Perovskite for Resistive Random Access Memory Devices. *Adv. Mater.* **2015**, *27*, 6170-6175.

(10) Park, H.; Ha, C.; Lee, J.-H., Advances in piezoelectric halide perovskites for energy harvesting applications. *J. Mater. Chem. A* **2020**, *8*, 24353-24367.

(11) Wang, Z. L.; Song, J., Piezoelectric Nanogenerators Based on Zinc Oxide Nanowire Arrays. *Science* **2006**, *312*, 242-246.

(12) Bowen, C. R.; Kim, H. A.; Weaver, P. M.; Dunn, S., Piezoelectric and ferroelectric materials and structures for energy harvesting applications. *Energy Environ. Sci.* **2014**, *7*, 25-44.

(13) Briscoe, J.; Dunn, S., Piezoelectric nanogenerators – a review of nanostructured piezoelectric energy harvesters. *Nano Energy* **2015**, *14*, 15-29.

(14) Jella, V.; Ippili, S.; Eom, J.-H.; Pammi, S. V. N.; Jung, J.-S.; Tran, V.-D.; Nguyen, V. H.; Kirakosyan, A.; Yun, S.; Kim, D.; Sihn, M. R.; Choi, J.; Kim, Y.-J.; Kim, H.-J.; Yoon, S.-G., A comprehensive review of flexible piezoelectric generators based on organic-inorganic metal halide perovskites. *Nano Energy* **2019**, *57*, 74-93.

(15) Ippili, S.; Jella, V.; Eom, J.-H.; Kim, J.; Hong, S.; Choi, J.-S.; Tran, V.-D.; Van Hieu, N.; Kim, Y.-J.; Kim, H.-J.; Yoon, S.-G., An eco-friendly flexible piezoelectric energy harvester that delivers high output performance is based on lead-free $MASnI_3$ films and $MASnI_3$-PVDF composite films. *Nano Energy* **2019**, *57*, 911-923.

(16) Kim, Y.-J.; Dang, T.-V.; Choi, H.-J.; Park, B.-J.; Eom, J.-H.; Song, H.-A.; Seol, D.; Kim, Y.; Shin, S.-H.; Nah, J.; Yoon, S.-G., Piezoelectric properties of $CH_3NH_3PbI_3$ perovskite thin films and their applications in piezoelectric generators. *J. Mater. Chem. A* **2016**, *4*, 756-763.

(17) Stoumpos, C. C.; Malliakas, C. D.; Kanatzidis, M. G., Semiconducting Tin and Lead Iodide Perovskites with Organic Cations: Phase Transitions, High Mobilities, and Near-Infrared Photoluminescent Properties. *Inorg. Chem.* **2013**, *52*, 9019-9038.

(18) Grätzel, M., The light and shade of perovskite solar cells. *Nat. Mater.* **2014**, *13*, 838-842.

(19) Lyu, M.; Yun, J.-H.; Cai, M.; Jiao, Y.; Bernhardt, P. V.; Zhang, M.; Wang, Q.; Du, A.; Wang, H.; Liu, G.; Wang, L., Organic–inorganic bismuth (III)-based material: A lead-free, air-stable and solution-processable light-absorber beyond organolead perovskites. *Nano Res.* **2016**, *9*, 692-702.

(20) Xu, G.; Li, Y.; Zhou, W.-W.; Wang, G.-J.; Long, X.-F.; Cai, L.-Z.; Wang, M.-S.; Guo, G.-C.; Huang, J.-S.; Bator, G.; Jakubas, R., A ferroelectric inorganic–organic hybrid based on NLO-phore stilbazolium. *J. Mater. Chem.* **2009**, *19*, 2179-2183.

(21) Zhang, J.; Han, S.; Ji, C.; Zhang, W.; Wang, Y.; Tao, K.; Sun, Z.; Luo, J., $[(CH_3)_3NH]_3Bi_2I_9$: A Polar Lead-Free Hybrid Perovskite-Like Material as a Potential Semiconducting Absorber. *Chem. Eur. J.* **2017**, *23*, 17304-17310.

(22) Szklarz, P.; Gągor, A.; Jakubas, R.; Zieliński, P.; Piecha-Bisiorek, A.; Cichos, J.; Karbowiak, M.; Bator, G.; Ciżman, A., Lead-free hybrid ferroelectric material based on formamidine: $[NH_2CHNH_2]_3Bi_2I_9$. *J. Mater. Chem. C* **2019**, *7*, 3003-3014.

(23) Zhang, H. Y.; Wei, Z.; Li, P. F.; Tang, Y. Y.; Liao, W. Q.; Ye, H. Y.; Cai, H.; Xiong, R. G. The narrowest band gap ever observed in molecular ferroelectrics: hexane-1,6-diammonium pentaiodobismuth(III). *Angew. Chem. Int. Ed.* **2018**, *57*, 526−530.

(24) Liu, Y.-H.; Peng, H.; Liao, W.-Q., A lead-free bismuth iodide organic–inorganic ferroelectric semiconductor. *Chem. Commun.* **2021**, *57*, 647-650.

(25) Jakubas, R.; Gągor, A.; Winiarski, M. J.; Ptak, M.; Piecha-Bisiorek, A.; Ciżman, A., Ferroelectricity in Ethylammonium Bismuth-Based Organic–Inorganic Hybrid: $(C_2H_5NH_3)_2[BiBr_5]$. *Inorg. Chem.* **2020**, *59*, 3417-3427.

(26) Piecha, A.; Białońska, A.; Jakubas, R., Structure and ferroelectric properties of $[C_3N_2H_5]_5[Bi_2Br_{11}]$. *J. Phys.: Condens. Matter* **2008**, *20*, 325224.

(27) Wojtaś, M.; Jakubas, R., Structure and properties of $[(CH_3)_4P]_3[Sb_2Cl_9]$ and $[(CH_3)_4P]_3[Bi_2Cl_9]$. *J. Phys.: Condens. Matter* **2004**, *16*, 7521-7534.

(28) Wojtaś, M.; Jakubas, R.; Ciunik, Z.; Medycki, W., Structure and phase transitions in $[(CH_3)_4P]_3[Sb_2Br_9]$ and $[(CH_3)_4P]_3[Bi_2Br_9]$. *J. Solid State Chem.* **2004**, *177*, 1575-1584.

(29) Sheldrick, G. M. A short history of SHELX. *Acta Crystallogr., Sect. A: Found. Crystallogr*. **2008**, *64*, 112−122.

(30) Spek, A. Structure validation in chemical crystallography. *Acta Crystallogr., Sect. D: Biol. Crystallogr*. **2009**, *65*, 148−155.

(31) Yang, W.; Chu, K.-B.; Zhang, L.; Ding, X.; Sun, J.; Liu, J. Z.; Song, J.-L.; Zheng, C.; Deng, J., Lead-free molecular ferroelectric [N,N-dimethylimidazole]$_3Bi_2I_9$ with narrow bandgap. *Mater. Des.* **2020**, *193*, 108868.

(32) Ghasemi, M.; Lyu, M.; Roknuzzaman, M.; Yun, J.-H.; Hao, M.; He, D.; Bai, Y.; Chen, P.; Bernhardt, P. V.; Ostrikov, K.; Wang, L., Phenethylammonium bismuth halides: from single crystals to bulky-organic cation promoted thin-film deposition for potential optoelectronic applications. *J. Mater. Chem. A* **2019**, *7*, 20733-20741.

(33) Zhou, L.; Shi, P.-P.; Liu, X.-M.; Feng, J.-C.; Ye, Q.; Yao, Y.-F.; Fu, D.-W.; Li, P.-F.; You, Y.-M.; Zhang, Y.; Xiong, R.-G., An above-room-temperature phosphonium-based molecular ferroelectric perovskite, $[(CH_3)_4P]CdCl_3$, with Sb^{3+}-doped luminescence. *NPG Asia Mater.* **2019**, *11*, 15.

(34) Zhang, H.-Y.; Zhang, Z.-X.; Chen, X.-G.; Song, X.-J.; Zhang, Y.; Xiong, R.-G., Large Electrostrictive Coefficient in a Two-Dimensional Hybrid Perovskite Ferroelectric. *J. Am. Chem. Soc.* **2021**, *143*, 1664-1672.

(35) Zhang, H.-Y.; Chen, X.-G.; Zhang, Z.-X.; Song, X.-J.; Zhang, T.; Pan, Q.; Zhang, Y.; Xiong, R.-G., Methylphosphonium Tin Bromide: A 3D Perovskite Molecular Ferroelectric Semiconductor. *Adv. Mater.* **2020**, *32*, 2005213.

(36) Vijayakanth, T.; Ram, F.; Praveenkumar, B.; Shanmuganathan, K.; Boomishankar, R., Piezoelectric Energy Harvesting from a Ferroelectric Hybrid Salt $[Ph_3MeP]_4[Ni(NCS)_6]$ Embedded in a Polymer Matrix. *Angew. Chem. Int. Ed.* **2020**, *59*, 10368-10373.

(37) Jesse, S.; Mirman, B.; Kalinin, S. V., Resonance enhancement in piezoresponse force microscopy: Mapping electromechanical activity, contact stiffness, and Q factor. *Appl. Phys. Lett.* **2006**, *89*, 022906.

(38) Du, K.-z.; Tu, Q.; Zhang, X.; Han, Q.; Liu, J.; Zauscher, S.; Mitzi, D. B., Two-Dimensional Lead (II) Halide-Based Hybrid Perovskites Templated by Acene Alkylamines: Crystal Structures, Optical Properties, and Piezoelectricity. *Inorg. Chem.* **2017**, *56*, 9291-9302.

(39) Liao, W.-Q.; Zhang, Y.; Hu, C.-L.; Mao, J.-G.; Ye, H.-Y.; Li, P.-F.; Huang, S. D.; Xiong, R.-G., A lead-halide perovskite molecular ferroelectric semiconductor. *Nat. Commun.* **2015**, *6*, 7338.

(40) Sha, T.-T.; Xiong, Y.-A.; Pan, Q.; Chen, X.-G.; Song, X.-J.; Yao, J.; Miao, S.-R.; Jing, Z.-Y.; Feng, Z.-J.; You, Y.-M.; Xiong, R.-G., Fluorinated 2D Lead Iodide Perovskite Ferroelectrics. *Adv. Mater.* **2019**, *31*, 1901843.

(41) Zhang, H.-Y.; Song, X.-J.; Chen, X.-G.; Zhang, Z.-X.; You, Y.-M.; Tang, Y.-Y.; Xiong, R.-G., Observation of Vortex Domains in a Two-Dimensional Lead Iodide Perovskite Ferroelectric. *J. Am. Chem. Soc.* **2020**, *142*, 4925-4931.

(42) Li, M.; Xu, Y.; Han, S.; Xu, J.; Xie, Z.; Liu, Y.; Xu, Z.; Hong, M.; Luo, J.; Sun, Z., Giant and Broadband Multiphoton Absorption Nonlinearities of a 2D Organometallic Perovskite Ferroelectric. *Adv. Mater.* **2020**, *32*, 2002972.

(43) Grinberg, I.; West, D. V.; Torres, M.; Gou, G.; Stein, D. M.; Wu, L.; Chen, G.; Gallo, E. M.; Akbashev, A. R.; Davies, P. K.; Spanier, J. E.; Rappe, A. M., Perovskite oxides for visible-light-absorbing ferroelectric and photovoltaic materials. *Nature* **2013**, *503*, 509-512.

(44) Liu, S.; Zheng, F.; Grinberg, I.; Rappe, A. M., Photoferroelectric and Photopiezoelectric Properties of Organometal Halide Perovskites. *J. Phys. Chem. Lett.* **2016**, *7*, 1460-1465.

(45) Singh, S. K.; Muduli, S.; Dhakras, D.; Pandey, R.; Babar, R.; Singh, A.; Kabra, D.; Kabir, M.; Boomishankar, R.; Ogale, S., High power mechanical energy harvester based on

exfoliated black phosphorous–polymer composite and its multiple applications. *Energy Fuels* **2019**, *3*, 1943-1950.

(46) Singh, S. K.; Kumar, P.; Magdum, R.; Khandelwal, U.; Deswal, S.; More, Y.; Muduli, S.; Boomishankar, R.; Pandit, S.; Ogale, S., Seed Power: Natural Seed and Electrospun Poly(vinyl difluoride) (PVDF) Nanofiber Based Triboelectric Nanogenerators with High Output Power Density. *ACS Appl. Bio Mater.* **2019**, *2*, 3164-3170.

(47) Lee, K. Y.; Kim, D.; Lee, J.-H.; Kim, T. Y.; Gupta, M. K.; Kim, S.-W., Unidirectional High-Power Generation via Stress-Induced Dipole Alignment from $ZnSnO_3$ Nanocubes/Polymer Hybrid Piezoelectric Nanogenerator. *Adv. Funct. Mater.* **2014**, *24*, 37-43.

(48) Saravanakumar, B.; Soyoon, S.; Kim, S.-J., Self-Powered pH Sensor Based on a Flexible Organic–Inorganic Hybrid Composite Nanogenerator. *ACS Appl. Mater. Interfaces* **2014,** *6* (16), 13716-13723.

(49) Jella, V.; Ippili, S.; Yoon, S.-G., Halide (Cl/Br)-Incorporated Organic–Inorganic Metal Trihalide Perovskite Films: Study and Investigation of Dielectric Properties and Mechanical Energy Harvesting Performance. *ACS Appl. Electron. Mater.* **2020,** *2* (8), 2579-2590.

(50) Alam, M. M.; Ghosh, S. K.; Sultana, A.; Mandal, D., Lead-free $ZnSnO_3$/MWCNTs-based self-poled flexible hybrid nanogenerator for piezoelectric power generation. *Nanotechnology* **2015,** *26* (16), 165403.

(51) Arous, M.; Hammami, H.; Lagache, M.; Kallel, A., Interfacial polarization in piezoelectric fibre–polymer composites. *J. Non-Cryst. Solids* **2007**, *353*, 4428-4431.

(52) Ding, R.; Liu, H.; Zhang, X.; Xiao, J.; Kishor, R.; Sun, H.; Zhu, B.; Chen, G.; Gao, F.; Feng, X.; Chen, J.; Chen, X.; Sun, X.; Zheng, Y., Flexible Piezoelectric Nanocomposite Generators Based on Formamidinium Lead Halide Perovskite Nanoparticles. *Adv. Funct. Mater.* **2016**, *26*, 7708-7716.

(53) Deswal, S.; Singh, S. K.; Rambabu, P.; Kulkarni, P.; Vaitheeswaran, G.; Praveenkumar, B.; Ogale, S.; Boomishankar, R., Flexible Composite Energy Harvesters from Ferroelectric A_2MX_4-Type Hybrid Halogenometallates. *Chem. Mater.* **2019,** *31*, 4545-4552.

(54) Deswal, S.; Singh, S. K.; Pandey, R.; Nasa, P.; Kabra, D.; Praveenkumar, B.; Ogale, S.; Boomishankar, R., Neutral 1D Perovskite-Type ABX_3 Ferroelectrics with High Mechanical Energy Harvesting Performance. *Chem. Mater.* **2020,** *32*, 8333-8341.

(55) Zhang, Y.; Wu, M.; Zhu, Q.; Wang, F.; Su, H.; Li, H.; Diao, C.; Zheng, H.; Wu, Y.; Wang, Z. L., Performance Enhancement of Flexible Piezoelectric Nanogenerator via Doping and Rational 3D Structure Design For Self-Powered Mechanosensational System. *Adv. Funct. Mater.* **2019**, *29*, 1904259.

(56) Xu, S.; Hansen, B. J.; Wang, Z. L., Piezoelectric-nanowire-enabled power source for driving wireless microelectronics. *Nat. Commun.* **2010**, *1*, 93.

End of Chapter 4

Chapter 5

Design and Mechanical energy harvesting properties of a new ferroelectric N-methylated aminophosphazenium salt

5.1 Introduction

Ever since the discovery of ferroelectricity in Rochelle salt and KH_2PO_4, ferroelectrics have become a burgeoning class of functional materials.[1,2] They are employed as ferroelectric random-access memories, capacitors, sensors, actuators, electromechanical transducers, field-effect transistors, efficient photovoltaics and as mechanical energy harvesters.[3-8] While the most studied inorganic oxides dominated the commercial market for decades, molecular ferroelectrics were investigated to a considerably lesser extent owing to their low polarization and T_c values.[9-11] However, the growing environmental concerns have escalated the technology interest in molecular ferroelectrics as they contain lightweight elements, exhibit structural tunability, flexibility and easy processability and are environment-friendly in comparison with their inorganic counterparts.[12-17]

Aided by non-covalent interactions, supramolecular chemistry offers a versatile platform for designing new ferroelectric materials with desired functionalities.[18] A wide array of complexes with hydrogen-bonded architectures have been well studied in the past with the demonstration of good ferroelectric attributes.[19-22] However, the targeted synthetic approach to yield of such supramolecular architectures is often challenging owing to the strict requirement of a non-centrosymmetric arrangements of the molecular constituents in the solid state. Thus, engineering intra- and intermolecular interactions and directing the correlated motion of molecules becomes a vital aspect for achieving and tuning ferroelectricity. Hence, there is ongoing research for systematically developing new scaffolds that can crystallize with diverse supramolecular structures along with the possibility of fine tuning their functional properties as desired for a variety of technological applications. One of the most successful strategies to realize polar order in molecular materials is by designing suitable two component systems that can further engage in non-covalent interactions. In this effort, a number of two component systems supported by acyclic cations such as ammonium and phosphonium ions and cyclic cationic scaffolds such as DABCO, pyridinium and quinuclidium ions have been investigated for ferroelectricity in the presence of mono- and polyatomic anions.[16,23-25]

Cyclotriphosphazenes are a versatile class of cyclic inorganic systems. Characterized by a six-membered ring structure of alternating phosphorus and nitrogen atoms with six replaceable Cl atoms on the P atoms, it enables wide array of organic substituents to be attached with multitude of possibilities for derivatization.[26] The hexachlorocyclotriphosphazene can be functionalized with various substituents and can be polymerized to produce a number of functional molecules and materials with desired properties. Endowed with biodegradability and biocompatibility together with richness of functionalization, cyclotriphosphazene derivatives have been favoured for promising applications in antibacterial agents, heterogeneous catalysts, fluorescent dyes and sensors, biomedical materials and flame retardants.[27-33] However, despite significant advancements, ferroelectricity in such hybrid systems has never been explored. Inspired by the ease of their derivatization and their ability to self-assemble into supramolecular arrays, useful for establishing the long range polar order, we envisioned that these cyclic P-N ring compounds can serve as potential platforms for the design of ferroelectric two-component systems.[34] Particularly, by protonating or alkylating the highly basic amino functionalized cyclophosphazenes, it is possible to design two-component systems with acentric crystal symmetry.[35] In addition, the peripheral amino protons of the ring can engage in rich H-bonding interactions with the ring N-atoms and the anionic moieties leading to diverse supramolecular structures ranging from discrete entities to two dimensional sheets.[26,35] Moreover, unlike benzene, phosphazenes can take up both planar and puckered conformations, depending on the substituents on the backbone, and further aid in the stabilization of noncentrosymmetric structures suitable for ferroelectric properties.[35]

Herein, we report the first-ever cyclotriphophazene chemistry enabled generation of a new two-component ferroelectric, $[(PhCH_2NH)_6P_3N_3Me]I$ **([PMe]I)**, crystallized in the polar monoclinic space group *Pc*. Extensive network of classical and non-classical hydrogen bonding among the adjacent phosphazenes and the iodide ions resulted in 2D-network and aids in the stabilization of the long-range polar order in it. Ferroelectric measurements on the compound resulted in a remnant polarization (P_r) value of 5 $\mu C\ cm^{-2}$. Owing to its robust polarization characteristics, the complex was tested for the mechanical energy harvesting application in the form of thermoplastic polyurethane (TPU) composite. The maximum output voltage of 20.1 V_{oc} and the power density

value of 3.2 μW cm^{-2} was recorded for the 20 wt % of **[PMe]I/TPU** device. Finally, the output voltages generated by the device was utilized to charge different electrolytic capacitors, further demonstrating the enormous potential of this class of materials for a range of emerging applications. The study unfolds a hitherto unknown application for the organophosphazenes in the area of non-linear dielectrics and nanogenerators and paves the way to new research.

5.2 Experimental section

5.2.1 General remarks

The starting materials hexachlorocyclotriphosphazene, benzylamine and methyl iodide were purchased from Sigma Aldrich and used without further purification. The thermoplastic polyurethane (TPU) polymer (Elastollan 85 A) was obtained from BASF and used without any treatment. The hexakis(cyclohexylamino)cyclotriphosphazene **(P)** was synthesized according to the literature procedure [26] The NMR spectra were recorded on a Bruker 400 MHz spectrometer ($^{31}P\{^{1}H\}$ NMR: 161.97 MHz) at room temperature using 85% H_3PO_4 as an internal standard reference sample for the experiments. Thermal analysis data was acquired using a PerkinElmer STA6000 thermogravimetric analyzer at a heating rate of 10 °C/min in a nitrogen atmosphere. Differential scanning calorimetry (DSC) measurements were performed on a TA Q20 differential scanning calorimeter (DSC) at heating and cooling rates of 10 °C/min under the nitrogen atmosphere. Powder X-ray diffraction (PXRD) data were measured on a Bruker D8 Advance diffractometer for the polycrystalline samples obtained by grinding the single crystals and for the composite films. The PXRD scans were collected in the 2θ range of 5−50˚ at 2 seconds per degree rate. Melting points were analyzed using an electrothermal melting point apparatus and were uncorrected. FT-IR spectra were recorded on a PerkinElmer spectrophotometer in the ATR mode. The surface morphologies and the thicknesses of the composites were characterized with the help of field-emission scanning electron microscopy (Zeiss ultra plus FESEM instrument). Kurtz and Perry's method was utilized to measure the second harmonic generation (SHG) effect on the powder unsieved sample. Q-switch Nd:yttrium aluminum garnet laser generated the fundamental wavelength of 1064 nm. Powdered potassium dihydrogen phosphate (KDP) was used as a reference.

5.2.2 Synthesis of N-methyl hexakis(cyclohexylamino) cyclotriphosphazenium Iodide ([PMe]I)

To a stirred solution of **P** in toluene at room temperature was added excess of methyl iodide (> 2 mol eq.). The solution was then refluxed for a period of 24 hrs, which resulted in the formation of white precipitate upon cooling. The obtained precipitate was subsequently dissolved in methanol and kept for crystallization (Scheme 5.1). Colourless plate like crystals suitable for X-ray diffraction analysis were obtained after a week. Yield 80%. M.P. 185-187˚C. $^{31}P\{^{1}H\}$ NMR (162 MHz, $CDCl_3$) δ 11.68 (t), 14.99 (d). HRMS (ESI) m/z calculated for $C_{43}H_{51}N_9P_3(M)^+$: 786.3475, Observed: 786.3488. FT-IR (cm^{-1}): 953, 1091, 1147, 1386, 1457, 2410, 2467, 2714, 2820, 2904, 2957, 3731, 3840. Anal. Calcd.: C 56.52; H 5.63; N 13.80. Found: C 56.62; H 5.59; N 13.88.

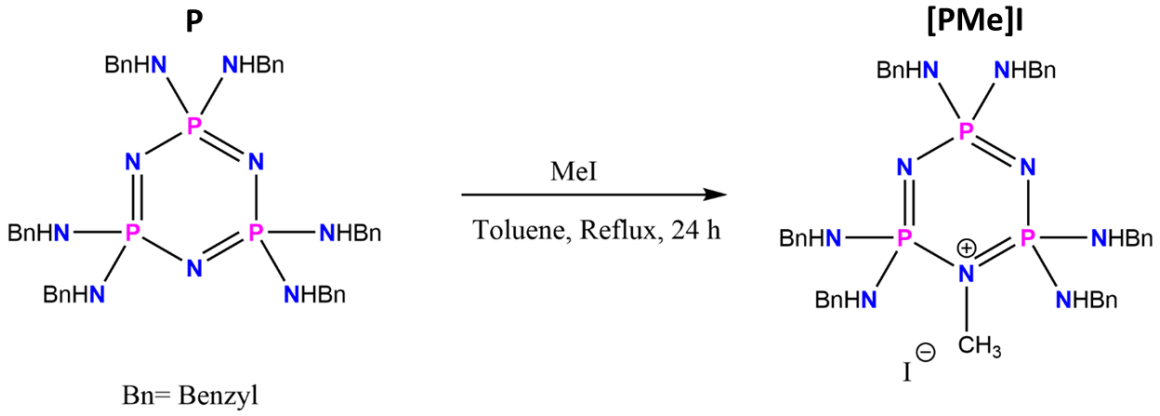

Scheme 5.1. Schematic for the preparation of **[PMe]I.**

5.2.3 Crystallography: Reflections for **[PMe]I** was collected on a Bruker Smart Apex Duo diffractometer at various temperatures using Mo Kα radiation (λ = 0.71073 Å). Crystal structures were solved using the direct method and then refined by full-matrix least squares against F^2 using SHELXL-2014/7 built in the Apex 3 program.[36] All the nonhydrogen atoms were refined anisotropically while the hydrogen atoms were constrained in geometric positions to their parent atoms.[37] One of the phosphazene rings and three benzyl groups attached to it are disordered. The atom fragments of the disordered moieties were refined with similar distances and similar U-restraints. The

crystallographic data for the compounds are listed in Table 5.1 and the selected bond lengths and angles are listed in Table 5A.1(Appendix 5).

Table 5.1: Details of crystallographic data of [PMe]I.

Compound	[PMe]I (120 K)	[PMe]I (298 K)
Chemical formula	C_{86} H_{102} I_2 N_{18} P_6	C_{86} H_{102} I_2 N_{18} P_6
Formula weight	1827.47	1827.47
Temperature	120(2) K	298(2) K
Crystal system	Monoclinic	Monoclinic
Space group	*Pc*	*Pc*
a(Å): α(°)	14.5949(18); 90	14.936(12); 90
b(Å); β(°)	30.127(4); 95.229(4)	30.70(2); 96.29
c (Å); γ (°)	19.564(2); 90	20.058(15); 90
V(Å^3); Z	8566.6(18); 4	9143(12); 4
P(calc.) mg m^{-3}	1.417	1.253
μ(Mo K_α)mm^{-1}	0.902	0.843
$2\theta_{max}$ (°)	50.05	56.57
R (int)	0.1009	0.1124
Completeness to θ	100	99.7
Data/param.	30154/ 1995	42532/ 1741
GOF	1.184	1.025
R1[F>4σ(F)]	0.0792	0.0846
wR2 (all data)	0.1767	0.2726
max. peak/hole (e.Å^{-3})	1.760/ -1.461	1.169/ -1.091

5.2.4 Fabrication of hybrid composite mechanical energy harvester: The polymer composite films were prepared by solution casting method at room temperature. First, a known quantity of TPU was dissolved in DMF at 100˚C by continuous stirring till a clear solution was formed. Predetermined quantities of ferroelectric crystallites were then added to the TPU solution and the mixture was allowed to stir continuously at 100˚C for 8 hours. The obtained homogeneous composite mixture was eventually drop casted onto Al wrapped PET sheet and finally cured at 100˚C in an oven. Al electrode was then integrated to the cured composite as the top electrode. Finally, the whole device was laminated with Kapton Tape to achieve electrical isolation and to enhance the device mechanical robustness. The thickness and the effective size of the as fabricated devices are ~0.31 mm and 1.7 X 1.5 cm^2, respectively.

5.2.5 Dielectric measurements: The dielectric data for **[PMe]I** was measured using the Solartron Analytical Impedance Analyzer 1260 coupled with a Dielectric Interface

1296A operating with a Janis 129610A cryostat sample holder and a Lakeshore 336 model temperature controller. The powder sample of **[PMe]I** was compacted in the form of circular discs and aluminium adhesive foils were applied as top and bottom electrodes to the compacted discs for the dielectric measurements.

5.2.6 Ferroelectric measurements: The ferroelectric hysteresis loop was recorded on the thin film sample of **[PMe]I** by using a Sawyer-Tower circuit setup. A chemical solution procedure was employed for preparing the thin film of the compound. A solution of DMF containing **[PMe]I** was drop casted on Al sheet acting as the bottom electrode. The drop casted sample was then heated in oven at 70˚ C for 5 hours after which Al adhesive tape was assimilated as the top electrode. The polarization measurements were performed by using an aixACCT TF-2000E model hysteresis loop analyzer. Leakage currents were measured dynamically for varied voltage steps in the course of the hysteresis loop measurements.

5.2.7 Mechanical Energy Harvesting measurements: For evaluating the mechanical energy-harvesting performance of the thin-film device of **[PMe]I,** a home-built vertical impact force setup operating at a periodic compression and release function coupled with a digital multimeter was used. The fabricated devices were subjected to an impact force of 40 N with a tapping frequency of 20 Hz on an active area of 1.7 X 1.5 cm^2. The output voltage measurement was recorded on a Keithley DMM7510 7.5 multimeter at an input impedance of 10 MΩ.

5.3 Results and discussion

5.3.1 Synthesis, characterization and crystal structure: The molecular hybrid $[(PhCH_2NH)_6P_3N_3Me]I$ **[PMe]I** was synthesized from Hekakis(benzylamino)cyclotriphosphazene $(PhCH_2NH)_6P_3N_3$ **(P)** as depicted in Scheme 5.1. The ^{31}P-NMR of the precursor P shows singlet at 17.53 ppm (Figure 5A.1, Appendix 5). Upon the ring N-alkylation, the P-atoms of the heterocycle becomes non-equivalent and gives rise to two signals, a triplet and a doublet centred at 11.68 and 14.99 ppm, respectively, (Figure 5A.2, Appendix 5). Further, N-alkylated product (**[PMe]I)** displays an extra added mass of a methyl group in comparison to its parent precursor **P** (See Section 5.2.2). Colourless crystals of **[PMe]I** were obtained from the slow evaporation of its methanolic solution at room temperature The single

crystal X-ray diffraction analysis reveals that the compound crystallizes in polar monoclinic space group *Pc*, which corresponds to one of the 10 polar point groups suitable for ferroelectricity (Table 5.1).

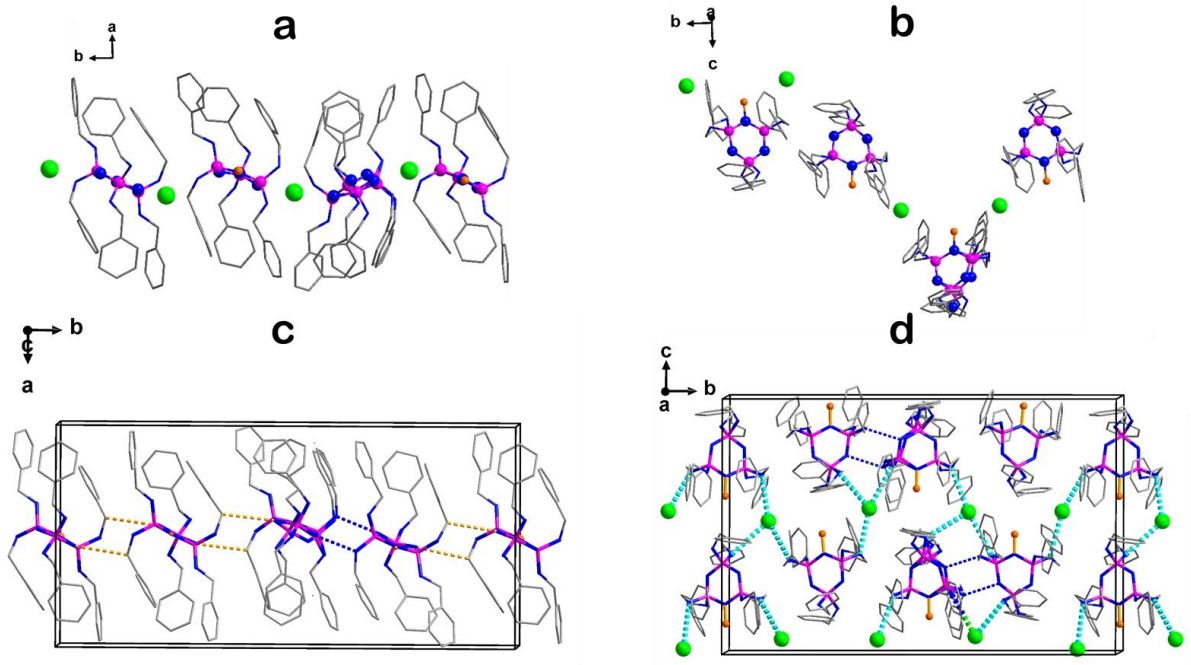

Figure 5.1: *(a) Asymmetric unit of* ***[PMe]I*** *viewed down (a) c- and (b) a-axes displaying disordered benzylic substituents in one phophazenium unit (c) One dimensional polymeric chain of hydrogen bonded phosphazenium cations and (d) their interlinking with the iodide ions to generate a 2D supramolecular arrangement along b axis. The protons of the amino groups have been omitted for clarity.*

The asymmetric unit features four crystallographically independent molecules comprised of N-methylphospazenium cations and iodide anions (Figures 5.1a-b). The P-N (alkyl) bonds in the compound are found to be 1.697(12) Å and 1.661 (12) Å and are noticeably larger than the neighbouring P-N bonds, in accord with the similar N-alkylated systems reported in the literature (Table 5A.1, Appendix 5).[35] This suggests that the elongation of P-N bonds caused by alkylation is compensated by some distinctive shortening of adjoining P-N bonds. Moreover, P-N-P angles associated with the alkylated and non-alkylated N atoms measure 126.28˚ and 115.22˚ respectively, indicating the puckered nature of the ring. Interestingly, among the existing unique

discrete molecules, part of one phosphazenium ring including three benzylic substituents are highly disordered (Figures 5.1a-b).

A closer inspection at the crystal structure reveals the formation of supramolecular arrangement that holds these individual strands together. Of the four independent molecules, only two of them are involved in NH···N bonds yielding a H-bonded dimer. The distances between the other motifs are too far for hydrogen bonding (N···N > 4 A), however, they are connected by close CH···N interactions between benzylic protons and N-ring atoms (Figure 5.1c). This generates one dimensional polymeric chain of hydrogen-bonded phosphazenium cations, which get further interlinked with I¯anions to render a 2D supramolecular arrangement (Figure 5.1d). The unhindered rotation of the exocyclic P-N bonds and the benzylic substituent employed assists in the generation of the noncentrosymmetric arrangement of the molecule in the crystal structure.

The bulk phase purity of **[PMe]I** was established by Powder X-ray diffraction (PXRD) measurements. The obtained experimental PXRD profiles reflect a good match with the respective simulated profile drawn from its single-crystal structure at 298 K (Figure 5A.3, Appendix 5). The non-centrosymmetric packing of **[PMe]I** was further confirmed by its second harmonic generation efficiency of 0.17 with respect to standard KDP on its powdered unsieved sample at room temperature. This indicates the distinct orientation of benzyl groups playing a critical role in imparting asymmetricity to the system. Moreover, the compound exhibits high thermal stability up to 526 K as identified by thermogravimetric analysis data (Figure 5A.4, Appendix 5). Differential scanning calorimetry profiles displays prominent peaks only due to its melting points corroborating well with the SCXRD analysis (Figure 5A.5, Appendix 5). The high structural stability of **[PMe]I** stem from the extensive intermolecular networking mediated by classical as well as non-classical hydrogen bonding in the solid state. Retention of ferroelectric ordered state for such a wide range of temperatures make **[PMe]I** highly suitable for harsh working environments.

5.3.2 Ferroelectric and dielectric studies

The potential ferroelectric nature of **[PMe]I** was investigated by performing Polarization vs Electric field (*P-E*) measurements on its thin film sample using the Sawyer-Tower

Circuit. The measurements manifested a well resolved rectangular hysteresis loop at an operating frequency of 0.01 Hz (Figure 5.2a). Reasonably good remnant polarization value of 5 μC cm^{-2} was obtained for the sample at room temperature**.** The attained value is comparable with the polarizations reported for various other emerging hybrid molecular ferroelectric materials.[38-43] The leakage current density plots of **[PMe]I** measured along the *P-E* loop exhibits two opposite peaks, signifying two stable states of opposite polarizations and thereby supports the ferroelectric nature of the obtained loops.

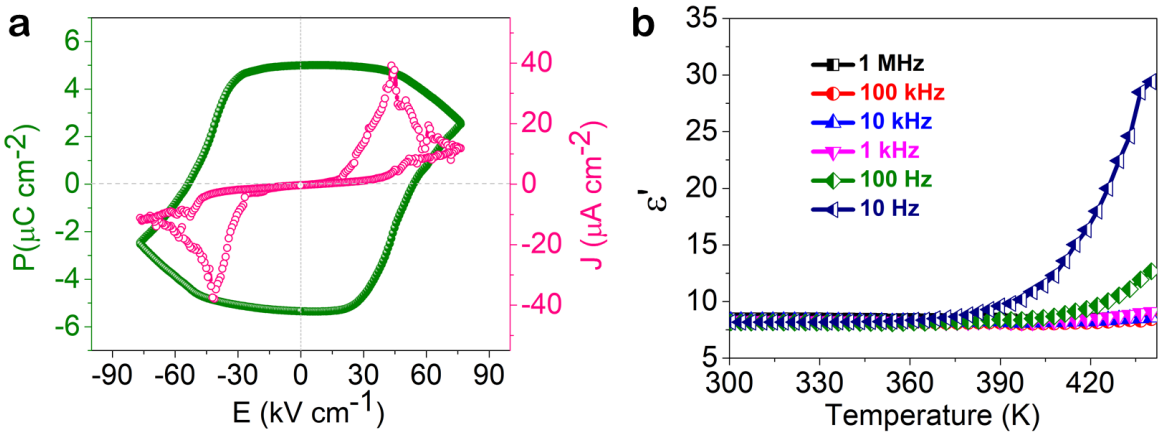

Figure 5.2: *(a) P-E hysteresis loop and leakage current density plot of* ***[PMe]I*** *film measured at room temperature. (b) Temperature-dependent real part of dielectric permittivity (ε') of* ***[PMe]I*** *at various frequencies.*

To gain deeper insights into any phase transitions occurring in the compound, dielectric response as a function of temperature was investigated on its compacted pellet at various frequencies. No noticeable anomalies as evidenced from the real part of the complex dielectric permittivity substantiates the absence of phase transitions in the compound as evident from the temperature dependant Single crystal X-ray diffraction and DSC analysis (Figure 5.2b). However, a significant rise in the ε′ values is witnessed above 360 K, which stems from the presence of more polarizable domains and enhanced ionic conductivity in the compound closer to its melting point. A maximum ε′ value of 8.2 was obtained at room temperature for **[PMe]I** at 1 kHz. Moreover, the compound displays considerably low dielectric loss factors (tan δ) as observed from its

electrical energy dissipation, which mirrors the observed trends in the temperature vs. ε′ plot (Figure 5A.6, Appendix 5). Similar trends were observed from Frequency-dependent ε′ and tan δ plots with varying temperatures (Figures 5A.7-5A.8, Appendix 5). Also, the noticeable increase in the dielectric constant value with decreasing frequency suggests the contribution of all four polarization mechanisms at lower frequencies.

5.3.3 Mechanical Energy Harvesting Applications

Propelled by the excellent dielectric, ferroelectric and piezoelectric properties exhibited by **[PMe]I**, we set out to explore its efficacy towards mechanical energy harvesting devices. For these studies, polymer composites with varying weight percentages (wt%)

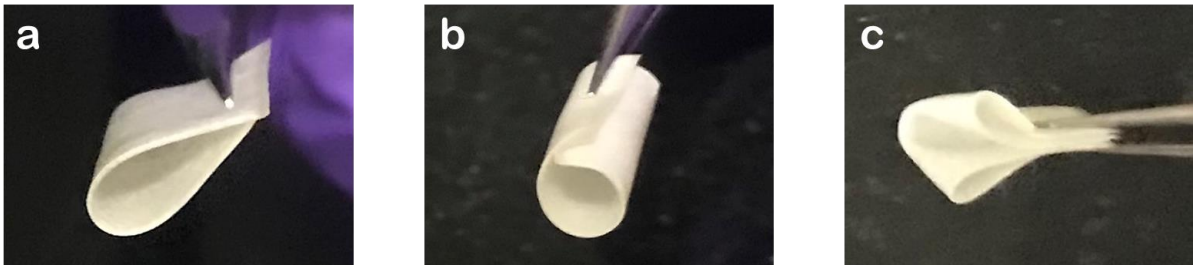

Figure 5.3: *Photographs of flexible 20 wt% **[PMe]I/TPU** composite film exhibiting (a) bending (b) rolling and (c) folding operations.*

were prepared by independently dissolving **[PMe]I** in suitable quantities into a homogeneous solution containing thermoplastic polyurethane (TPU) in DMF (Table 5A.2, Appendix 5). All of the formulated composites exhibited excellent mechanical flexibility as presented in Figure 5.3. The microstructure of the composite films was studied by PXRD, which revealed the presence of crystalline composite layers. A rise in the PXRD peak intensities is evident upon increasing the loading of the ferroelectric crystallites in the composite films (Figure 5A.9, Appendix 5). The surface morphologies of the composite films were probed by SEM, which indicated the random distribution of the ferroelectric crystallites in the polymer matrix (Figure 5A.10, Appendix 5). From the cross-sectional SEM image, the thickness of the composite films was found to be 0.31 mm. Evidently, the film exhibits a compact sandwich structure along with the Al-electrodes (Figure 5A.11, Appendix 5).

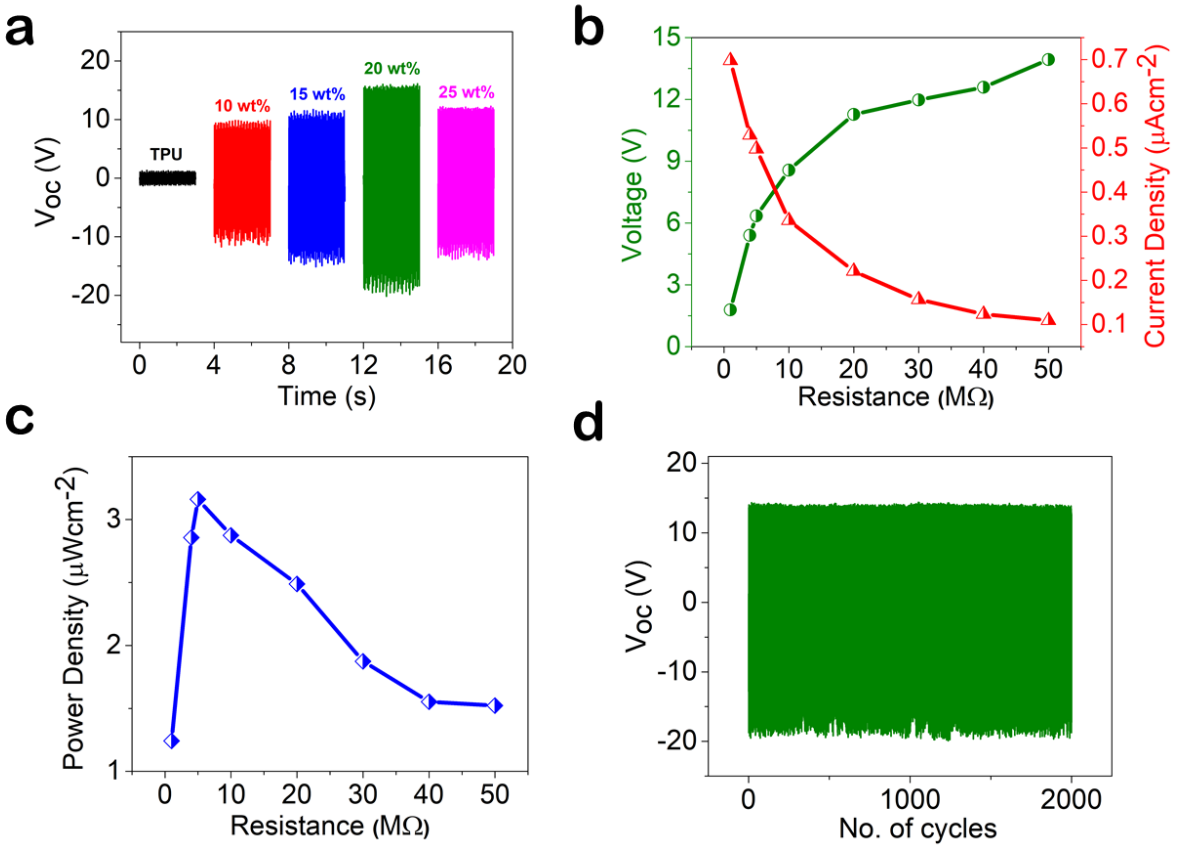

Figure 5.4: *(a) Comparative output voltage performance of all wt% **[PMe]I /TPU** composite devices with a shifted time axis. (b) Voltage, current density, (c) and power density plots as a function of load resistance corresponding to the 20 wt% **[PMe]I /TPU** device. Lines are drawn to guide the eyes. (d) Mechanical durability test performed on the 20 wt % **[PMe]I /TPU** device with an applied force of 40 N and frequency of 20 Hz.*

Piezoelectric energy harvesting experiments were performed by applying a periodic compressive force directly on the as-prepared device using a home-built vertical impact set up coupled with a digital multimeter.[44] The open-circuit voltages (V_{oc}) were recorded for all the devices of **[PMe]I/TPU** under a constant force of 40 N at a frequency of 20 Hz. The measured V_{oc} exhibits a strong correlation with the concentration of the ferroelectric particles present in the composite. As the particle concentration increases from 10 to 20 wt %, for **[PMe]I/TPU**, the V_{oc} increases from 8.5 to 20.1 V (Figure 5.4a). The noteworthy improvements in the output performances of the devices can be attributed to the enhanced piezoelectricity of the composites, which stems from Maxwell-Sillars polarization developing at the interfaces between

the ferroelectric fillers and the bulk polymer.[45-46] The lower performance of the 25 wt% composite is most likely attributed to the agglomeration of the ferroelectric crystallites, which hinders the alignment of electric dipoles at longer range. This eventually weakens the electromechanical coupling effect and polarizability in the composite ferroelectric films.

The output characteristics of the best performing 20 wt% device was further evaluated over a wide range of load resistances ranging from 1 to 50 MΩ. The output voltage is found to increase sharply and then saturates with increasing resistance. As expected, an opposite trend is observed for the output current with increasing load resistances (Figure 5.4b). A maximum power density (PD) value of 3.2 μW cm^{-2} was recorded at an optimal load of 5 MΩ for the device based on 20 wt % **[PMe]I/TPU** (Figure 5.4c)**.** Furthermore, mechanical durability tests performed on the optimized device (20 wt % **[PMe]I /TPU**) reveals no degradation in signal amplitude even after 2000 cycles of continuous impact with an applied force of 40 N at a frequency of 20 Hz (Figure 5.4d).

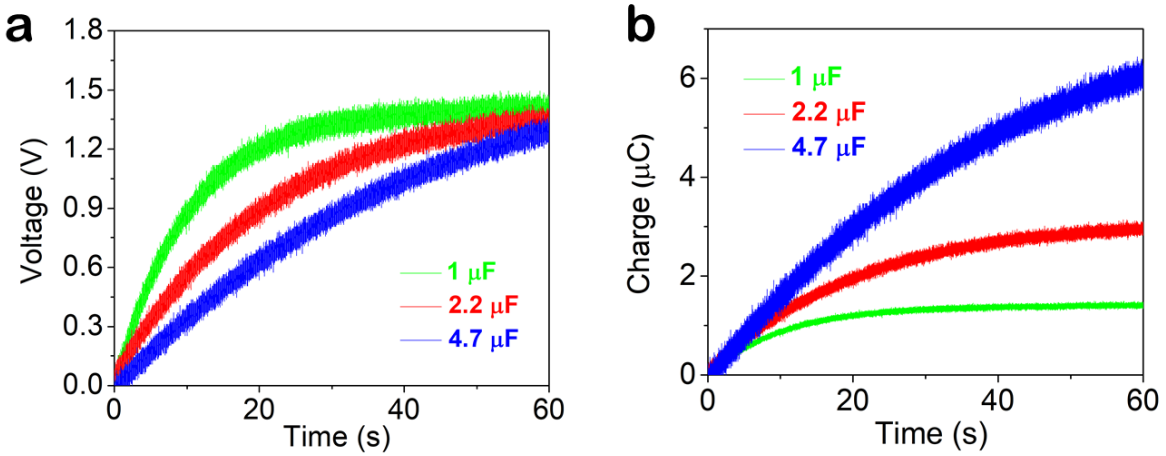

Figure 5.5: *(a) Capacitor charging traces and (b) the plot of accumulated charges data for the capacitors with varied capacitance values employing the 20 wt % **[PMe]I/TPU** as a piezoelectric power source.*

To demonstrate the practical utility of the fabricated composites, the electricity generated from the optimized **[PMe]I/TPU** device was directly applied to charge aluminium electrolytic capacitors using a full-wave bridge rectifier circuit. As observed from the charging curves in Figure 5.5a, the 20 wt% **[PMe]I/TPU** device was found to

charge the 1.1, 2.2 and 4.7 µF capacitors within 60s with the maximum accumulated voltages of 1.44, 1.37 and 1.29 V, respectively. The stored electrical energies (µJ) and the measured charges (µC) corresponding to 1.1, 2.2 & 4.7µF capacitors were computed to be 1.0, 2.1 & 3.9 µJ and 1.44, 3.0 & 6.1 µC for the 20 wt% **[PMe]I/TPU** (Figure 5.5b). From these experiments, it is evident that devices based on the hybrid phosphazenes polymeric composites can serve as promising electrical sources for low power electronic circuits and systems.

5.4 Conclusion

In summary, a newly designed two-component ferroelectric consisting of N-methyl phosphazenium cation and Iodide ions was synthesized and examined for ferroelectric properties and subsequently used in mechanical energy harvesting devices. The compound was crystallized in polar space group *Pc* and the ferroelectric measurements on its thin-film sample displayed a remnant polarization value of 5 μC cm^{-2} at room temperature. Moreover, its potential application for energy harvesting devices was studied in the form of TPU composites. A maximum V_{oc} of 20.1 V and the highest power density of 3.2 μW cm^{-2} was obtained from 20 wt% **[PMe]I/TPU** composite. The electricity generated was subsequently utilized to charge an external capacitor further illustrates the tremendous potential of these novel supramolecular ferroelectrics for use in self-powered electronics. Organophosphazenes are versatile synthons, and this work lays the foundation for exploring them in the design of robust two-component supramolecular arrays for ferroelectric nanogenerators and beyond.

5.5 References

(1) Valasek, J., Piezo-Electric and Allied Phenomena in Rochelle Salt. *Phys. Rev.* **1921,** *17*, 475-481.

(2) Busch, G.; Scherrer, P., Eine neue seignette-elektrische Substanz. *Naturwissenschaften* **1935,** *23*, 737.

(3) Scott, J. F., Applications of Modern Ferroelectrics. *Science* **2007,** *315*, 954-959.

(4) Ye, Z.-G., Handbook of Advanced Dielectric, Piezoelectric and Ferroelectric Materials: Synthesis, Properties and Applications; Elsevier, 2008.

(5) Park, B. H.; Kang, B. S.; Bu, S. D.; Noh, T. W.; Lee, J.; Jo, W., Lanthanum-substituted bismuth titanate for use in non-volatile memories. *Nature* **1999**, *401*, 682-684.

(6) Yang, S. Y.; Seidel, J.; Byrnes, S. J.; Shafer, P.; Yang, C. H.; Rossell, M. D.; Yu, P.; Chu, Y. H.; Scott, J. F.; Ager, J. W.; Martin, L. W.; Ramesh, R., Above-bandgap voltages from ferroelectric photovoltaic devices. *Nat. Nanotech.* **2010**, *5*, 143-147.

(7) Hoffman, J.; Pan, X.; Reiner, J. W.; Walker, F. J.; Han, J. P.; Ahn, C. H.; Ma, T. P., Ferroelectric Field-Effect Transistors for Memory Applications. *Adv. Mater.* **2010**, *22*, 2957-2961.

(8) Bowen, C. R.; Kim, H. A.; Weaver, P. M.; Dunn, S., Piezoelectric and ferroelectric materials and structures for energy harvesting applications. *Energy Environ. Sci.* **2014**, *7*, 25-44.

(9) Haertling, G. H., Ferroelectric Ceramics: History and Technology. *J. Am. Ceram. Soc.* **1999**, *82*, 797-818.

(10) Goossens, D. J., Local Ordering in Lead-Based Relaxor Ferroelectrics. *Acc. Chem. Res.* **2013,** *46*, 2597-2606.

(11) Damjanovic, D., Ferroelectric, dielectric and piezoelectric properties of ferroelectric thin films and ceramics. *Rep. Prog. Phys.* **1998**, *61*, 1267-1324.

(12) Zhang, W.; Xiong, R.-G., Ferroelectric Metal–Organic Frameworks. *Chem. Rev.* **2012,** *112*, 1163-1195.

(13) Li, W.; Wang, Z.; Deschler, F.; Gao, S.; Friend, R. H.; Cheetham, A. K., Chemically diverse and multifunctional hybrid organic–inorganic perovskites. *Nat. Rev. Mater.* **2017,** *2*, 16099.

(14) Tang, Y.-Y.; Li, P.-F.; Liao, W.-Q.; Shi, P.-P.; You, Y.-M.; Xiong, R.-G., Multiaxial Molecular Ferroelectric Thin Films Bring Light to Practical Applications. *J. Am. Chem. Soc.* **2018,** *140*, 8051-8059.

(15) Zhang, H.-Y.; Tang, Y.-Y.; Shi, P.-P.; Xiong, R.-G., Toward the Targeted Design of Molecular Ferroelectrics: Modifying Molecular Symmetries and Homochirality. *Acc. Chem. Res.* **2019**, *52*, 1928-1938.

(16) Liu, H.-Y.; Zhang, H.-Y.; Chen, X.-G.; Xiong, R.-G., Molecular Design Principles for Ferroelectrics: Ferroelectrochemistry. *J. Am. Chem. Soc.* **2020**, *142*, 15205-15218.

(17) Hou, Y.; Wu, C.; Yang, D.; Ye, T.; Honavar, V. G.; Duin, A. C. T. v.; Wang, K.; Priya, S., Two-dimensional hybrid organic–inorganic perovskites as emergent ferroelectric materials. *J. Appl. Phys.* **2020**, *128*, 060906.

(18) Tayi, A. S.; Kaeser, A.; Matsumoto, M.; Aida, T.; Stupp, S. I., Supramolecular ferroelectrics. *Nat. Chem.* **2015,** *7*, 281-294.

(19) Horiuchi, S.; Kumai, R.; Tokura, Y., Hydrogen-bonded donor–acceptor compounds for organic ferroelectric materials. *Chem. Commun.* **2007,** 23, 2321-2329.

(20) Kumai, R.; Horiuchi, S.; Sagayama, H.; Arima, T.-h.; Watanabe, M.; Noda, Y.; Tokura, Y., Structural Assignment of Polarization in Hydrogen-Bonded Supramolecular Ferroelectrics. *J. Am. Chem. Soc.* **2007,** *129* (43), 12920-12921.

(21) Horiuchi, S.; Kumai, R.; Tokura, Y., High-Temperature and Pressure-Induced Ferroelectricity in Hydrogen-Bonded Supramolecular Crystals of Anilic Acids and 2,3-Di(2-pyridinyl)pyrazine. *J. Am. Chem. Soc.* **2013,** *135* (11), 4492-4500.

(22) Kobayashi, K.; Horiuchi, S.; Ishibashi, S.; Kagawa, F.; Murakami, Y.; Kumai, R., Structure–Property Relationship of Supramolecular Ferroelectric [H-66dmbp][Hca] Accompanied by High Polarization, Competing Structural Phases, and Polymorphs. *Chem. Eur. J.* **2014,** *20* (52), 17515-17522.

(23) Vijayakanth, T.; Srivastava, A. K.; Ram, F.; Kulkarni, P.; Shanmuganathan, K.; Praveenkumar, B.; Boomishankar, R., A Flexible Composite Mechanical Energy Harvester from a Ferroelectric Organoamino Phosphonium Salt. *Angew. Chem. Int. Ed.* **2018,** *130* (29), 9192-9196.

(24) Vijayakanth, T.; Ram, F.; Praveenkumar, B.; Shanmuganathan, K.; Boomishankar, R., All-Organic Composites of Ferro-and Piezoelectric Phosphonium Salts for Mechanical Energy Harvesting Application. *Chem. Mater.* **2019,** *31* (15), 5964-5972.

(25) Vijayakanth, T.; Ram, F.; Praveenkumar, B.; Shanmuganathan, K.; Boomishankar, R., Piezoelectric Energy Harvesting from a Ferroelectric Hybrid Salt $[Ph_3MeP]_4$ $[Ni(NCS)_6]$ Embedded in a Polymer Matrix. *Angew. Chem. Int. Ed.* **2020,** *59* (26), 10368-10373.

(26) Bickley, J. F.; Bonar-Law, R.; Lawson, G. T.; Richards, P. I.; Rivals, F.; Steiner, A.; Zacchini, S., Supramolecular variations on a molecular theme: the structural diversity of phosphazenes $(RNH)_6P_3N_3$ in the solid state. *Dalton Trans.* **2003,** (7), 1235-1244.

(27) Su, X.; Wang, L.; Xie, J.; Liu, X.; Tomás, H., Cyclotriphosphazene-based derivatives for antibacterial applications: an update on recent advances. *Curr. Org. Chem.* **2021,** *25* (2), 301-314.

(28) Yang, S.; Zhu, Y.; Cao, C.; Peng, L.; Li, S.; Zhai, D.; Song, W., A general route to coat poly (cyclotriphosphazene-co-4, 4′-sulfonyldiphenol) on various substrates and the derived N, P, S-doped hollow carbon shells for catalysis. *Nanoscale* **2017,** *9* (36), 13538-13545.

(29) Liu, P.; Wang, L.; Yang, Y.; Qu, Y.; Ming, L.-J., Recent advances of cyclotriphosphazene derivatives as fluorescent dyes. *Dyes Pigm.* **2021**, 109214.

(30) Çetindere, S.; Tümay, S. O.; Kılıç, A.; Durmuş, M.; Yeşilot, S., Hexa-BODIPY Linked-Triazole Based on a Cyclotriphosphazene Core as a Highly Selective and Sensitive Fluorescent Sensor for Fe^{2+} Ions. *J. Fluoresc.* **2016,** *26* (4), 1173-1181.

(31) Wang, L.; Yang, Y.-X.; Shi, X.; Mignani, S.; Caminade, A.-M.; Majoral, J.-P., Cyclotriphosphazene core-based dendrimers for biomedical applications: an update on recent advances. *J. Mater. Chem. B* **2018,** *6* (6), 884-895.

(32) Steiner, A., 20 Supramolecular Structures of Cyclotriphosphazenes. *Polyphosphazenes for Biomedical Applications* **2009**, 411.

(33) Dutkiewicz, M.; Przybylak, M.; Januszewski, R.; Maciejewski, H., Synthesis and flame retardant efficacy of hexakis (3-(triethoxysilyl) propyloxy) cyclotriphosphazene/silica coatings for cotton fabrics. *Polym. Degrad. Stab.* **2018,** *148*, 10-18.

(34) Uslu, A.; Yeşilot, S., Recent advances in the supramolecular assembly of cyclophosphazene derivatives. *Dalton Trans.* **2021,** *50* (7), 2324-2341.

(35) Benson, M. A.; Zacchini, S.; Boomishankar, R.; Chan, Y.; Steiner, A., Alkylation and Acylation of Cyclotriphosphazenes. *Inorg. Chem.* **2007,** *46* (17), 7097-7108.

(36) Sheldrick, G. M. *Acta Crystallogr., Sect. A* **2008,** *64*, 112–122.

(37) Spek, A. L. *Acta Crystallogr., Sect. D* **2009**, *D65*, 148–155.

(38) Song, X.-J.; Zhang, T.; Gu, Z.-X.; Zhang, Z.-X.; Fu, D.-W.; Chen, X.-G.; Zhang, H.-Y.; Xiong, R.-G., Record Enhancement of Curie Temperature in Host-Guest Inclusion Ferroelectrics. *J. Am. Chem. Soc.* **2021,** *143* (13), 5091-5098.

(39) Huang, C.-R.; Li, Y.; Xie, Y.; Du, Y.; Peng, H.; Zeng, Y.-L.; Liu, J.-C.; Xiong, R.-G., The First High-Temperature Supramolecular Radical Ferroics. *Angew. Chem. Int. Ed.* **2021,** *60* (30), 16668-16673.

(40) Zhang, H.-Y.; Zhang, Z.-X.; Chen, X.-G.; Song, X.-J.; Zhang, Y.; Xiong, R.-G., Large Electrostrictive Coefficient in a Two-Dimensional Hybrid Perovskite Ferroelectric. *J. Am. Chem. Soc.* **2021,** *143* (3), 1664-1672.

(41) Chen, X.-G.; Song, X.-J.; Zhang, Z.-X.; Zhang, H.-Y.; Pan, Q.; Yao, J.; You, Y.-M.; Xiong, R.-G., Confinement-Driven Ferroelectricity in a Two-Dimensional Hybrid Lead Iodide Perovskite. *J. Am. Chem. Soc.* **2020,** *142* (22), 10212-10218.

(42) Deswal, S.; Singh, S. K.; Pandey, R.; Nasa, P.; Kabra, D.; Praveenkumar, B.; Ogale, S.; Boomishankar, R., Neutral 1D Perovskite-Type ABX_3 Ferroelectrics with High Mechanical Energy Harvesting Performance. *Chem. Mater.* **2020**, *32*, 8333-8341.

(43) Deswal, S.; Singh, S. K.; Rambabu, P.; Kulkarni, P.; Vaitheeswaran, G.; Praveenkumar, B.; Ogale, S.; Boomishankar, R., Flexible Composite Energy Harvesters from Ferroelectric A_2MX_4-Type Hybrid Halogenometallates. *Chem. Mater.***2019**, *31*, 4545-4552.

(44) Singh, S. K.; Muduli, S.; Dhakras, D.; Pandey, R.; Babar, R.; Singh, A.; Kabra, D.; Kabir, M.; Boomishankar, R.; Ogale, S., High power mechanical energy harvester based on

exfoliated black phosphorous–polymer composite and its multiple applications. *Sustain. Energy Fuels* **2019**, *3*, 1943-1950.

(45) Lee, K. Y.; Kim, D.; Lee, J.-H.; Kim, T. Y.; Gupta, M. K.; Kim, S.-W., Unidirectional High-Power Generation via Stress-Induced Dipole Alignment from $ZnSnO_3$ Nanocubes/Polymer Hybrid Piezoelectric Nanogenerator. *Adv. Funct. Mater.* **2014**, *24*, 37-43.

(46) Arous, M.; Hammami, H.; Lagache, M.; Kallel, A., Interfacial polarization in piezoelectric fibre–polymer composites. *J. Non-Cryst. Solids* **2007**, *353*, 4428-4431.

End of Chapter 5

Chapter 6

Thesis Conclusion and Future Perspectives

In summary, this thesis describes the synthesis of non-centrosymmetric polar ferroelectric molecules derived from diverse ammonium, phosphonium and alkylated-phosphazenium hybrid salts and their application for mechanical energy harvesting devices.

In the first part of the thesis, we explored discrete hybrid hallogenometallates of the A_2MX_4 type by engaging a quasi-spherical approach. The variation of alkyl groups on the flexible benzyl functionalized ammonium cations on the A site played a pivotal role in imparting asymmetricity to the system. Interestingly, the methylated and propylated derivatives of the cations successfully yielded the ferroelectric ordered state, while the ethylated product crystallized in centrosymmetric structure at room temperature. Their subsequent deployment for piezoelectrical energy harvesting furnished very high open-circuit voltages, presenting a significant step towards realizing next-generation self-powered electronics (Chapter 2).

In another work, we have rationally designed and synthesized an unusual neutral perovskite-type hybrid ferroelectric ABX_3 compound. Unlike the prototype 1D perovskites containing face-sharing infinite metal-halide octahedra and discrete cations, this compound featured a 1D structure of edge-sharing $CdCl_5O$ octahedra that was closely positioned to its cation via OH···Cl interactions. Facilitated by a long-range ordering of the cations and anions along the polar axis, the compound displayed remarkably high polarization values. Piezoelectric energy harvesting experiments conducted using the polymeric composites demonstrated exceedingly high output power density among the well known reported hybrid ferroelectrics (Chapter 3).

In Chapter 4, we explored and designed a new phosphonium based discrete perovskite like hybrid ferroelectric based on a relatively less toxic bismuth anionic framework. Besides good ferroelectric and piezoelectric attributes, the compound demonstrated intriguing semiconducting behaviour opening enormous possibilities for the design of multifunctional devices.

Finally, in the last chapter, for the very first time, we demonstrated a metal-free hybrid ferroelectric derived from N-methyl phosphazenium cation and Iodide ion. The interplay of classical and non-classical hydrogen bonding enabled the generation of a

new two-component ferroelectric salt in which the long-range order is restored by the presence of supramolecular forces. Furthermore, flexible composites were fabricated for mechanical energy harvesting applications using the thermoplastic polyurethane as the matrix. The optimal device resulted in a good output performance in comparison with the known best-performing metal-free systems. Finally, the electricity generated was subsequently utilized to charge an external capacitor, further illustrating the tremendous potential of these novel supramolecular ferroelectrics for use in self-powered electronics (Chapter 5).

The electromechanical responses of some of the composite devices reported in the thesis are of immense interest for academic researchers and, to some extent, outperforms several well-known hybrid ferroelectrics. The present thesis also addresses many crucial factors related to hybrid perovskite like ferroelectrics in terms of the stability of structures and the retention of mechanical output performance.

Even though the output characteristics of cadmium containing composite devices are highly encouraging, their toxicity in a key concern for their realization for future flexible and wearable electronics. In this regard, comparatively less toxic bismuth-based discrete perovskites do serve as a promising platform for self-powered wearable electronics. However, they showed exhibited relatively low output performance due to its semiconducting property. Nevertheless, its inherent multifunctionality offers a great platform towards the development of multi-modal energy harvesting devices for e-skin and wearable electronic device applications. Strikingly, the exploration of organophosphazene chemistry is a significant advancement because of its biocompatibility and biodegradability. Such approaches could therefore address in efficient disposal of these electronic materials in a benign protocol after their wear and tear. However, the output performance obtained from this device was comparatively low, which calls for further improvement in design strategies involving these materials. Therefore, engineering appropriate devices by adopting advanced manufacturing techniques like additive manufacturing would render judicious control over obtaining notable output performance.

***Table 6.1**: Output performance comparison of piezo- and ferroelectric based composite materials with the hybrid molecular ferroelectrics reported in the thesis.*

Polymeric composites	Output voltage	Power/Power density	Active area (cm^2)	Reference
$MAPbI_3$-PVDF	1.8 V	2.5 μW cm^{-2}	1*1	1
$MASnI_3$-PVDF	6 V	-	1*1	2
$FAPbBr_3$-PDMS	4 V	-	1*1	3
$MAPbBr_3$-PVDF	5 V	0.28 μW cm^{-2}	2.4*1.5	4
$MAPbI_3$-PDMS	1 V	-	1*1	5
$FASnI_3$-PVDF	23 V	35 mW cm^{-2}	2*2	6
$MAPbI_3$-PVDF	9.43 V	-	1*1	7
$MAPbI_3$-PDMS	108 V	0.3 mW cm^{-3}	2.5*3.5	8
$DPDP.PF_6$/PDMS	8.5(V_{pp})	0.14 μW cm^{-2}	3*1.3	9
$DPDP.BF_4$/TPU	8.95(V_{pp})	0.20 μW cm^{-2}	3*1.3	10
$TPAP.BF_4$/TPU	7.37(V_{pp})	0.09 μW cm^{-2}	3*1.3	10
$TIAP.BF_4$/TPU	4.75(V_{pp})	0.04 μW cm^{-2}	3*1.3	10
$[Me(Ph)_3P]_4[Ni(NCS)_6]$	19.29(V_{pp})	50.26 μW cm^{-2}	3*1.3	11
$[BnNMe_3]_2CdBr_4$/PDMS	52.9 V	13.8 μW cm^{-2}	3*3	Chapter-2 (12)
$[BnNMe_2{}^nPr]_2CdBr_4$/PDMS	63.8 V	37.1 μW cm^{-2}	3*3	Chapter-2 (12)
$[NMe_3OH]CdCl_3$/PDMS	55.2 V	70.9 μW cm^{-2}	2*2	Chapter-3 (13)
$[Me(Ph)_3P]_3[Bi_2Br_9]$ /PDMS	22.9 (V_{pp})	7 μW cm^{-2}	1.5*1.5	Chapter-4
[PMeI]/TPU	20.1 V	3.2 μW cm^{-2}	1.7*1.5	Chapter-5

6.2 References

(1) Sultana, A.; Sadhukhan, P.; Alam, M. M.; Das, S.; Middya, T. R.; Mandal, *ACS Appl. Mater. Interfaces* **2018,** *10*, 4121-4130.

(2) Ippili, S.; Jella, V.; Eom, J.-H.; Kim, J.; Hong, S.; Choi, J.-S.; Tran, V.-D.; Van Hieu, N.; Kim, Y.-J.; Kim, H.-J.; Yoon, S.-G., *Nano Energy* **2019,** *57*, 911-923.

(3) Ding, R.; Liu, H.; Zhang, X.; Xiao, J.; Kishor, R.; Sun, H.; Zhu, B.; Chen, G.; Gao, F.; Feng, X., *Adv. Funct. Mater.* **2016,** *26*, 7708-7716.

(4) Sultana, A.; Alam, M. M.; Sadhukhan, P.; Ghorai, U. K.; Das, S.; Middya, T. R.; Mandal, D., *Nano Energy* **2018,** *49*, 380-392.

(5) Kim, Y.-J.; Dang, T.-V.; Choi, H.-J.; Park, B.-J.; Eom, J.-H.; Song, H.-A.; Seol, D.; Kim, Y.; Shin, S.-H.; Nah, J., *J. Mater. Chem. A* **2016,** *4*, 756-763.

(6) Pandey, R.; SB, G.; Grover, S.; Singh, S. K.; Kadam, A.; Ogale, S.; Waghmare, U. V.; Rao, V. R.; Kabra, D., *ACS Energy Lett.* **2019,** *4*, 1004-1011.

(7) Jella, V.; Ippili, S.; Eom, J.-H.; Choi, J.; Yoon, S.-G., *Nano Energy* **2018,** *53*, 46-56.

(8) Dhar, J.; Sil, S.; Hoque, N. A.; Dey, A.; Das, S.; Ray, P. P.; Sanyal, D., *ChemistrySelect* **2018,** *3*, 5304-5312.

(9) Vijayakanth, T.; Srivastava, A. K.; Ram, F.; Kulkarni, P.; Shanmuganathan, K.; Praveenkumar, B.; Boomishankar, R., *Angew. Chem. Int. Ed.* **2018,** *130*, 9192-9196.

(10) Vijayakanth, T.; Ram, F.; Praveenkumar, B.; Shanmuganathan, K.; Boomishankar, R., *Chem. Mater.* **2019,** *31*, 5964-5972.

(11) Vijayakanth, T.; Ram, F.; Praveenkumar, B.; Shanmuganathan, K.; Boomishankar, R., *Angew. Chem. Int. Ed.* **2020,** *59*, 10368-10373.

(12) Deswal, S.; Singh, S. K.; Rambabu, P.; Kulkarni, P.; Vaitheeswaran, G.; Praveenkumar, B.; Ogale, S.; Boomishankar, R., *Chem. Mater.* **2019,** *31*, 4545-4552.

(13) Deswal, S.; Singh, S. K.; Pandey, R.; Nasa, P.; Kabra, D.; Praveenkumar, B.; Ogale, S.; Boomishankar, R., *Chem. Mater.* **2020,** *32*, 8333-8341.

****

Appendix

Table 2A.1: Selected bond lengths [Å] and angles [°] for compound **1**, **2** and **3**.

Compound	Bond Length	Bond Angle
1	Cd(1)-Br(3): 2.5745(18) Cd(1)-Br(4): 2.5873(17) Cd(1)-Br(2): 2.6011(17) Cd(1)-Br(1): 2.6130(16) N(1)-C(2): 1.472(16) N(1)-C(3): 1.490(16) N(1)-C(1): 1.507(15) N(1)-C(11): 1.528(15)	Br(3)-Cd(1)-Br(4): 113.71(6) Br(3)-Cd(1)-Br(2): 110.93(5) Br(4)-Cd(1)-Br(2): 104.53(5) Br(3)-Cd(1)-Br(1): 107.22(6) Br(4)-Cd(1)-Br(1): 108.47(5) Br(2)-Cd(1)-Br(1): 112.04(6) C(2)-N(1)-C(1): 110.4(10) C(3)-N(1)-C(1): 109.3(10) C(2)-N(1)-C(11): 112.3(10)
2	Cd(1)-Br(2): 2.5765(14) Cd(1)-Br(3): 2.5956(16) Cd(1)-Br(1): 2.5984(15) Cd(1)-Br(4): 2.6086(14) N(1)-C(4): 1.489(14) N(1)-C(5): 1.490(15) N(1)-C(3): 1.519(14) N(1)-C(11): 1.520(15)	Br(2)-Cd(1)-Br(3): 111.59(6) Br(2)-Cd(1)-Br(1): 113.18(5) Br(3)-Cd(1)-Br(1): 105.53(5) Br(2)-Cd(1)-Br(4): 106.89(5) Br(3)-Cd(1)-Br(4): 109.03(6) Br(1)-Cd(1)-Br(4): 110.60(6) C(4)-N(1)-C(3): 110.8(8) C(5)-N(1)-C(3): 110.2(10) C(4)-N(1)-C(11): 110.6(9)
3	Cd(1)-Br(1): 2.5799(7) Cd(1)-Br(2): 2.5840(6) Cd(1)-Br(4): 2.6029(7) Cd(1)-Br(3): 2.6166(7) N(1)-C(3): 1.498(5) N(1)-C(4): 1.498(5) N(1)-C(2): 1.519(5) N(1)-C(11): 1.531(5)	Br(1)-Cd(1)-Br(2): 113.91(2) Br(1)-Cd(1)-Br(4): 106.10(2) Br(2)-Cd(1)-Br(4): 112.50(2) Br(1)-Cd(1)-Br(3): 110.12(2) Br(2)-Cd(1)-Br(3): 104.64(2) Br(4)-Cd(1)-Br(3): 109.59(2) C(3)-N(1)-C(4): 109.0(3) C(3)-N(1)-C(2): 110.2(3) C(3)-N(1)-C(11): 106.7(3)

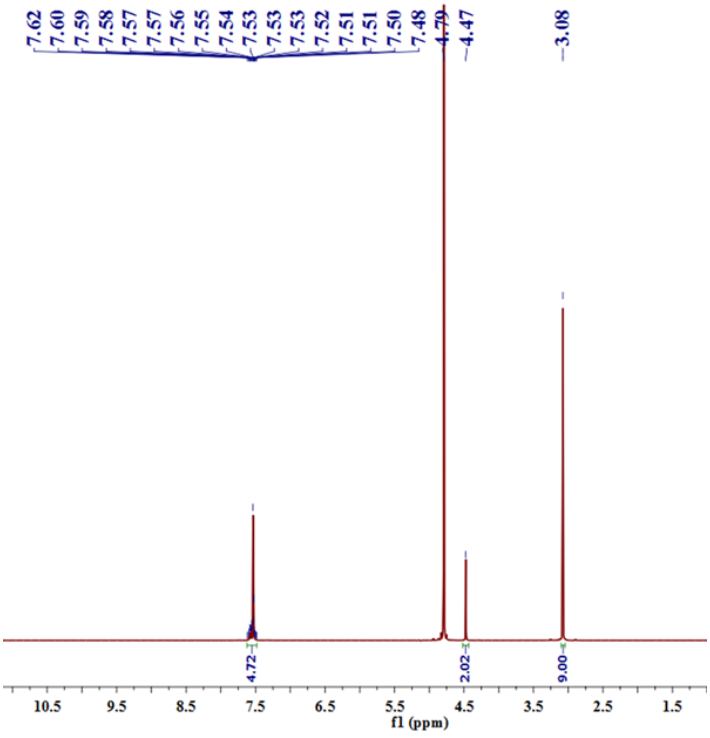

Figure 2A.1: ^{1}H NMR spectrum of **1**.

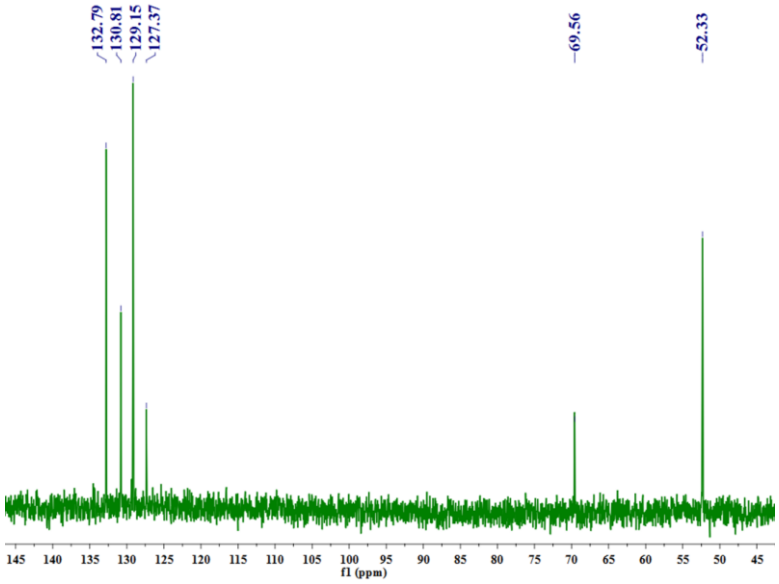

Figure 2A.2: ^{13}C NMR spectrum of **1**.

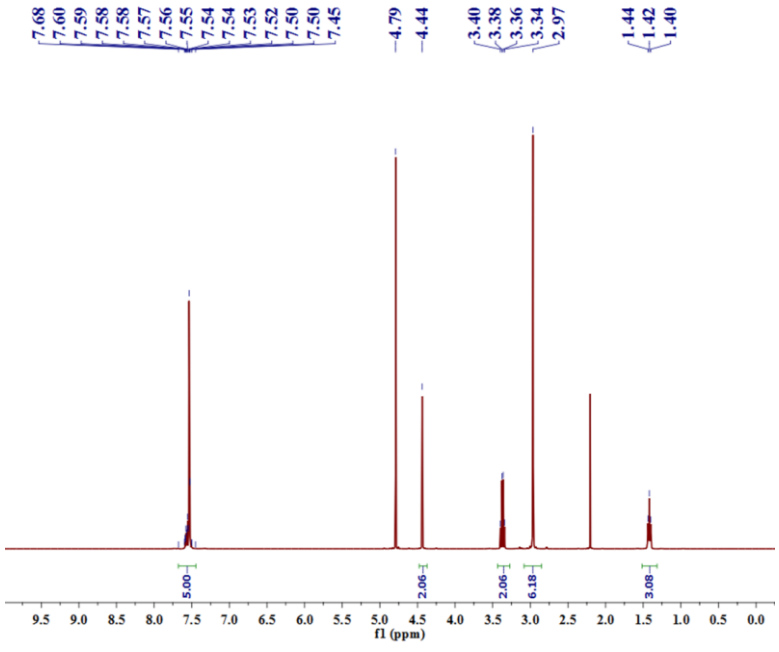

Figure 2A.3: ^{1}H NMR spectrum of **3**·Br.

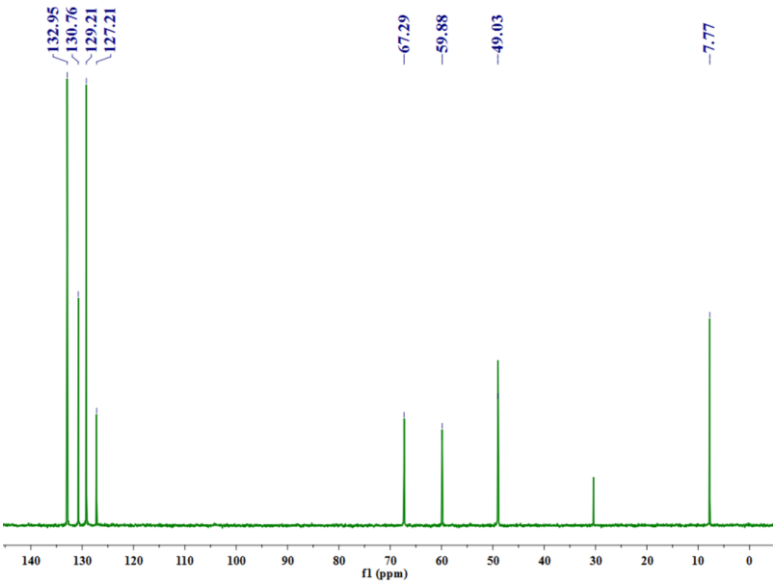

Figure 2A.4: ^{13}C NMR spectrum of **3**·Br.

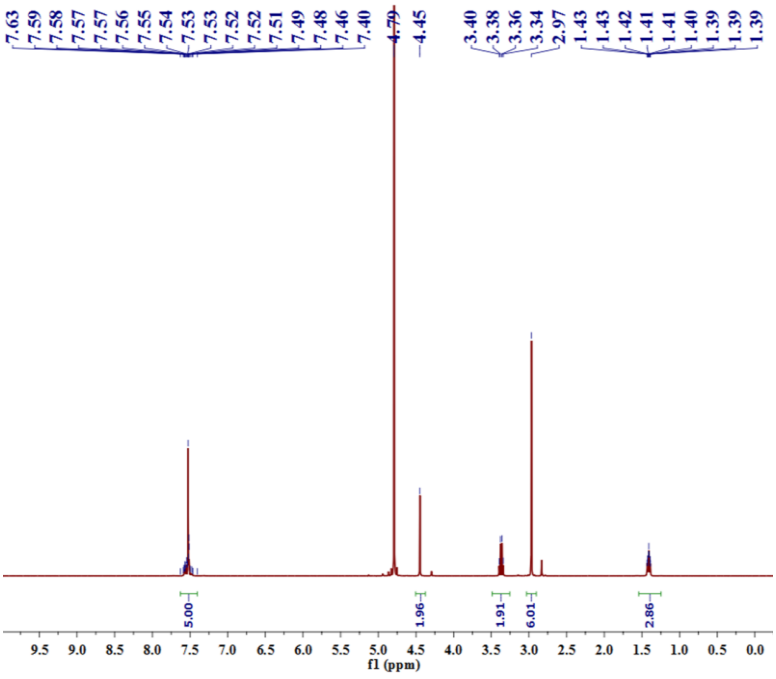

Figure 2A.5: ^{1}H NMR spectrum of **3**.

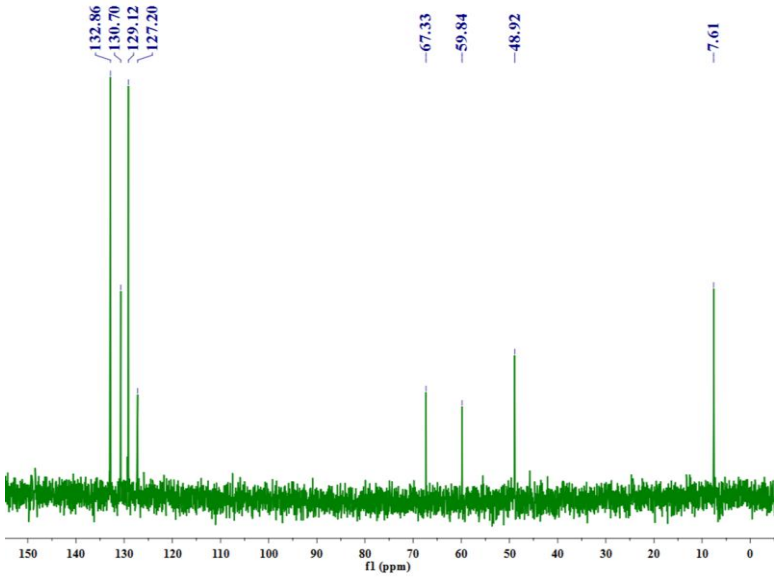

Figure 2A.6: ^{13}C NMR spectrum of **3**.

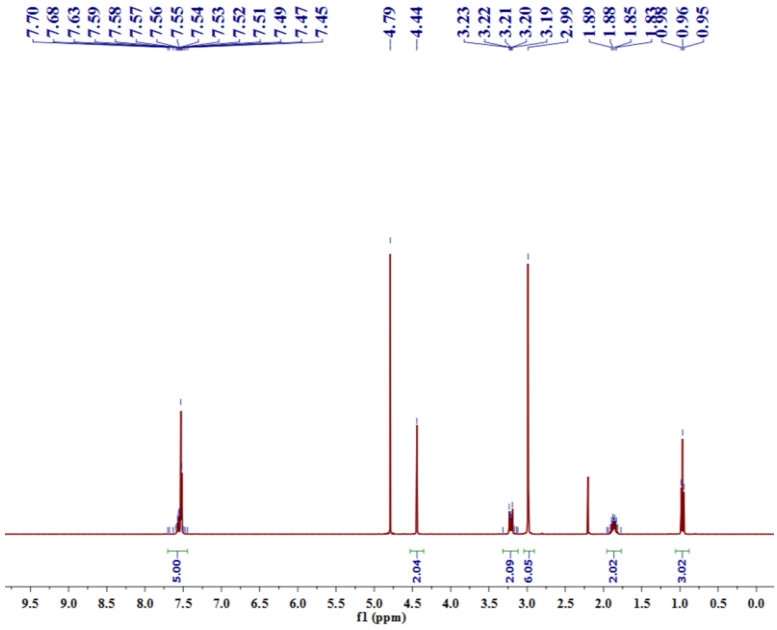

Figure 2A.7: ^{1}H NMR spectrum of **2**·Br.

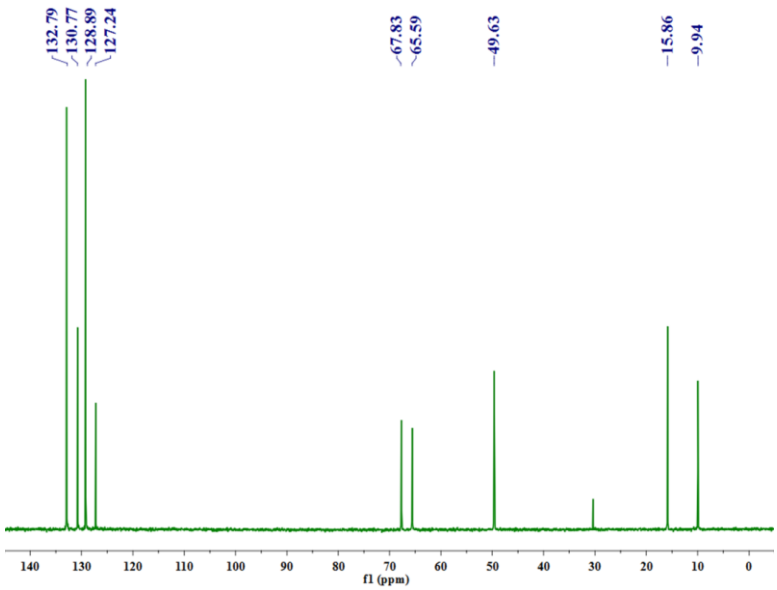

Figure 2A.8: ^{13}C NMR spectrum of **2**·Br.

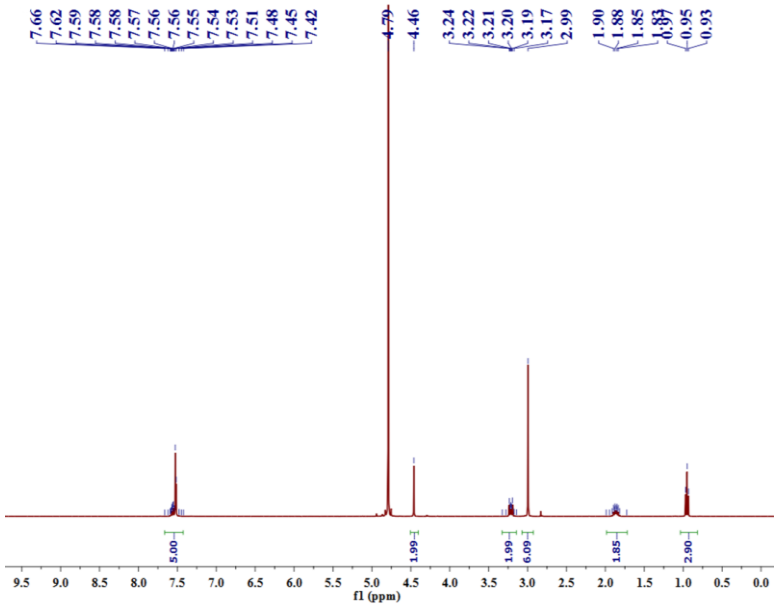

Figure 2A.9: ^{1}H NMR spectrum of **2**.

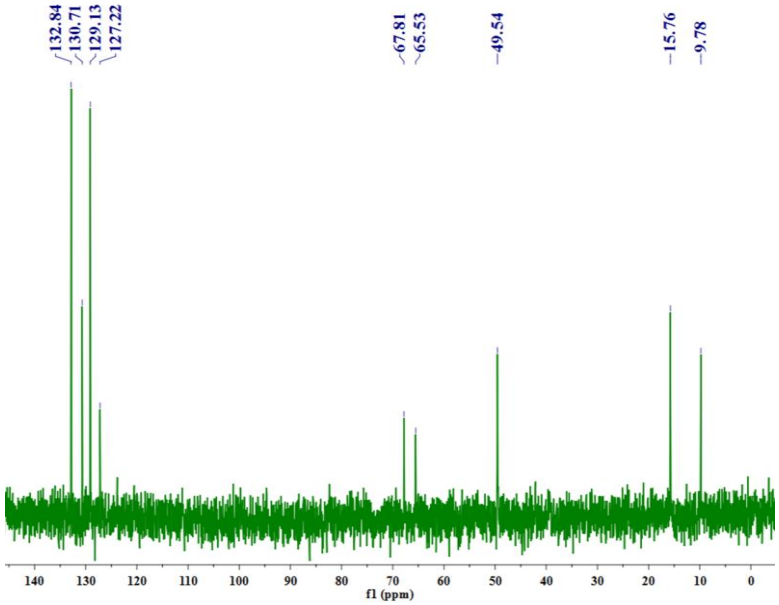

Figure 2A.10: ^{13}C NMR spectrum of **2**.

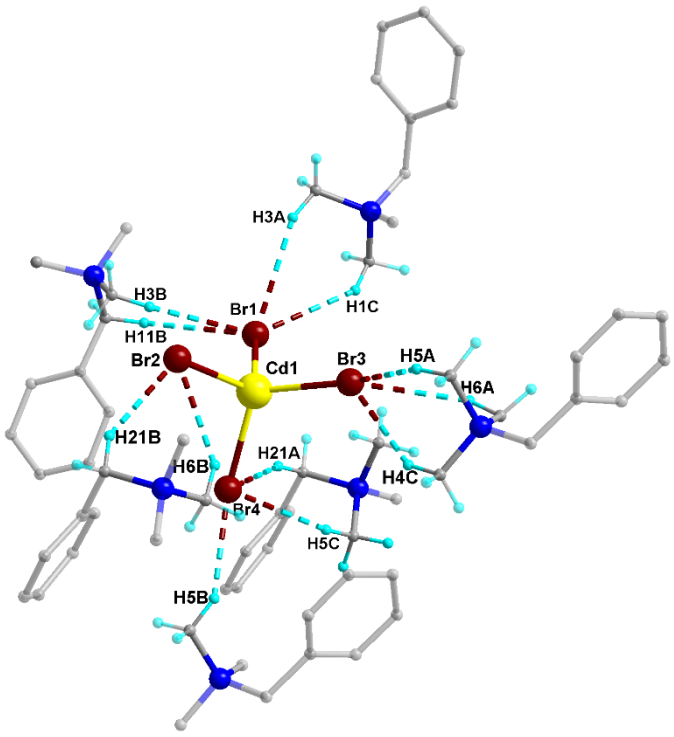

Figure 2A.11: Non-classical hydrogen bonding C-H…Br interactions involving a single $(CdBr_4)^{2-}$ unit in **1**.

Table 2A.2. Non-classical hydrogen bonding distances (Å) and angles (˚) for compound **1**.

D-H…A	d(H…A) Å	d(D…A) Å	<(DHA)˚	Symmetry transformations to generate equivalent atoms
C(1)-H(1C)…Br(1)	3.1083(16)	3.9523(13)	145.029(75)	x, -1+y, z
C(3)-H(3A)…Br(1)	3.1470(16)	4.0623(13)	156.028(80)	x, -1+y, z
C(3)-H(3B)…Br(1)	2.9710(16)	3.9077(14)	160.278(82)	1-x, -0.5+y, 1-z
C(4)-H(4C)…Br(3)	3.0805(19)	3.9576(14)	149.634(80)	2-x, -0.5+y, -z
C(5)-H(5A)…Br(3)	2.9682(18)	3.8628(13)	152.198(73)	2-x, -0.5+y, -z
C(5)-H(5B)…Br(4)	2.8665(15)	3.7136(12)	145.192(73)	1-x, -0.5+y, -z
C(5)-H(5C)…Br(4)	2.8788(16)	3.8118(13)	159.334(76)	1+x, -1+y, z
C(6)-H(6A)…Br(3)	2.9732(18)	3.8654(16)	151.891(87)	2-x, -0.5+y, -z
C(6)-H(6B)…Br(2)	2.9595(16)	3.8317(15)	148.910(87)	1+x, y, z
C(11)-H(11B)…Br(1)	3.0701(16)	3.9684(14)	151.590(74)	1-x, -0.5+y, 1-z
C(21)-H(21A)…Br(4)	2.8989(18)	3.8207(13)	155.294(74)	1+x, -1+y, z
C(21)-H(21B)…Br(2)	2.9454(15)	3.8418(13)	151.107(75)	1+x, y, z

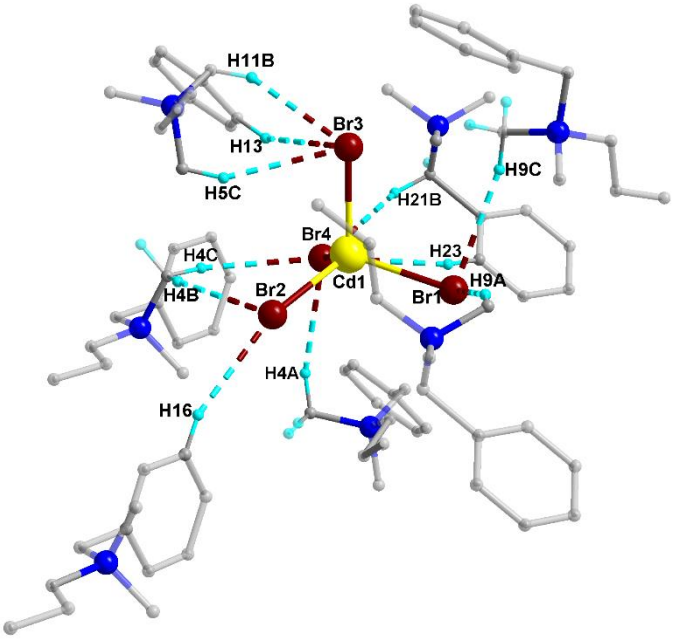

Figure 2A.12: Non-classical hydrogen bonding C-H…Br interactions involving a single $(CdBr_4)^{2-}$ unit in **2**.

Table 2A.3: Non-classical hydrogen bonding distances (Å) and angles (˚) for compound **2**.

D-H…A	d(H…A) Å	d(D…A) Å	<(DHA)˚	Symmetry transformations to generate equivalent atoms
C(4)-H(4A)…Br(4)	2.9074(11)	3.8511(12)	161.990(69)	x, y, z
C(4)-H(4B)…Br(2)	2.9955(13)	3.8462(11)	145.886(64)	0.5+x, 0.5-y, -1+z
C(4)-H(4C)…Br(4)	2.9395(10)	3.8405(11)	153.303(61)	0.5+x, 0.5-y, -1+z
C(5)-H(5C)…Br(3)	2.9783(13)	3.8739(12)	152.712(72)	1+x, y, -1+z
C(9)-H(9A)…Br(1)	3.0377(15)	3.9886(19)	163.184(11)	x, y, z
C(9)-H(9C)…Br(1)	2.9980(15)	3.8881(17)	151.710(99)	-x, 1-y, -0.5+z
C(11)-H(11B)…Br(3)	2.7913(15)	3.7131(11)	154.908(61)	1+x, y, -1+z
C(13)-H(13)…Br(3)	3.0000(15)	3.8523(13)	149.866(75)	1+x, y, -1+z
C(16)-H(16)…Br(2)	3.0449(13)	3.9422(13)	157.830(78)	0.5+x, 0.5-y, -2+z
C(21)-H(21B)…Br(4)	2.9774(11)	3.8746(16)	151.411(94)	x, y, z
C(23)-H(23)…Br(4)	3.031(10)	3.8836(97)	150.052(58)	x, y, z

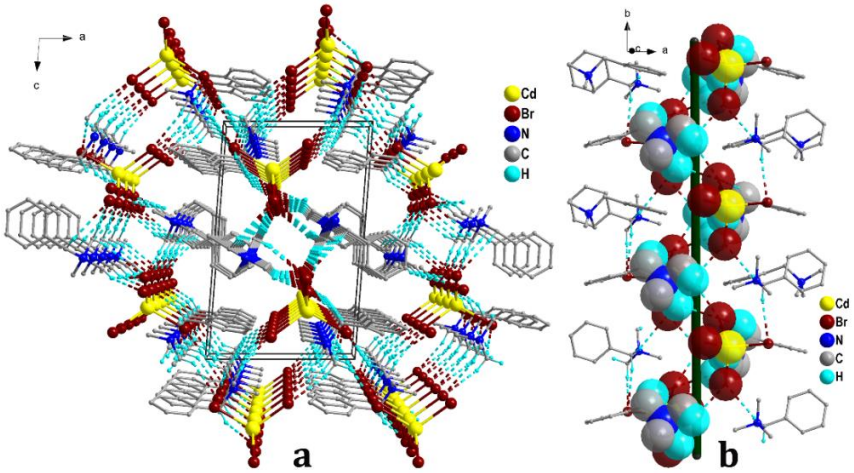

Figure 2A.13: Packing diagram of **1** along the b-axis (a) and view of one of the helical chains down the b-axis (b). The atoms aligned around the helical axis are depicted in the space-fill model.

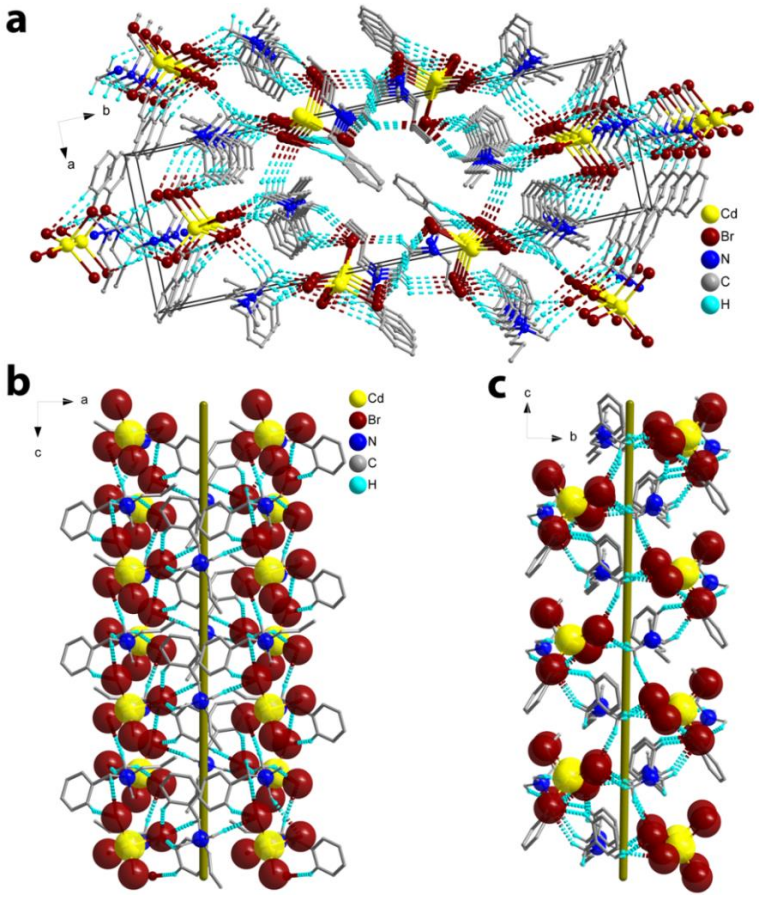

Figure 2A.14: (a) Packing diagram of **2** along c-axis showing the central tubular channel surrounded by other smaller channels. (b) and (c) View of the central tubular channel along the b- and a-axes, respectively.

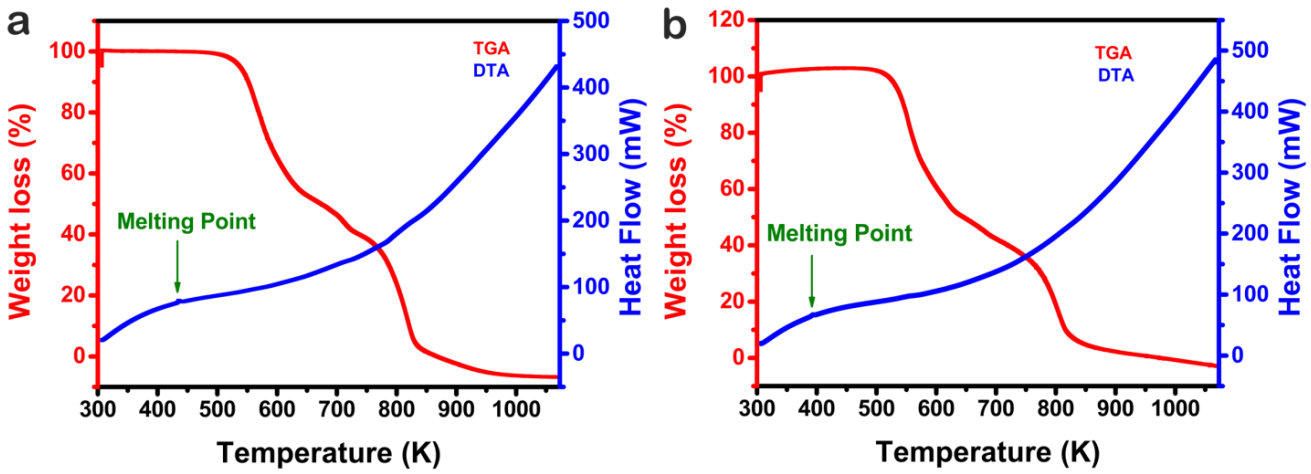

Figure2A15: TGA-DTA Data for (a) **1** and (b) **2**.

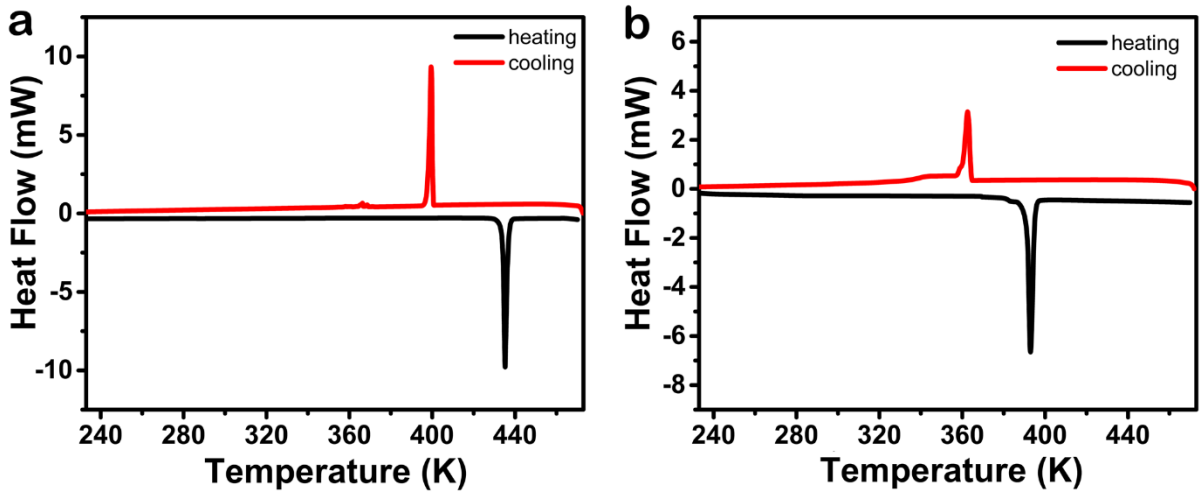

Figure 2A.16: DSC Data for (a) **1** and (b) **2**.

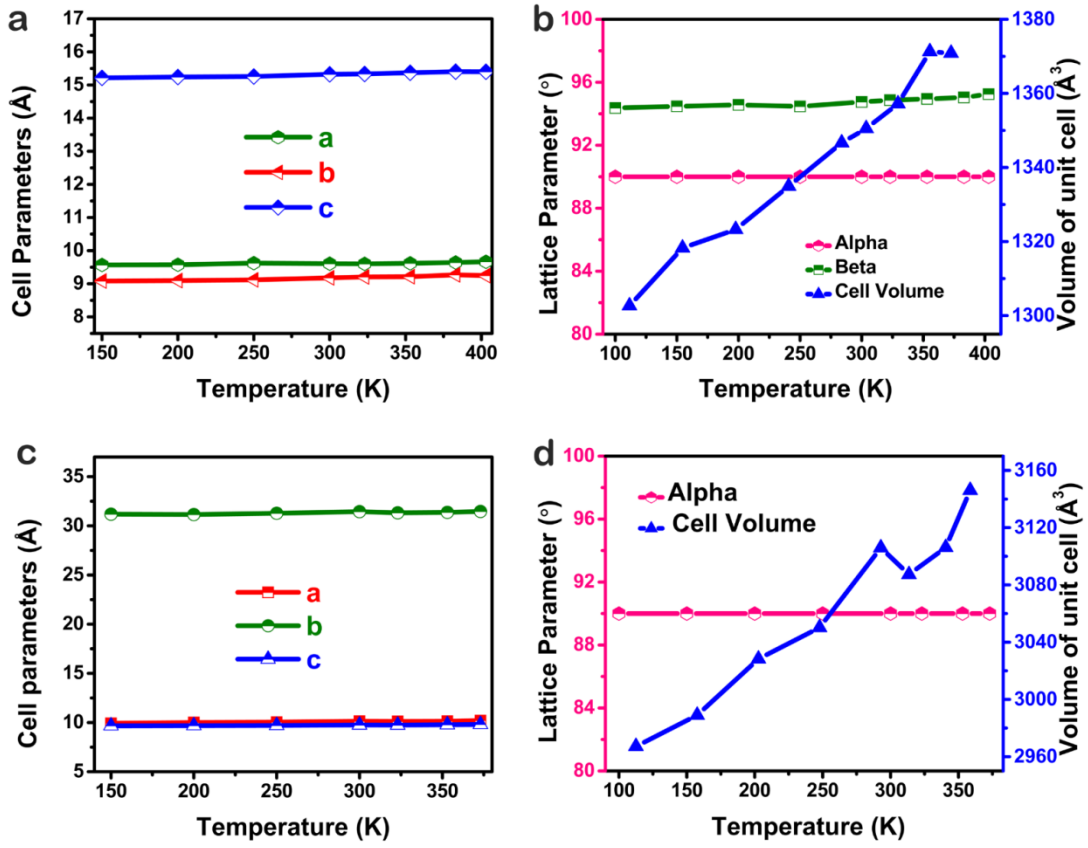

Figure 2A.17: (a), (b) Unit cell parameters of **1** as a function of temperature; (c), (d) Unit cell parameters of **2** as a function of temperature.

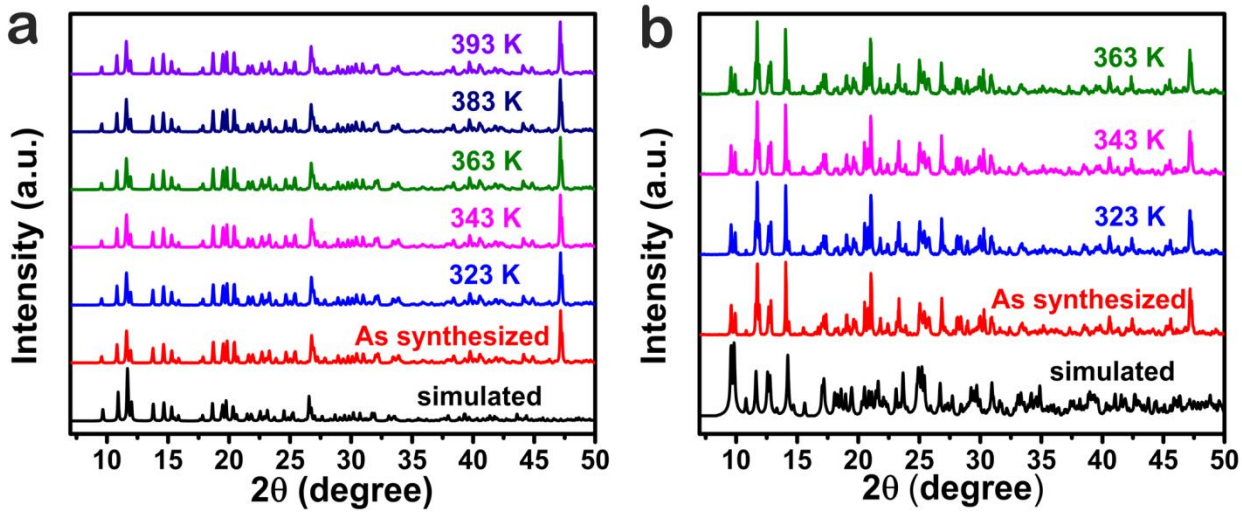

Figure 2A.18: Variable temperature PXRD patterns of (a) **1** and (b) **2**.

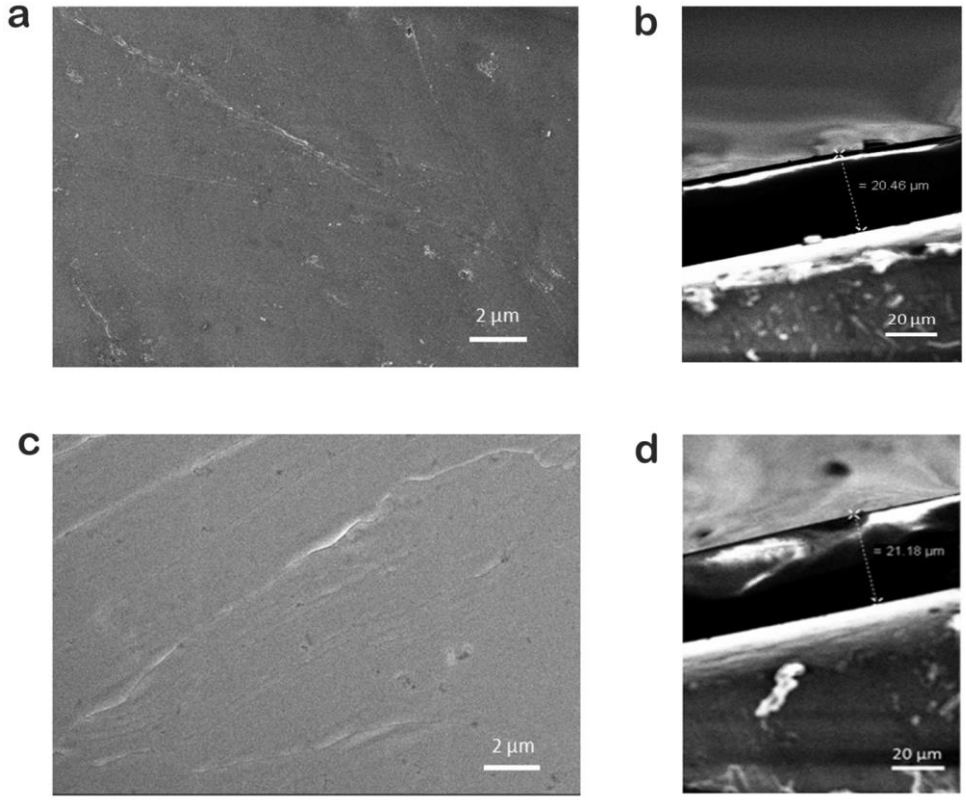

Figure 2A.19: SEM images of (a) **1** and (c) **2** films deposited on Al substrate revealing homogeneous film formation. Cross-sectional SEM image of ~20 µm thick film of (b) **1** and (d) **2** deposited on the Al substrate.

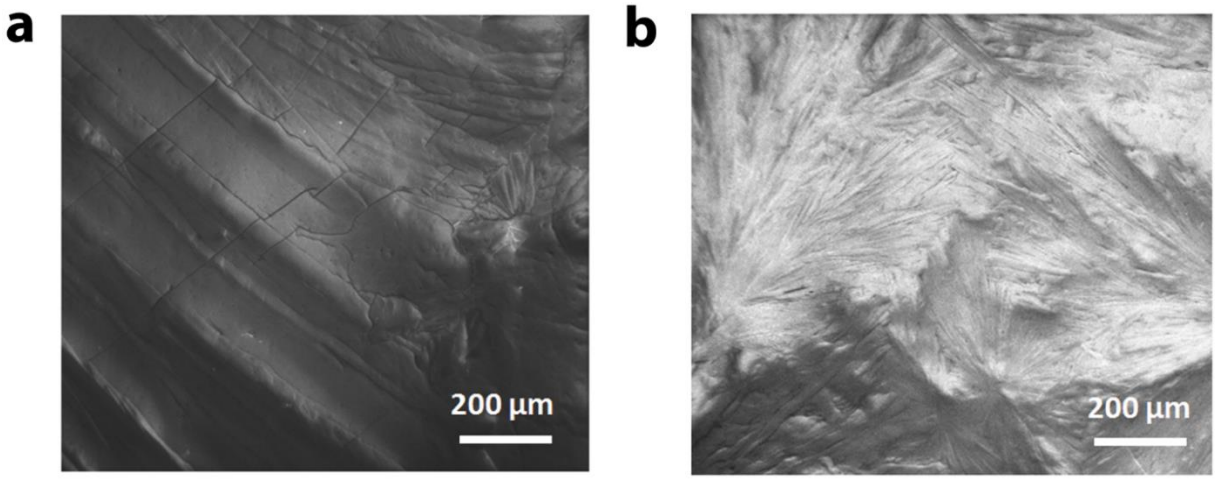

Figure 2A.20: SEM images of (a) **1** and (b) **2** films deposited on Al substrate displaying orientation of planes along all directions.

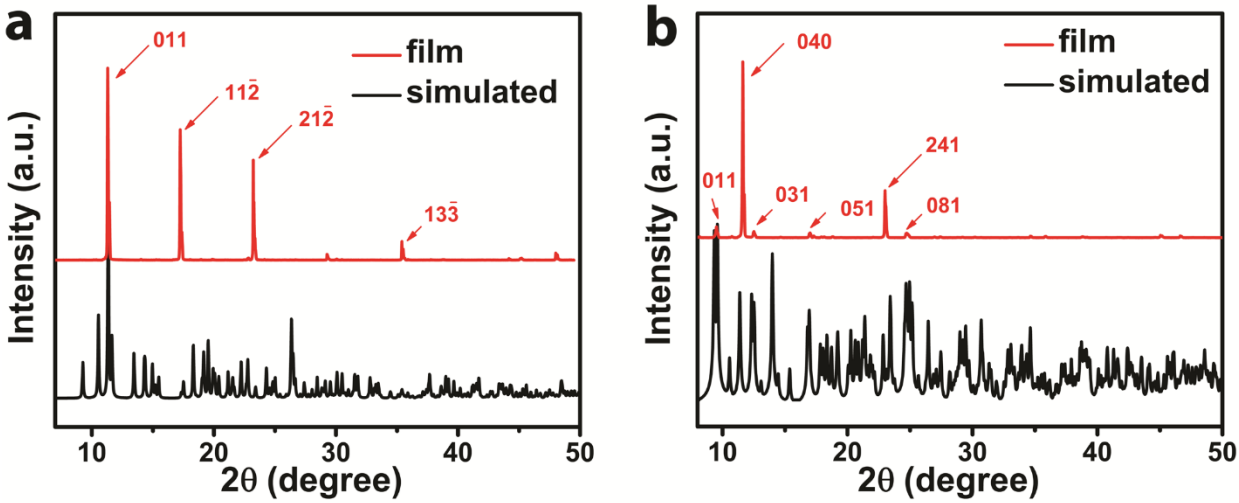

Figure 2A.21: XRD diffraction pattern for the thin film of (a) **1** and (b) **2** deposited on Al substrate depicting polycrystalline film formation.

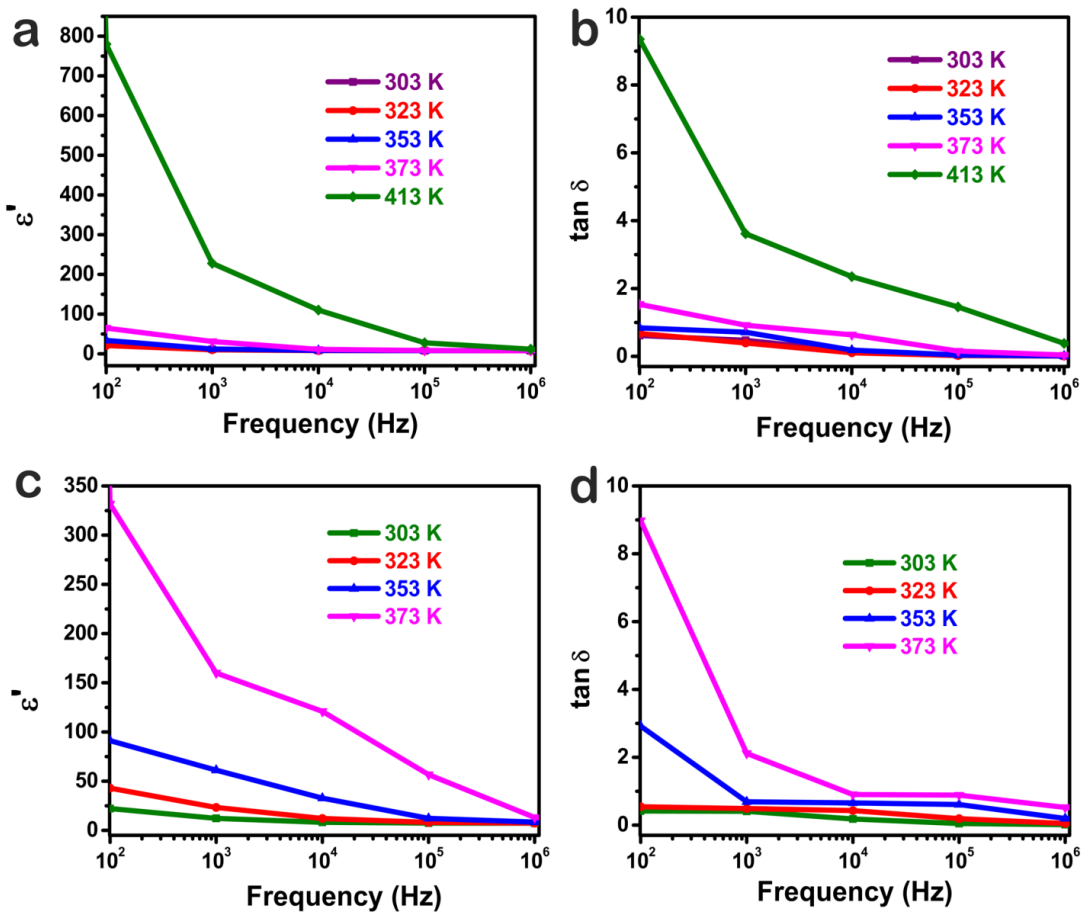

Figure 2A.22: Frequency dependence of the real part of the complex dielectric permittivity of (a) **1** and (c) **2** and the corresponding dielectric loss (tan δ) of (b) **1** and (d) **2** at various temperatures.

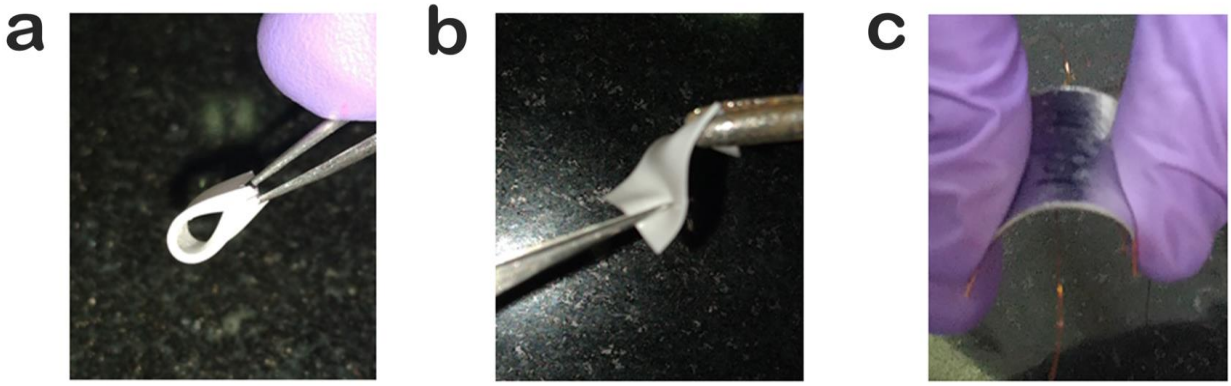

Figure 2A.23: Flexible composites exhibiting (a) rolling (b) twisting (c) bending operations.

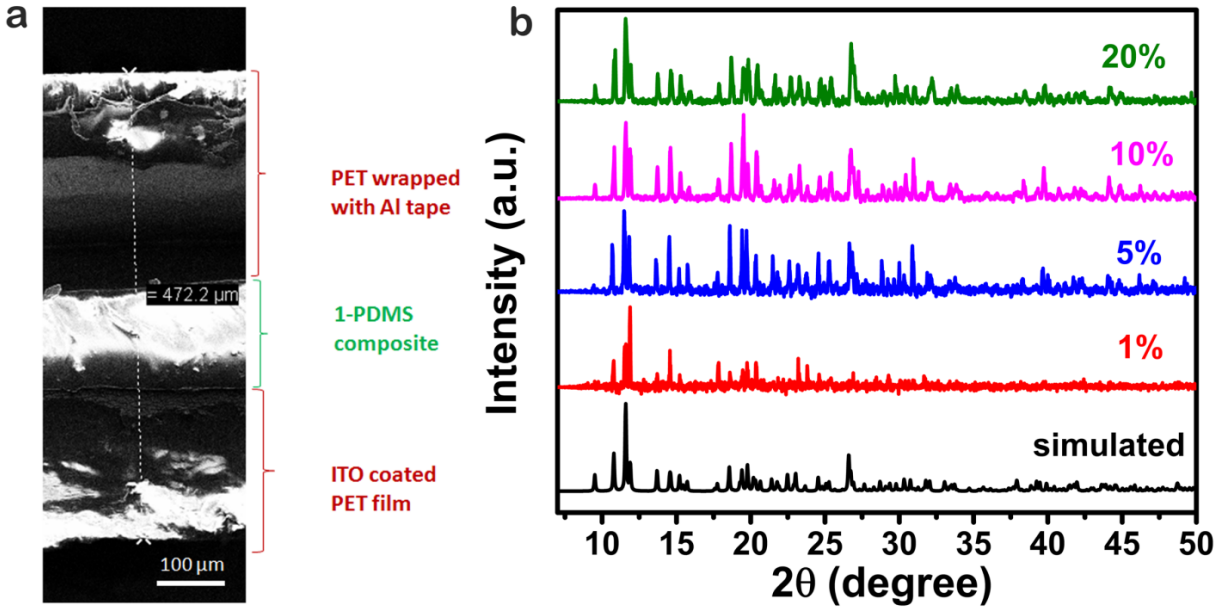

Figure 2A.24: (a) Cross-sectional SEM image of **1**-PDMS based mechanical harvester. (b) PXRD data of **1**-PDMS composite.

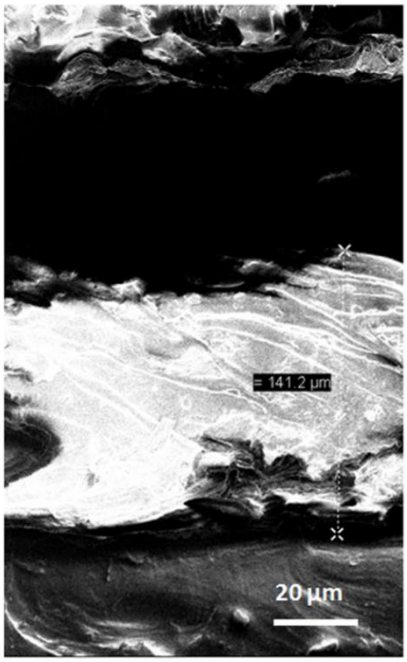

Figure 2A.25: Cross-sectional SEM image of **1**-PDMS based mechanical harvester showing a thickness of ~140 µm for the embedded film of **1**.

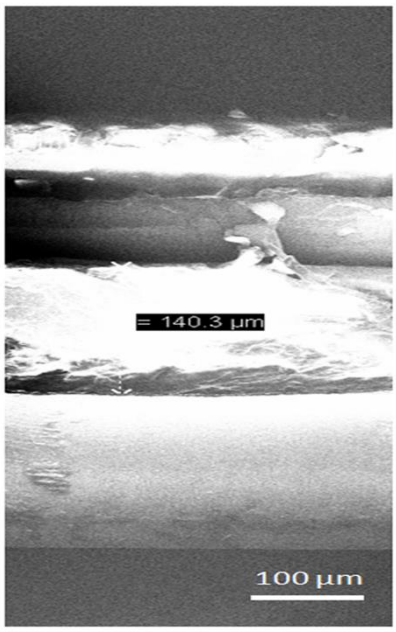

Figure 2A.26: Cross-sectional SEM image of **2**-PDMS based mechanical harvester showing a thickness of ~140 µm for the embedded film of **2**.

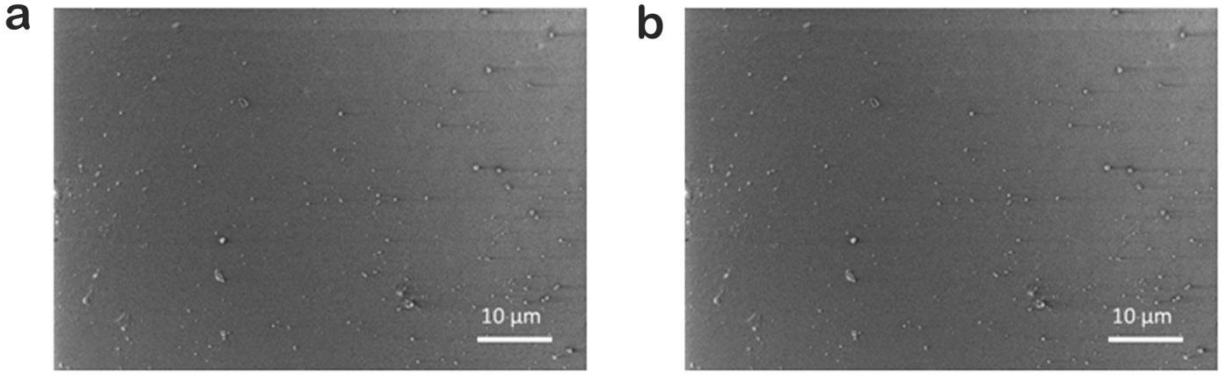

Figure 2A.27: SEM images of (a) **1** and (b) **2** in the PDMS Matrix (20 wt.%) showing the agglomeration of the particles in the embedded films.

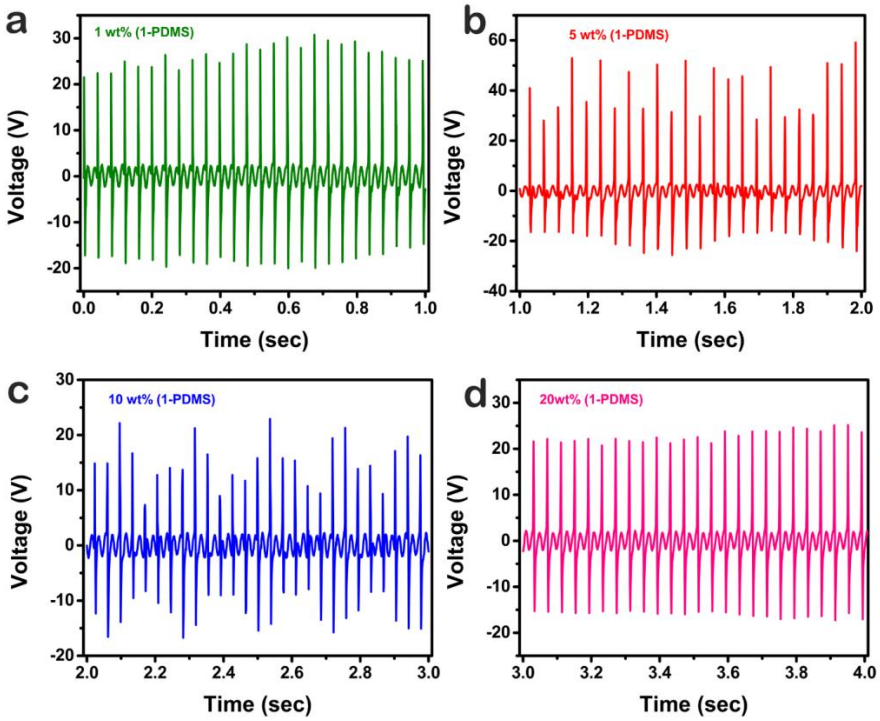

Figure 2A.28: Output voltage measurement for all weight percentage of **1**-PDMS composite materials.

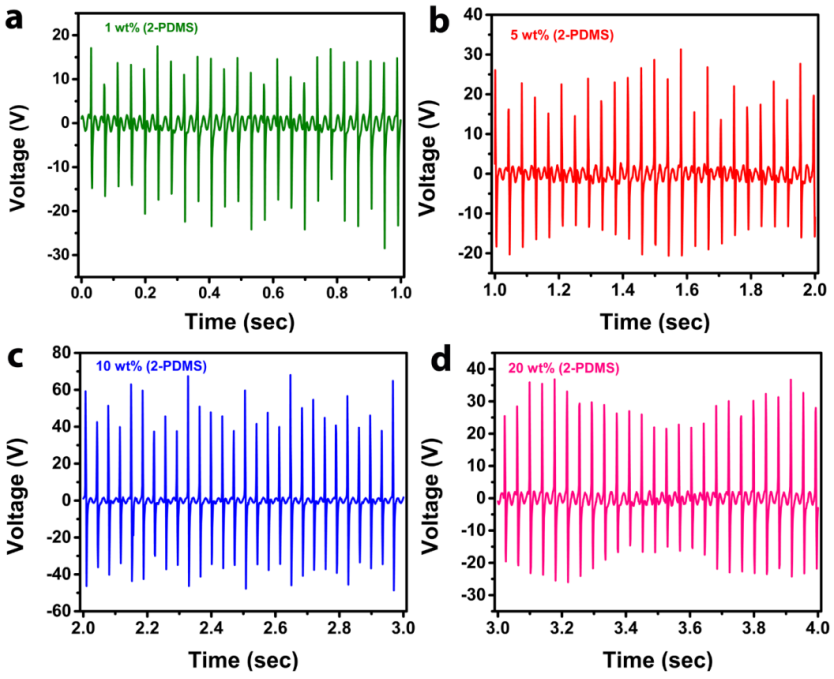

Figure 2A.29: Output voltage measurement for all weight percentage of **2**-PDMS composite materials.

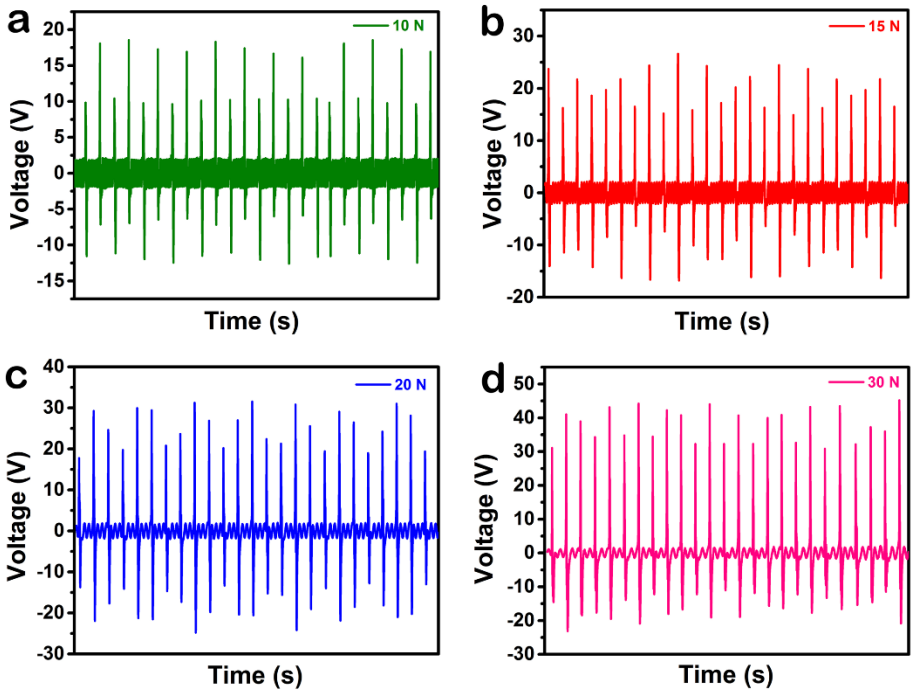

Figure 2A.30: Output voltage measurements performed on 5 wt.% **1**-PDMS under different applied forces.

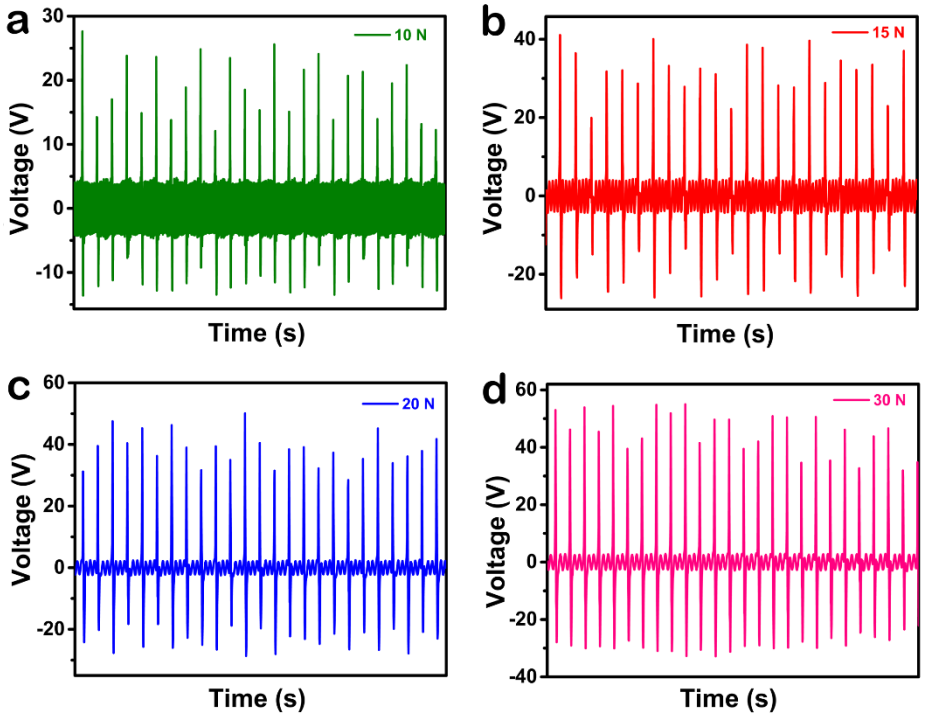

Figure 2A.31: Output voltage measurements performed on 10 wt.% **2**-PDMS under different applied forces.

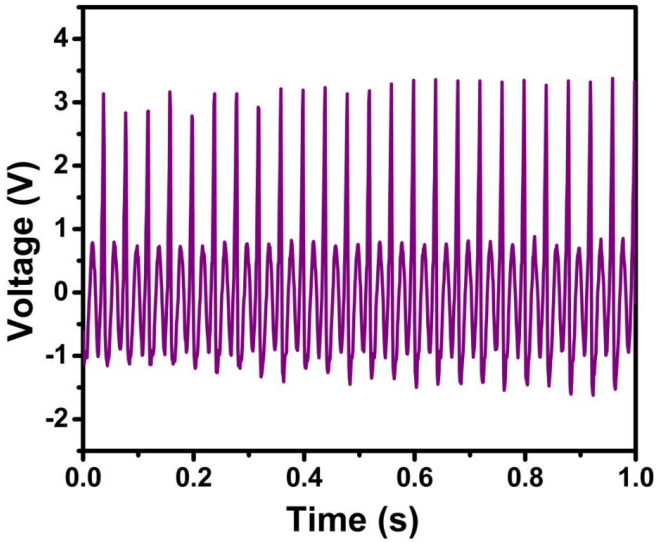

Figure 2A.32: Output voltage generation from pure PDMS device.

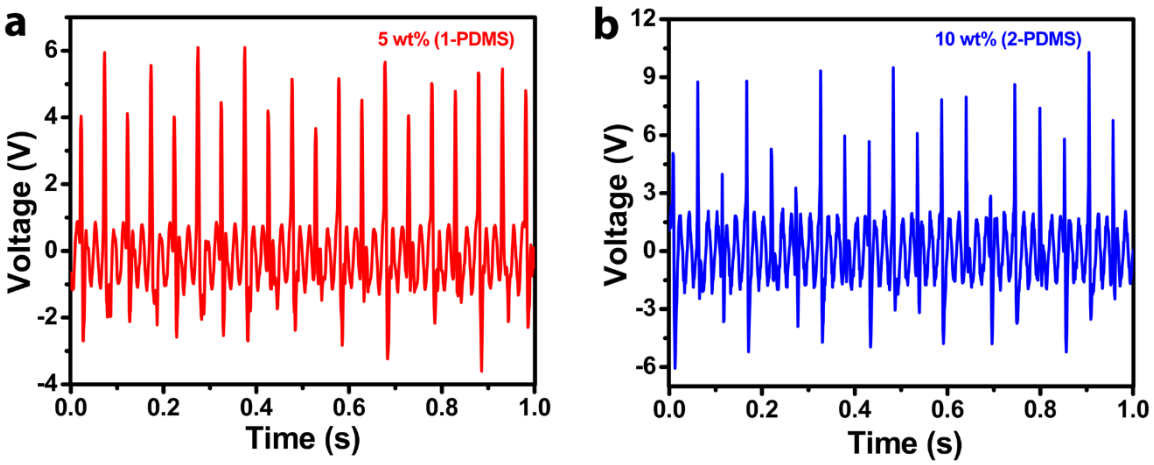

Figure 2A.33: Single electrode measurements performed on (a) 5 wt.% **1**-PDMS (b) 10 wt.% **2**-PDMS.

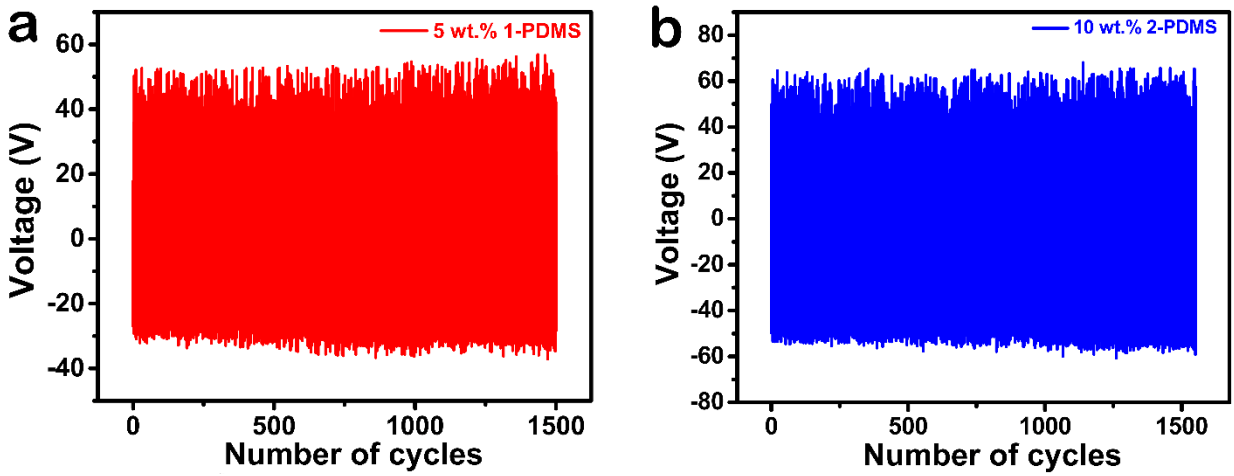

Figure 2A.34: Mechanical durability tests performed on (a) 5 wt.% **1**-PDMS (b) 10 wt.% **2**-PDMS with an applied force of 40 N.

****

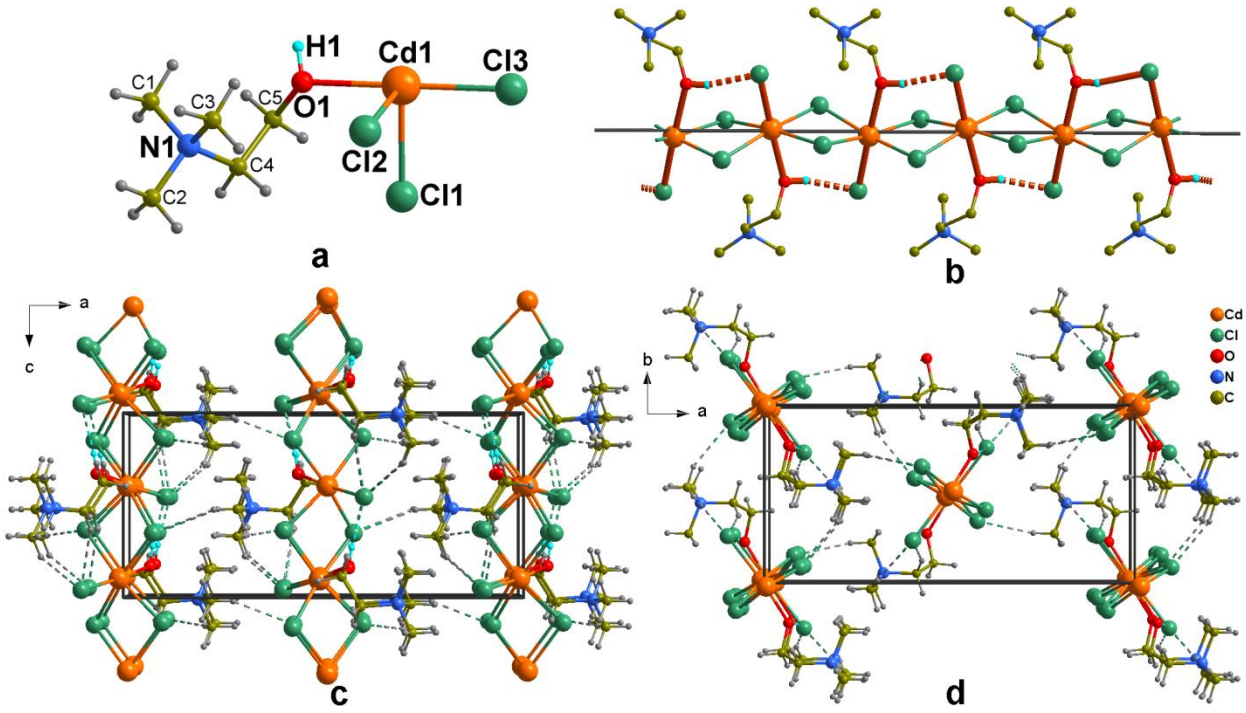

Figure 3A.1: (a) The asymmetric unit of **1** and (b) view of its zig-zag intra-chain O-H···Cl interactions along the polar c-axis. Packing diagram of **1** showing the inter-chain non-classical C-H···Cl interactions viewed down (c) the b- and (d) c-axes.

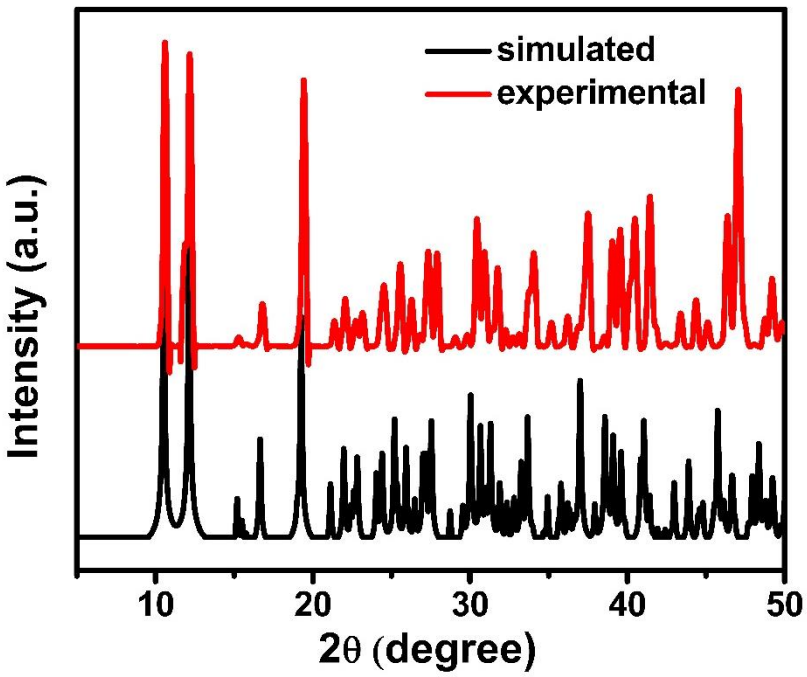

Figure 3A.2: The PXRD pattern of **1.**

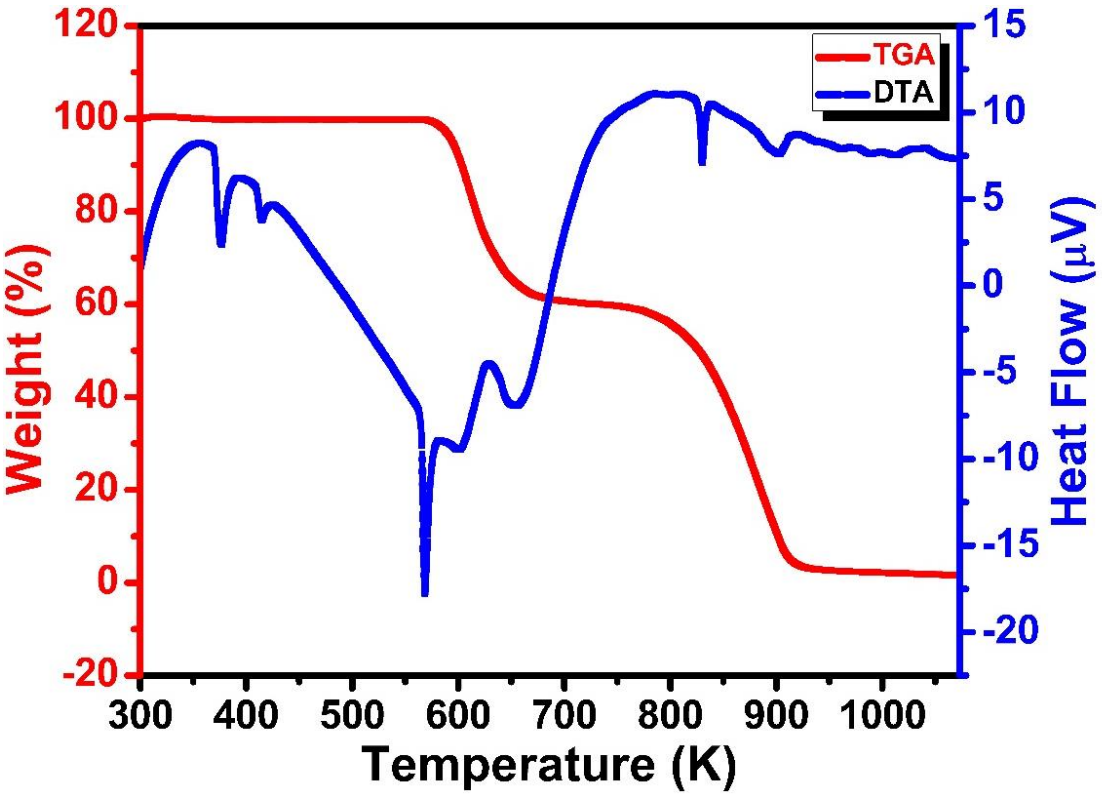

Figure 3A.3: The TGA-DTA Data for **1**.

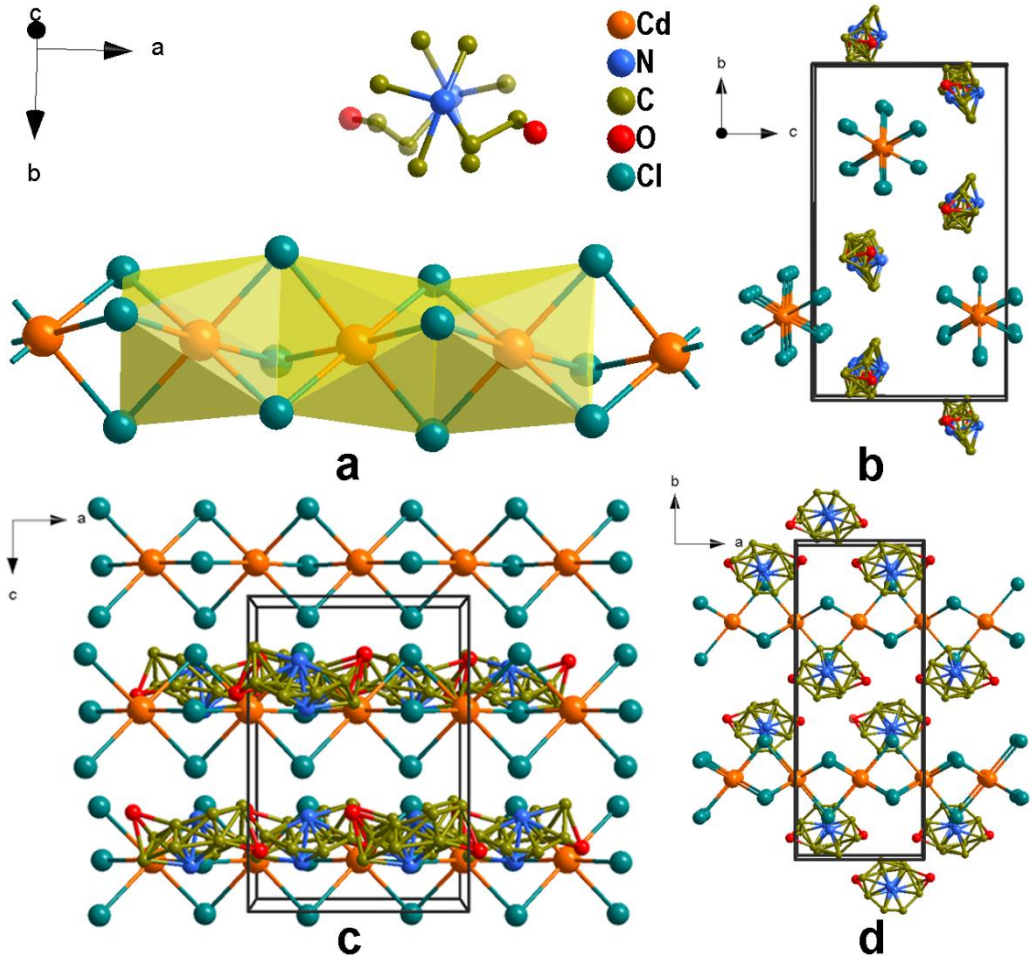

Figure 3A.4: (a) Molecular structure of **1'** obtained via the single-crystal to single-crystal transformation at 363 K. The coordination around the Cd(II) ions are depicted as the face-sharing $CdCl_6$ octahedra (shaded in yellow). The uncoordinated HETMA cation is disordered which is modelled over two positions. The crystal packing diagrams of **1'** viewed along (b) a-axis, (c) b-axis and (d) c-axis. The disordered fragments have been retained in all the figures.

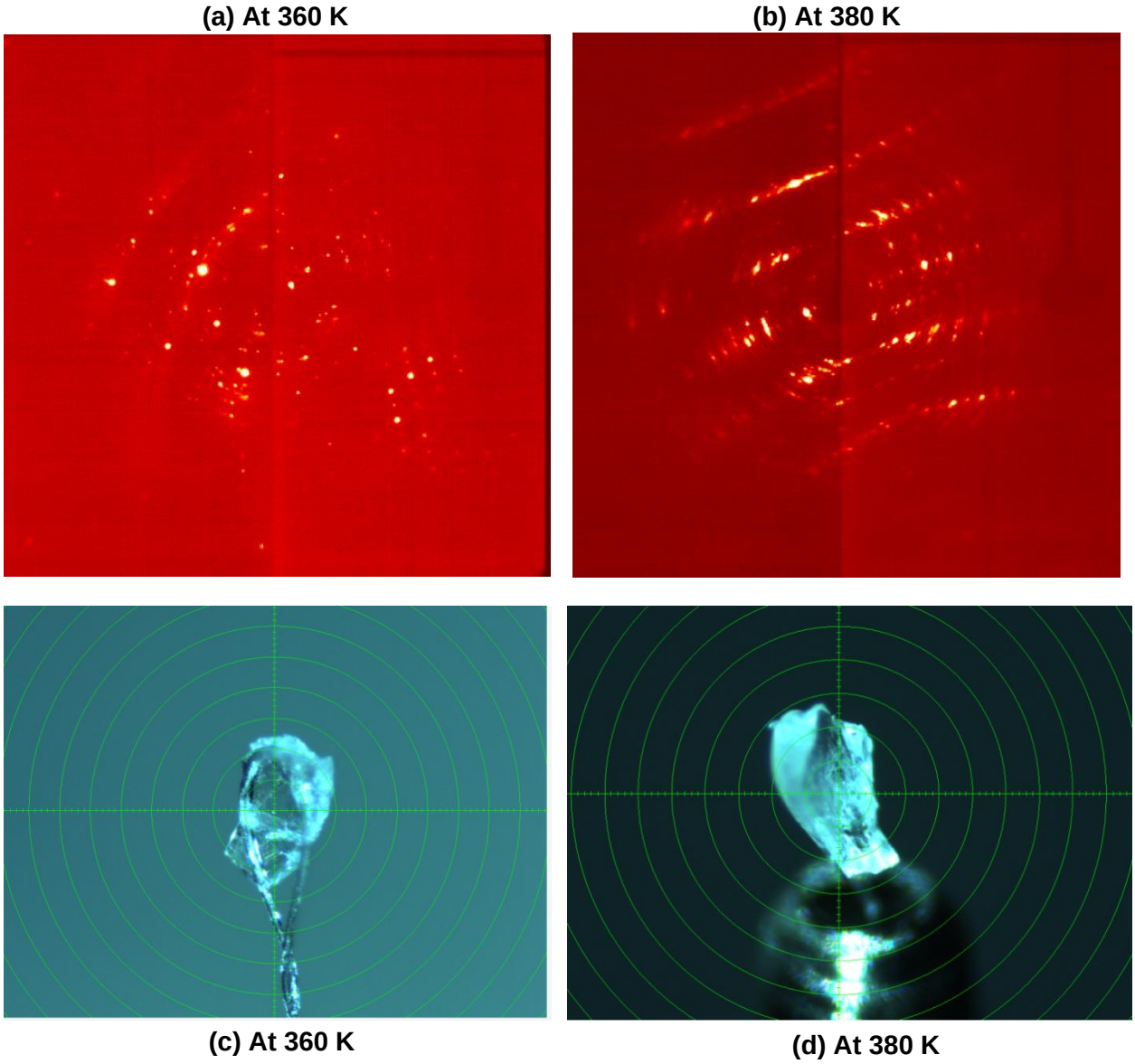

Figure 3A.5: (a) and (b) Diffraction spots on a single frame of the crystal at two different temperatures. (c) and (d) Photographs of the crystal on the goniometer at the two temperatures.

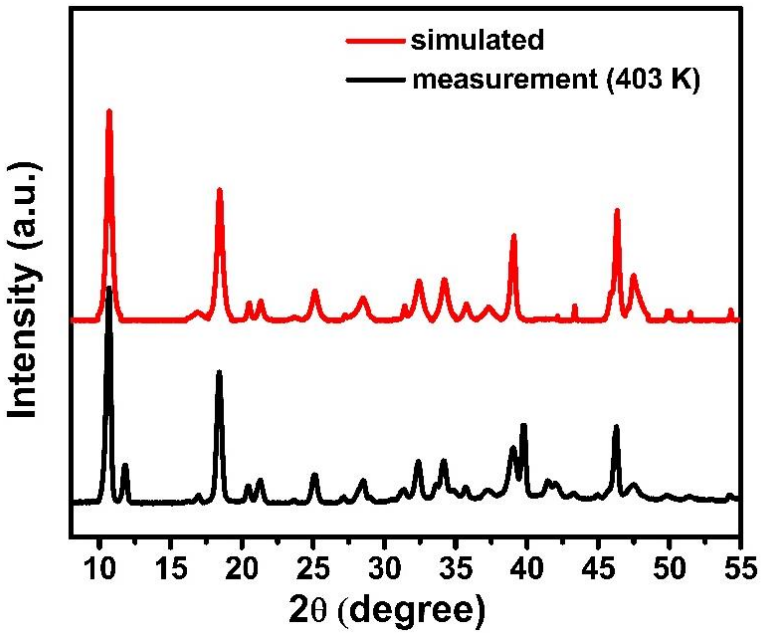

Figure 3A.6: Comparison of the experimental PXRD data of **1** at 403 K and the simulated pattern from the unit cell.

Table 3A.1: PXRD indexed unit-Cell parameters for **1'** in HTP at 403 K[a]

Crystal System	Hexagonal	
Space group	*P6₃/mmc*	
Cell parameters		ESDs
a [Å]	9.634393	0.004227
b [Å]	9.634393	0.004227
c [Å]	6.753254	0.003419
alpha [°]	90	0
beta [°]	90	0
gamma [°]	120	0
Volume[Å^3]	542.86570	0

[a]The PXRD data of **1** at 403K was analyzed using HighScore Plus software suite. TREOR algorithm was used to index the pattern and cell parameters were refined for zero 2-theta shift.

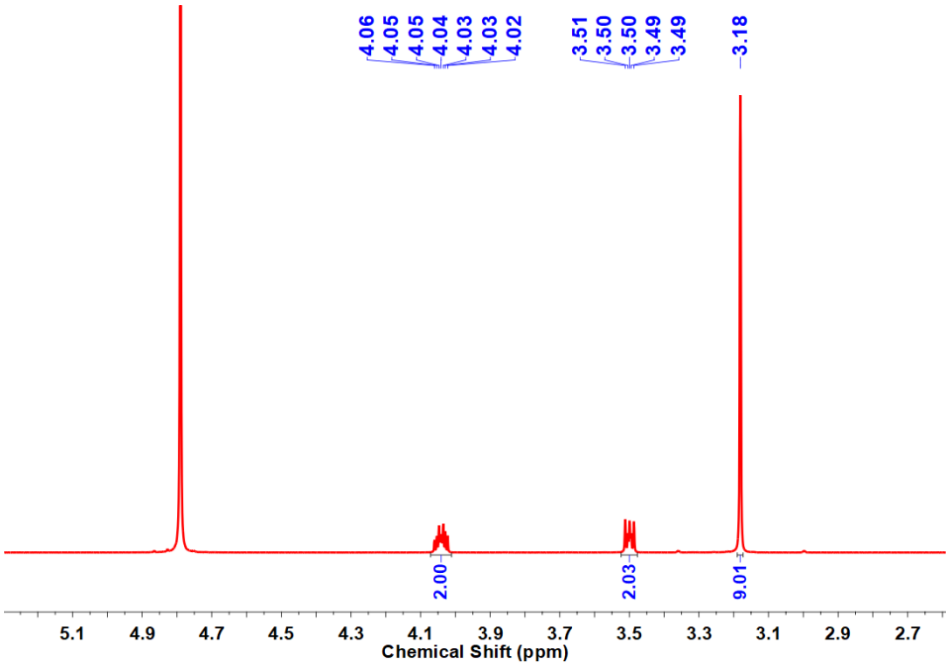

Figure 3A.7: ^{1}H NMR spectrum of **1.**

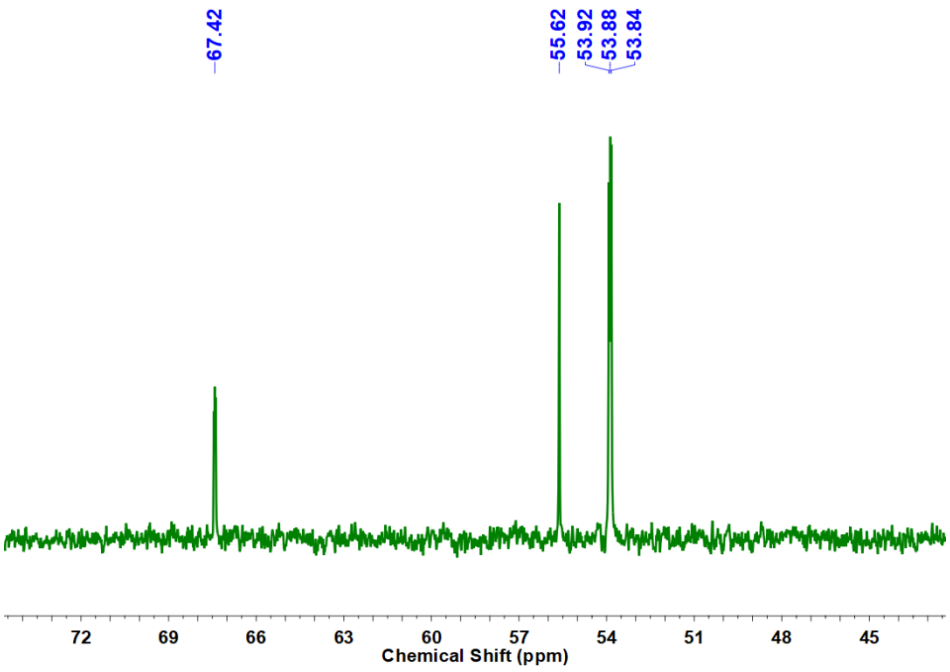

Figure 3A.8: ^{13}C NMR spectrum of **1**.

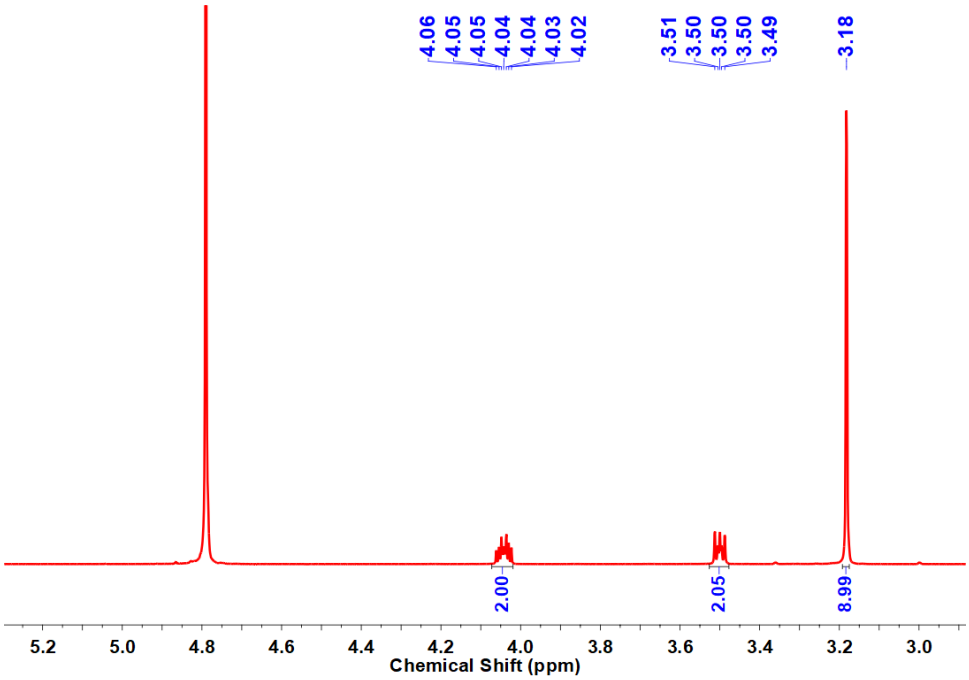

Figure 3A.9: ^{1}H NMR spectrum of **1**$_{HT}$.

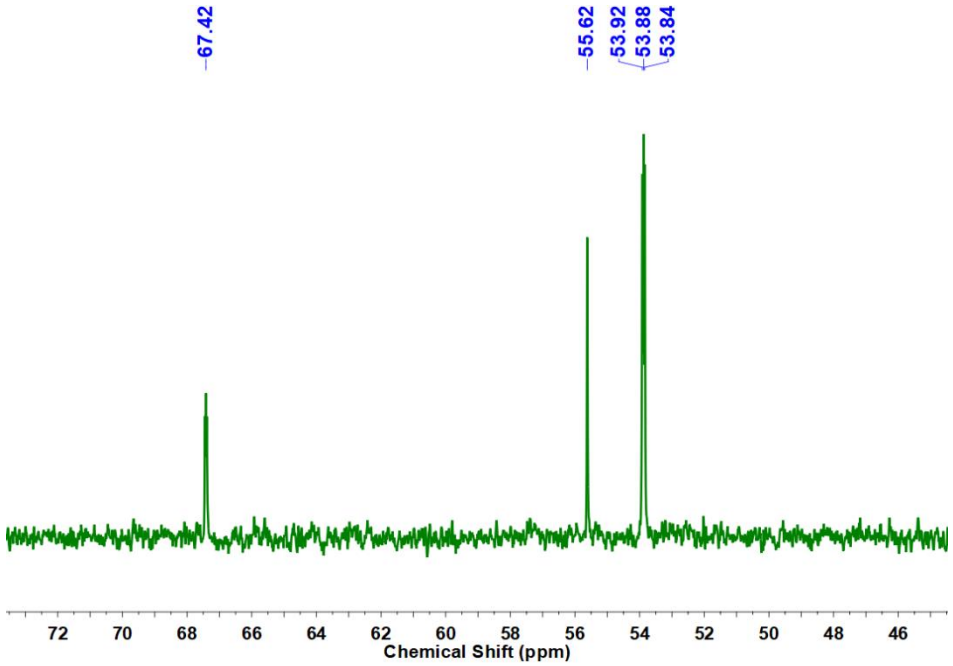

Figure 3A.10: ^{13}C NMR spectrum of **1**$_{HT}$.

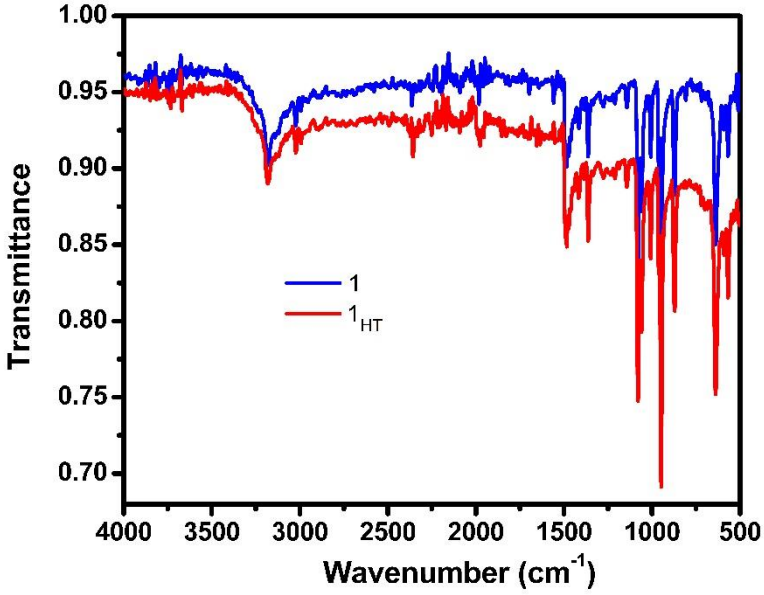

Figure 3A.11: Infrared Spectra of **1** and **1_{HT}**.

Table 3A.2. Point charge model analysis of **1**, (HETMA)$CdCl_3$.[a]

Atoms	Atom coordinates		Center Coordinates
X	X1 (0.480, 0.447, 0.093) X2 (0.520, 0.553, 0.593)	X3 (0.020, 0.947, 0.593) X4 (0.980, 0.053, 0.093)	(0.5, 0.5, 0.343)
N	N1 (0.31936, 0.0506, 0.4867) N2 (0.68064, 0.9494, 0.9867)	N3 (0.18064, 0.5506, 0.9867) N4 (0.81936, 0.4494, 0.4867)	(0.5, 0.5, 0.737)

[a] According to the crystal structure data collected at 298K, we select a unit cell and assume that the centers of the positive charges of the (HETMA) cations are located on the N atoms and the negative charges of the ($CdCl_5$ polyhedron) chains are located on the centroid (denoted as X) of 5 Cl^- ions. The polarization has been computed as given below.

$P_s = \lim \frac{1}{V} \sum q_i r_i$

$= (q_{Cd} r_{Cd} + q_N r_N) / V$

$= [(-e \times 0.343) + (e \times 0.737)] \times 4 \times c/V$

$= [0.394 \times 4 \times 1.6 \times 10^{-19} \times 7.811 \times 10^{-10}\ C\ m] / (1085.4 \times 10^{-30}\ m^3)$

$P_s = 18.1 \times 10^{-2}\ C\ m^{-2} = 18.1\ \mu C\ cm^{-2}$

Table 3A.3. Point charge model analysis of **1'**, (HETMA)$CdCl_3$.[a]

Atoms	Atom coordinates		Center Coordinates
Cd	Cd1 (0.4943, 0.750, 0.359) Cd2 (0.9943, 0.750, 0.359)	Cd3 (0.0057, 0.250, 0.859) Cd4 (0.5057, 0.250, 0.859)	(0.5, 0.5, 0.609)
N	N1 (0.250, 0.093, 0.282) N2 (0.250, 0.593, 0.782)	N3 (0.750, 0.407, 0.282) N4 (0.750, 0.907, 0.782)	(0.5, 0.5, 0.532)

[a] According to the crystal structure data collected at 363 K, we select a unit cell and assume that the centers of the positive charges of the (HETMA) cations and centers of the negative charges of the $(CdCl_3)_n^-$ chains are located on the N atoms and Cd atoms, respectively. The polarization has been computed as given below.

$P_s = \lim \frac{1}{V} \sum q_i r_i$

$= (q_{Cd} r_{Cd} + q_N r_N) / V$

$= [(-e \times 0.609) + (e \times 0.532)] \times 4 \times c/V$

$= [0.077 \times 4 \times 1.6 \times 10^{-19} \times 9.65 \times 10^{-10}\ C\ m] / (1084.39 \times 10^{-30}\ m^3)$

$P_s = 4.38 \times 10^{-2}\ C\ m^{-2} = 4.38\ \mu C\ cm^{-2}$

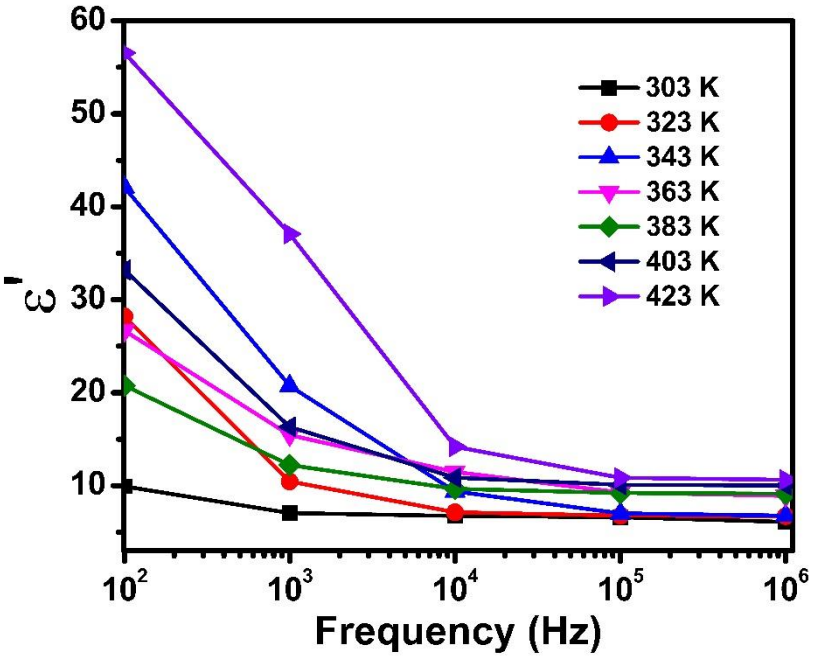

Figure 3A.12: Frequency dependence of the real part of the complex dielectric permittivity of **1** at various temperatures.

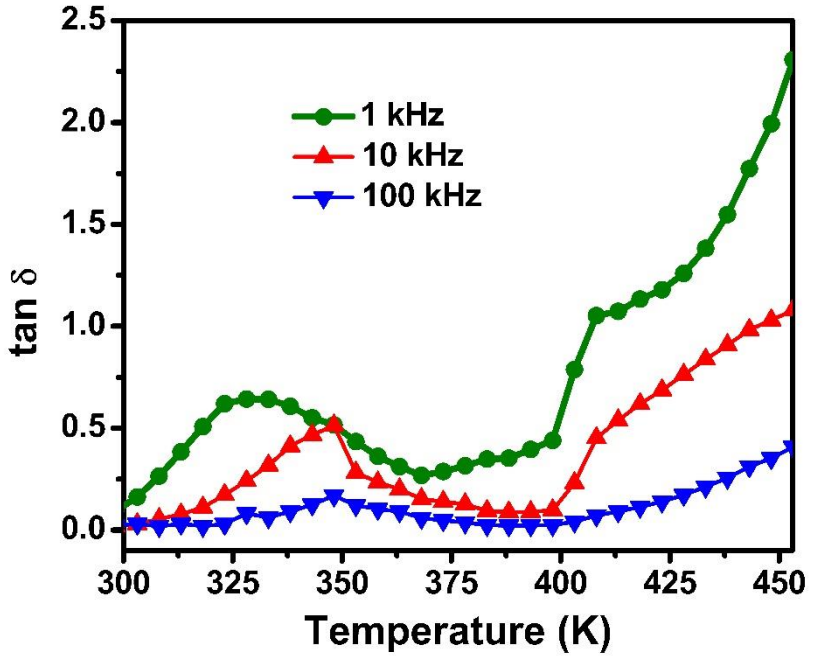

Figure 3A.13: Temperature dependent dielectric loss (tan δ) of **1** at various frequencies.

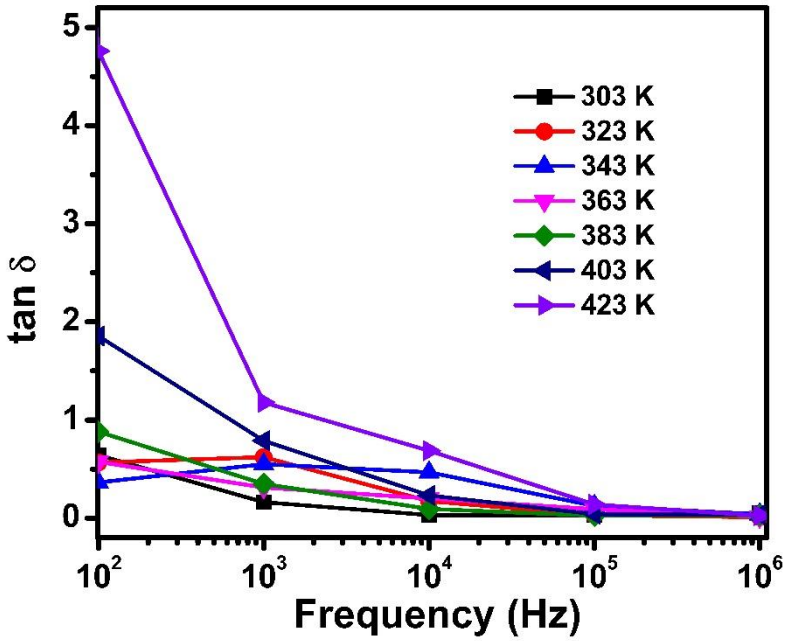

Figure 3A.14: Frequency dependent dielectric loss (tan δ) of **1** at various temperatures.

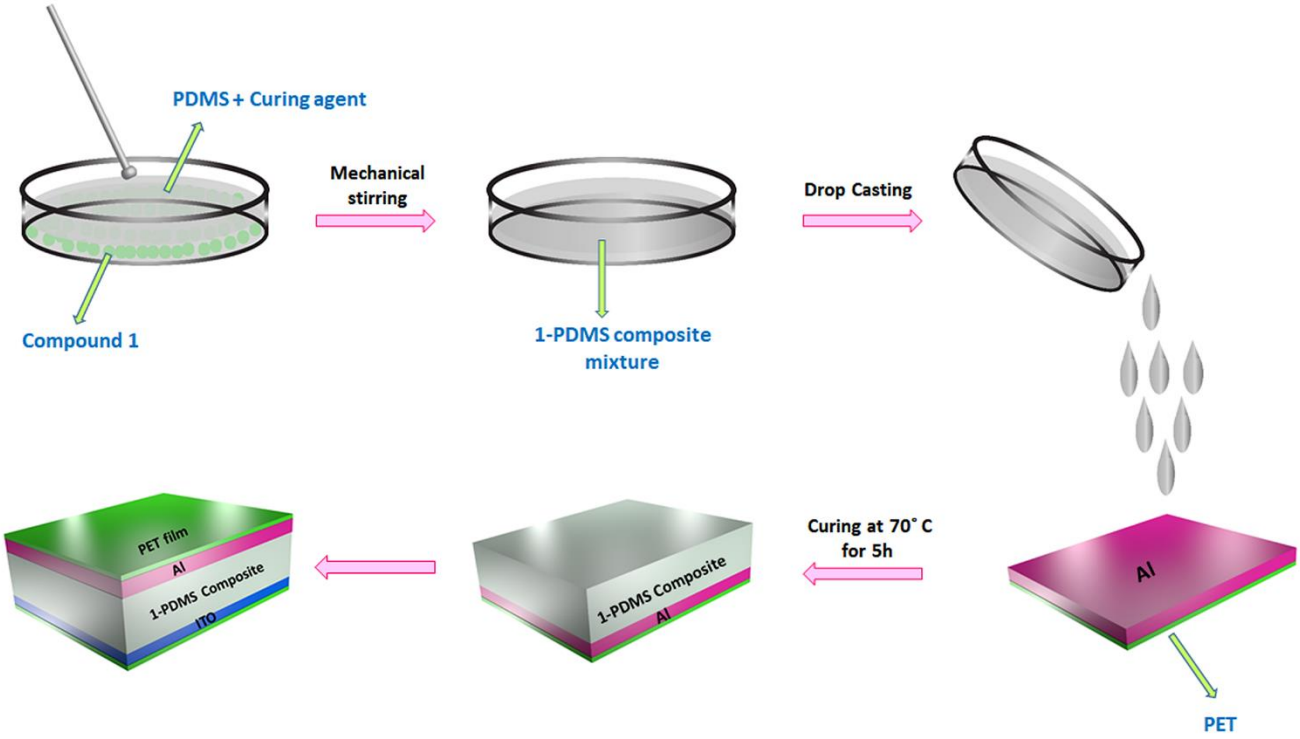

Figure 3A.15: Detailed fabrication procedure for the fabrication of **1**-PDMS composite mechanical energy harvesting device.

Table 3A.4. Detailed weight percentage calculations for **1**-PDMS composites

Composite Materials (%)	1 (in mg)	PDMS + curing agent (in mg)
5	29	550
10	61.1	550
15	97	550
20	137.5	550

Figure 3A.16: Flexible composites exhibiting (a) bending (b) rolling and (c) stretching operations.

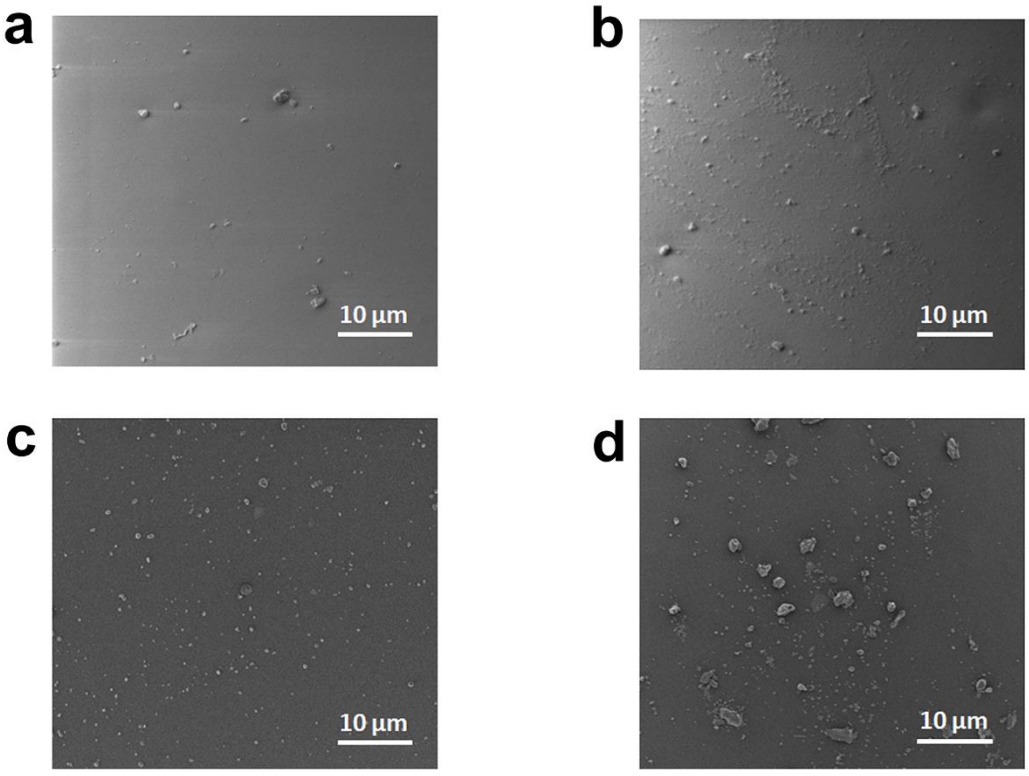

Figure 3A.17: SEM images of the (a) 5 (b) 10 (c) 15 and (d) 20 wt % **1**-PDMS composite films.

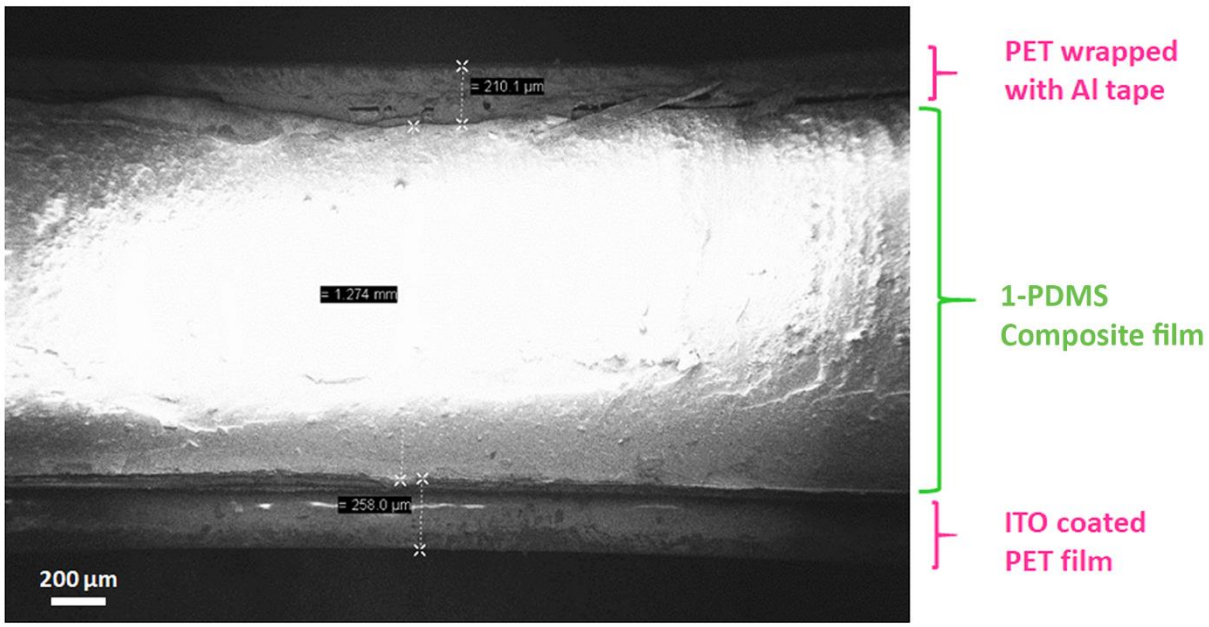

Figure 3A.18: Cross-sectional SEM image of **1**-PDMS based mechanical harvester showing a thickness of ~1.3 mm for the embedded film of **1**.

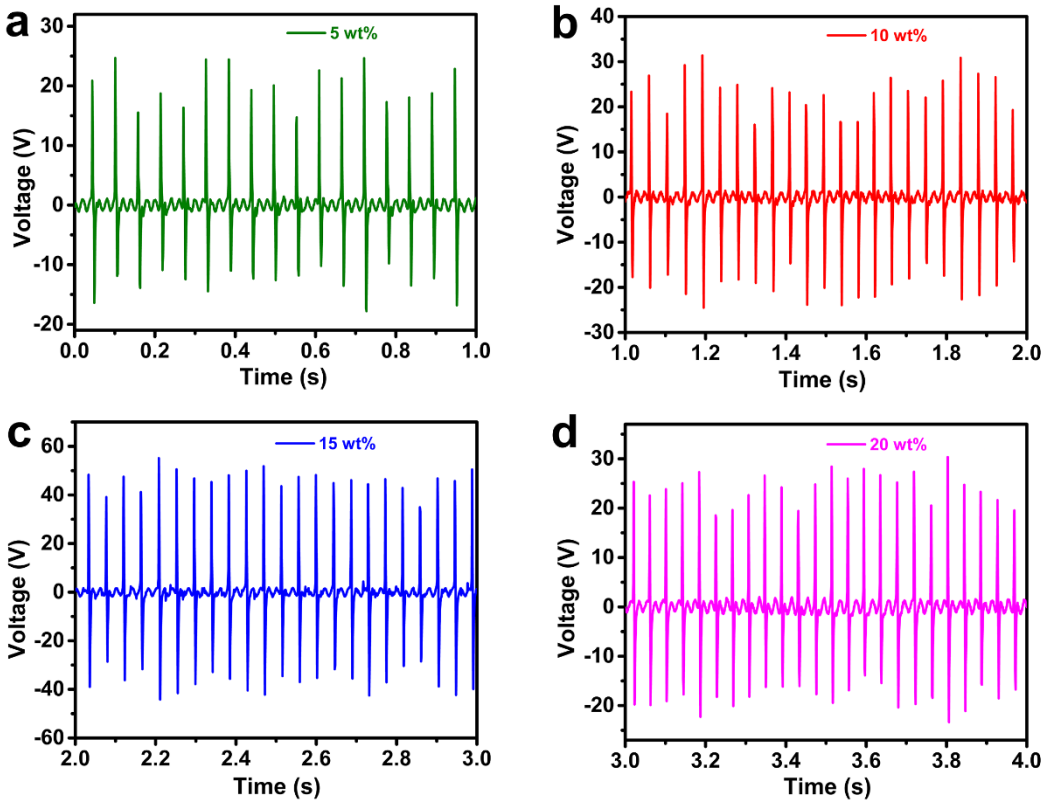

Figure 3A.19: Output voltage measurements for all the weight percentage of **1**-PDMS composite devices**.**

Table 3A.5. Output voltage of all weight % of **1**-PDMS composites

Composites (wt%)	Output Voltage (V)
5	24.7
10	31.4
15	55.2
20	30.4

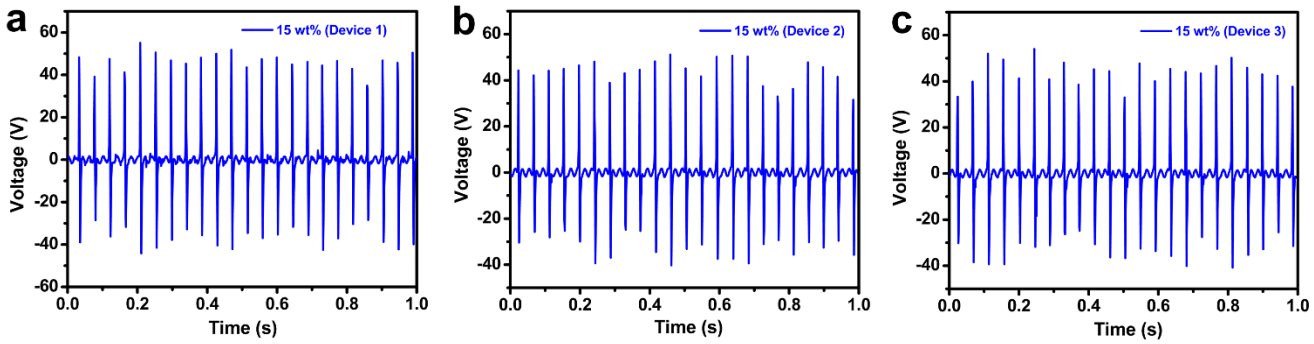

Figure 3A.20: Open circuit voltage measurements performed on three independent 15 wt % **1**-PDMS composite devices.

Table 3A.6. Average Open Circuit Voltage (V_{oc}) of 15 wt % of **1**-PDMS composite device

	Device 1	Device 2	Device 3	Average Open Circuit Voltage (V_{oc})
Open Circuit Voltage (V_{oc})	55.2	51.2	54.0	53.5

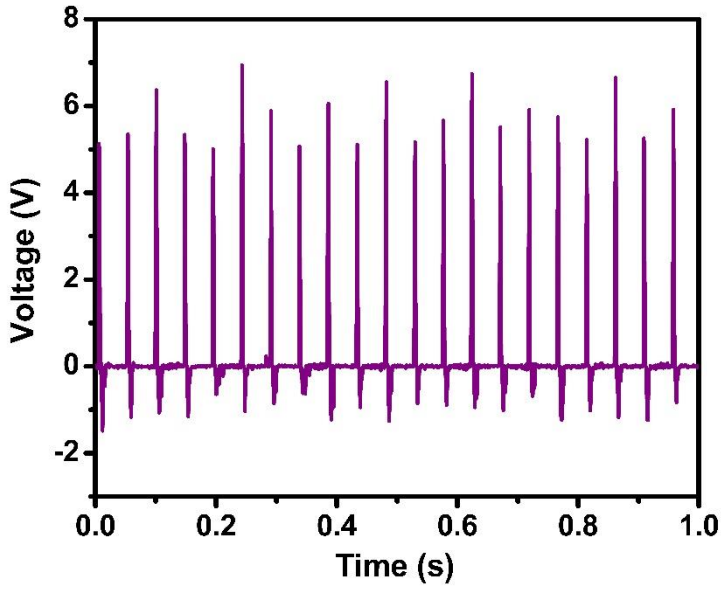

Figure 3A.21: Output voltage generation from the pure PDMS device**.**

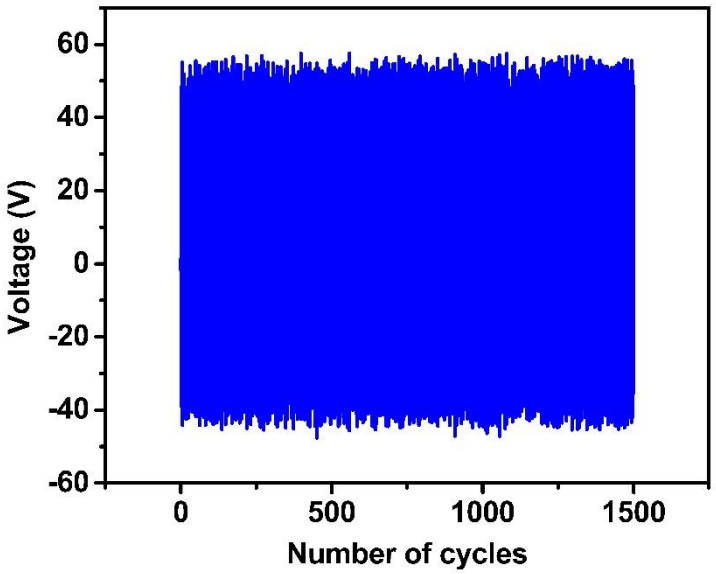

Figure 3A.22: Mechanical durability test performed on the 15 wt % **1-**PDMS device with an applied force of 40 N and frequency of 25 Hz.

****

Table 4A.1: Selected bond lengths [Å] and angles [°] for compound **MTPBB**.

Compound	Bond Length		Bond Angle	
MTPBB	Bi(1)-Br(1)$^{\#2}$	2.716(2)	Br(1)$^{\#2}$-Bi(1)-Br(1)$^{\#1}$	92.17(7)
120 K	Bi(1)-Br(1)$^{\#1}$	2.716(2)	Br(1)$^{\#2}$-Bi(1)-Br(1)	92.17(7)
	Bi(1)-Br(1)	2.716(2)	Br(1)$^{\#1}$-Bi(1)-Br(1)	92.17(7)
	Bi(1)-Br(2)	3.061(2)	Br(1)$^{\#2}$-Bi(1)-Br(2)	91.18(7)
	Bi(1)-Br(2)$^{\#2}$	3.061(2)	Br(1)$^{\#1}$-Bi(1)-Br(2)	170.99(7)
	Bi(1)-Br(2)$^{\#1}$	3.061(2)	Br(1)-Bi(1)-Br(2)	96.06(6)
	Bi(2)-Br(3)$^{\#2}$	2.787(2)	Br(1)$^{\#2}$-Bi(1)-Br(2)$^{\#2}$	96.06(6)
	Bi(2)-Br(3)$^{\#1}$	2.787(2)	Br(1)$^{\#1}$-Bi(1)-Br(2)$^{\#2}$	91.18(7)
	Bi(2)-Br(3)	2.787(2)	Br(1)-Bi(1)-Br(2)$^{\#2}$	170.99(7)
	Bi(2)-Br(2)	2.971(2)	Br(2)-Bi(1)-Br(2)$^{\#2}$	80.15(6)
	Bi(2)-Br(2)$^{\#2}$	2.971(2)	Br(1)$^{\#2}$-Bi(1)-Br(2)$^{\#1}$	170.99(7)
	Bi(2)-Br(2)$^{\#1}$	2.971(2)	Br(1)$^{\#1}$-Bi(1)-Br(2)$^{\#1}$	96.06(6)
	C(1)-P(1)	1.78(2)	Br(1)-Bi(1)-Br(2)$^{\#1}$	91.18(7)
	P(1)-C(21)	1.77(3)	Br(2)-Bi(1)-Br(2)$^{\#1}$	80.15(6)
	P(1)-C(11)	1.77(2)	Br(2)$^{\#2}$-Bi(1)-Br(2)$^{\#1}$	80.15(6)
	P(1)-C(11')	1.78(3)	Br(3)$^{\#2}$-Bi(2)-Br(3)$^{\#1}$	94.32(6)
	P(1)-C(21')	1.790(19)	Br(3)$^{\#2}$-Bi(2)-Br(3)	94.32(6)
	P(1)-C(31)	1.81(2)	Br(3)$^{\#1}$-Bi(2)-Br(3)	94.32(6)
			Br(3)$^{\#2}$-Bi(2)-Br(2)	171.94(7)
			Br(3)$^{\#1}$-Bi(2)-Br(2)	89.82(6)
			Br(3)-Bi(2)-Br(2)	92.25(6)
			Br(3)$^{\#2}$-Bi(2)-Br(2)$^{\#2}$	92.25(6)
			Br(3)$^{\#1}$-Bi(2)-Br(2)$^{\#2}$	171.94(7)
			Br(3)-Bi(2)-Br(2)$^{\#2}$	89.82(6)
			Br(2)-Bi(2)-Br(2)$^{\#2}$	83.10(6)
			Br(3)$^{\#2}$-Bi(2)-Br(2)$^{\#1}$	89.83(6)
			Br(3)$^{\#1}$-Bi(2)-Br(2)$^{\#1}$	92.25(6)
			Br(3)-Bi(2)-Br(2)$^{\#1}$	171.94(7)
			Br(2)-Bi(2)-Br(2)$^{\#1}$	83.10(6)
			Br(2)$^{\#2}$-Bi(2)-Br(2)$^{\#1}$	83.10(6)
			Bi(2)-Br(2)-Bi(1)	81.99(5)
			C(21)-P(1)-C(11)	124(2)
			C(21)-P(1)-C(1)	104.9(18)
			C(11)-P(1)-C(1)	108.0(13)
			C(11')-P(1)-C(1)	106(2)
			C(11')-P(1)-C(21')	114(2)
			C(1)-P(1)-C(21')	108.4(12)
			C(21)-P(1)-C(31)	95(2)
			C(11)-P(1)-C(31)	113.0(12)
			C(11')-P(1)-C(31)	105(2)
			C(1)-P(1)-C(31)	110.4(9)
			C(21')-P(1)-C(31)	112.4(10)
MTPBB	Bi(1)-Br(1)$^{\#1}$	2.783(2)	Br(1)$^{\#1}$-Bi(1)-Br(1)	94.09(7)
298 K	Bi(1)-Br(1)	2.783(2)	Br(1)$^{\#1}$-Bi(1)-Br(1)$^{\#2}$	94.09(7)
	Bi(1)-Br(1)$^{\#2}$	2.783(2)	Br(1)-Bi(1)-Br(1)$^{\#2}$	94.09(7)

	Bi(1)-Br(2)$^{\#2}$	2.978(2)	Br(1)$^{\#1}$-Bi(1)-Br(2)$^{\#2}$	171.80(7)
	Bi(1)-Br(2)$^{\#1}$	2.978(2)	Br(1)-Bi(1)-Br(2)$^{\#2}$	92.79(7)
	Bi(1)-Br(2)	2.978(2)	Br(1)$^{\#2}$-Bi(1)-Br(2)$^{\#2}$	89.86(7)
	Bi(2)-Br(3)$^{\#2}$	2.714(2)	Br(1)$^{\#1}$-Bi(1)-Br(2)$^{\#1}$	89.86(7)
	Bi(2)-Br(3)$^{\#1}$	2.714(2)	Br(1)-Bi(1)-Br(2)$^{\#1}$	171.80(7)
	Bi(2)-Br(3)	2.714(2)	Br(1)$^{\#2}$-Bi(1)-Br(2)$^{\#1}$	92.79(7)
	Bi(2)-Br(2)	3.060(2)	Br(2)$^{\#2}$-Bi(1)-Br(2)$^{\#1}$	82.77(7)
	Bi(2)-Br(2)$^{\#2}$	3.060(2)	Br(1)$^{\#1}$-Bi(1)-Br(2)	92.79(7)
	Bi(2)-Br(2)$^{\#1}$	3.060(2)	Br(1)-Bi(1)-Br(2)	89.86(7)
	P(1)-C(21)	1.76(2)	Br(1)$^{\#2}$-Bi(1)-Br(2)	171.80(7)
	P(1)-C(21')	1.76(2)	Br(2)$^{\#2}$-Bi(1)-Br(2)	82.77(7)
	P(1)-C(11')	1.77(2)	Br(2)$^{\#1}$-Bi(1)-Br(2)	82.77(7)
	P(1)-C(11)	1.77(2)	Br(3)$^{\#2}$-Bi(2)-Br(3)$^{\#1}$	92.04(8)
	P(1)-C(31)	1.79(2)	Br(3)$^{\#2}$-Bi(2)-Br(3)	92.04(8)
	P(1)-C(1)	1.804(18)	Br(3)$^{\#1}$-Bi(2)-Br(3)	92.04(8)
			Br(3)$^{\#2}$-Bi(2)-Br(2)	91.39(7)
			Br(3)$^{\#1}$-Bi(2)-Br(2)	96.05(7)
			Br(3)-Bi(2)-Br(2)	171.10(7)
			Br(3)$^{\#2}$-Bi(2)-Br(2)$^{\#2}$	171.10(7)
			Br(3)$^{\#1}$-Bi(2)-Br(2)$^{\#2}$	91.39(7)
			Br(3)-Bi(2)-Br(2)$^{\#2}$	96.05(7)
			Br(2)-Bi(2)-Br(2)$^{\#2}$	80.08(7)
			Br(3)$^{\#2}$-Bi(2)-Br(2)$^{\#1}$	96.04(7)
			Br(3)$^{\#1}$-Bi(2)-Br(2)$^{\#1}$	171.10(7)
			Br(3)-Bi(2)-Br(2)$^{\#1}$	91.40(7)
			Br(2)-Bi(2)-Br(2)$^{\#1}$	80.08(7)
			Br(2)$^{\#2}$-Bi(2)-Br(2)$^{\#1}$	80.08(7)
			Bi(1)-Br(2)-Bi(2)	82.27(6)
			C(21')-P(1)-C(11')	115.3(17)
			C(21)-P(1)-C(11)	102.3(17)
			C(21)-P(1)-C(31)	114.6(15)
			C(21')-P(1)-C(31)	104.3(15)
			C(11')-P(1)-C(31)	110.9(12)
			C(11)-P(1)-C(31)	112.7(13)
			C(21)-P(1)-C(1)	102.6(16)
			C(21')-P(1)-C(1)	113.9(15)
			C(11')-P(1)-C(1)	103.1(14)
			C(11)-P(1)-C(1)	114.8(14)
			C(31)-P(1)-C(1)	109.4(10)

Symmetry transformations used to generate equivalent atoms:
#1 -x+y+1,-x+1,z #2 -y+1,x-y,z

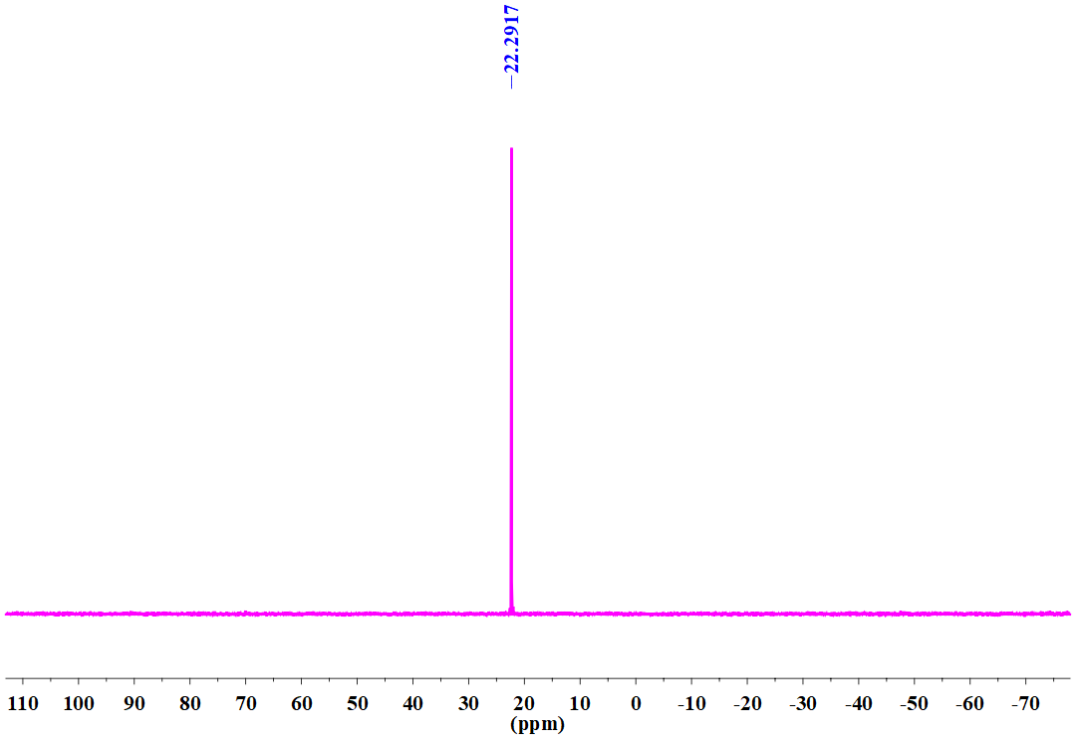

Figure 4A.1: ^{31}P NMR spectrum of **MTPBB.**

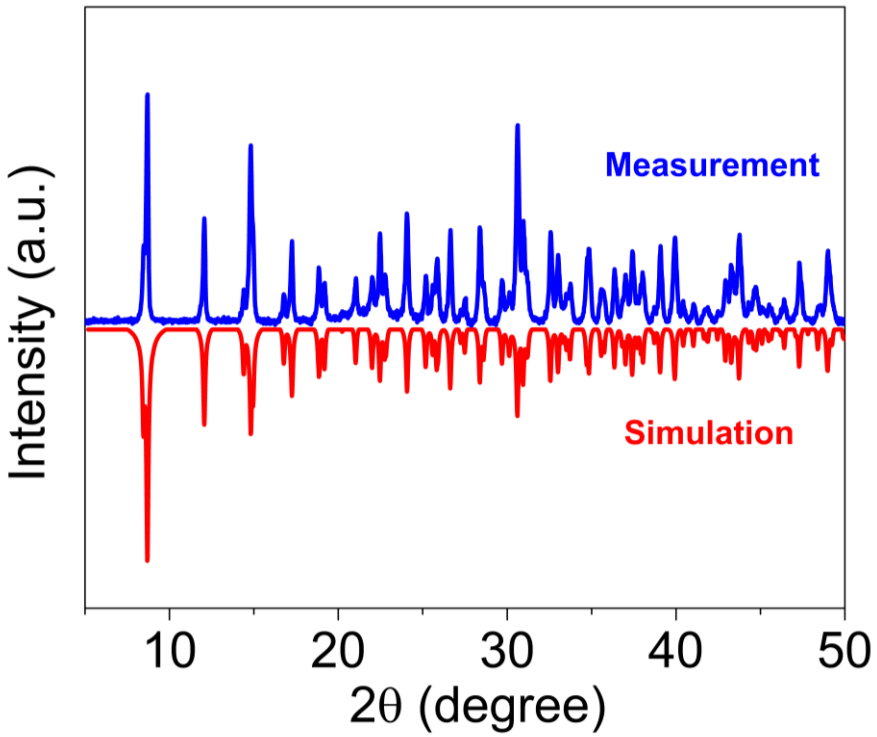

Figure 4A.2: PXRD Patterns of **MTPBB.**

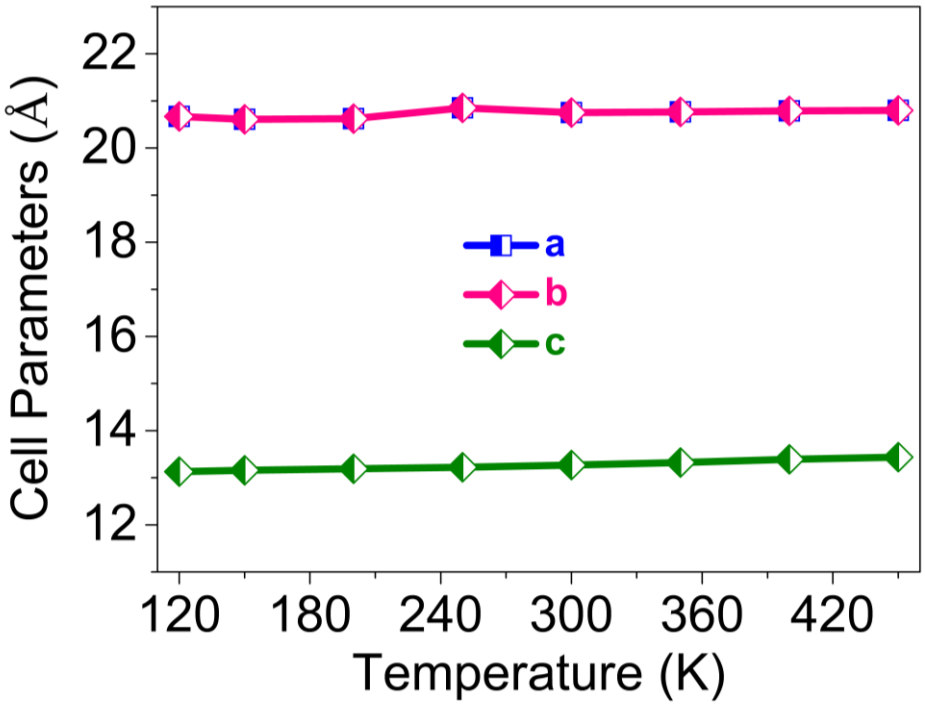

Figure 4A.3: The unit cell parameters of **MTPBB** at various temperature obtained from single crystal X-ray diffraction data

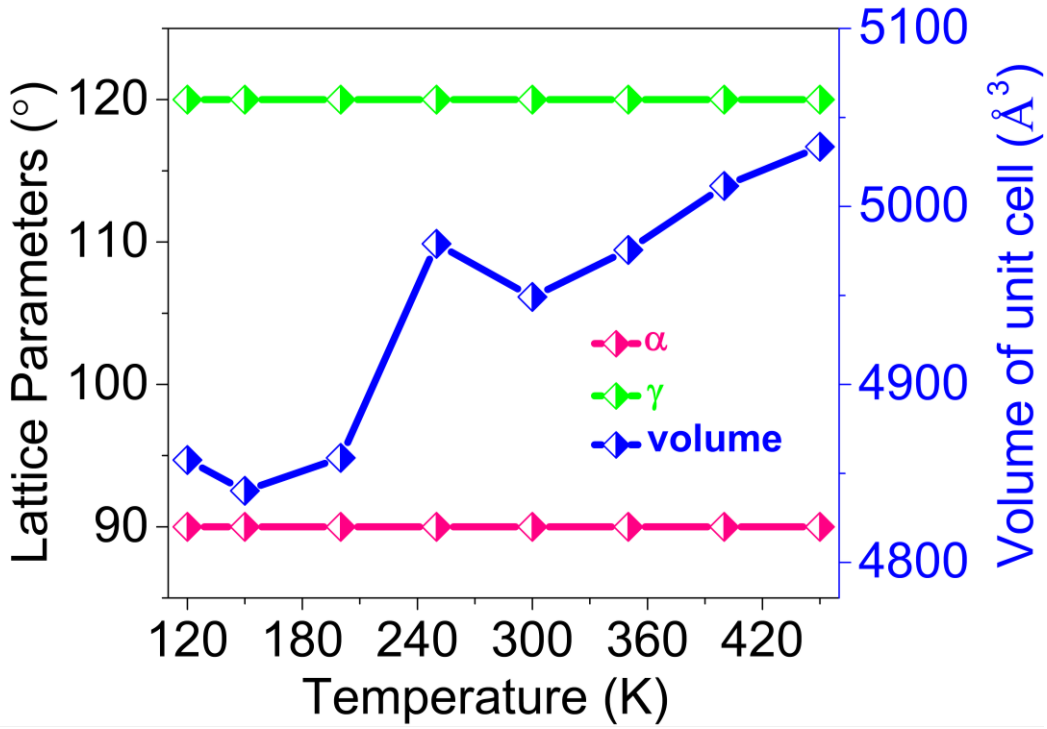

Figure 4A.4: The lattice parameters of **MTPBB** at various temperature obtained from single crystal X-ray diffraction data.

Table 4A.2: Unit cell parameters of **MTPBB** drawn from single crystal X-ray diffraction at various temperatures.

Temperature (K)	a=b (Å)	c (Å)	α=β (˚)	ɣ (˚)	Volume (Å^3)
120	20.670(3)	13.128(4)	90	120	4857.47
150	20.609(5)	13.159(9)	90	120	4840.25
200	20.624(11)	13.190(18)	90	120	4858.71
250	20.853(10)	13.222(6)	90	120	4978.97
300	20.753(4)	13.269(7)	90	120	4949.15
350	20.766(4)	13.323(7)	90	120	4975.52
400	20.788(4)	13.391(7)	90	120	5011.52
450	20.798(6)	13.437(11)	90	120	5033.57

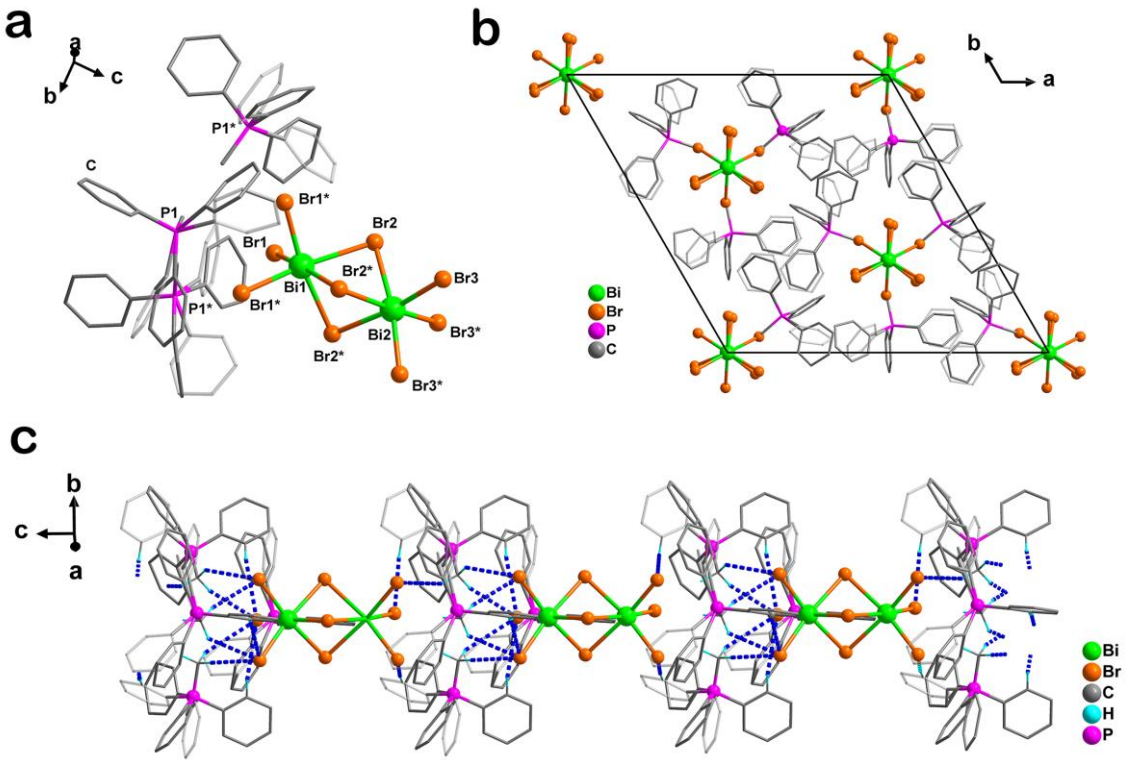

Figure 4A.5: (a) Molecular structure of **MTPBB** and (b) its Packing diagram viewed along the polar c-axis at 120 K. The disordered phenyl fragments are shown as semi-transparent motifs. Note the differences in the disorder of the phenyl rings at 298 and 120 K data. As observed at 298 K structure, the phosphonium cations are located along the edges of the triangle formed around the C3 axis. (c) The hydrogen-bonded structure of **MTPBB** along the polar axis mediated by C-H···Br interactions at 120 K.

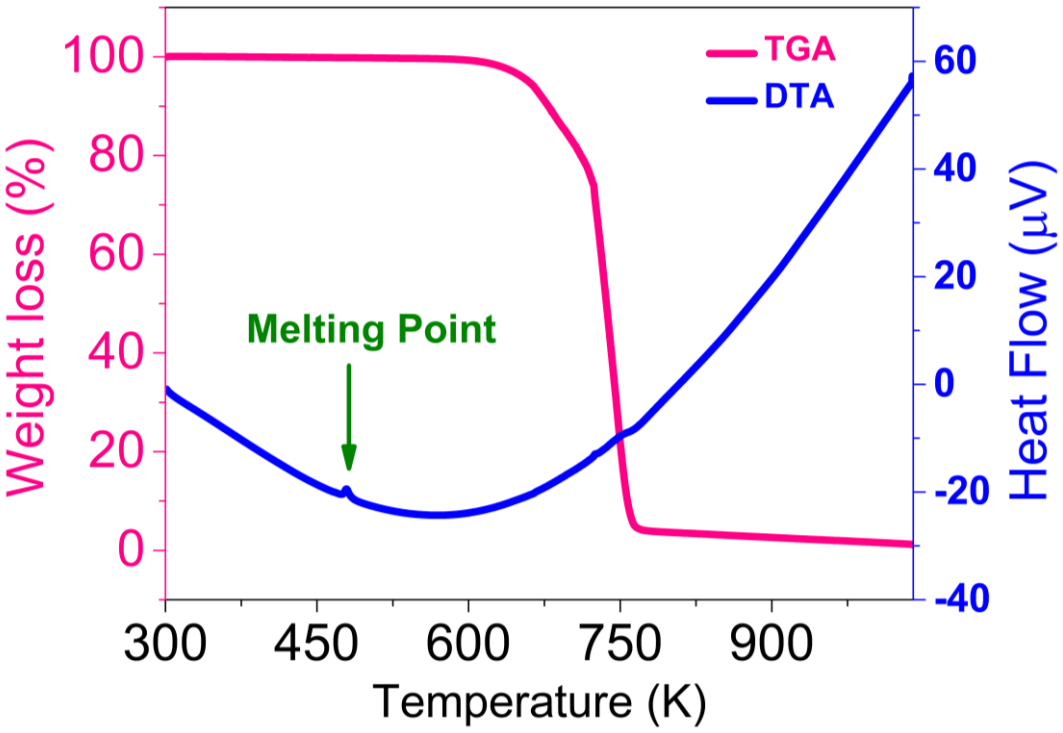

Figure A4.6: TGA-DTA data of **MTPBB.**

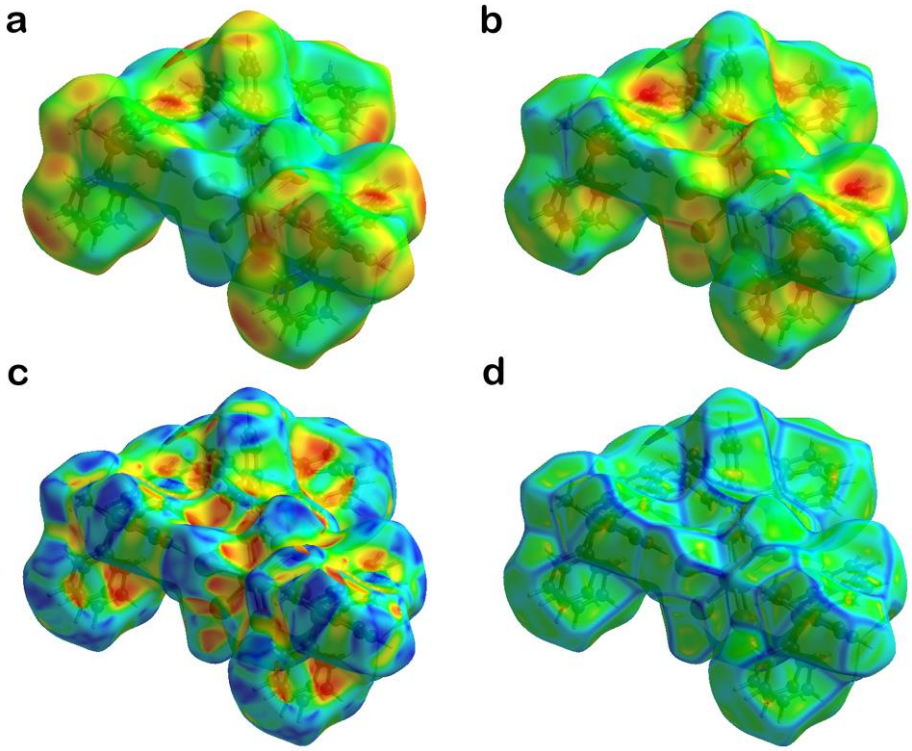

Figure 4A.7: The 3D colour mapping Hirshfield surface analysis of **MTPBB** at 298 K showing (a) de, (b) di, (c) shape index and (d) curvedness**.**

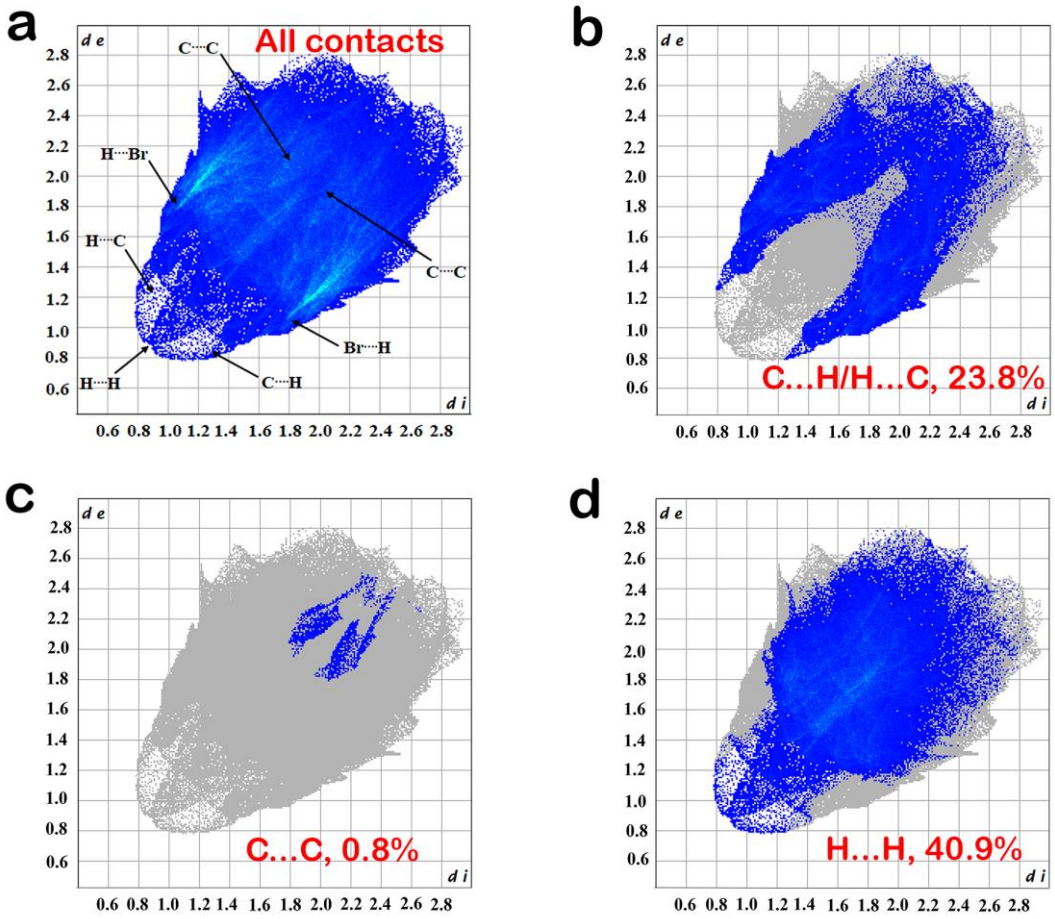

Figure 4A.8: 2D Fingerprint plot (de vs di) of **MTPBB** at 298 K**.**

Table 4A.3: Hirshfield surface analysis of **MTPBB** at 298 K**.**

Surface Property	Range (Minimum/Maximum)	Globularity and Asphericity	Surface volume (Å^3) and Area (Å^2)
d_i	0.7870/2.9684	0.607 and 0.232	1631.57 and 1104.08
d_e	0.7866/2.8292		
d_{norm}	-0.5396/1.4460		
Shape index	-0.9976/0.9994		
Curvedness	-3.4119/0.2623		

Table 4A.4: Non-classical hydrogen bonding distances (Å) and angles (˚) for **MTPBB** at 120 K.

D-H…A	d(H…A) Å	d(D…A) Å	<(DHA)˚	Symmetry transformations to generate equivalent atoms
C1-H1B···Br3	2.99	3.86(2)	148.1	-y+1, x-y, z-1
C1-H1C···Br1	3.15	3.83(2)	128.3	x, y, z
C1-H1A···Br3	3.01	3.87(2)	146.3	-x+y+1, -x+1, z-1
C22-H22···Br3	2.98	3.77(5)	140.6	x-1/3, y+1/3, z-2/3
C26'-H26'···Br1	2.90	3.84(3)	174.5	x, y, z
C36-H36···Br3	3.14	3.94(2)	142.5	-y+1, x-y, z-1

Table 4A.5: Non-classical hydrogen bonding distances (Å) and angles (˚) for **MTPBB** at 298 K.

D-H…A	d(H…A) Å	d(D…A) Å	<(DHA)˚	Symmetry transformations to generate equivalent atoms
C12-H12···Br3	2.89	3.82(4)	174.7	-y+2/3, x-y+1/3, z-2/3
C12'-H12'···Br3	2.95	3.88(4)	175.3	-y+2/3, x-y+1/3, z-2/3
C1-H1B···Br3	3.11	3.93(2)	143.9	-y+2/3, x-y+1/3, z-2/3
C1-H1C···Br1	2.96	3.90(2)	166.9	-x+y+2/3, -x+4/3, z+1/3

Table 4A.6. Point charge model analysis of **MTPBB.**

According to the crystal structure data collected at 298 K, we select a unit cell and assume that the centers of the positive charges of the cations are located on P and Bi atoms and the negative charges of the anions are located on the Br atoms.

Atoms (count)	Center Coordinates
P^{+} (9)	(0.444, 0.556, 0.380)
Bi^{3+} (4)	(0.5, 0.5, 0.475)
$Bi^{6/8+}$ (8)	(0.5, 0.5, 0.225)
Br^{-}(27)	(0.519, 0.481, 0.558)

Along c-axis

$P_s = \lim \frac{1}{V} \sum q_i r_i$

$= (q_P r_p + q_{Bi} r_{Bi} - q_{Br} r_{Br}) / V$

$= (0.380 \times 9 + 0.475 \times 4 \times 3 + 0.225 \times 8 \times 6/8 - 0.558 \times 27) \times 1.6 \times 10^{-19} \times 13.269 \times 10^{-10}$ Cm/ $(4949.15 \times 10^{-30}\ m^3)$

$= 19.7 \times 10^{-2}\ Cm^{-2}$

$P_s = 19.7\ \mu Ccm^{-2}$

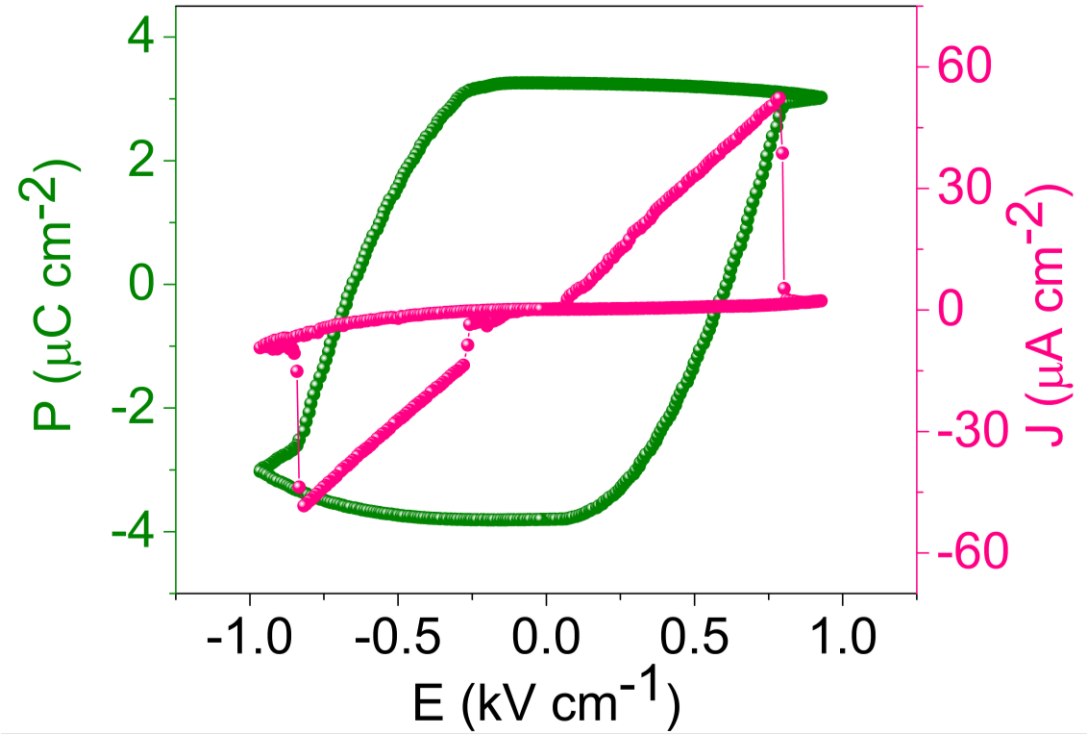

Figure 4A.9: P-E hysteresis loop and leakage current density plot of **MTPBB** single crystal measured at 0.8 Hz at room temperature**..**

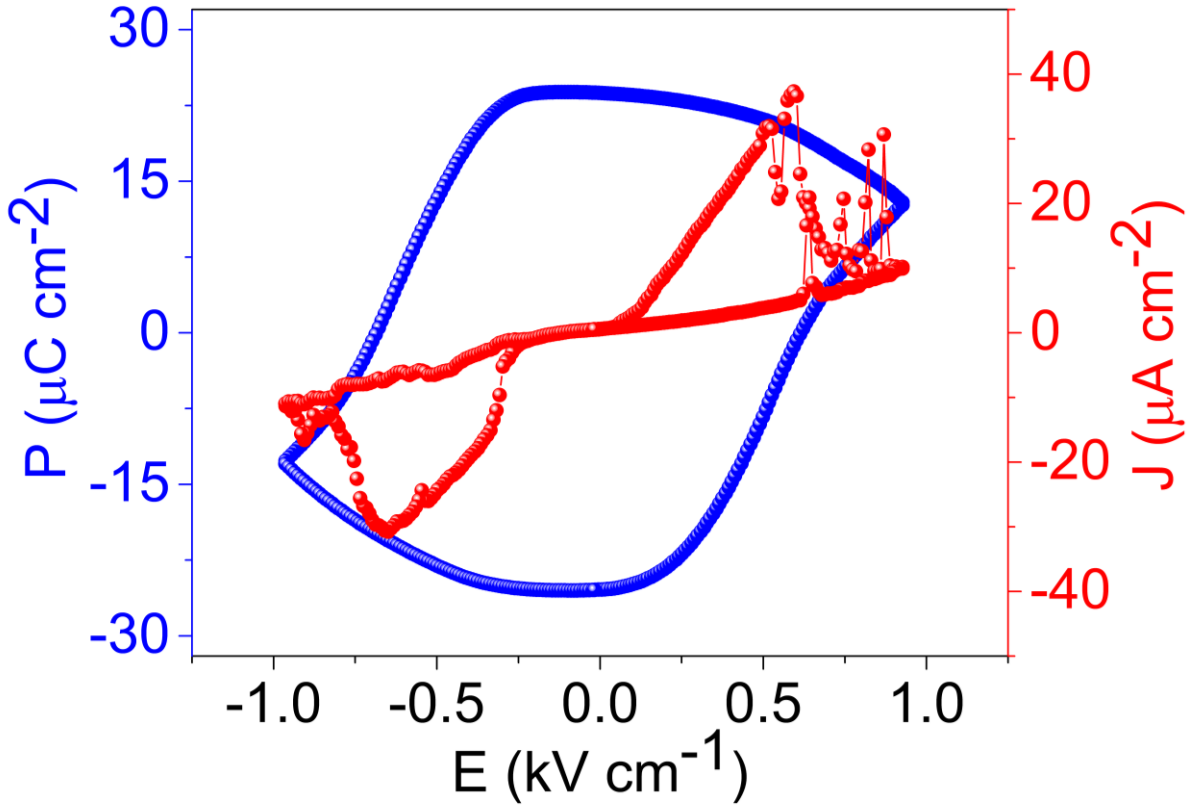

Figure 4A.10: P-E hysteresis loop and leakage current density plot of **MTPBB** single crystal measured at 0.1 Hz at room temperature**.**

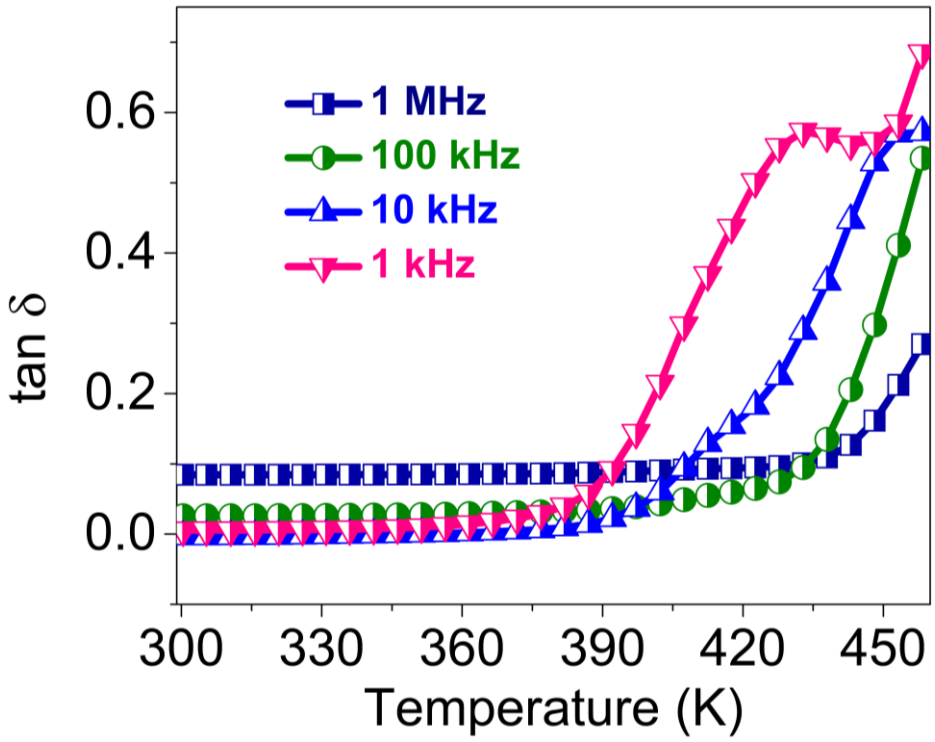

Figure 4A.11: Temperature dependent dielectric loss (tan δ) of **MTPBB** at various frequencies.

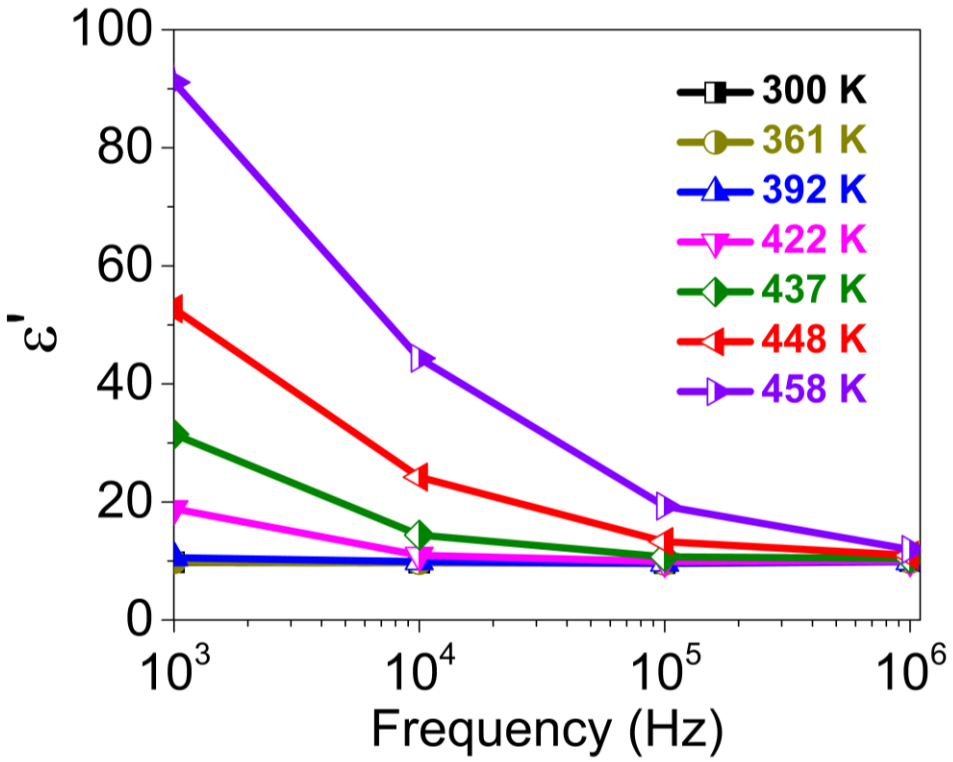

Figure 4A.12: Frequency-dependent dielectric constant (ε′) of **MTPBB** at various temperatures.

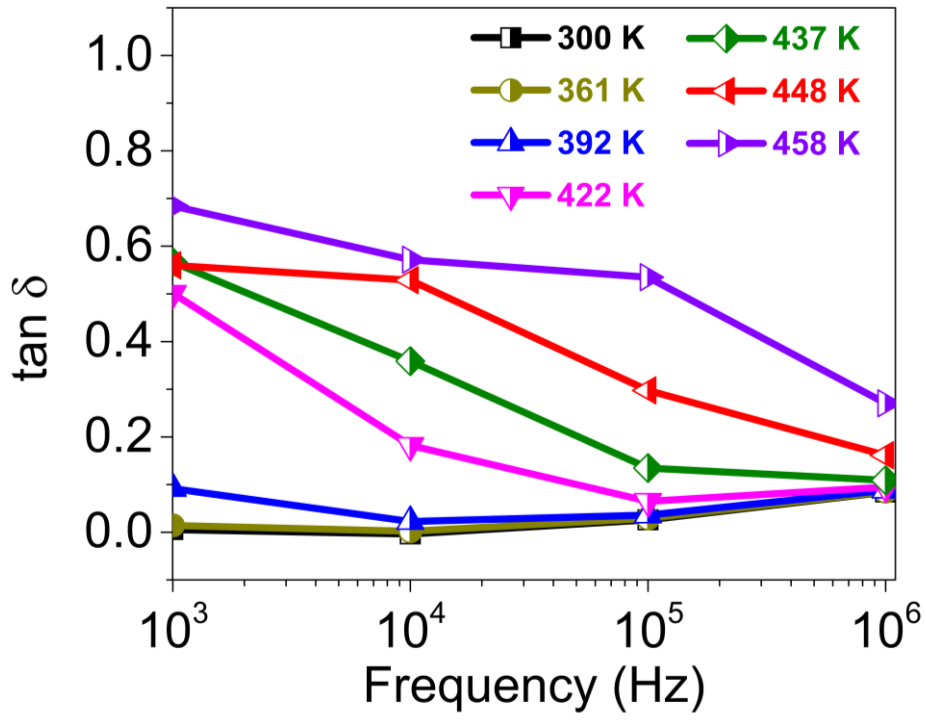

Figure 4A.13: Frequency dependent dielectric loss (tan δ) of **MTPBB** at various temperatures.

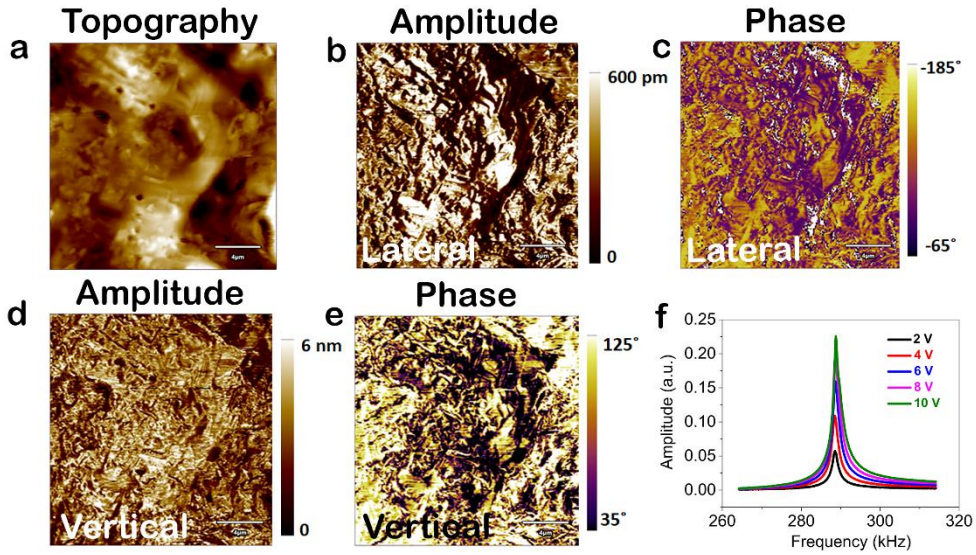

Figure 4A.14: (a) Topography of the single crystal surface. (b) Lateral PFM amplitude and (c) phase images. (d) vertical PFM amplitude and (e) phase images recorded on a single crystal of **MTPBB**. (f) PFM resonance peaks under a set of drive voltages.

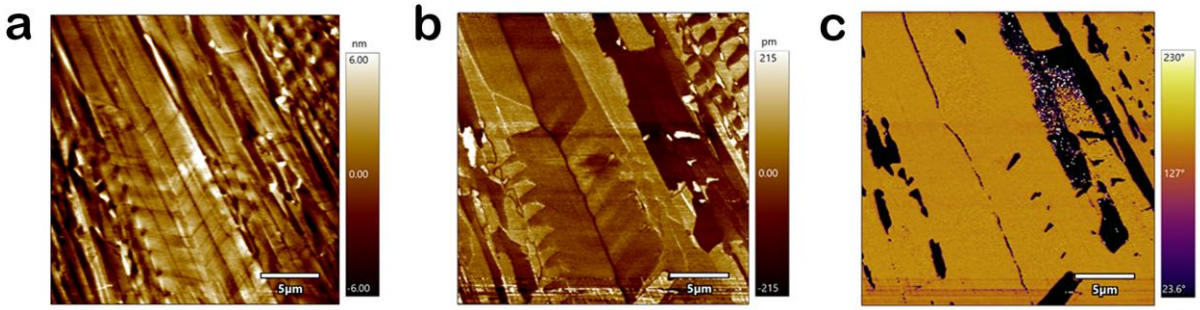

Figure 4A.15: (a) Topography (b) Vertical PFM amplitude and (c) phase images recorded on thin film of **MTPBB**.

Figure 4A.16: Photograph of the broken crystal while performing d_{33} measurements on piezometer

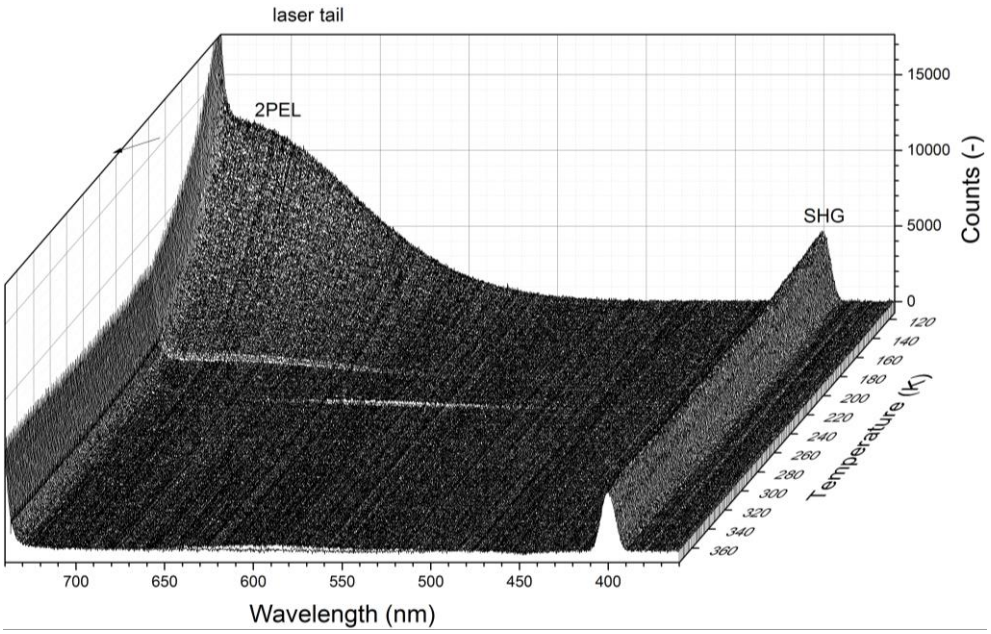

Figure 4A.17: Temperature dependent two-photon excitation luminescence (2PEL) of **MTPBB.**

Table 4A.7: Detailed weight percentage calculations for **MTPBB/PDMS** composites.

Composite Materials (%)	**MTPBB(in mg)**	**PDMS + curing agent (in mg)**
5	29	550
10	61.1	550
15	97	550
20	137.5	550
25	183.3	550

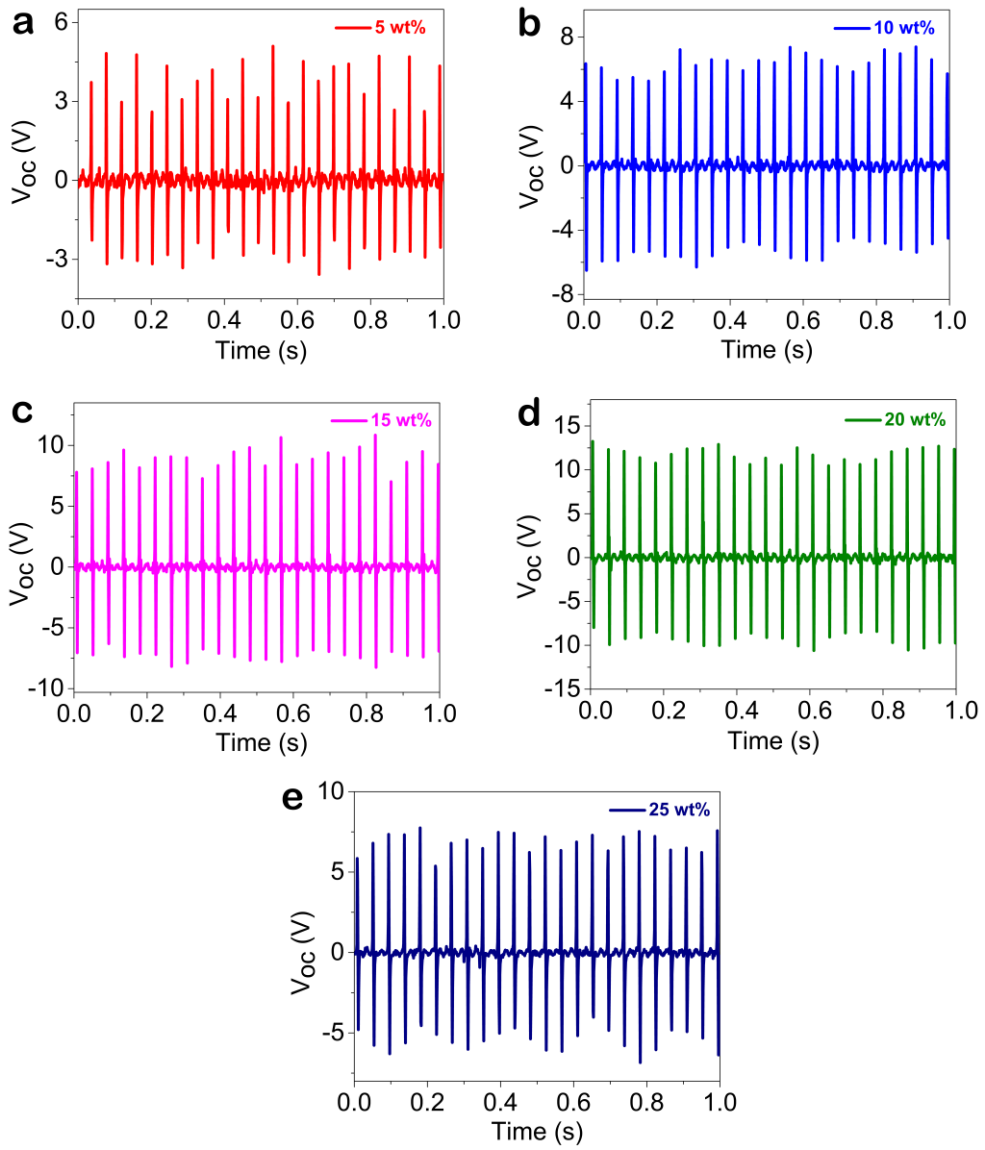

Figure 4A.18: Output Voltage measurements of all the weight % **MTPBB/PDMS** composite films.

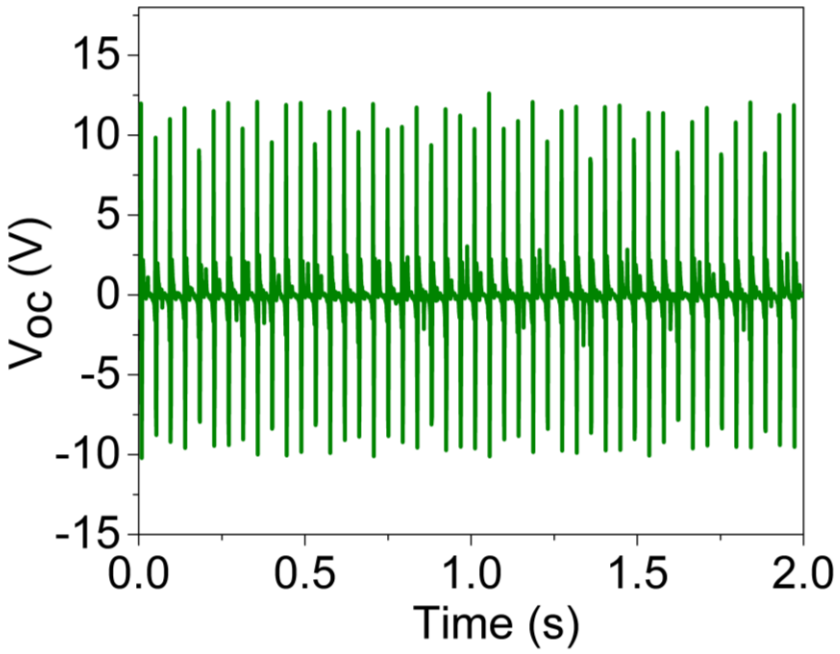

Figure 4A.19: Output Voltage measurement of poled (25 kV, 2h) 20 wt % **MTPBB/PDMS** composite device.

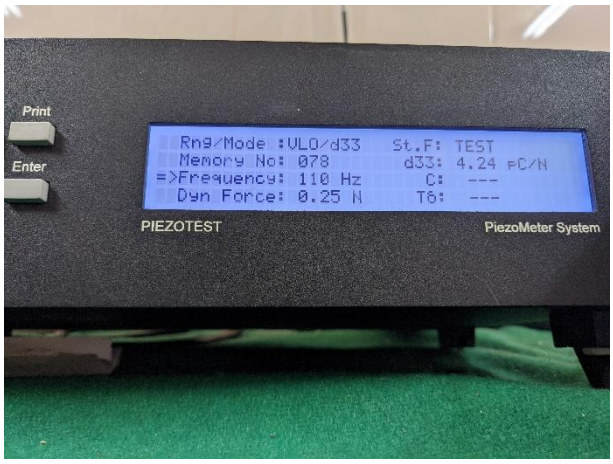

Figure 4A.20: Photograph of the piezometer displaying the d_{33} value obtained on an of unpoled 20 wt% **MTPBB/PDMS** film.

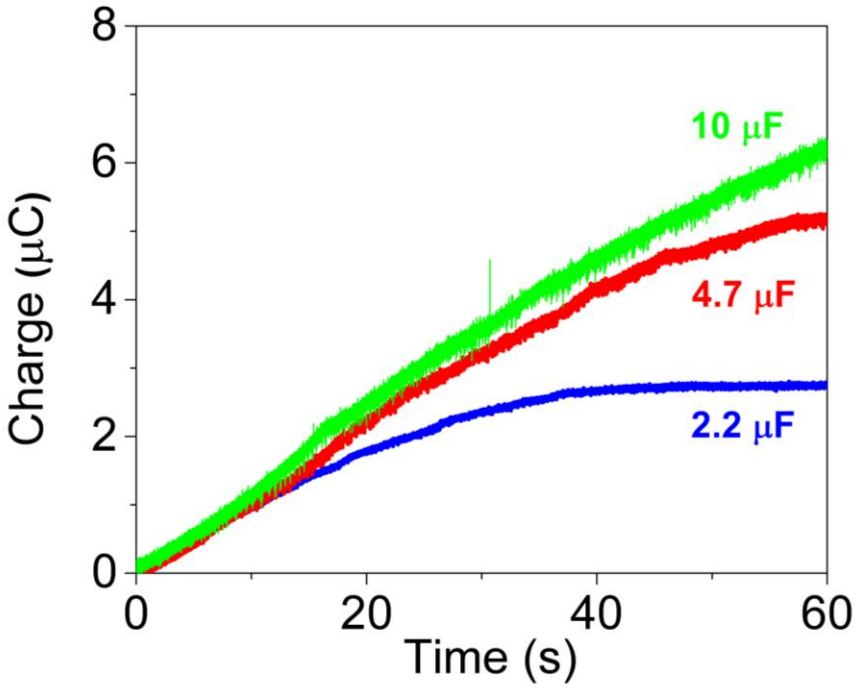

Figure 4A.21: The plot of accumulated charges for 2.2, 4.7 and 10 μF capacitor employing the 20 wt% **MTPBB/PDMS** composite device.

****

Table 5A.1: Selected bond lengths [Å] and angles [°] for compound **[PMe]I**.

Compound	Bond Length		Bond Angle	
[PMe]I	P(1)-N(2)	1.553(13)	N(2)-P(1)-N(21)	111.7(7)
120 K	P(1)-N(21)	1.601(13)	N(2)-P(1)-N(11)	117.5(7)
	P(1)-N(11)	1.654(12)	N(21)-P(1)-N(11)	102.9(6)
	P(1)-N(1)	1.661(12)	N(2)-P(1)-N(1)	111.5(7)
	P(2)-N(2)	1.585(14)	N(21)-P(1)-N(1)	111.6(6)
	P(2)-N(31)	1.61(3)	N(11)-P(1)-N(1)	101.0(6)
	P(2)-N(3)	1.625(15)	N(2)-P(2)-N(31)	110.9(8)
	P(2)-N(41)	2.03(3)	N(2)-P(2)-N(3)	114.0(7)
	P(3)-N(3)	1.542(15)	N(31)-P(2)-N(3)	106.4(12)
	P(3)-N(61)	1.617(12)	N(2)-P(2)-N(41)	90.3(11)
	P(3)-N(51)	1.638(17)	N(31)-P(2)-N(41)	121.9(13)
	P(3)-N(1)	1.697(12)	N(3)-P(2)-N(41)	113.0(11)
	N(1)-C(1)	1.455(19)	N(3)-P(3)-N(61)	109.7(8)
			N(3)-P(3)-N(51)	119.0(9)
			N(61)-P(3)-N(51)	102.1(7)
			N(3)-P(3)-N(1)	110.2(7)
			N(61)-P(3)-N(1)	111.1(6)
			N(51)-P(3)-N(1)	104.3(7)
			C(1)-N(1)-P(1)	117.1(9)
			C(1)-N(1)-P(3)	115.7(10)
[PMe]I	P(1)-N(2)	1.577(17)	N(2)-P(1)-N(11)	112.4(9)
298 K	P(1)-N(11)	1.600(17)	N(2)-P(1)-N(21)	114.1(9)
	P(1)-N(21)	1.632(17)	N(11)-P(1)-N(21)	104.1(10)
	P(1)-N(1)	1.674(13)	N(2)-P(1)-N(1)	111.1(8)
	P(2)-N(2)	1.573(18)	N(11)-P(1)-N(1)	112.1(8)
	P(2)-N(3)	1.619(18)	N(21)-P(1)-N(1)	102.6(8)
	P(2)-N(31)	1.649(19)	N(2)-P(2)-N(3)	116.3(8)
	P(2)-N(41)	1.65(2)	N(2)-P(2)-N(31)	109.4(9)
	P(3)-N(3)	1.580(17)	N(3)-P(2)-N(31)	104.2(11)
	P(3)-N(61)	1.647(14)	N(2)-P(2)-N(41)	99.2(12)
	P(3)-N(1)	1.689(14)	N(3)-P(2)-N(41)	114.1(10)
	P(3)-N(51)	1.710(19)	N(31)-P(2)-N(41)	114.0(12)
	N(1)-C(1)	1.51(2)	N(3)-P(3)-N(61)	112.0(9)
			N(3)-P(3)-N(1)	109.4(8)
			N(61)-P(3)-N(1)	111.1(7)
			N(3)-P(3)-N(51)	117.2(10)
			N(61)-P(3)-N(51)	101.0(8)
			N(1)-P(3)-N(51)	105.7(8)
			C(1)-N(1)-P(1)	116.8(11)
			C(1)-N(1)-P(3)	115.2(10)

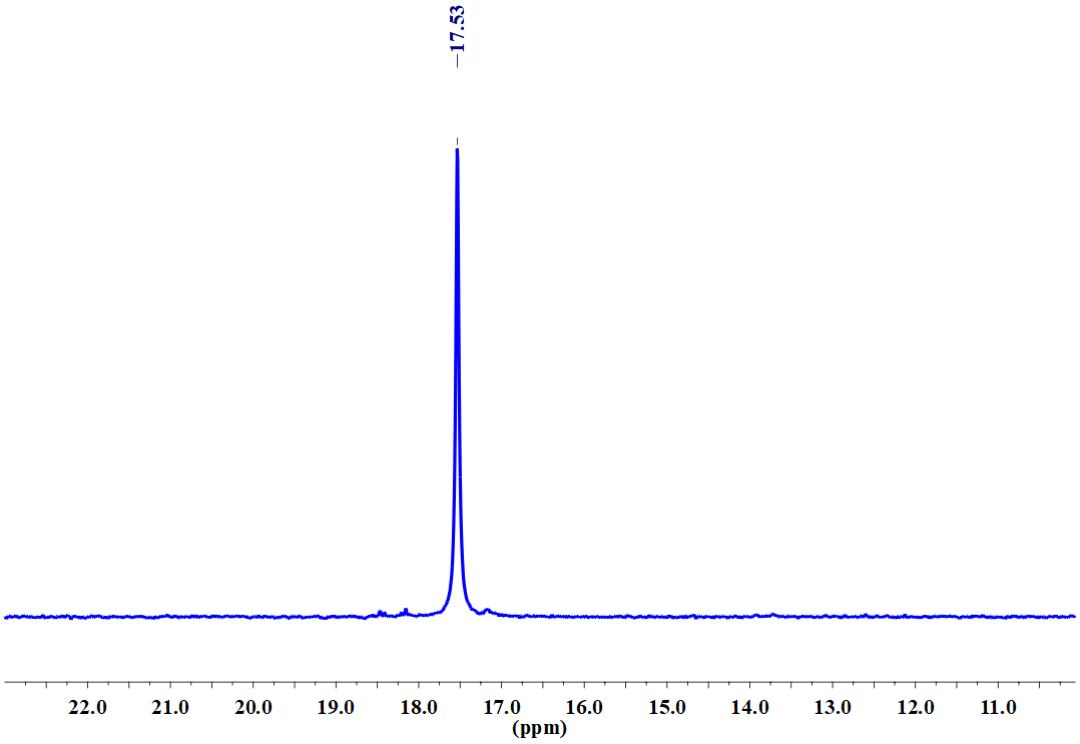

Figure 5A.1: The ^{31}P NMR spectrum of **P**.

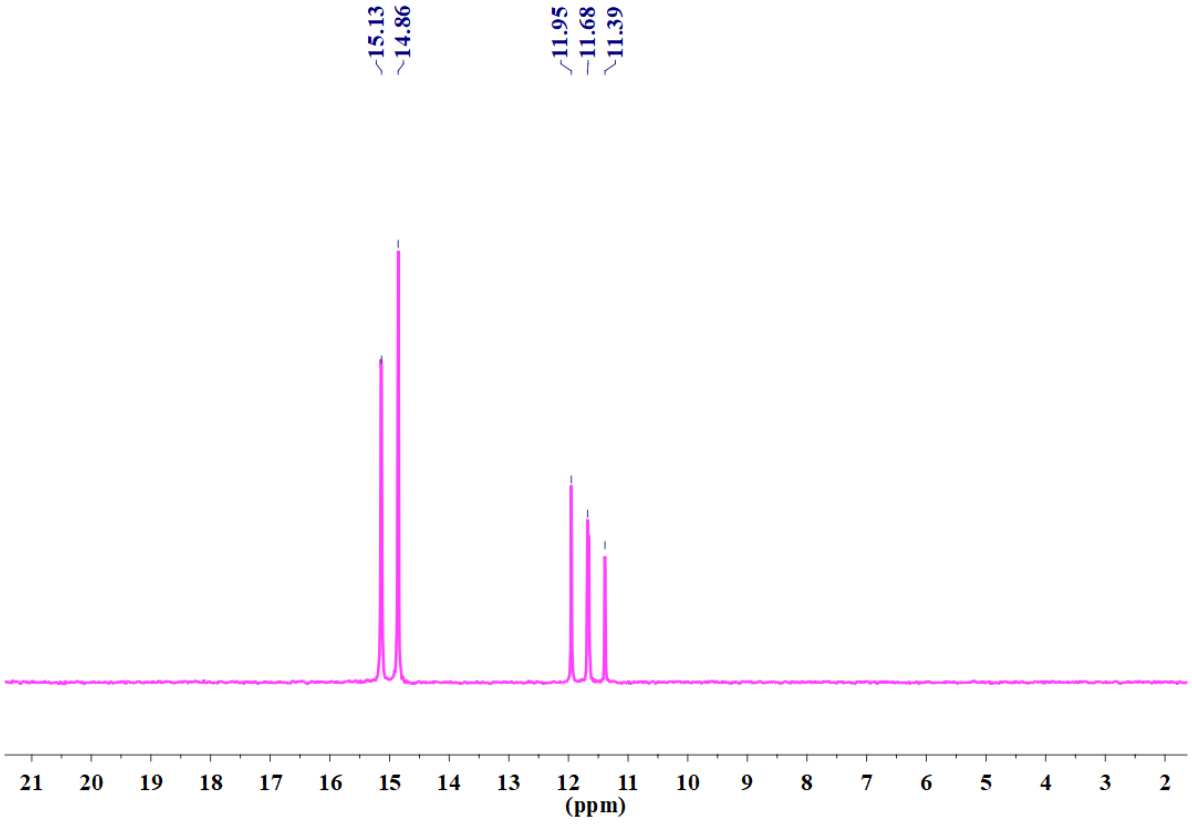

Figure 5A.2: The ^{31}P NMR spectrum of **[PMe]I**.

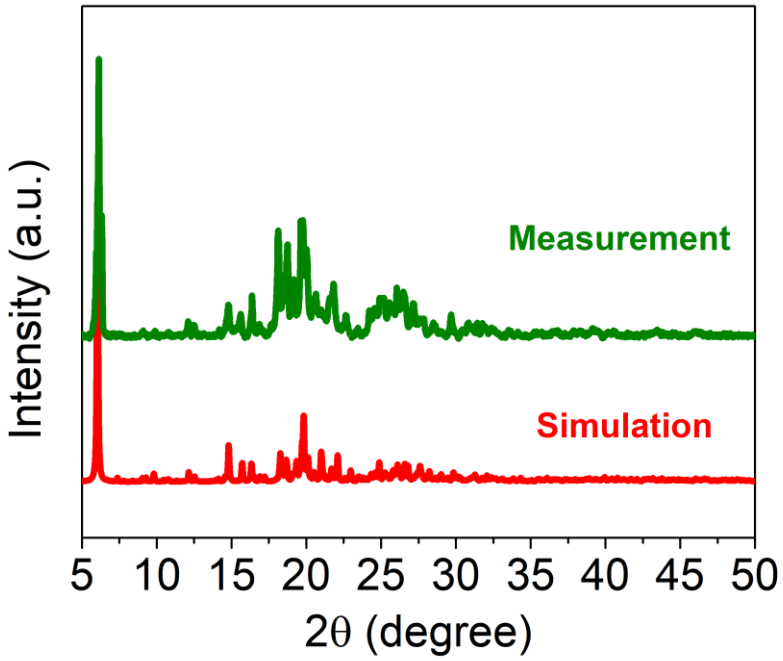

Figure 5A.3: PXRD Patterns of **[PMe]I.**

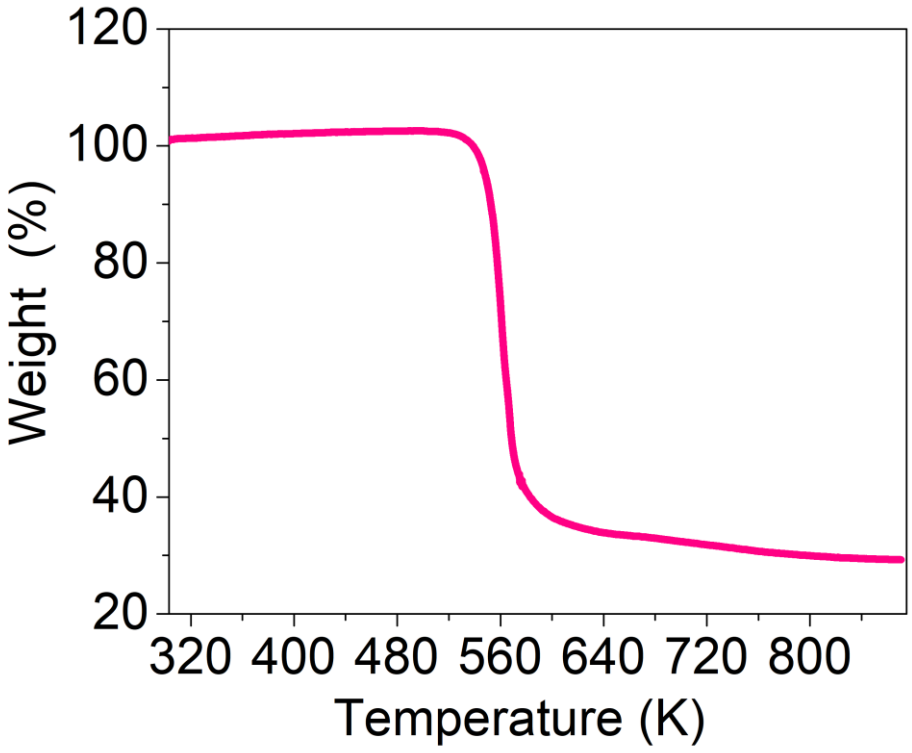

Figure 5A.4: The TGA profile of **[PMe]I.**

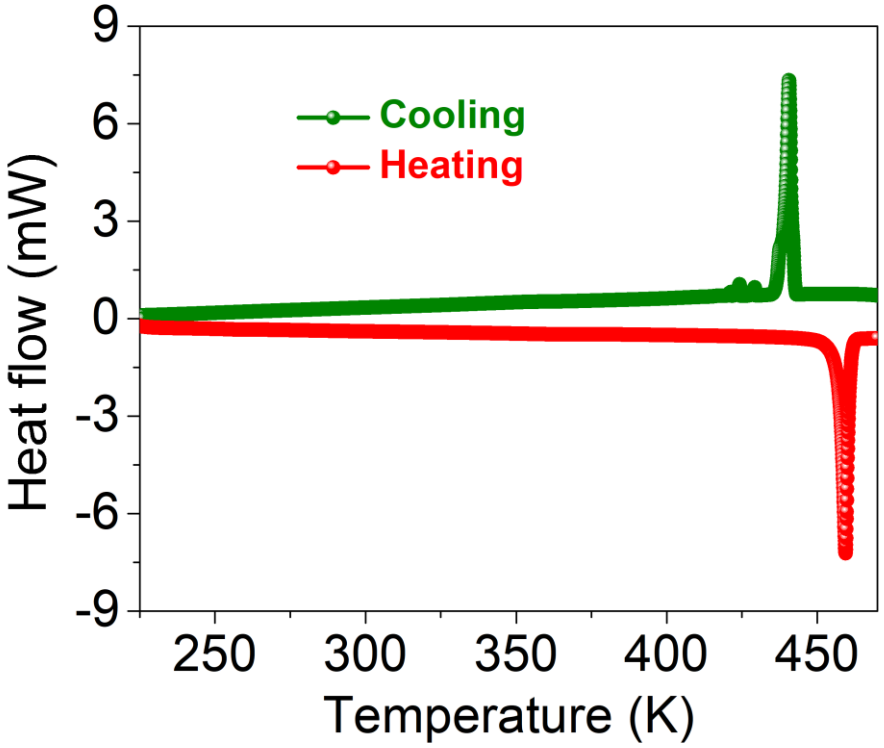

Figure 5A.5: The DSC curves of **[PMe]I.**

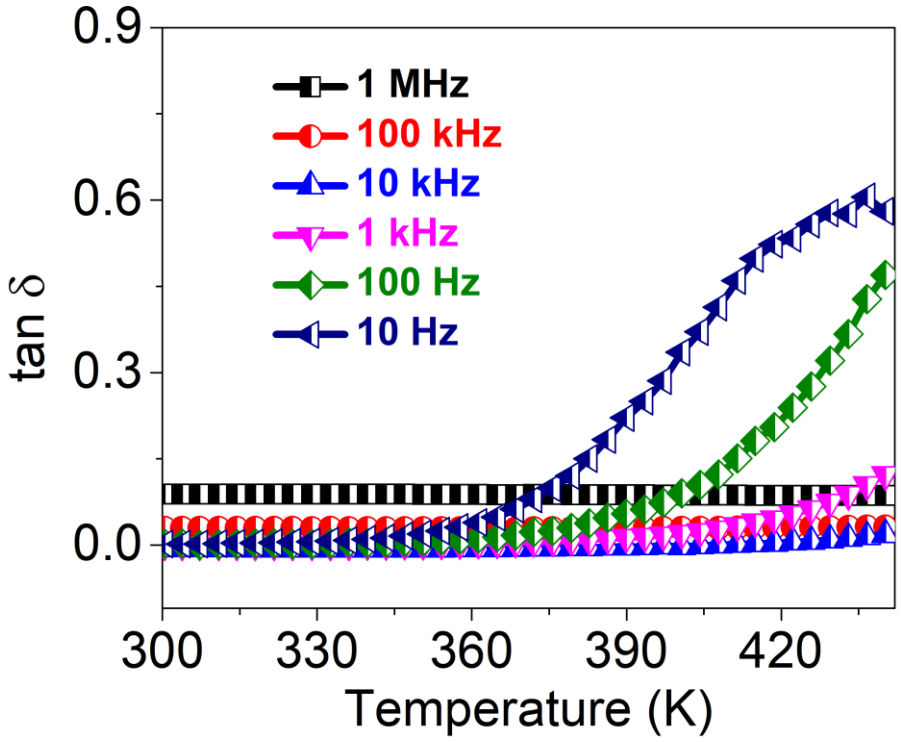

Figure 5A.6: Temperature dependent dielectric loss (tan δ) of **[PMe]I** at various frequencies.

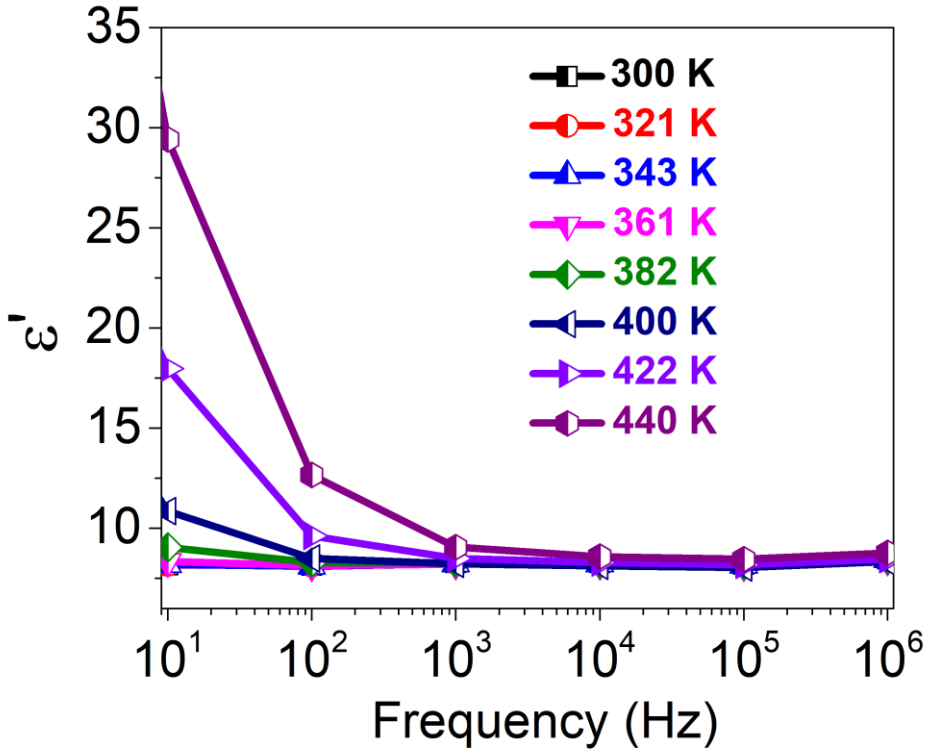

Figure 5A.7: Frequency-dependent dielectric constant (ε′) of **[PMe]I** at various temperatures.

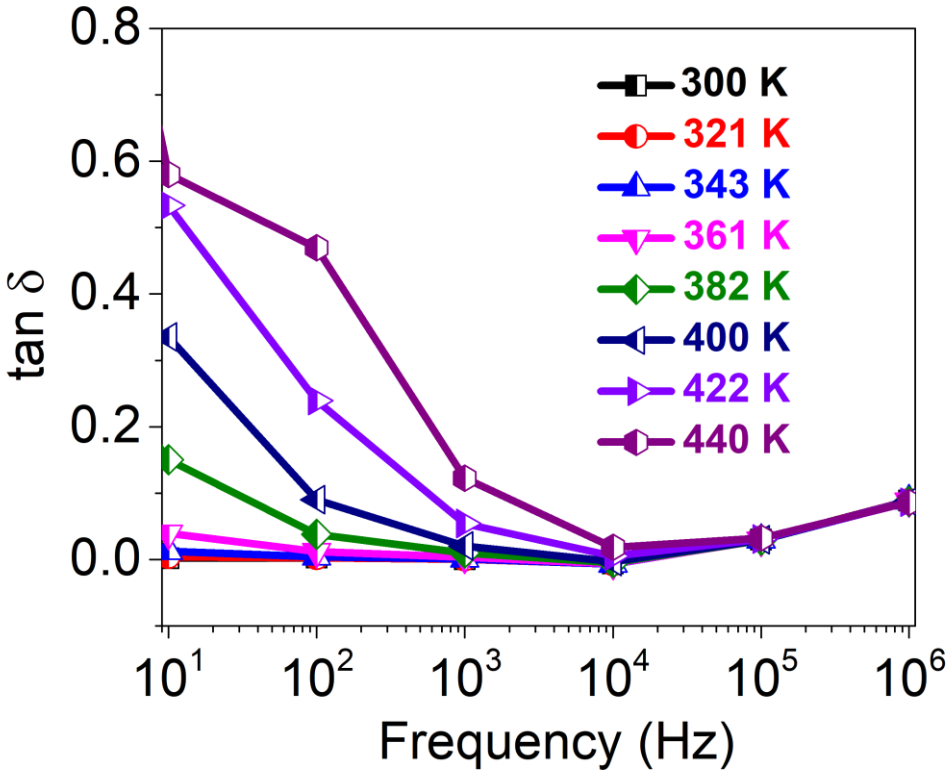

Figure 5A.8: Frequency dependent dielectric loss (tan δ) of **[PMe]I** at various temperatures.

Table 5A.2: Details about the preparation of various weight percentage (wt %) **[PMe]I/TPU** composites.

Composite Materials (%)	[PMe]I (in mg)	[PMe]I + TPU (in mg)
10	13.88	138.88
15	22.05	147.05
20	31.25	156.25
25	41.66	166.66

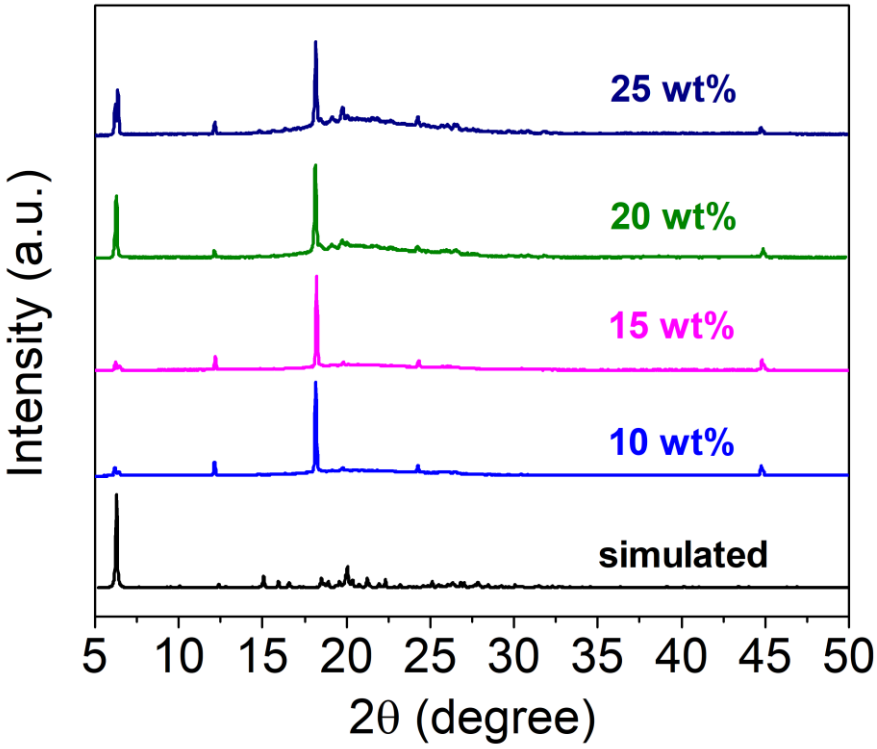

Figure 5A.9: PXRD data of the as-prepared composites with varying concentrations of **[PMe]I.**

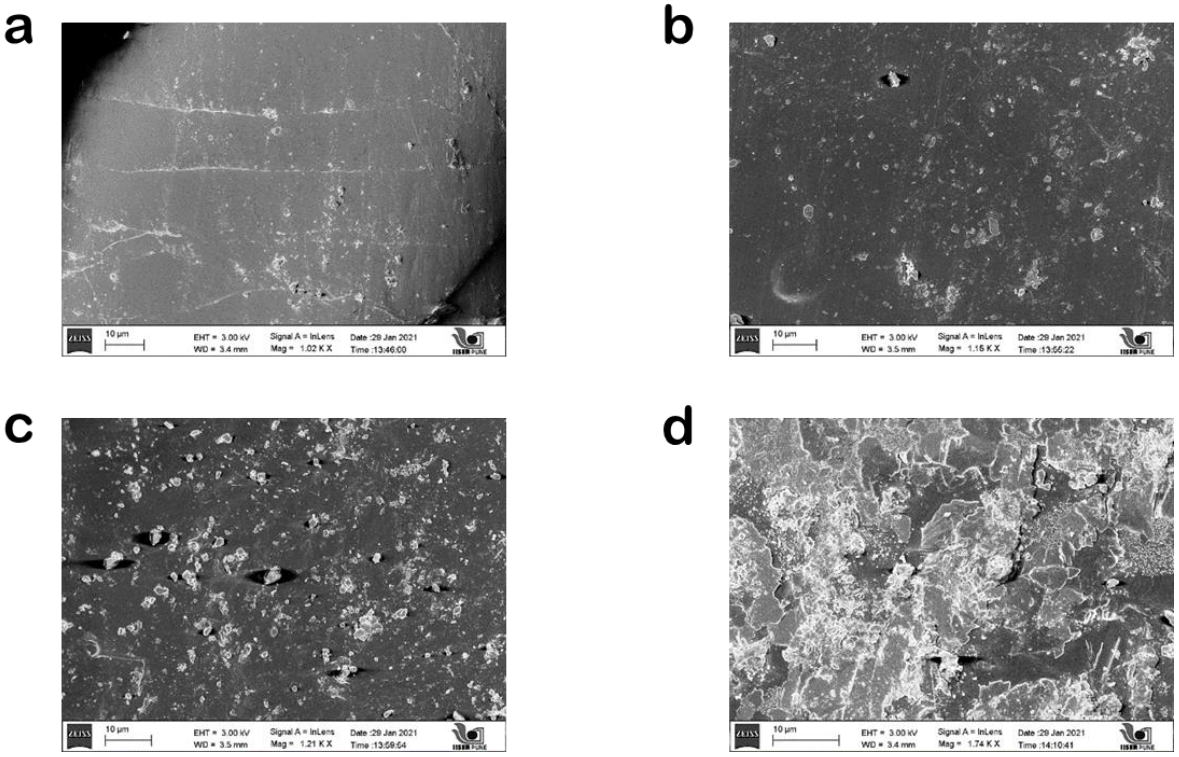

Figure 5A.10: SEM images of (a) 10 (b) 15 (c) 20 and (d) 25 wt % **[PMe]I /TPU** composite films**.**

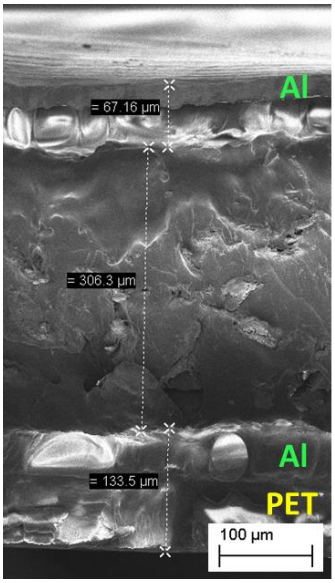

Figure 5A.11: Cross-sectional SEM image of **[PMe]I /TPU** based device showing a thickness of ~0.31 mm for the embedded film of **[PMe]I**.

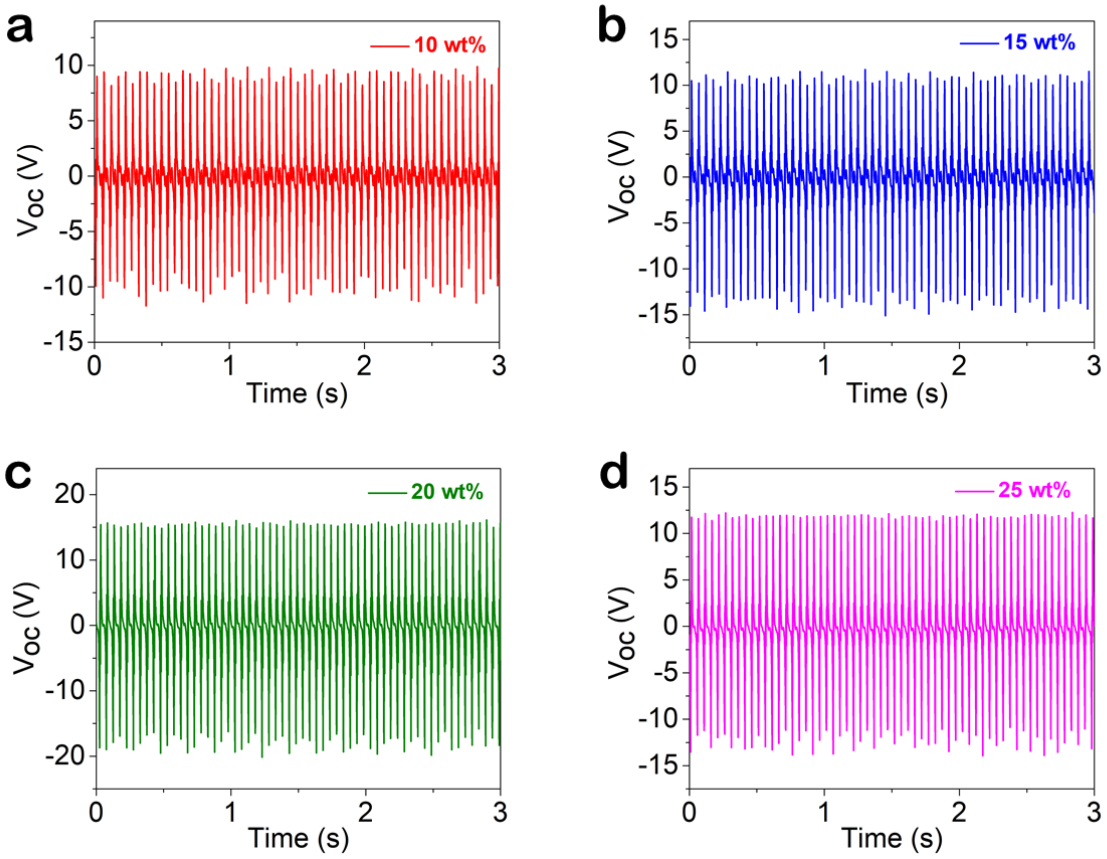

Figure 5A.12: Output Voltage measurements of all the weight % **[PMe]I/TPU** composite films.

****